

Structural Optimization of Mechanical Components for the Wind Industry

Pitch Support Static and Fatigue Analysis

Rui Miguel da Rocha Magalhães

Dissertation submitted to
Faculdade de Engenharia da Universidade do Porto
for the degree of:

Master in Mechanical Engineering

Faculty Supervisor:
Prof. José Correia

Faculty Co-Supervisor:
Prof. Abílio de Jesus

Company Supervisor:
Dr. Fernando de Sousa Marques

Company Co-Supervisor:
Eng. Gustavo Miranda Guimarães

The work presented in this dissertation was performed at the
Vestas Design Centre Porto
Centro Empresarial Lionesa
R. Lionesa Edifício B, 4465-671
Leça do Balio, Portugal.

Rui Miguel da Rocha Magalhães
E-mail: up201506096@fe.up.pt

Faculdade de Engenharia da Universidade do Porto
Departamento de Engenharia Mecânica

Abstract

The main goal of this study is to perform a structural optimization, with both static and fatigue analysis, on a wind turbine component, namely the pitch suspension from Vestas V164-8.0MW wind turbine. An additional study was made, aiming to perform a benchmark of several multiaxial fatigue models, accompanied with a proper damage calculation comparison.

A topology optimization procedure was made to an initial design, aiming for a fast and valid approach on how the optimal shape of the component should look like. This topology optimization aimed to maximize the overall stiffness and resulted in a lug-like shape at the cylinder connectors on the top region of the pitch support. Later, a more refined size optimization of a parametric design based on the results of the topology analysis was made, aiming to achieve the final optimal design. First, the parametric optimization was only applied to a specific portion of the design, referred to the lug-like shape, aiming to minimize the total mass with ultimate failure and fatigue life restrictions. Secondly, a simplified finite element method (FEM) model was developed in order to minimize the complexity of the problem, while ensuring accurate results, leading to faster and less computational demanding simulations. The fatigue life calculations were made with the help of Vestas own fatigue analysis software, Fatigue Wizard (FatWiz). The outcome of this optimization resulted in a lighter component that ensured the necessary performance, as well as an additional financial revenue.

The project further contributes with the development and implementation of a parametric optimization program, using a genetic algorithm optimizer, which allows to perform the optimization of the design while making the static and fatigue life calculations in each iteration, thus handing a solution that is fully ready and meets all structural restrictions. This program is also very versatile, in the sense that it can be applied to all sorts of parametric geometries and restrictions, with some change in the code.

Finally, the additional study on the multiaxial fatigue damage models provided good insight on new approaches and compared them in a quantitative way, with a proportional variable amplitude load case. Several models were tested as well as the one from Fatigue Wizard (Vestas internal software), and a result comparison was performed. In the end, it was verified that, for the analysed load case, Fatigue Wizard provided smaller damage values when compared to Findley's criterion, which is on the non-conservative side.

Keywords: Wind Industry, Structural Optimization, Multiaxial Fatigue, Topology Optimization, Parametric Optimization, Genetic Algorithm, Ansys, MATLAB

Resumo

O principal objetivo deste estudo é realizar a otimização estrutural, acompanhada de análises estáticas e à fadiga, de um componente de uma turbina eólica, nomeadamente a *pitch support* da turbina V164-8.0MW da Vestas. Um estudo adicional foi feito, tendo em vista a realização de uma análise comparativa de vários modelos de fadiga multi-axial, com o respectivo cálculo de dano referente a um espectro de carga.

Foi executada uma otimização topológica num design inicial, tendo em vista uma rápida e eficiente abordagem do formato ideal do componente. Esta análise teve como objectivo maximizar a rigidez e resultou num formato similar ao de um olhal nos conectores do cilindro hidráulico, na região superior do *pitch support*. De seguida, uma análise mais refinada foi feita através de uma otimização paramétrica de uma geometria parametrizada, baseada na análise topológica, esperando-se obter o design final. Em primeiro lugar, esta análise foi apenas feita para os conectores com formato em olhal, tendo como objetivo minimizar a massa, com as restrições de condição extrema e vida à fadiga. Depois, foi desenvolvido um modelo de elementos finitos simplificado, para minimizar a complexidade da análise, resultando em simulações mais rápidas e computacionalmente menos exigentes. Os cálculos relacionados com a fadiga foram feitos com a ajuda do software interno da Vestas, de nome *Fatigue Wizard*. O resultado desta otimização forneceu um componente mais leve que assegura a performance necessária, bem como um rendimento financeiro adicional.

O projeto contribui ainda com o desenvolvimento e implementação de um programa de otimização paramétrica, utilizando como otimizador o algoritmo genético, que permite a otimização da geometria enquanto realiza análises estáticas e de vida à fadiga em cada iteração, fornecendo uma solução que respeita todas as características de performance necessárias. Este programa é também bastante versátil, sendo que pode ser aplicado a todo o tipo de geometrias e restrições, com alguma alteração do código.

Finalmente, o estudo adicional que compara vários modelos de fadiga multi-axiais forneceu um bom conhecimento de novas abordagens e comparou as mesmas de uma forma quantitativa, com um caso de carregamento proporcional e amplitude variável. Vários modelos foram testados bem como aquele referente ao *Fatigue Wizard* (software interno da Vestas), e a comparação dos resultados foi feita. No final, foi verificado que, para o carregamento analisado, o *Fatigue Wizard* forneceu valores de dano inferiores aos fornecidos pelo critério de Findley, sendo por isso resultados não conservativos.

Palavras-chave: Indústria Eólica, Otimização Estrutural, Fadiga Multiaxial, Otimização Topológica, Otimização Paramétrica, Algoritmo Genético, Ansys, MATLAB

To my parents José and Estela whom
I find the privilege to have as role models.

To my brothers Álvaro and David
for the long-lasting love and support.

To my friends for the ever joyful
companionship and brotherhood.

‘Stay Hungry, Stay Foolish’

Steve Jobs

Acknowledgements

I would like to express my deep gratitude to Vestas team, for welcoming me so well and the constant support in the day-to-day tasks concerning the project, ensuring I had all the necessary means and information to perform my work. A special tank you and word of admiration to Dr. Fernando Marques and Eng. Gustavo Guimarães, for all the support and critics throughout the project, proving to be absolutely critical in the development of this thesis, to Eng. Daniel Rodrigues for all the support while manager of the team, and Eng. José Rodrigues for the help with manufacturing the prototypes from additive manufacturing.

I also want to extend my sincere appreciation and thank you to professors Abílio de Jesus and José Correia for the support during the final stage of the project, specially regarding the multiaxial fatigue models. Their help and guidance was decisive in ensuring that the project would follow through with every goal that was set up. Moreover, the supply of literary information at the early stages of the project.

I would also want to express my gratitude to professor Paulo Tavares de Castro, for supplying me with many of the fatigue bibliography that would later be the ground base for all the fatigue information present in this study was very helpful.

To Beatriz Sousa, I would like to express my gratitude and deep admiration for being the perfect right-arm and friend during the project's timeline, supporting me in assuming the additional responsibilities of leading a team at FEUP's students association. Moreover, for all the help given in revising the content and spelling of this report.

To my brother Álvaro, I would like to mention a special thank you for the support and help in learning and exploring the Ansys Workbench functionalities, ensuring me all the necessary information to learn how to use the software faster and more efficiently.

To my family, I would like express my sincere gratitude, for the continuous support and guidance throughout my life, assuming a determining influence in what and where I am.

To my friends, Carlos, Natália, Nuno, Rita and Raquel, a warm thanks for accompanying me in this journey and all the great laughs and experiences that I would take with me in the future. If nothing, they are a significant influence in what I become.

Contents

Abstract	i
Resumo	iii
Acknowledgements	ix
1 Introduction	1
1.1 Motivation	1
1.2 Objectives	3
1.3 Thesis outline	5
2 Background theory	7
2.1 A Review on Wind Turbines	7
2.1.1 The value of wind energy	7
2.1.2 Fundamentals	15
2.1.3 Wind energy conversion systems and working principle	17
2.1.4 Wind turbine	19
2.2 A Review on Fatigue	39
2.2.1 Definition	39
2.2.2 Fatigue stages, influencing factors and regimes	40
2.2.3 Conventional approaches	48
2.2.4 Multiaxial fatigue	64
2.3 A Review on Structural Optimization	77
2.3.1 Optimality criteria methods	78
2.3.2 Fatigue constrained optimization	82
2.3.3 Mathematical programming algorithms	84
2.3.4 Special algorithms	87
3 Pitch support optimization	93
3.1 Introduction	93
3.2 Pitch system	94
3.3 Pitch cylinder support	95
3.3.1 Material requirements	95
3.3.2 Installation requirements	97
3.3.3 Loads	99
3.4 Overview on the optimization method	101

4	Topology optimization	103
4.1	Mesh and contacts	103
4.2	Boundary conditions	104
4.3	Optimization setup	105
4.4	Model simplification	105
4.5	Results	106
4.5.1	Optimal shape	107
4.5.2	Performance comparison	108
5	Parametric optimization	109
5.1	CAD parametrization	109
5.2	Mesh	110
5.3	Boundary conditions	110
5.4	Convergence analysis	111
5.5	Optimization setup	112
5.5.1	Algorithm	114
5.5.2	Fatigue Wizard	116
5.6	Results	119
5.6.1	Ultimate failure	119
5.6.2	Fatigue condition	119
5.6.3	Ultimate failure and fatigue conditions	120
5.6.4	Economic outlook	121
5.6.5	Analysis comparison	123
5.6.6	Equivalent fatigue stress condition	124
6	Fatigue benchmark	127
6.1	Material properties	128
6.2	Multiaxial fatigue damage models	130
6.2.1	Signed von Mises equivalent stress	131
6.2.2	Critical plane normal stress (DNV GL)	131
6.2.3	Findley criterion	131
6.2.4	Dang Van criterion	132
6.3	Fatigue Wizard	133
6.4	Results	133
7	Conclusions	135
7.1	Main conclusions	136
7.2	Future work	137
	References	139
A	Kuhn-Tucker conditions	149
B	Vestas V164-8.0MW	151
B.1	Technical data	151
B.2	Pitch system patent	153

C	Fatigue properties for EN-GJS-400-18LT	155
C.1	Introduction	155
C.2	Reference fatigue strength	155
C.3	Correction factors	155
C.3.1	Mean stresses	156
C.3.2	Surface condition	156
C.3.3	Size/thickness effect	157
C.3.4	Effect of chill casting	158
C.3.5	Quality/NDT	159
C.3.6	Highly stressed volume effect	159
C.3.7	Variable amplitude loading	159
C.3.8	Min/max cut-off	160
C.4	Component fatigue strength	160
D	Ansys element reference	163
D.1	Structural solid elements	163
D.1.1	SOLID185	164
D.1.2	SOLID186	164
D.1.3	SOLID187	165
D.2	Structural plane elements	166
D.2.1	PLANE182	166
D.2.2	PLANE183	167
D.3	Other elements	168
D.3.1	CONTA174	168
D.3.2	TARGE170	168
D.3.3	SURF154	169
D.3.4	BEAM188	170
E	Lug optimization - analytic approximation	173
E.1	Lug analysis - transverse force	173
E.2	Lug optimization	175
E.3	Results	176
E.4	MATLAB code	177
E.4.1	Optimization mainframe	177
E.4.2	Fitness function	181
F	Minimum edge distance for bolted connections	183
G	Comparison between first and superior order elements	185
G.1	Quadrilateral 4-node element	185
G.2	Quadrilateral 8-node element	186
G.3	Mesh comparison	187
H	Parametric optimization program	189
H.1	Matlab code	189
H.1.1	Optimization mainframe	189
H.1.2	Fitness function for the extreme condition	193
H.1.3	Fitness function for the fatigue condition	194
H.1.4	Fitness function for extreme/fatigue combined conditions	195
H.1.5	External programs interaction	196

H.1.6	Stress distribution overwriting	198
H.1.7	Video from run	199
H.2	APDL code	199
H.2.1	Model generation for extreme condition	199
H.2.2	Model generation for fatigue condition	203
H.2.3	Fatigue results post-processing	208
H.3	Batch files	209
H.3.1	Run Ansys for the extreme condition	209
H.3.2	Run Ansys for the fatigue condition	209
H.3.3	Run Fatigue Wizard	210
H.3.4	Run Fatigue post processing	210
I	Estimation of fatigue curves under unknown fatigue data	211
I.1	Introduction	211
I.2	Estimation of fatigue properties with tensile data	211
I.3	Estimation of strain-life curves based on hardness and the elasticity modulus	212
I.4	Methodology	214
I.5	Results	215
J	Matlab programs for the fatigue benchmarking	217
J.1	Bi-linear extrapolation of stress spectrum	217
J.2	Critical plane normal stress (DNV GL)	218
J.3	Dang Van criterion	220
J.4	Findley criterion	222
J.5	Signed Von Mises equivalent stress	224
K	Ansys examples	227
K.1	Cantilever beam	227
K.1.1	Mesh	228
K.1.2	Boundary conditions	228
K.1.3	Optimization setup	229
K.1.4	Results	229
K.2	Hook support	232
K.2.1	Mesh	232
K.2.2	Contacts and joints	233
K.2.3	Boundary conditions	233
K.2.4	Optimization setup	234
K.2.5	Results	234
K.2.6	Additional notes	236

List of Figures

1.1	Structural optimization of the engine pylon [1]	1
1.2	Structural optimization of the wing box rib [2]	2
1.3	Ferrari 458 Italia front hood: reference model and new layout from the optimization results [3]	2
1.4	Front plate	3
1.5	Optimal solution from the optimization	4
2.1	Top markets in 2019 for onshore and offshore wind power generation [4] . .	7
2.2	Top markets in 2019 for onshore and offshore wind power generation [4] . .	8
2.3	Annual investment in wind energy 2009-2019 [4]	9
2.4	Total installed cost of wind projects and prospects for 2030 and 2050 [7] . .	10
2.5	Top 15 wind turbine suppliers in 2018 [7]	11
2.6	Global market share by turbine technology in 2018 [7]	11
2.7	Global power capacity outlook for 2040 [23]	13
2.8	New installations in 2020 - 2024 [4]	14
2.9	Expected annual offshore wind installation by state, 2020-2026 (MW) [4] . .	15
2.10	Schematics of air flow at velocity U through area A . The cylinder depicts the volume flowing in unit time ∂t through area A [24]	15
2.11	Rotor concepts of VAWTs [26]	17
2.12	Power coefficients of wind rotors of different designs [27]	18
2.13	Wind rotor concepts combined with static structures for concentrating wind energy [26]	19
2.14	<i>Fixed-speed wind turbines</i> - Type 1 [31]	20
2.15	<i>Limited variable-speed wind turbines</i> - Type 2 [31]	21
2.16	<i>Variable-speed wind turbines with partial-scale power converter</i> - Type 3 [31]	21
2.17	<i>Variable-speed wind turbines with full-scale power converter</i> - Type 4 [31] .	22
2.18	A schematic of the gearless <i>Goldwind</i> wind turbine [32]	22
2.19	Main systems of Vestas V150-5.6 MW TM	23
2.20	Wind turbine different components and systems	23
2.21	Power train of the Vestas V-39 in standard design [26]	24
2.22	Rotor blade standard designs	25
2.23	Blade connections to the rotor hub	27
2.24	Cast rotor hub of the Nordex N-80 wind turbine [26]	28
2.26	Hydraulic blade pitch systems	29
2.27	Electrical blade pitch system of the Dutch Lagerwey LW-72 inside the rotor hub [26]	30
2.28	Mechanical transmission concepts	31
2.29	Examples of rotor brakes	32
2.30	Examples of gearbox concepts	33

2.31	Yaw system with assembly of the Westinghouse WTG-0600 [35]	35
2.32	Tower configurations	37
2.33	Schematic of initiation life fraction N_i/N vs. total life or stress excursion [37]	40
2.34	Schematic view of STAGE I, STAGE II and STAGE III of fatigue [37]	40
2.35	<i>S-N curve</i> , cyclic stress σ_a versus number of cycles to failure N , also known as <i>Wöhler's diagram</i> , showing the three regions that characterize fatigue behaviour [37]	41
2.36	Difference between <i>S-N curve</i> derived using equivalent ideally elastic stress procedure and conventional <i>S-N curve</i> obtained directly in stress controlled tests [37]	43
2.37	Two types of <i>S-N curves</i> [37]	43
2.38	Two-fold <i>S-N curve</i> type concept [39]	44
2.39	Effect of surface finish on the <i>fatigue limit</i> of steel [43]	45
2.40	Effects of mechanical treatments in fatigue life	46
2.41	Typical ultrasonic fatigue test results for high strength steels	47
2.42	Relative <i>S-N</i> behaviour under various environmental conditions [36]	48
2.43	Fatigue test results for conventional JIS-S35C carbon steel [50]	48
2.44	<i>Fatigue limit</i> versus ultimate strength for various steels and cast iron [51]	49
2.45	Comparison between Murakami predictions for different defect area and experimental data of Fig. 2.44 [37]	50
2.46	a) Schematic showing engineering curve $\varepsilon - \sigma$ and true strain-true stress curve $\varepsilon_t - \sigma_t$, b) Schematic of traction specimen at necking [37]	51
2.47	Haibach correction to the Basquin line [37]	52
2.48	a) Fully reversed cycle with zero mean stress ($\sigma_m = 0$); b) Non-symmetric cycle ($\sigma_m > 0$) and minimum stress $\sigma_{min} > 0$; c) Pulsating cycle fluctuating from zero or from the origin ($\sigma_m = \sigma_a > 0$, $\sigma_{min} = 0$) [37]	53
2.49	Wöhler's curves or S-N diagram obtained on a 2024-T351 aluminum alloy for various R ratios [57]	53
2.50	Lines of constant fatigue life, uniaxial stress amplitude with tensile mean stress proposed by Gerber, Goodman and Soderberg, respectively [37]	54
2.51	Haigh diagram showing the mean stress sensitivity factor M and its dependence on mean stress [37]	55
2.52	$\tau_m - \tau_a$ diagram for unnotched torsion members of ductile metal [62]	56
2.53	<i>Haigh diagram</i> representing the safety domain for any combination $\sigma_m - \sigma_a$ [37]	56
2.54	<i>Smith or Modified Goodman diagram</i> for axial and bending fully reversed loads, ductile metals [37]	57
2.55	<i>Master curve</i> for AISI 4340 steel [63]	57
2.56	Schematic of flexural loads induced in an airplane wing during a flight [37]	58
2.57	Illustration of the rainflow counting technique. Identification of reversals and loading cycles [65]	59
2.58	ASTM <i>three point cycle counting</i> rule [36]	61
2.59	Time histories with different orders of application [37]	62
2.60	Non-linear damage progression and accumulation [37]	62
2.61	<i>S-N curve</i> of different types of materials	63
2.62	Model for extrapolating high-cycle fatigue beyond 10^6 cycles by using elastic line segments of progressively reduced slope [75]. a) Slope steeper than 0.12; b) Slope shallower than 0.12.	64
2.63	R^2 values for various values of α in the new model [39]	65

2.64	Predictions of behaviour in VHCF for SCM440 [39]	65
2.65	Strain or stress conditions for IP and NP loading	66
2.66	Example of IP and OP load paths and illustration of NP factor [37]	66
2.67	Equivalent stress–strain response of 1050 QT and 304L SS under non NP hardening and NP hardening conditions [37]	67
2.68	Monotonic and cyclic curves and corresponding stresses at a given strain [37]	68
2.69	A normal stress on the critical plane enables the micro-crack to open over- coming friction interlocking effects [37]	72
2.70	Types of cracks in Brown and Miller failure model [37]	73
2.71	Illustration of PDMR cycle counting procedure (2D problem) [105]	75
2.72	PDMR applications 3-D problems [105]	76
2.73	Unit cell with material and void domain [106]	79
2.74	Design domains and the level set model [113]	81
2.75	Reproduction and mutation processes in GAs [125]	89
2.76	Optimization histories [126]	91
3.1	Vestas V164-8.0MW	93
3.2	Pitch system assembly	94
3.3	Exploded view of the segmented pitch ring [128]	95
3.4	Current design of pitch cylinder support	96
3.5	Overview of the proposed designs	96
3.6	Calculated fatigue data (for $R = -1$)	98
3.7	EN-GJS-400-18U-LT tension $S-N$ curve	98
3.8	Installation requirements for the cylinder support	98
3.9	Loading coordinate system	99
3.10	Pitch system loading configuration	100
3.11	Bolted connections in the pitch support system	100
3.12	Example of a time history from the pitch force of a Vestas V164-8MW turbine	101
3.13	Phases of the optimization methods	102
4.1	Topology optimization model mesh	104
4.2	Topology optimization model boundary conditions	105
4.3	Load application in the simplified model for the topology optimization	106
4.4	Topology results for the initial model	107
4.5	Topology results for the simplified model	108
4.6	Model comparison for the topology optimization	108
5.1	Parametric CAD model of the lug	109
5.2	Mesh and boundary conditions for the parametric analysis	111
5.3	Convergence analysis overview	112
5.4	Relation between the damage and SRF	113
5.5	Parametric optimization program overview	115
5.6	Fatigue wizard workflow	117
5.7	Stress interpolation scheme	118
5.8	Results for the optimal design regarding the ultimate failure and fatigue conditions separate	121
5.9	Results for the optimal design regarding the ultimate failure and fatigue conditions	122
5.10	Design results for the parametric optimization	122
5.11	Overview on the analysis running times	124

LIST OF FIGURES

5.12	Equivalent fatigue stress results	125
6.1	Stress spectrum for the fatigue benchmark	128
6.2	Pure torsion S - N curve	129
6.3	Evolution of material parameter κ in <i>high cycle fatigue</i>	130
6.4	Equivalent fatigue stress spectrum for all models	134
B.1	Mounting points of hydraulic drives in PCT application WO 2017/005264 A1153	
B.2	Exploded view of the pitch system [129]	153
C.1	Fatigue test results corrected for $T = 70$ mm	156
C.2	Surface correction factor for machined surfaces	157
C.3	Effects of machined and casting thickness	158
C.4	Formulation of HBV correction factor	160
C.5	SN curve for EN GJS400-18LT	161
D.1	Structural solid elements geometry [135]	163
D.2	Structural plane elements geometry [135]	166
D.3	CONTA174 element geometry [135]	168
D.4	TARGE170 geometry overview [135]	169
D.5	SURF154 geometry overview [135]	169
D.6	BEAM188 geometry overview [135]	170
E.1	Lug Schematic	174
E.2	Efficiency factor computation	175
E.3	Solutions design space analysis	177
F.1	Overview on the minimum edge distance	183
G.1	Coordinate system for 2D quadrilateral elements	185
G.2	Mesh comparison for both meshes	188
I.1	Results for EN-GJS-400-18U-LT	215
K.1	Cantilever initial geometry	228
K.2	Meshing aspects for the cantilever beam example	228
K.3	Boundary conditions for the cantilever beam example	229
K.4	Optimal solutions for load case 1	229
K.5	Stress results for load case 1	230
K.6	Optimal solutions for load case 2	230
K.7	Stress results for load case 2	231
K.8	Hook initial geometry	232
K.9	Meshing aspects for the hook example	232
K.10	Boundary conditions for the hook example	233
K.11	Optimal solutions for the hook example	235
K.12	Stress results for the hook example	235

List of Tables

1.1	Overview on the deformation results from the topology optimization of the front plate, for three load cases	4
2.1	Wind Power Classes Measured at 50 m Above Ground According to NREL Wind Power Density-Based Classification [24]	16
2.2	IEC 61400-1 classification of wind turbines [30]	19
2.3	Mechanical Failure Models [36]	39
2.4	Cycle counts based on rainflow counting technique	60
2.5	PDMR counting results for loading path shown in Fig. 2.71 [105]	76
3.1	Material properties of the current pitch support system	97
3.2	Safety factors for the materials in the current solution	97
3.3	Summary of the installation restrictions	98
3.4	Summary of the bolted connections	101
4.1	Material designation and model properties	103
4.2	Mesh quality and overview	104
4.3	Contact overview for the topology optimization model	104
4.4	Optimization setup overview	106
4.5	Mesh quality and overview	107
5.1	Parameter set-up: lower and upper boundaries of the first population	110
5.2	Genetic algorithm options set	116
5.3	Filter size for the adaptive approach	117
5.4	Fatigue Wizard options set	119
5.5	Result overview for the ultimate failure condition parametric optimization	120
5.6	Result overview for the fatigue condition parametric optimization	120
5.7	Result overview for the ultimate failure and fatigue conditions parametric optimization	121
5.8	Production summary of the intervening parts	122
5.9	Economic outlook summary	123
5.10	Result performance summary	124
6.1	Parameter set for the reference model used in the fatigue benchmark	127
6.2	Fatigue data overview	129
6.3	Result summary for the fatigue benchmark	133
B.1	Design and operation aspects of Vestas V164-8.0MW [134]	151
B.2	Electrical aspects of Vestas V164-8.0MW [134]	152
B.3	Constructive aspects of Vestas V164-8.0MW [134]	152

LIST OF TABLES

C.1	Correction factors for quality of casting	159
E.1	Lug analysis problem constants	174
E.2	Overview on the genetic algorithm setting for the lug analysis	176
E.3	Result overview of the lug analysis	176
I.1	Summary of Conffi-Manson's parameters estimations [140]	216
K.1	Material properties of Ansys structural steel	227
K.2	Geometry and loading aspects for the cantilever beam example	228
K.3	Results overview for load case 1	230
K.4	Results overview for load case 2	231
K.5	Overview of contact/joint modelling for the hook example	233
K.6	Overview on boundary conditions for the hook example	234
K.7	Overview of the optimization setup for the hook example	234
K.8	Results overview for the hook example	235

Introduction

1.1 Motivation

Once again, humanity is on the brink of another revolutionary breakthrough. Throughout the history, there have been 4 major eras: hunter-gatherer, agricultural, industrial and information; and specialists around the world state that the next era is very near, which is called the augmented era. It goes by this name due to an improvement of individual and collective capabilities through a series of technologies that will allow humans to prosper in the next few generation. Some examples may already be presented such as the smart-phone or laptop, which are practically extensions of ourselves on the everyday life and allow things otherwise impossible in the XX century.

One important aspect to this study are the computational developments, both in terms of software and hardware, which led to augmented procedures in engineering as well. The introduction of finite element analysis (FEA) and subsequent optimization algorithms revolutionized the structural optimization procedures, leading the markets to invest millions of dollars into the development and design of new optimized solutions of their products. Also, major developments in the manufacturing processes, e.g. additive manufacturing, made possible to design almost every conceivable shape with less restrictions than conventional processes, e.g. casting or machining. This allowed for top edge companies, e.g. the automotive and aeronautical sector, to achieve high performance products with cost efficient prices, tearing down the competition.

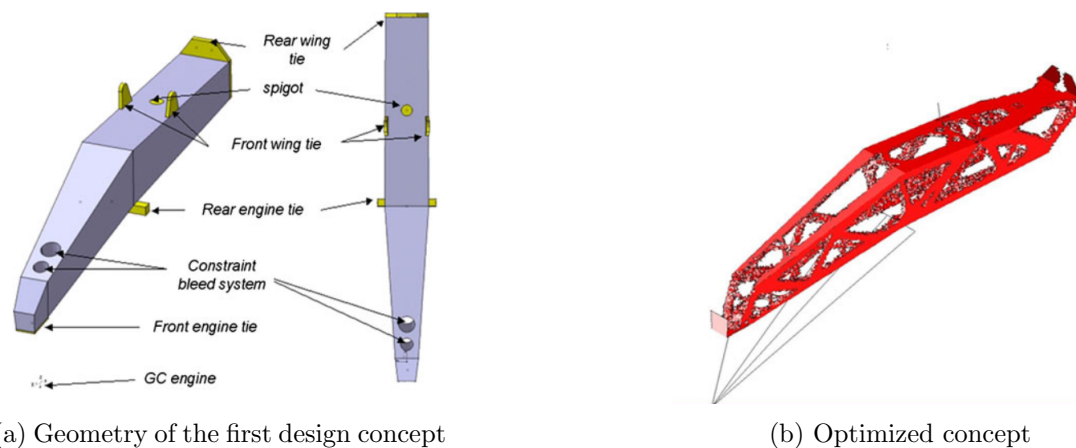


Figure 1.1: Structural optimization of the engine pylon [1]

For instance, in the aeronautical sector, structural optimization can be implemented

on the aircraft pylon (see Fig. 1.1a [1]) or wing box ribs (see Fig. 1.2a [2]). In both studies [1; 2], the goal was to minimize compliance, which is the inverse of stiffness, thus making the structures lighter and stronger, while considering several load cases at the same time, by a weighted sum. In terms of the pylon, Fig. 1.1b [1] clearly depicts the weight improvement while ensuring performance.

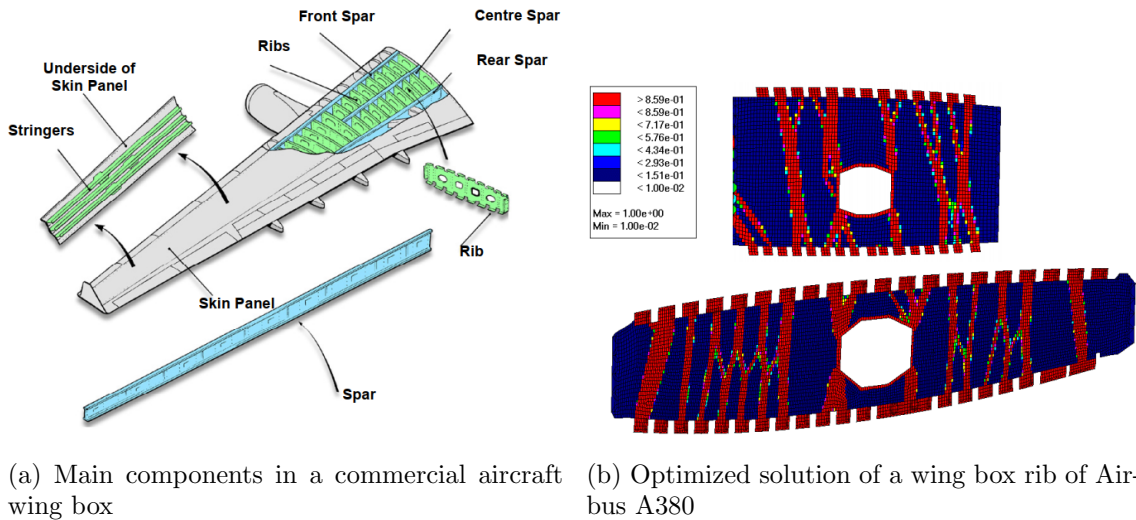


Figure 1.2: Structural optimization of the wing box rib [2]

The automotive industry also uses FEA coupled with topology optimization algorithms in order to optimize parts. Fig. 1.3 [3] displays the design optimization process of the hood of the Ferrari 458 Italia front hood, aiming to reduce weight while maintaining performance and manufacturability targets. The optimized region represented the internal frame, respecting a combination of bending and torsion static load cases, compliance when closing the hood and deformations under aerodynamic loads. The optimal design (see Fig. 1.3c [3]) characterized a 12 percent weight reduction, yet respecting all the performance requirements.

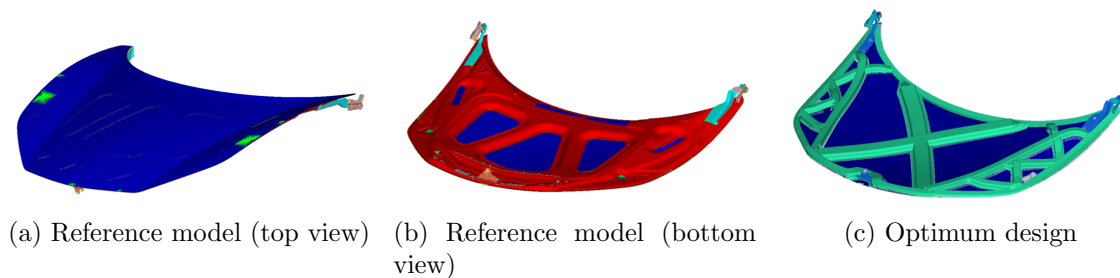


Figure 1.3: Ferrari 458 Italia front hood: reference model and new layout from the optimization results [3]

It is also important to emphasize a more “down to earth” aspect that comes by ensuring that the design meets the expectations. In product life, one major aspect is fatigue analysis, since it is generally responsible for the products failure or end of life. So it is imperative to either insert the fatigue analysis directly into the optimization procedure, commonly inferred as a constraint, or post-analysing the optimal design to ensure it resists the fatigue loads throughout its entire lifetime.

Note that all optimum designs show complex almost “strange” like structures, that would be very hard to be conceived without the help of computational software. This is the most important aspect of the current product design. Combining the rational knowledge of the engineer with the unparalleled potential of computational aided mechanics, allowing companies to develop the most efficient products with relative ease.

Vestas has also invested in the optimization of its products, aiming for lowering the levelized cost of energy (LCOE) while improving performance. An example of this is the optimization of the front plate (see Fig. 1.4a). As it can be seen in Fig. 1.4b, the component is responsible for connecting the hub to the structure of the nacelle. The goal was to improve stiffness and weight.

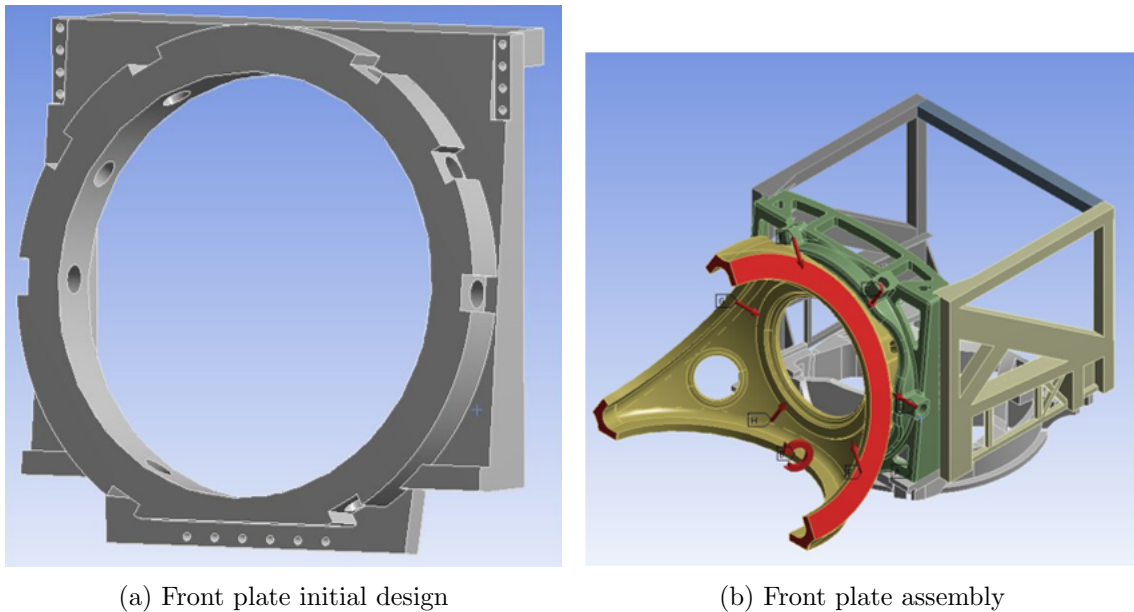


Figure 1.4: Front plate

A topology optimization was made, recurring to TOSCA, and the optimized shape is shown in Fig. 1.5a. After some shape redesign and smoothing the final shape (see Fig. 1.5b) delivered a 19.8 percent weight reduction. In terms of stress, there were no significant changes. On the other hand, the deformation showed more critical results with a maximum increase of 3.49 percent. Table 1.1 displays an overview of the results.

In line with this example, this study proposes to optimize a component from Vestas portfolio of wind turbines, aiming to reduce the costs while maintaining, or even bettering, the performance.

1.2 Objectives

In line with the growing motivation of leading companies such as Vestas, this study proposes to optimize the pitch support of a wind turbine, focusing on the main goals:

- Reduce mass
- Ensure the component’s performance in terms of:
 1. Ultimate failure
 2. Fatigue life

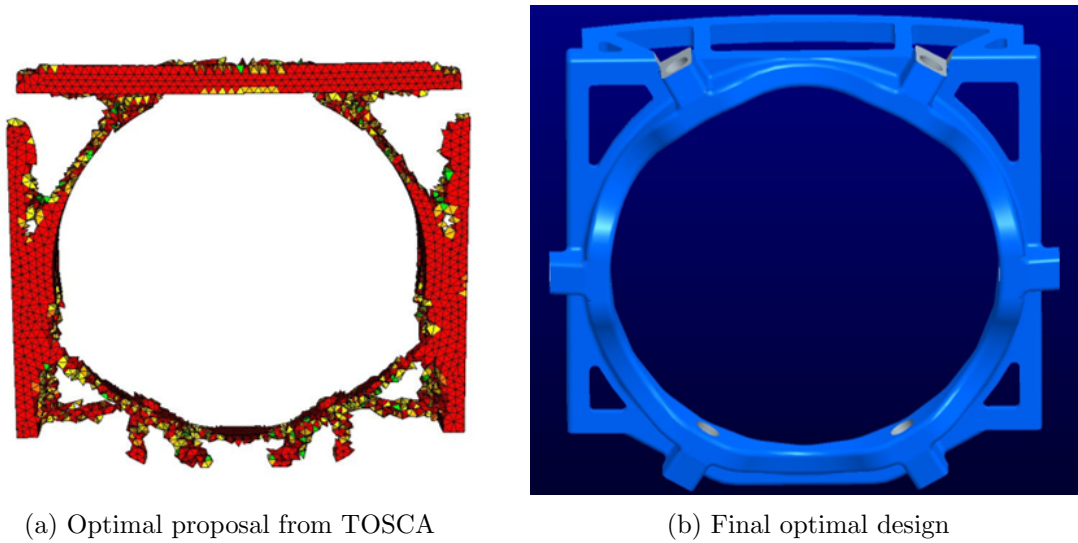


Figure 1.5: Optimal solution from the optimization

Absolute results

Design	Weight [t]	Front plate [mm]			Hole model [mm]		
		LC1	LC2	LC3	LC1	LC2	LC3
Initial	17.20	3.30	0.55	0.34	8.03	3.15	2.93
Optimal	13.80	3.38	0.56	0.35	8.22	3.26	2.98

(a) Absolute values

Result comparison

Design	Weight reduction [%]	Front plate [%]			Hole model [%]		
		LC1	LC2	LC3	LC1	LC2	LC3
Optimal	19.77	2.42	1.82	2.94	2.37	3.49	1.71

(b) Comparative analysis

Table 1.1: Overview on the deformation results from the topology optimization of the front plate, for three load cases

In order to achieve these goals, the following task were defined:

- Develop static FEM models to represent the several load cases
- Perform a topology optimization aiming to maximize stiffness
 - Combine load cases
 - Define optimal shapes
- Perform a parametric optimization aiming to minimize weight
 - Perform static analysis in extreme loading conditions
 - Perform a fatigue analysis with the real time history
 - Develop a parametric optimization program, with ultimate failure and fatigue life restrictions

On the other hand, in order to assess the safety of the fatigue analysis procedures at Vestas, this study also proposes to perform a comparison between multiaxial models, focusing on the following aspects:

- Widen the multiaxial fatigue knowledge
 - Study multiple multiaxial fatigue damage models
 - Define differences between the models
- Model comparison
 - Perform a fatigue analysis with a reference time history
 - Compare results

All previously mentioned analysis were performed in Ansys 2019 R3, for creation of FEA models and topology optimization, with the help of MATLAB to side-process some optimization algorithms for special cases later to be reported.

In parallel with this practical objective, a complete review on the state of art is made, concerning the following areas:

- Wind market, policies and technologies
- Fatigue review
 - Conventional uniaxial approaches
 - Multiaxial models
- Structural optimization review
 - Topology optimization models
 - Fatigue constrained optimization
 - Special optimization algorithms

1.3 Thesis outline

Following this brief introduction, the document is composed by six different chapters aiming to present the state of art of the approached subjects, the case study, methods used, results and conclusions:

- Chapter 2 concerns the background fundamentals of the different subjects. It starts with a brief review on the wind energy market and technologies, followed by a summary of fatigue models and approaches, finalizing with an overview on the structural optimization techniques and algorithms
- Chapter 3 describes the case study and the proposed mainframe methodology
- Chapter 4 explains the topology optimization study and its results
- Chapter 5 focuses on the parametric optimization of the optimal design, explaining the developed program and setup, and its results
- Chapter 6 displays the additional study on the benchmark of multiaxial fatigue models, with a brief model comparison
- Finally, the conclusions drawn from the project, the main contributors and suggestions for future work follows in Chapter 7

Background theory

2.1 A Review on Wind Turbines

2.1.1 The value of wind energy

The wind power generation market has grown exponentially in the beginning of the 21st century (see Fig. 2.1 [4]), from 17 GW [5] to 651 GW of global cumulative installed capacity in 2019 [4], with an compound annual growth rate (CAGR) of 21 percent since 2000. The growing social and political environmental interests combined with the evolution of available technology propelled the so-called renewable energy sources and the wind power stakeholders and investors quickly positioned themselves into the second most dominant energy source in the renewable market, just below the hydropower. An early political and private investment towards the renewable energy generation among many countries, to achieve the energy transition, namely in wind energy projects, has led the industry to develop even more efficient solutions and wind power is now an important player in the sector.

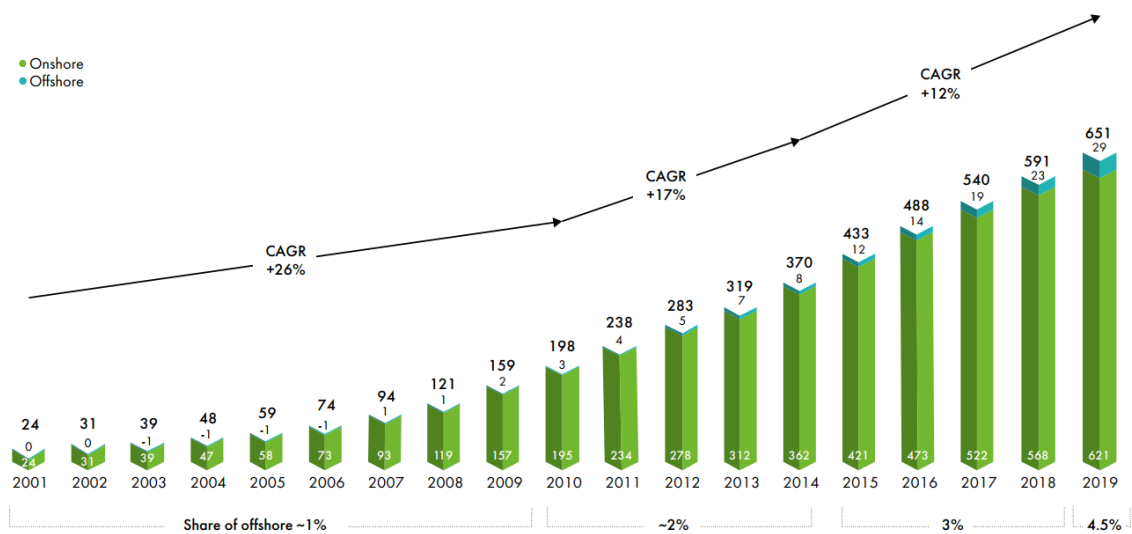


Figure 2.1: Top markets in 2019 for onshore and offshore wind power generation [4]

Market overview

Although wind energy is still rather insignificant in the global energy resources picture, it must be noted that this accounts for every aspect of energy conversion, from transportation to the electricity generation, in which wind power only truly states itself. In 2015, wind as a primary resource would account for less than 1 percent of energy consumption in the world, but in power generation, it amounted 4 percent (432 GW) of global capacity [6].

In terms of the most relevant markets around the world, three definite powerhouses can be distinguished: China, USA and Europe, in that order. Fig. 2.2 [4] displays the top markets in wind power by 2019. One can verify the China's supremacy in terms of wind power generation, followed by the USA and Europe. Looking more specifically to 2019, there was a 60.4 GW increase, with China and USA remaining the world's largest markets, accounting for more than 60 percent of new onshore additions. Although Germany's market shrunk by 55 percent, Europe still saw a 30 percent year-over-year (YoY) growth mostly due to strong investments in Spain, Sweden and Greece [4]. This increase in capacity is followed by an increase in the global investments in both onshore and offshore projects (see Fig. 2.3 [4]) amounting a total of USD 142.7 billion.

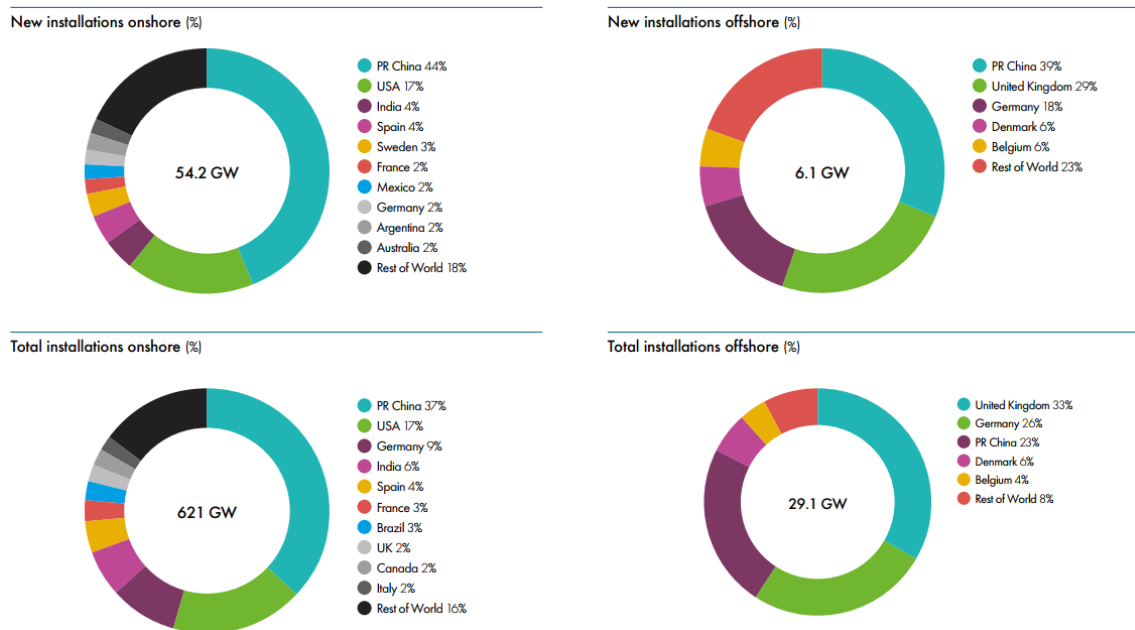


Figure 2.2: Top markets in 2019 for onshore and offshore wind power generation [4]

Another important aspect to consider are the investment costs and the levelized cost of energy (LCOE) which is an effective way to account the installation and operation costs in the project life, thus reflecting the competitiveness of the technology. Throughout the last decade, the technological advancements combined with the policy investments have pushed the prices down. In 2018, the average LCOE reached a value of 0.06 USD/kWh for onshore wind and 0.13 USD/kWh, representing a reduction of 25 percent and 19 percent, respectively, comparing to the values of 2010 [7]. Regarding the costs, the average installation costs amounted for 1497 USD/kW (see Fig. 2.4a [7]) for onshore projects and 4353 USD/kW (see Fig. 2.4b [7]) for offshore projects, representing a decrease of percent 22 and 5 percent, respectively, when compared with values from 2010. In addition, Lazard's [8] 2019 LCOE analysis estimates that some wind technologies are approaching

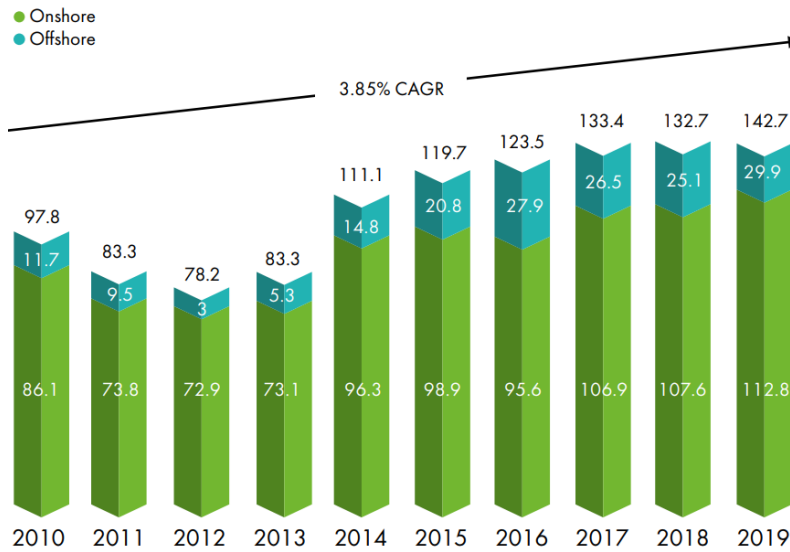
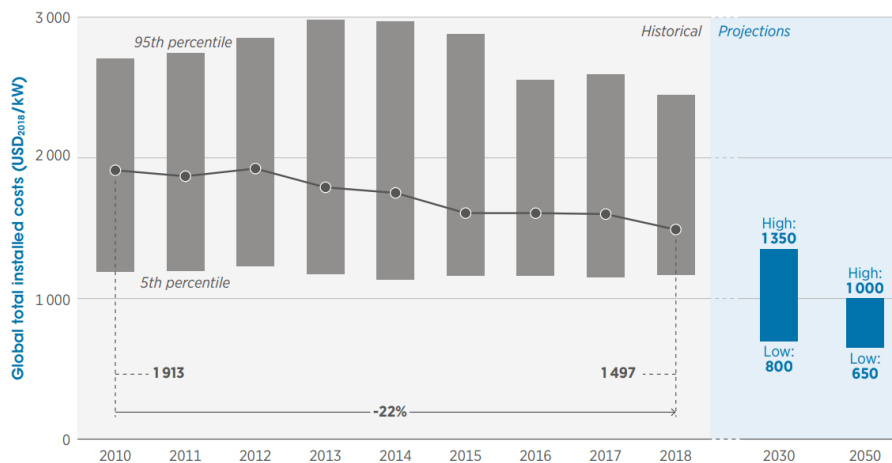


Figure 2.3: Annual investment in wind energy 2009-2019 [4]

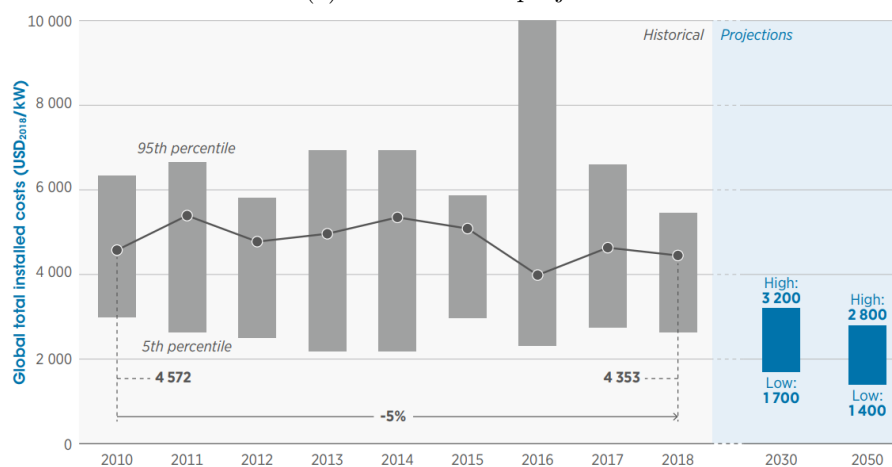
an unsubsidized LCOE that is competitive with the conventional generation technologies, such as coal and nuclear. Despite this focused analysis, it becomes more and more clear that the wind power competitiveness should be analysed in a broader system value, beyond LCOE. In order to achieve a successful energy transition, the stakeholders and investors should look for grid and balancing costs, pollutant emissions, energy system flexibility needs and socio-environmental impacts. This because, for instance, the LCOE does not account for the economic burden of polluting fossil fuels, i.e. wind energy would be even more competitive if greenhouse gas emissions taxes are accounted for [4].

In 2018, a total of 37 manufacturers supplied over 20 000 individual wind turbines, with the European producers occupying a dominant position with a major share of the market (see Fig. 2.5 [7]). The Danish producer Vestas remained the world's largest wind turbine supplier with approximately 20 percent of the market share, followed by the Chinese Goldwind (13.8%), German Siemens-Gamesa (12.3%) and American GE (10%). Supplier presence is also, naturally, heterogeneous across the globe. China is partially isolated from the global market, with Chinese manufacturers supplying nearly 95 percent of the overall market, led by Goldwind (31.7%). The small non-Chinese presence is held by three main foreign manufacturers: Vestas (2%), Siemens-Gamesa (1%) and GE (1%). Most of Europe's turbines are also produced locally, with Vestas (29%) and Siemens-Gamesa (26%) dominating the market share holding more than half of the European market. The only foreign supplier with a meaningful presence is GE (6%). The US market is slightly different from the other markets, since it is dominated by a foreign producer. Denmark's Vestas leads with a 35.4 percent share, followed by US-based GE (29.4%) and Siemens-Gamesa (23.2%) [7]. To sum up, one can conclude that the foreign presence of Vestas in the US, leading the market, holds decisive in ensuring the global leading position in 2018.

When looking at the technology, the market shows that the trend continues to give a large advantage to the geared wind turbine solutions (see Fig. 2.6 [7]). The conventional geared system continues to be the mainstream with more than 70 percent of market share, dividing in high-speed geared systems and medium-speed geared systems, holding 69.7 percent and 3.7 percent, respectively. The reduction in wind turbine installations performed by German Enercon in 2018, led to a 2 percent reduction, thus negatively impacting the 26.6 percent market share for direct drive turbine technology in 2018 [7].



(a) Onshore wind projects



(b) Offshore wind projects

Figure 2.4: Total installed cost of wind projects and prospects for 2030 and 2050 [7]

Policy overview

At early stages, the wind market benefited from large policy measures and investments in accordance to the energy transition that countries in general pursue. This helped to drop down the project costs and energy prices, therefore, promoting a competitive market to face the conventional energy sources, such as natural gas or coal, which are much more mature. Leading this front-line is the European Union, launching a 10 years plan by 2001 with specific targets for each member-state regarding renewable power generation until 2010 [9]. This plan rapidly evolved into a 20 years plan with a renewable energy share of 20 percent [10] and later to a 30 years plan leading to the current EU minimum target of 32 percent for the share of renewable energy consumed in the EU [11].

The political priority of being a global leader in renewables is underpinned in 5 areas: *energy security*, *internal energy market*, *energy efficiency*, *decarbonisation* and *innovation*. In terms of *energy security*, the renewable energy is a solid option since it reduces the dependency on fossil fuels dominated by foreign markets. The EU has already reduced the importation of fossil fuels by 12 percent in 2016, comparing to 2005, and aims to reduce Europe’s imports of oil and gas from the current 55 percent share to 20 percent by 2050. For the *internal energy market*, the renewables play an increasing role in the power market,

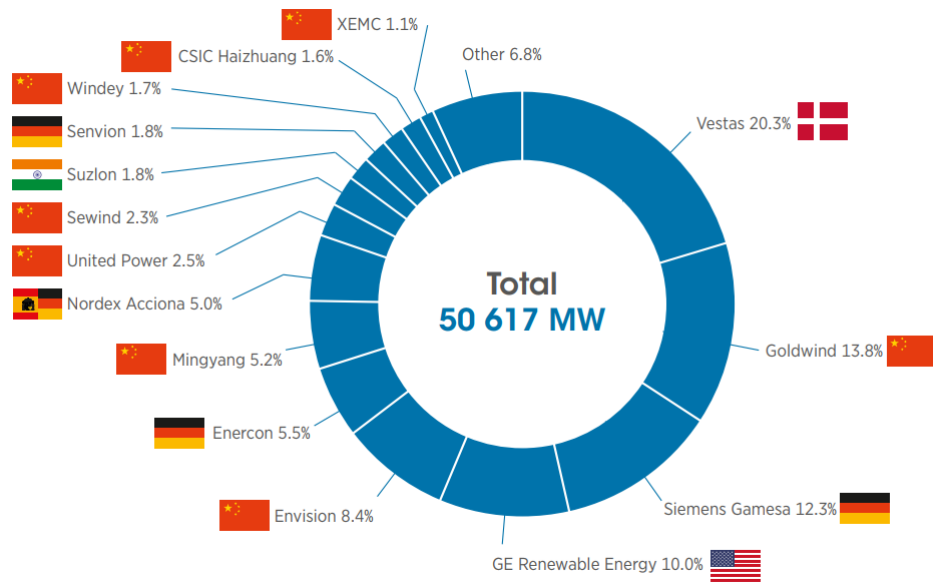


Figure 2.5: Top 15 wind turbine suppliers in 2018 [7]

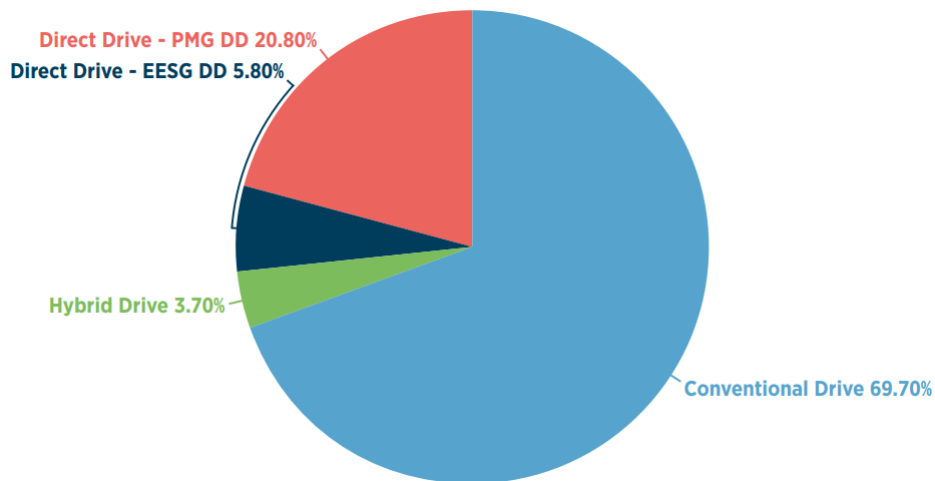


Figure 2.6: Global market share by turbine technology in 2018 [7]

with a 30.8 percent share in gross electricity production by 2017. On *energy efficiency*, a reduced energy consumption is tightly linked to the higher share of renewables and the increased integration of small-scale renewables in buildings. Furthermore, the renewable energy plays a significant role in *decarbonization* and in 2016 renewables have contributed to 460 Mt of gross avoided CO₂ emissions (more than the total greenhouse gas emissions of Italy in 2016). Lastly, Europe is a leader in *innovation* at the renewables sector with 53 percent of inventions from EU based companies acquiring patent protection outside Europe, demonstrating the value of European technology in foreign markets [12].

The taxation policy also helps to promote the so-called energy transition in great extent, investing on renewable energy programs. The European heavy taxation on fossil fuels helps not only to attenuate the high price volatility and discourage polluting behaviours, as well as provide revenues to governments, that can later be invested in the renewable sector. Taxes and levies make up 40 percent of average EU energy prices and in 2016, en-

ergy taxes collected by the EU member states amounted to EUR 280 billion or 4.7 percent of total tax revenue, of which the largest part is the excise duties (of which 80% comes from oil products). The energy subsidies planned in the 20 years plan until 2020, after which there will be a phase-out, in 2016 amounted EUR 169 billion (14% increase since 2008), and aimed to facilitate decarbonization and innovation in the energy sector, both in households and transportation [13].

Moving on to the US policy, during the Obama administration - from 2008 to 2016 - the congress approved the extension of two tax credits for investment and production of renewable energy: the *investment tax credit* (ITC) and the *production tax credit* (PTC). These tax incentives allowed to lower the LCOE for wind and solar generation projects, making them cost-effective. The US Departments of Energy (DOE) fund for renewable energy increased from USD 1.24 billion in 2008 to USD 2.07 billion by 2016 (67% increase), of which solar and wind power investments grew from USD 215 million to USD 337 million (57% increase) [14]. For the following years, from 2016 to 2019, the congress approved a phase-out plan in which the PTC phases down 20 percent each year, i.e. for projects starting construction in 2017 receive 80 percent of PTC value, and so on for 2018 (60%) and 2019 (40%), and projects that commence construction in 2020 or after no longer will receive the PTC [15].

In China, ever since the Renewable Energy Law (REL) implementation in 2005, the following five-year-plans foresaw the Chinese commitment to renewable energy developments. The REL set up guaranteed grid access and cross-subsidization as primary means to ensure revenue for renewables projects. Not only all energy distributors shall sign renewable energy projects with all grid-connected electricity but also the energy prices are not regulated by the market, instead they follow government-guided prices. Logically, in order to successfully implement these measures, the Chinese government opened public subsidies and funds in order to support the economy [16]. China National Renewable Energy Center (CNREC) estimates that just in the 12th five-year-plan (2011 to 2015) renewable energy subsidies make up for USD 48.5 billion [17]. And investments tend to increase with the 13th five-year-plan (2016 to 2020) aiming for a non-fossil energy ratio of 15 percent by 2020, with a CAGR in capacity of 21.2 percent in solar and 9.9 percent in wind [18]. Therefore, increasing the renewable power capacity to 680 GW of which 210 GW is wind power. However, highly-subsidized development is not sustainable and statistics show that the subsidy gap in China has already reached approximately USD 14 billion in 2019 and estimates to reach USD USD 0.14 trillion by 2030, if no policy changes are made. So China is already discussing the phase-out for the 14th five-year-plan (2021 to 2025) but grid parity is yet not possible due to poor distribution and connection to the grid, with very high values of wind curtailment [19].

Future prospects

Wind power has only made its statement in the global energy market in the last few decades, but its potential is still yet to be fully explored and there is also lots of room for improvement, not only technologically but also economically. One has already covered the past and present market as well as diplomatic measures that had a major impact in the largest markets. Now it is time to glimpse into the future, in terms of wind potential and what the market estimates.

As a source of energy, its endless availability makes wind energy very interesting, but its variability challenges the grid connection and cost-efficiency of the whole wind project. Progress has been made throughout the decades in order to make the conversion systems more adaptable to weather conditions turning around the power output intermittence.

Despite all these, wind is still a very strong, viable energy source for the future. Marvel et al. [20] states that just wind harvesting yields a global potential of 400.000 GW, disregarding any sort of social-economic constraints. Yet, Enevoldsen et al. [21] concludes that, even taking into account social-economic constraints such as land restrictions, the realizable onshore wind power potential in Europe alone is $138.090 \text{ TW h year}^{-1}$, which is enough to supply the global energy demand from now until 2050. Also, accordingly to the National Renewable Energy Laboratory (NREL) of the United States, the US wind power potential is $37.000 \text{ TW h year}^{-1}$ or $44.700 \text{ TW h year}^{-1}$, considering either 80 m or 100 m hub heights, respectively, only in windy regions [22].

According to the International Energy Agency (IEA) [23], the global electricity generation will grow by 55 percent between 2018 and 2040 (14.770 TW h), of which solar photovoltaics (PV) and wind will provide just over half of the growth in generation capacity (8.074 TW h). According to Fig. 2.7 [23], solar energy will become the largest source of installed capacity by 2035 and wind power capacity will triple, with offshore wind taking off in Europe, China and the United States. Logically, this pairs up with the projected future investments in power, where there is a major shift from coal to renewables, with global average annual investments of approximately USD 398 billion by 2040 (29% increase compared with values from 2018). Moreover, investments in energy efficiency are set to triple between 2018 and 2040, to USD 635 billion annually. The global generation mix will definitely shift towards the renewables, rising from 26 percent in 2018 to 44 percent by 2040, with wind and solar PV share growing from 7 percent to 24 percent.

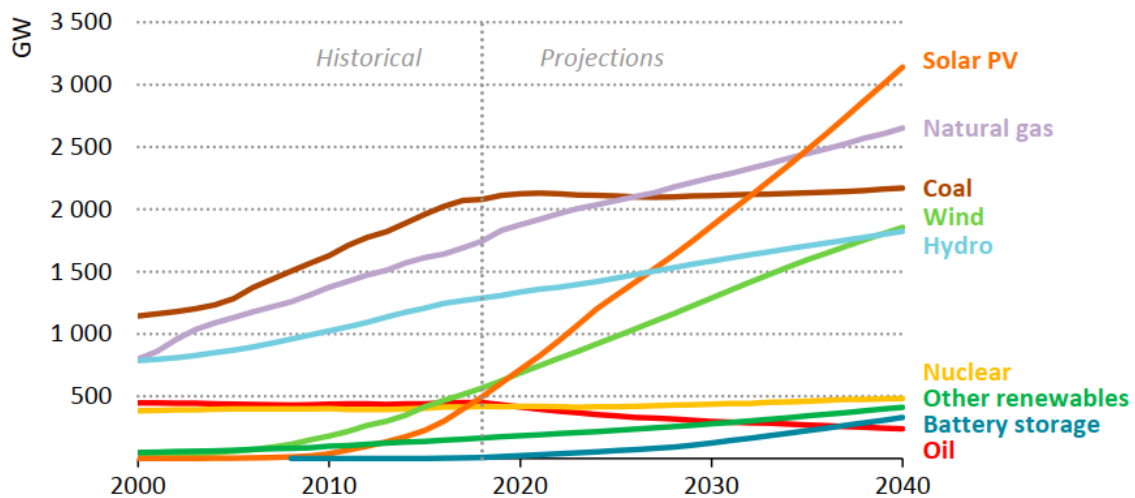


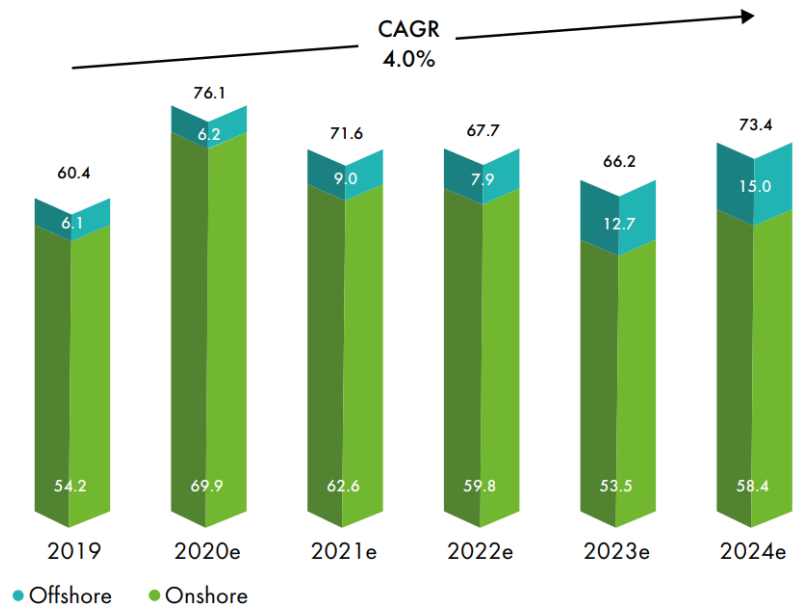
Figure 2.7: Global power capacity outlook for 2040 [23]

Developing economies will surely be the most promising markets until 2040. The advanced economies electricity demand share will drop down to 32 percent by 2040, seeing an annual growth of 0.7 percent, a value about four-times lower than the growth in developing countries (3%), which account for nearly 90 percent of global demand growth by 2040. The United States and Europe will continue to be the major developed markets by 2040, accounting for nearly 70 percent of demand in advanced economies, with increases of 510 TW h and 360 TW h, respectively. The developing economies promise to double the electricity demand by 2040, with China still being the biggest market, with a 70 percent increase between 2018 and 2040, accounting for 40 percent of global demand growth.

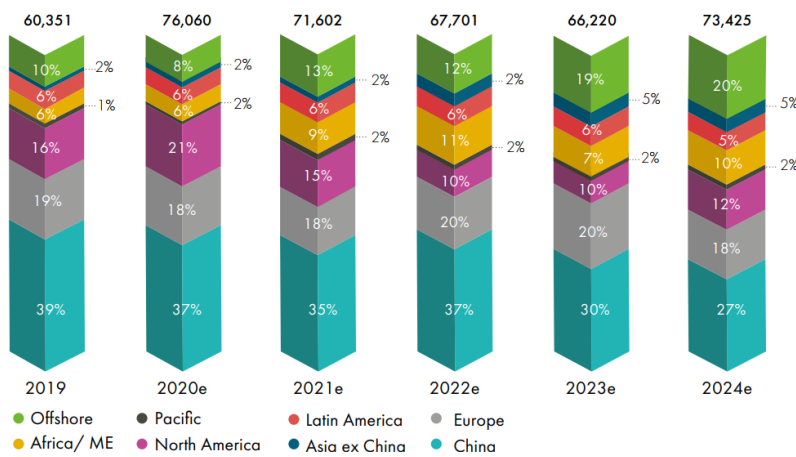
In a short-term projection, GWEC [4] foresees a CARG of 4 percent for onshore and offshore new installations until 2024, with a total of 355 GW of new capacity installed

2. Background theory

worldwide (see Fig. 2.8a [4]), with China and Europe still being the two major markets worldwide (see Fig. 2.8b [4]).



(a) Onshore and offshore (MW)



(b) By region (MW and percent, onshore and offshore)

Figure 2.8: New installations in 2020 - 2024 [4]

Offshore wind is a particular market to look for, since it is expected to grow to 15 GW in 2024, increasing its market share in new installations to 20 percent. In the US, which expects a total of 10.603 MW offshore wind projects to be commissioned by 2026 (see Fig. 2.9 [4]), expects the first utility scaled offshore installations (>800 MW) towards 2023, when offshore wind will become a truly global business.

Lastly, it is important to refer that these projections relate to a pre pandemic scenario, that certainly will take its toll on the global economy, and therefore on wind market. Currently, the impacts cannot yet be accounted for, although projects are already being delayed for more than one month. China has already managed to get the virus under control in nearly two months, but damage has been done, and a 1 to 2 months delay is expected, specially in onshore wind projects [4].

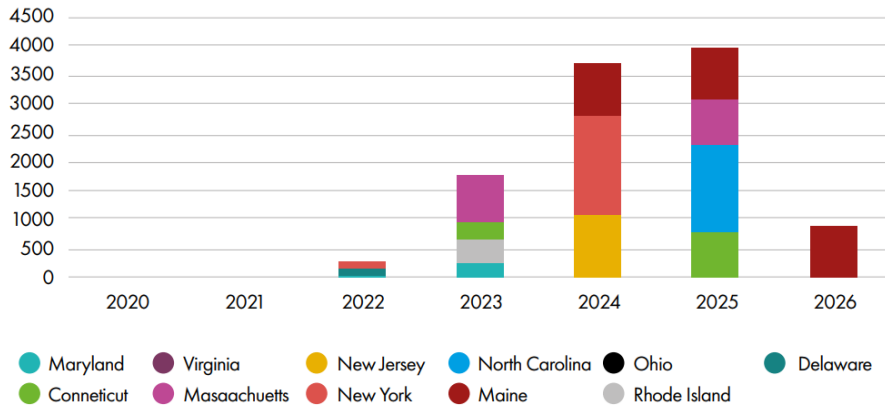


Figure 2.9: Expected annual offshore wind installation by state, 2020-2026 (MW) [4]

2.1.2 Fundamentals

Wind is air in motion. Its phenomena starts at the electromagnetic radiation coming from the sun which is unevenly absorbed by the Earth, stronger in the tropics and weaker in the high latitudes. Moreover, the different materials present, e.g. soil, rock, water and vegetation, add up to this different heat absorption rate. This uneven heating is converted through convective processes into air motion, which is adjusted by the rotation of the Earth. The convective processes are described by disturbances in the hydrostatic balance whereby otherwise stagnant air masses are displaced and move in reaction to forces induced by the changes in air density and buoyancy due to temperature differences. Air is pushed from high to low-pressure regions, balancing friction and inertial forces due to the rotation of the Earth. The velocity of the air motion defines the strength of wind and is directly related to the amount of energy in the wind, i.e. *kinetic energy* [24].

This “strength of wind” quantifies the *wind power*, which is the time-rate energy of the wind. First, consider an element A and a flow of magnitude U , as described in Fig. 2.10 [24]. It can be easily understood that the mass flow rate $\partial m/\partial t$ can be described as

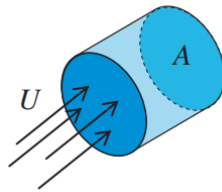


Figure 2.10: Schematics of air flow at velocity U through area A . The cylinder depicts the volume flowing in unit time ∂t through area A [24]

$$\frac{\partial m}{\partial t} = \rho \cdot A \cdot U \quad (2.1)$$

where ρ is the density of the flow. As stated earlier, the wind energy is quantified by its *kinetic energy* (only motion related), thus being expressed as

$$E_k = \frac{1}{2} \cdot m \cdot U^2 \quad (2.2)$$

and from Eq. (2.2) derives the *wind power*

$$P = \frac{\partial E_k}{\partial t} = \frac{1}{2} \cdot \frac{\partial m}{\partial t} \cdot U^2 \quad (2.3)$$

Including the mass flow rate of Eq. (2.1), one finally achieves

$$P = \frac{1}{2} \cdot \rho \cdot A \cdot U^3 \quad (2.4)$$

which is the fundamental equation in wind power analysis [24]. By analysing Eq. (2.4), it can be concluded that there is a linear dependence on air density, and implicit non-linear quadratic dependence on the radius of a wind turbine swept area and a non-linear cubic dependence on wind velocity. This highlights the importance of constant high-speeds of wind in the wind farm site, as well as the advantages of longer wind turbine blades.

In order to compare the wind resources from several sites independently of the turbine size, wind velocity and turbulence is the quantitative basis for standard classification of wind resources at NREL. In Table 2.1 [24], one can find the typical values of wind power classes with the corresponding power densities and mean wind speeds. Naturally, there

Wind Power Classification

Wind Power Class	Resource Potential	Wind Power Density/ W m^{-2}	Wind Speed/ m s^{-1}
1	Poor	0-200	0.0-5.9
2	Marginal	200-300	
3	Fair	300-400	6.7-7.4
4	Good	500-600	7.4-7.9
5	Excellent	500-600	7.9-8.4
6	Outstanding	600-800	8.4-9.3
7	Superb	>800	>9.3

Table 2.1: Wind Power Classes Measured at 50 m Above Ground According to NREL Wind Power Density-Based Classification [24]

is always a loss in power conversion from the wind resource, quantified by the *Power Coefficient* (C_p), which is the ratio of the power extracted by the wind turbine to the total power of the wind resource $C_p = P_T/P_{wind}$. Therefore, turbine power capture can be defined by

$$P_T = \frac{1}{2} \cdot \rho \cdot A \cdot U^3 \cdot C_p. \quad (2.5)$$

In fact, there exists a theoretical limit on the maximum extractable power fraction - known as the *Betz limit*. According to Betz theory [25], the maximum possible power coefficient is $C_p = 16/27$, i.e. 59 percent efficiency is the best a conventional wind turbine can do in extracting power from the wind. This is due to a dependence on the continuous flow of the wind in order to extract power, i.e. *Betz limit* defines the optimal balance of the largest wind slowdown that still maintains sufficiently fast flow past the turbine.

The last key metric when addressing the issue is the *Capacity Factor* (CF) which quantifies the fraction of installed generating capacity that actually generates power

$$CF = \frac{E_{actual}}{E_{ideal}} = \frac{\Delta t \cdot \bar{P}}{\Delta t \cdot P_N} = \frac{\bar{P}}{P_N} \quad (2.6)$$

where \bar{P} and P_N are the average and nominal power, respectively. The *Capacity Factor* considers an energy conversion under conditions which are not ideal, due to the variable aspect of the wind resource [24].

2.1.3 Wind energy conversion systems and working principle

Throughout time there have been many different inventions aiming to convert the wind's kinetic energy into mechanical work. Wind energy converters can be characterized in accordance with their aerodynamic function and constructive design. The rotor's aerodynamic function is classified whether it captures its power exclusively from the aerodynamic drag or lift. Moreover, one may also classify according to the aerodynamic *tip speed ratio* into "low-speed" and "high-speed" rotors. The classification according to construction design is the most practical and the most obvious characteristic is the position of the rotor's rotation azimuth.

The oldest wind energy converters were *Vertical Axis Wind Turbines* (VAWTs) and at early stages were only drag-type rotors. The *Savonius* rotor (see Fig. 2.11a [26]), a drag-type rotor, the *Darrieus* (see Fig. 2.11b [26]) rotor and its variation H-rotor (see Fig. 2.11c [26]), which are lift-type rotors, are typical examples of VAWTs. The *Savonius* rotor is generally used for small wind turbines, e.g. the cup anemometer, due to its low tip-speed ratio and power coefficient. For example, even with some improvements allowing the use of aerodynamic lift, the power coefficient does not exceeds 0.25. Due to its complicated geometric shape, the *Darrieus* rotor is difficult to manufacture. Like the *Darrieus* rotors, H-rotor wind turbines have a very high production costs, jeopardizing its competition with the horizontal axis rotors. To sum up, the VAWTs major drawbacks are the low tip-speed ratio and the inability to self-start and control the power output or speed. For these reasons and more, the presence of VAWTs in the wind market still cannot be foreseen in the long-term [26].

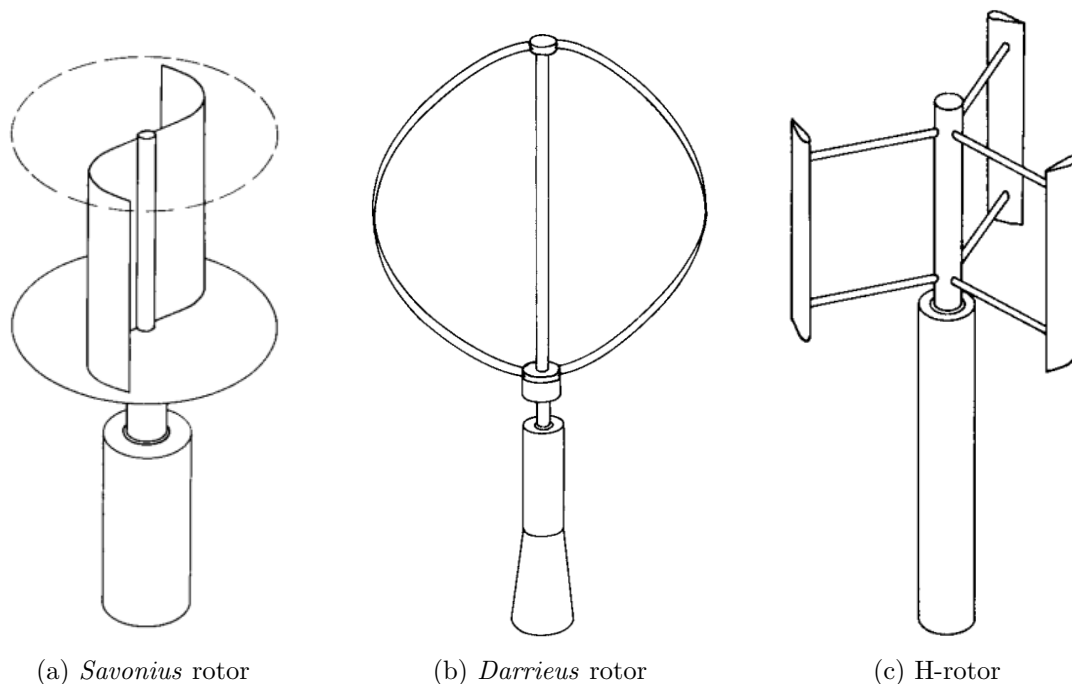


Figure 2.11: Rotor concepts of VAWTs [26]

The *Horizontal Axis Wind Turbines* (HWATs) are the dominant (almost exclusively) wind energy converters in the market, being the American wind turbine or modern wind turbine the most present converter. The undisputed superiority comes from the following characteristics:

2. Background theory

1. In rotor designs, rotor speed and power output can be controlled by pitching the rotor blades about their longitudinal axis (blade pitch control). Moreover, rotor blade pitching is the most effective protection against overspeed and extreme wind speeds, especially in large wind turbines;
2. The rotor blade shape can be aerodynamically optimised and it has been proven that it will achieve its highest efficiency when aerodynamic lift is exploited to a maximum degree;
3. Not least, the technological lead in the development of rotor design is a decisive factor.

The components and most important types of HWATs will be viewed in depth in the next section. As it can be seen in Figure 2.12 [27], the HWATs represent dominant advantages in terms of reliability and practical viability.

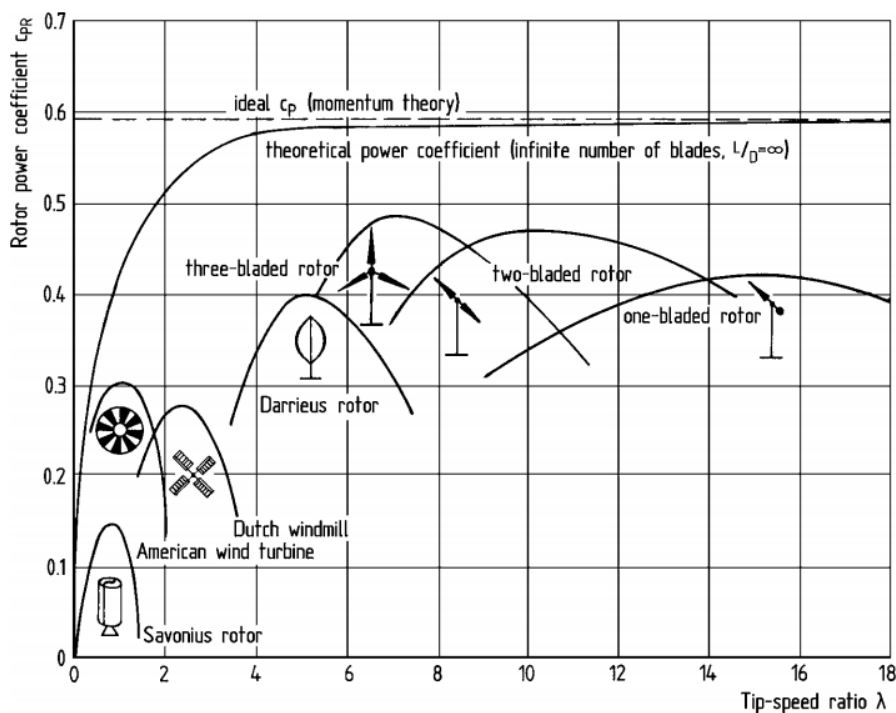


Figure 2.12: Power coefficients of wind rotors of different designs [27]

Finally, nowadays there has been some innovative concepts with the aim of increasing the power yield relation in relation to the rotor-swept area, i.e. increasing the *power coefficient* even further sometimes beyond the *Betz* limit. This is achieved by static structures which produce acceleration, in the low velocity, to the rotor, or generate concentrated vortices. The aim is to achieve a drastic reduction in rotor size while, at the same time, hoping the additional cost of the solution for “pre-concentrating” the wind energy will not become too expensive [28]. A promising concept is to enclose the rotor in a duct (see Fig. 2.13a [26]), preventing the narrowing of the flow tube before it reaches the converter. The achievable *power coefficient* exceeds the *Betz* limit up to a value of $C_p = 0.66$ [28]. Another variation of this concept is placing a rotor in a reversed funnel (see Fig. 2.13b [26]), i.e. a diffuser, thus improving the *power coefficient* even further to a value of $C_p = 0.75$.

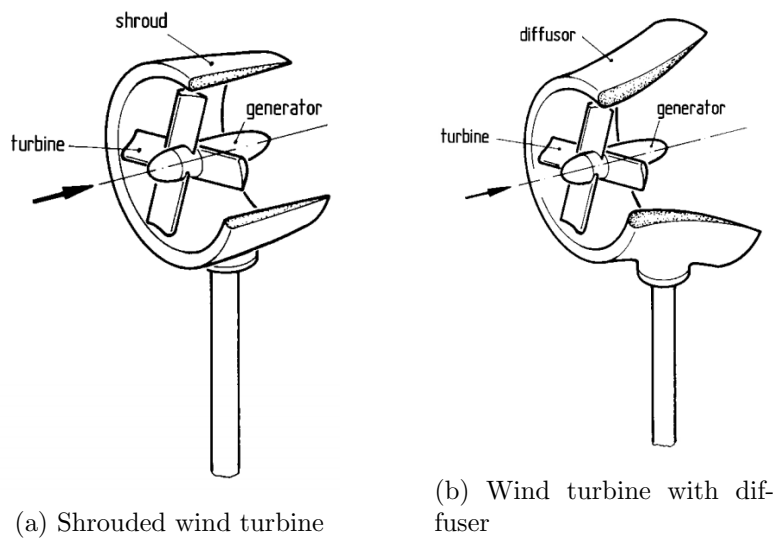


Figure 2.13: Wind rotor concepts combined with static structures for concentrating wind energy [26]

2.1.4 Wind turbine

As earlier stated, the market is dominated by the HAWTs and this section aims to get a deeper view at the several technologies and concepts that these wind turbines contemplate. First, it is important to classify the market products in terms of environment. Table 2.2 [29] displays the different wind turbine classes in terms of energy resource (wind). As it would seem as logic as true, from different operational environments incurs different sets of loadings, which is contemplated in this classification. Although the concept of the wind turbines may be the same, the design, material and construction must come in accordance to the loads, as it would be expected.

Wind turbine classification		
Class	Wind average speed m s^{-1}	Turbulence I_{ref}
1	10	a High (0.16)
		b Medium (0.14)
		c Low (0.12)
2	10	a High (0.16)
		b Medium (0.14)
		c Low (0.12)
3	10	a High (0.16)
		b Medium (0.14)
		c Low (0.12)

Table 2.2: IEC 61400-1 classification of wind turbines [30]

Contemporary wind turbine technologies

Modern wind turbines may appear in different concepts, each with its pros and cons and construction particularities. Depending on the generator type, power electronics, power and speed controllability, these concepts can be categorized into four categories:

1. Fixed-speed wind turbines (Type 1)
2. Limited variable-speed wind turbines (Type 2)
3. Variable-speed wind turbines with partial-scale power converter (Type 3)
4. Variable-speed wind turbines with full-scale power converter (Type 4)

Fixed-speed wind turbines use a multiple stage gearbox and a squirrel-cage induction generator (SCIG), directly connected to grid via a transformer, in order to convert the wind's kinetic energy into electrical power (see Fig. 2.14 [31]). Also, the electrical system contains a soft-starter for smoother grid connection and a capacitor bank to compensate the reactive power. The SCIG works in a narrow range around the synchronous speed, therefore the wind turbine operates at an almost constant speed. This means that wind fluctuations are converted into mechanical and electrical variations. Therefore, these turbines suffer from high mechanical and fatigue stress. Moreover, despite the low production cost and high robustness, the lack of reactive power consumption and speed control as well as limited power quality control are major drawbacks of these concepts. In order to mitigate some of the drawbacks some commercial *type 1* turbines have a pole changeable SCIG configuration corresponding to two rotation speeds, namely a generator winding with 8 pole for low wind speeds and 4 to 6 poles for medium and high wind speeds.

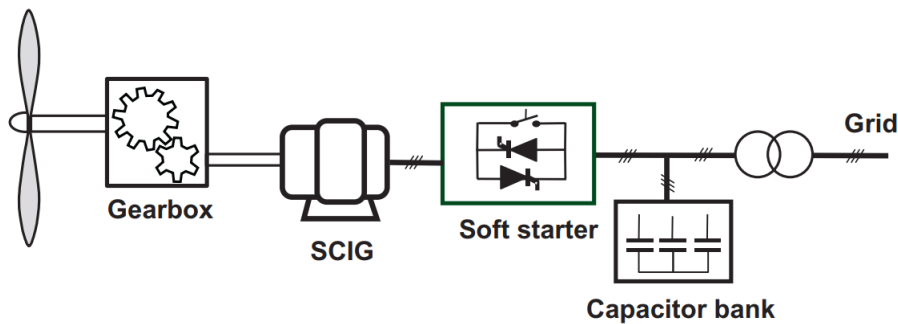


Figure 2.14: *Fixed-speed wind turbines* - Type 1 [31]

Limited variable-speed wind turbines also use a multiple stage gearbox connected and a wound-rotor induction generator (WRIG), from which the rotor is connected in series to a variable resistance controlled optically and changed dynamically by power electronics (see Fig. 2.15 [31]). By changing the rotor resistance size, the speed of the turbine can be modified and thus a variable speed operation can be achieved by controlling the energy extracted from the WRIG rotor. Therefore, the size of the resistance dictates the range of the variable speed, typically ranging values from 0 to 10 percent. It must be also noted that some power is dumped at the resistance by means of heat loss. That said, *type 2* turbines offer a simply circuit topology without slip rings (less maintenance) and improved operating range while reducing mechanical and power fluctuations. Besides this, lacks in limited speed range, power losses through the rotor resistance and poor control of active and reactive power.

Variable-speed wind turbines with partial-scale power converter are characterized by using a doubly-fed induction generator (DFIG) (see Fig. 2.16 [31]), which is described by a WRIG with a partial-scale back-to-back power converter (rated at approximately 30 percent of the nominal generator power) connected to the rotor typically through slip rings, controlling the rotor speed thus defining the speed range (typically ± 30 percent

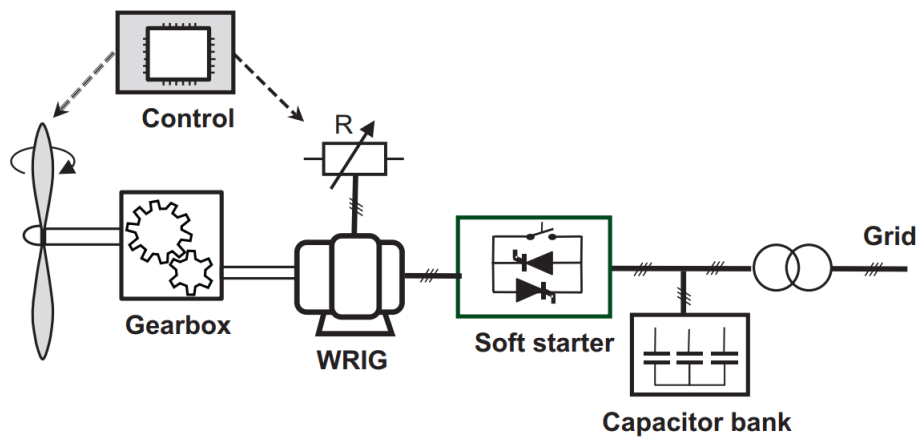


Figure 2.15: *Limited variable-speed wind turbines - Type 2* [31]

around the synchronous speed). The converter performs reactive power compensation and smooth grid interconnection and therefore this configuration need neither a soft starter nor a reactive power compensator. Besides this, the control system includes the electrical control of the converter and the pitch controller of the blades to limit the power when the turbine is working above the rated power. When compared to the *type 2* turbines, these models offer a wider range of dynamic speed control and less losses, since the rotor energy can be fed into the grid by the power converter. The main drawbacks are its cost, which is naturally more expensive compared to *type 1* and *type 2* concepts, and the use of slip rings which require regular maintenance and are less reliable.

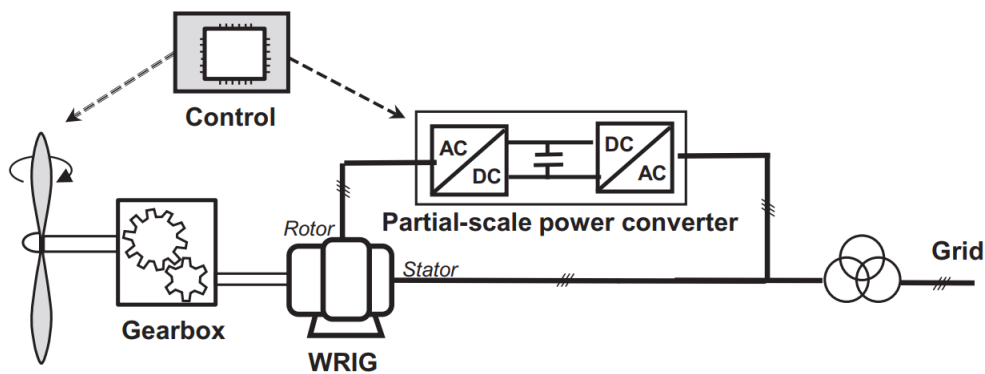


Figure 2.16: *Variable-speed wind turbines with partial-scale power converter - Type 3* [31]

In the *variable-speed wind turbines with full-scale power converter* the generator, which can be a wound-rotor synchronous generator (WRSG), a WRIG or a permanent-magnet synchronous generator (PMSG), is connected to the grid through a full-scale power converter (see Fig. 2.17 [31]), thus allowing for the control of the generator in a speed range up to 100 percent. This converter performs a smooth grid connection and reactive power compensation, thus neither a soft starter nor a reactive power compensator are needed. Similar to *type 3* turbines, this concept allows the electrical control of active and reactive power as well as pitch control to limit the rotor speed. These turbines offer better efficiency and grid support ability, full power and speed controllability, less complex grid-fault ride-through capability and are less prone to failure since there is no use of slip rings. The main drawbacks would be their higher cost, from using a full power converter as well as the

higher energy losses since all power is processed by the electronic power converter. Some of *type 4* turbines use no gearbox (depicted by the dotted line in Fig. 2.17 [31]) since the converter can control of the generator in the full range speed, where the direct-driven multipole generator is directly connected to the hub of the rotor (see Fig. 2.18 [32]). By removing the gearbox, these concepts not only reduce the energy losses and costs but are more reliable, since some rotating mechanical components are now out of the picture.

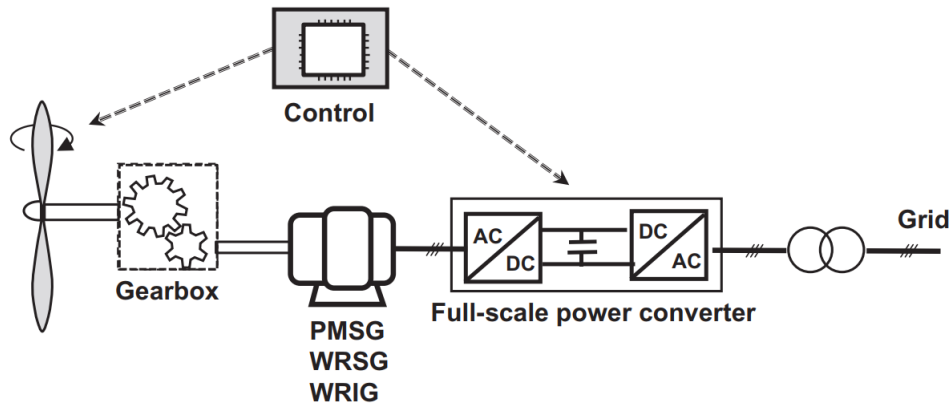


Figure 2.17: Variable-speed wind turbines with full-scale power converter - Type 4 [31]

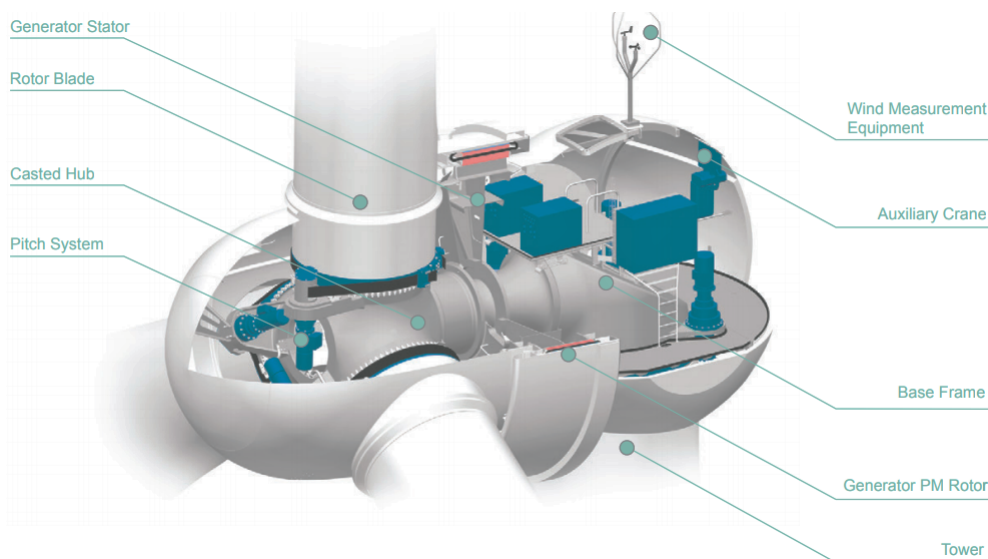


Figure 2.18: A schematic of the gearless *Goldwind* wind turbine [32]

Components

The standard configuration of a modern wind turbine consists in a tower holding the rotor connected to the nacelle (see Fig. 2.19), which contains several systems responsible for the energy conversion as well as control, so it can be said that is “where the magic happens”.

In this section one may get a particular knowledge in the current technologies of the different critical components and systems that make up wind turbines. Figures 2.20 and 2.21 [26] display the typical configuration of the rotor and nacelle. The rotor is composed



Figure 2.19: Main systems of Vestas V150-5.6 MW™

by the blades, responsible for harnessing the wind's kinematic energy through a aerodynamic phenomena, the pitch system, which controls the position of the blades around their longitudinal axis, thus preventing overloading in over-speed situations as well as optimizing the angle of attack to achieve optimal efficiency, and the hub which is the structure that transfers the loads from the blades to the rest of the power train. Inside the nacelle, the power is transferred from the main shaft to the generator through a gearbox (or not in case of some *type 4* turbines). An important component to look over is the yaw system, responsible for controlling the position of the whole top structure (rotor and nacelle assembly) around the longitudinal axis of the tower.

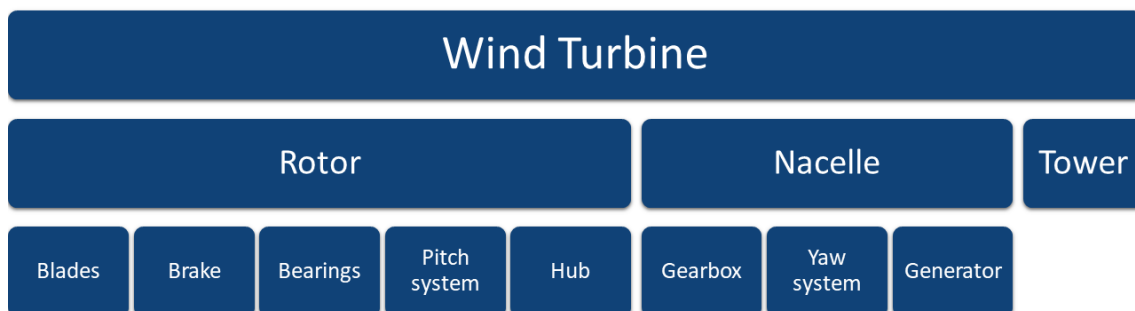


Figure 2.20: Wind turbine different components and systems

Rotor blades The blades are subjected to a very tough load spectrum, characterized by bending moment due to gravity load which alone makes up to 10^8 load cycle alternations, and the stochastic altering loads caused by wind turbulence. In addition there are the effects of ageing of the material due to the weather. Having that said, rotor blade technology is associated with lightweight aeronautical engineering that copes with finding designs, materials and manufacturing processes to produce lightweight, strong, complex

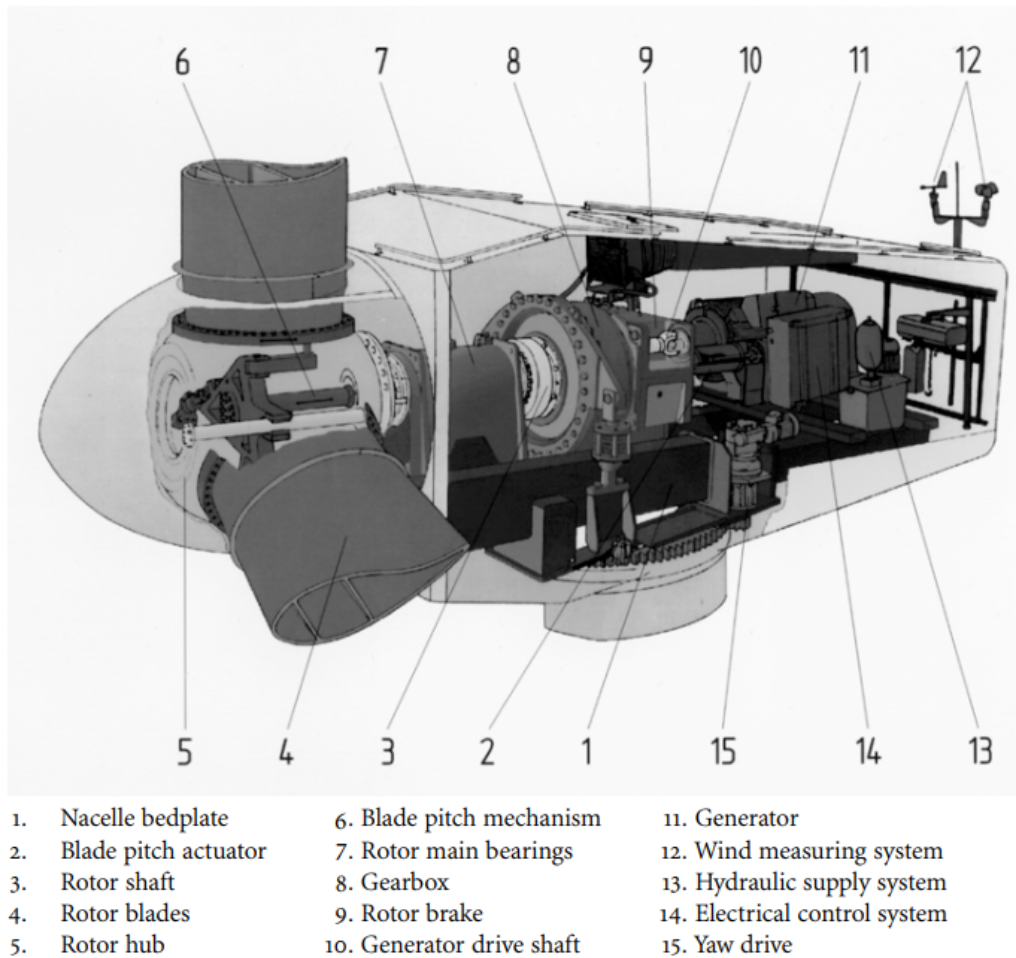


Figure 2.21: Power train of the Vestas V-39 in standard design [26]

aerodynamic shapes in a cost effective way.

The technology has evolved to the modern fibre-reinforced composite blades, due to its supremacy in low manufacturing cost. Fibre-reinforced composites are composed by fibres, responsible for the strength and stiffness properties, connected by a bonding agent called *matrix*, typically resins. The fibres can be made by three different materials:

1. Carbon fibre
2. Glass fibre
3. Organic aramid fibres (Kevlar)

Although *Kevlar* fibres present good strength properties, their hygroscopic characteristic (i.e. moisture absorption) and the lack of fatigue data on this material put them aside when it comes to rotor blades. On the other hand, *glass fibre* is the most widely used material for its extraordinary high strength despite the low specific elasticity modulus, leading to less stiffer components. This means that *glass fibre* structures cannot be used for very large rotor blades. Finally, *carbon fibres* stand out for their very high strength and elasticity modulus, almost steel-like, as well as good fatigue properties. The main drawback is the price, which remains too high, thus making *carbon fibres* only suitable in combination with *glass fibres* for reinforcing areas which are subjected to high stress.

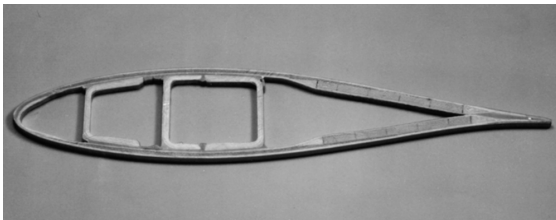
Considering practical aspects, the selection of *matrix* material is restricted to:

1. Polyester resins
2. Epoxy resins

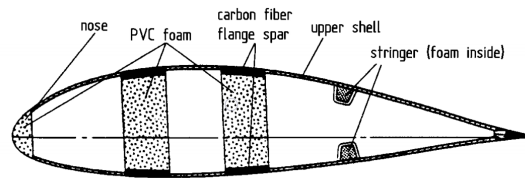
Polyester resins are inexpensive and quite suitable for medium stresses. However, many rotor blade manufacturers nowadays prefer to use the expensive, high-quality *epoxy resins*, for their better fatigue and strength characteristics. Moreover, they exhibit low shrinkage like the *polyester resins*. The weight of the components can be reduced significantly for the same application.

In terms of manufacturing, the most common processing technique is the *laminating technique*, where mats of fibre material are laid in layers into a female mould and are impregnated with synthetic resin. This technique allows to orient the fibres adapting them to the loading direction, thus exploiting the strength of the material to its optimal behaviour. The main drawback is that in the *laminating technique* most of the work is done by hand, even using pre-impregnated fibre mats. The *filament winding technique* attempts to avoid this problem, by impregnating the fibres through a resin bath, using a almost fully automatic process. Besides the advantage of manufacture, this technique lacks the ability of fibre orientation, which is dominated by the geometric shape, and surface quality is poor.

Nowadays, rotor blade manufacturers use light-weight spar webs (see Fig. 2.22b [26]). Although *polyester resin* is still used in small blades today, *epoxy resin* has increasingly gained popularity for mass-produced rotor blades, for its better strength properties. As stated earlier, *carbon fibre* is still too expensive, so it is used to reinforce highly loaded regions (see Fig. 2.22a [33]).



(a) Rotor blade cross-section of a modern rotor blade in laminated shell construction with spar box and spar webs [26]



(b) Rotor blade of the experimental Aeolus II turbine in mixed glass fibre/carbon fibre [33]

Figure 2.22: Rotor blade standard designs

Another critical aspect of blade design is the connection to the rotor hub. This aspect is particularly difficult to design because, from one side we have different materials (fibre composites to metallic) transferring loads between each other, and on the other side, rotor forces are concentrated around the areas of the blade root and rotor hub. Current rotor blades display the following essential concepts for the design of the blade connection:

1. Steel flange connection
2. Cross-bolt connection
3. Bonded-in lightweight flanges or sleeves
4. Bonded-in bolts

Steel flange connections are common in older rotor blades with a polyester matrix, where the blade root is clamped between an inner and outer flange and the two flanges are bolted together (see Fig. 2.23a [26]). The connection to the rotor hub is via an external flange ring with heavy-duty tension bolts. Rotor blade flanges of this design frequently constitute up to one third of the total rotor blade weight and the proportion of manufacturing cost of the rotor blade is correspondingly high.

Cross-bolt connection is a decisive step towards reducing blade weight and manufacturing costs. The connection uses a metallic pin that goes through the holes in the shell of the blade and screw in the bolt that goes along the thickness of the blade (see Fig. 2.23b [26]). This design received a big push due to the increasing utilization of epoxy resins since polyester resins are prone to plastic deformation under concentrated loads in one point (load transfer from pin).

Bonded-in lightweight flanges or sleeves are blade connections with high-strength aluminium bonded into the blade root structure (see Fig. 2.23c [26]), first developed by Vestas. These connections are extremely light, e.g. in the rotor blades of the Vestas V-39, with a rotor diameter of 39 m, the flange weighs less than 50 kg out of a 1100 kg blade. A further variant was developed by LM, which has a bonded-in metallic sleeves into which the fastening bolts are screwed (see Fig. 2.23d [26]).

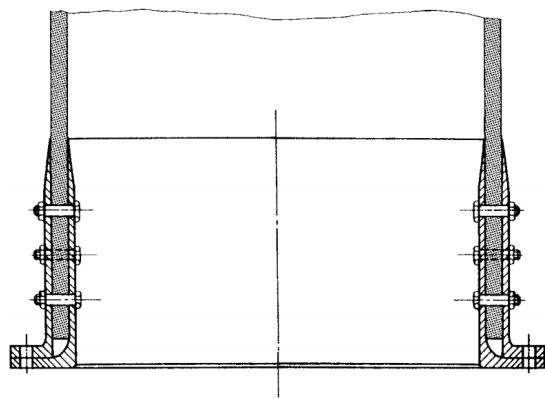
Bonded-in bolts are the simplest but riskiest connections, where the bolts are directly bonded into the blade root without any form-fitting. However, it may be possible to improve the design in the future in order to make it suitable for mass production.

Rotor hubs The hubs are responsible for transferring the loads from the rotor blades to the main shaft, hence it is one of the most highly stressed components of a wind turbine since almost all forces and moments are concentrated at the hub. Therefore, the material must be selected with great care in terms of fatigue life as well as the design must avoid local stress concentration regions. The three possible solutions for the material design are:

1. Welded sheet steel
2. Cast iron
3. Forged steel

Another point to note is that the hub design is greatly influenced by the overall design of the wind turbine, namely the number of blades. Regarding this aspect, three-bladed rotors dominate the market for their better load behaviour whereas two-bladed rotors require teetering or a flapping hinge in order to compensate the unfavourable loads. Due to this domination, cast iron has become an obvious preference, as no additional load balancing systems are required and a rigid body is enough. Still, some might question the use of cast iron in highly stressed components, but the evolution of the technology allowed for spheroidal graphite cast iron parts to be optimal for this solution (see Fig. 2.24 [26]).

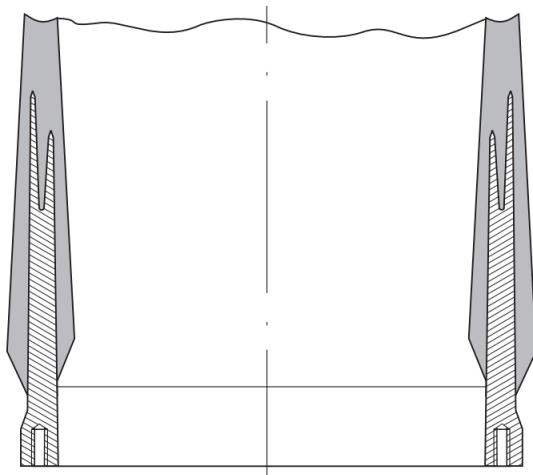
Blade pitch mechanisms The blade pitch mechanisms, generally, are equipped in larger wind turbines rotor blades. The mechanism has the main function of adjusting the blade pitch angle for controlling the power and speed of the rotor. A pitching range of 20 to 25 degrees is enough for this purpose. But apart from this main function, the blade pitch



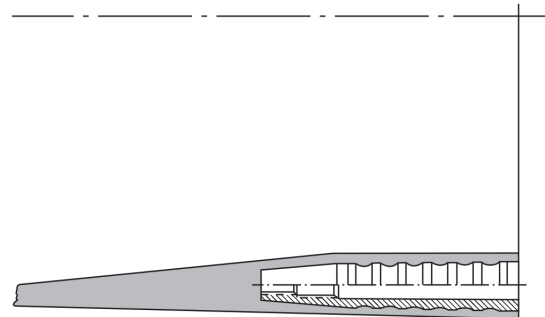
(a) Heavy dual steel flange in earlier rotor blades [26]



(b) Blade connection with cross-bolts [26]



(c) Bonded-in light aluminium flange of a rotor blade at the Vestas V39 [26]



(d) Bonded-in sleeves of a rotor blade for connection to the hub [26]

Figure 2.23: Blade connections to the rotor hub

mechanism must be able to break the rotor aerodynamically, which means a pitching range of approximately 90 degrees.

Rotor blade bearings are necessary to ensure the relative rotation between the blades and the hub. In terms of loading conditions, the situation is rather unfavourable for bearing life. Considering the high static loads, even when rotating movements are small and the permanent deformations of the bearing support, the criteria of rippling¹ and frictional corrosion must be taken into account in the design of roller bearings. In terms of concept, we can consider two types:

1. Live-ring bearing
2. Four-point contact bearing

In the *live-ring bearings* used in older types of wind turbines, the cylindrical rollers are arranged in planes perpendicular to each other (see Fig. 2.25a [26]). This type is relatively

¹formation of small waves on the surface

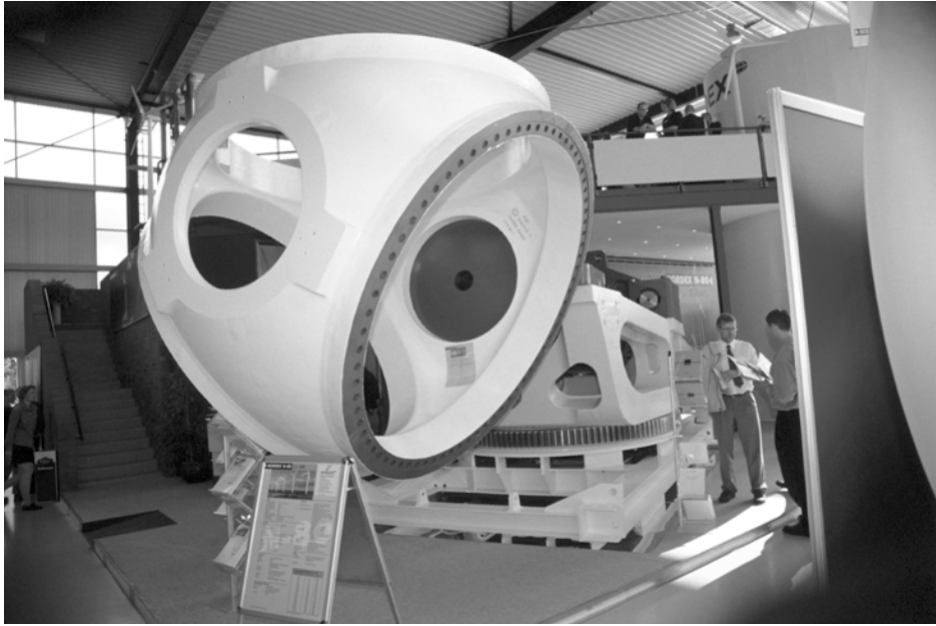
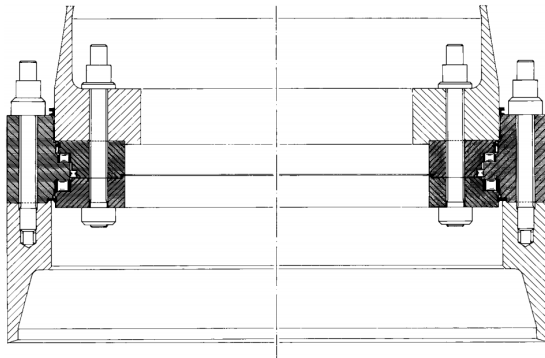
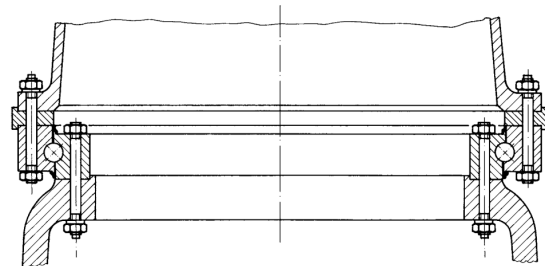


Figure 2.24: Cast rotor hub of the Nordex N-80 wind turbine [26]

complex, therefore, expensive. Double-row *angular-contact cylindrical* and *crossed roller bearings* are simpler. The *four-point contact bearings* are used almost exclusively (see Fig. 2.25b [26]). These bearing are less sensitive to the deformations of the bearing body, thus avoiding the concentrated peak loads occurring with cylindrical rollers under these circumstances. For small blades, a single-row arrangement suffices whereas large rotor blades require double-row arrangements.



(a) Rotor blade bearings with angular-contact roller bearings in the earlier Swedish WTS-75 [26]

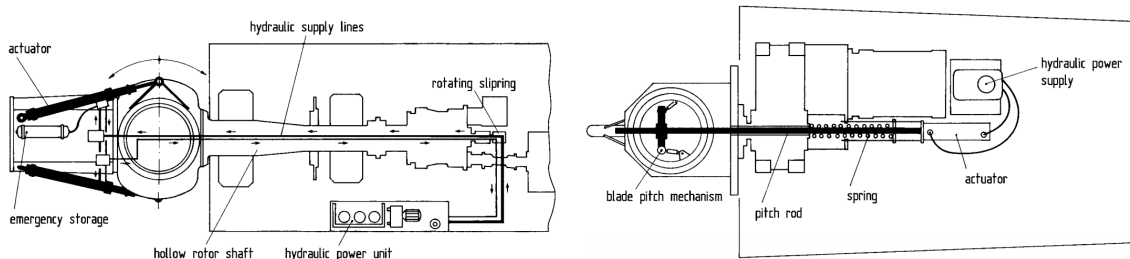


(b) Single-row four-point ball-bearing in the rotor blades of the earlier WKA-60 [26]

There can be several types of pitch systems, depending on its energy source, components and constructive solution. From the several concepts, three types may be distinguished:

1. Hydraulic blade pitch systems
2. Electrical blade pitch systems
3. Passive blade pitch systems

Hydraulic pitch systems use hydraulic actuators that may rotate the blades directly or via linkages². In either ways, the hydraulic power unit is usually placed in the nacelle. Some systems display the actuators in the rotor hub (see Fig. 2.26a [26]), therefore needing supply lines to be routed through the gearbox and the hollow rotor shaft into the hub, while other systems position the actuators inside the nacelle (see Fig. 2.26b [26]), thus needing a mechanical element, e.g. a connecting rod, in order to transfer the force. The hydraulic actuator works against a spring, so that in case of breakdown involving the complete loss of system pressure, the spring pushes the rotor blades into the feathered position, causing the rotor to stop. The general tendency is to avoid hydraulic pitch mechanisms, since they convey poor reliability due to oil leakages. On the other hand, there is a considerable progress in controlled electric motors, which offer many advantages as blade pitch drives.



(a) Blade pitch system of the WKA-60 with hydraulic drive and direct-acting actuators in the rotor hub [26]

(b) Blade pitch system in an earlier Windmaster turbine with hydraulic actuator in the nacelle and pushing rod to the rotor hub [26]

Figure 2.26: Hydraulic blade pitch systems

Electric pitch systems have become more present in turbines with the technological evolution. The electric configuration is rather complex because in order to control the position the electric motor needs a frequency converter or highly expensive direct-current units. But nowadays manufacturers are developing very compact electronically-controlled pitch motors making them exceptional for wind turbine manufacturers. In terms of mounting, the motor can be mounted on the outside flange ring or inside the hub. These concepts generally need a mechanical gear in order to transfer the force (see Fig. 2.27 [26]).

Mechanical transmission concepts The mechanical transmission solutions are very diverse and when it comes to concepts. But, in general, the primary objective is to make solutions more compact and lighter. From the many concepts, one can distinguish the most present ones:

1. Rotor shaft with separate bearings
2. Three-point suspension of rotor shaft and gearbox
3. Rotor shaft integrated into the gearbox
4. Rotor bearings integrated into the load-bearing nacelle structure
5. Rotor support on a fixed axle

²mechanical system to promote a certain movement

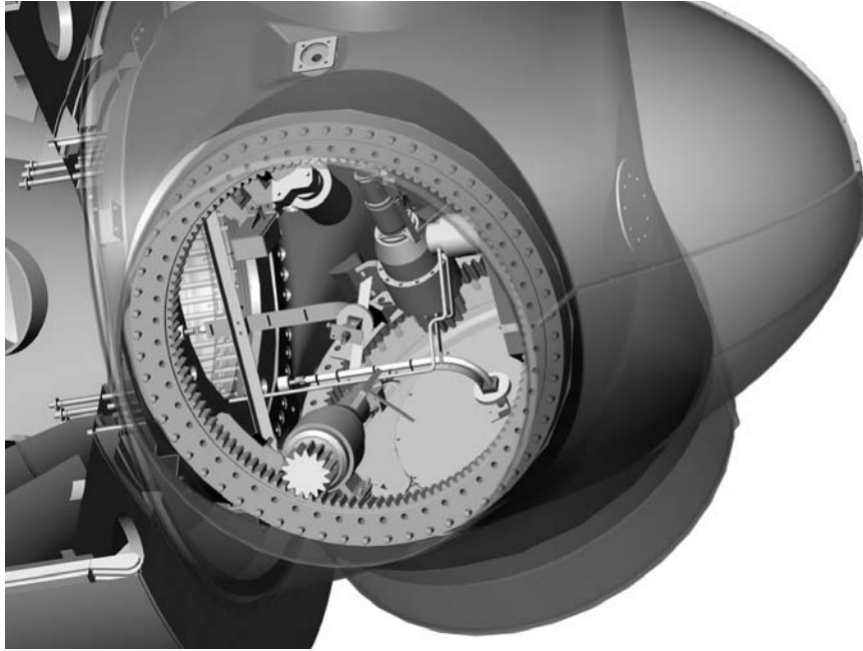


Figure 2.27: Electrical blade pitch system of the Dutch Lagerwey LW-72 inside the rotor hub [26]

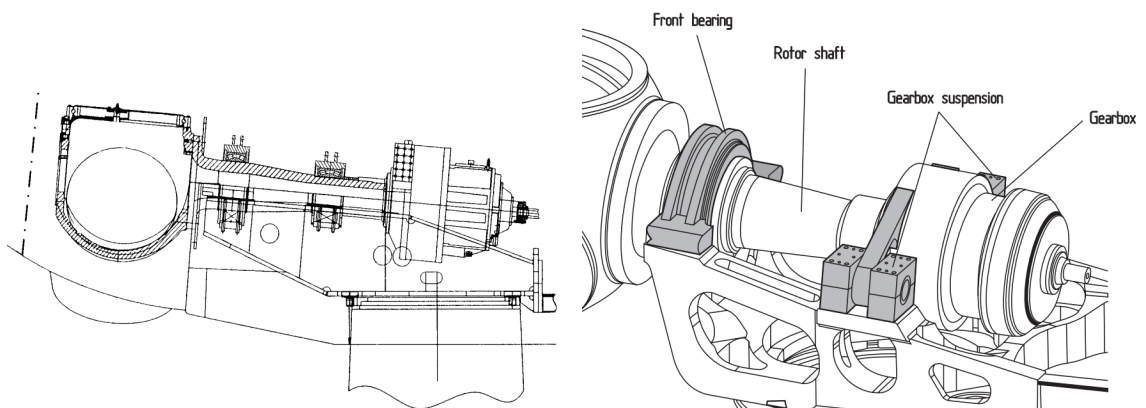
Rotor shafts with separate bearings are the traditional solution of rotor shaft and bearing assembly and are characterized by a “floating shaft” on a bedplate with two separate bearings (see Fig. 2.28a [26]). The rotor forces are transferred via the bedplate which is commonly a welded steel frame with longitudinal and cross beams. Moreover, the gearbox is arranged in a “slip on” transmissions so it only absorbs torque loads. For larger turbines, cast of forged steel shafts have been used. This solution is rather heavy due to the amount of material, which is rather disadvantageous in large quantities. The solution is only suitable for smaller quantities, where the simple and clear arrangement on a nacelle bedplate, use of standard gearboxes and bearings and easy accessibility compensate the larger overall mass.

Three-point suspensions propose a configuration where the rotor shaft and gearbox are supported at three points: the front rotor bearing and the two side bearings of the gearbox (see Fig. 2.28b [26]). This concept is becoming more successful recently in larger turbines due to the overall lighter weight, due to the shorter distance between the bearings, and easier installation since the rotor shaft, bearing and gearbox can be pre-assembled.

Rotor shaft integrated into the gearbox is an attempt to a more compact design where the rotor is directly supported by the gearbox (see Fig. 2.28c [26]). Moreover, other components such as the generator are also directly flanged into the gearbox. Therefore, this configuration offers a very small bedplate thus very low weight. Logically, the gearbox needs to be specially designed for the wind turbine and one has to have a particular caution to not let the unavoidable deformations and bending moments of the rotor affect the gear mechanism. Despite the very compact solution, this concept is not widely used in recent turbines.

Rotor bearings integrated into the load-bearing nacelle structure conveys a compact solution where the rotor is directly attached to the front part of the nacelle structure. This requires a very stiff load-bearing part in the nacelle structure to support the radial and axial forces as well as the bending moment from the rotor weight, and the external loads. Although this configuration did not show very promising experiences in the past, progress has been made in this concept. With this concept, significant weight reduction can be achieved, e.g. the Vestas V90 (see Fig. 2.28d [26]) weight could be kept at the same level as the V80 smaller model with large rotor shaft concept.

Rotor support on a fixed axle has been found in more recent turbines and tries to overcome the need of a large expensive component in order to sustain the high alternating loads. Here, the rotor is supported on a fixed shaft support which is only subjected to a static bending load (see Fig. 2.28e [26]). This approach is particularly well suited for gearless drive train *type 4* wind turbines since the torque is directly transmitted to the gearbox.



(a) Rotor shaft with two separate bearings in the Vestas V-66 [26]

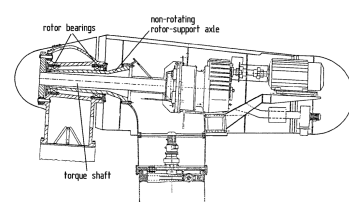
(b) Three point suspension of the rotor shaft/gearbox assembly of the Nordex N 80 [26]



(c) Drive train of an earlier Nordex wind turbine, with rotor and generator attached directly to the gearbox [26]



(d) Cast load-bearing structure with in-plane rotor bearing on a Vestas V90 [26]



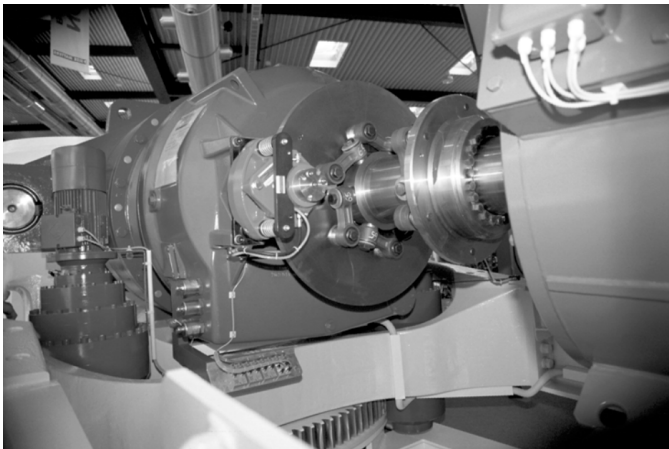
(e) Rotor bearing assembly on a fixed support shaft in the Bonus Mk V turbine [26]

Figure 2.28: Mechanical transmission concepts

Rotor brakes The rotor brakes fulfil the task of maintaining the rotor in a fixed or slowly driven state when out of operation. Besides, they can serve as a safety measure to prevent rotor runaway. Moreover, turbines in general have locking bolts between rotor hub and nacelle for extended periods of standstill and for servicing and repair work. Rotor brakes comes almost always in disk brakes, frequently adopted cost-effectively from solutions intended for other machines. In designing the rotor brakes as a pure parking brake,

they must fulfil the need for braking the rotor from full operation, thus being used as a second independent breaking system in a addition to aerodynamic braking increasing the reliability. However, for large turbines with rotor diameters above 60 m, the rotor brakes take massive dimensions if they are to brake during full-load operation and it becomes restricted to a only parking brake system.

Regarding installation, the rotor brake can be installed in either the “low-speed” or “high-speed” sides of the gearbox. Most turbines have the brake in the “high-speed” side in order to keep the brake dimensions small (see Fig. 2.29a [26]), due to the reduction of torque one or even two orders of magnitude in some gearbox ratios. This solution presents some drawbacks, which regard safety issues, since braking fails if the gearbox and preceding parts of the shaft fail, and rotor movement, as the standstill position must be retained by the gears which present some gaps due to wear, leading to oscillating movements in parking position. In order to prevent this last problem, some turbines do not lock the rotor during standstill but let it “spin” at low speed. To avoid these disadvantages, the rotor brake may be installed on the low-speed side of the gearbox, e.g. directly behind the hub (see Fig. 2.29b [26]). However, the high torque loads lead to considerable sizes even in pure parking brake systems. This poses a problematic approach for larger turbines and for that reason is out of the picture in almost all new systems.



(a) Rotor parking brake on the high-speed shaft of the gearbox in the Nordex N-80 [26]



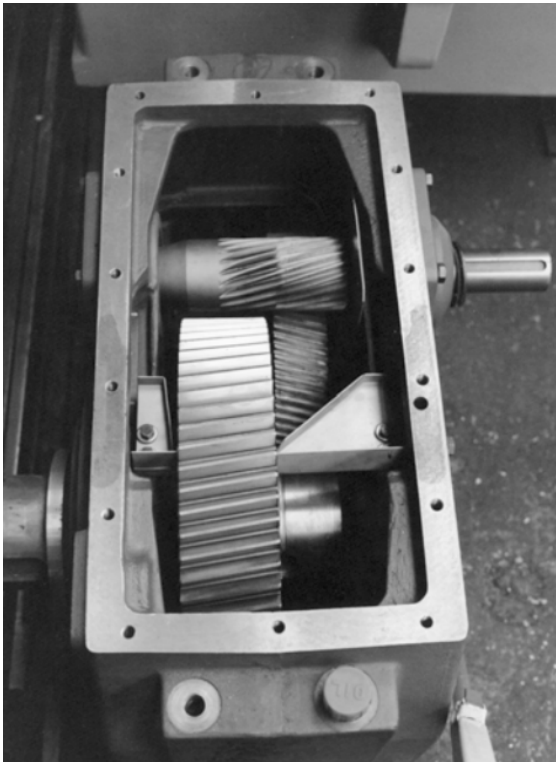
(b) Rotor parking brake at the low-speed side directly behind the hub in the earlier Howden HWP-1000 [26]

Figure 2.29: Examples of rotor brakes

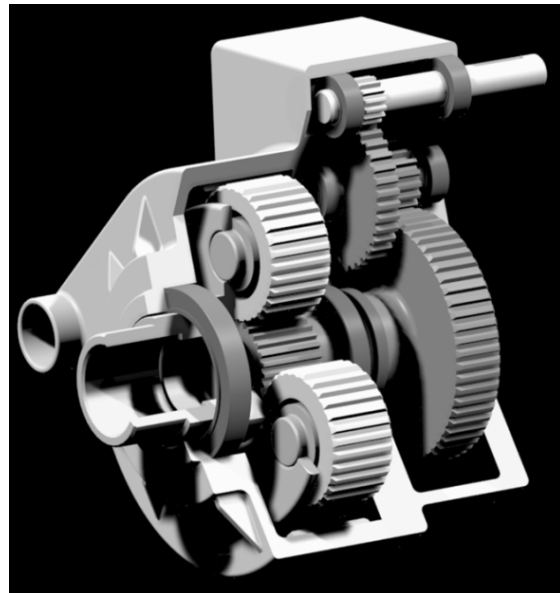
Gearbox The gearbox technology has come a long way, with high-performance solutions having gear ratios up to 1 : 100 and more, but still gearboxes are a source of failures and defects in many turbines. These defects are more related to the gearbox dimensioning problems than the gearbox itself. Regarding the constructive solution, gearboxes can be built in two different ways:

1. Parallel shaft or *spur-gear system*
2. *Planetary system*

Parallel shaft stages are built with a gear ratio of up to 1 : 5 while *planetary* stages have a gear ratio of up to 1 : 12. Thöbland [34] showed that the multi-stage *planetary* design has significant advantages in both mass and cost reductions, being clearly superior in the megawatt power class. In smaller turbines, parallel-shaft gears are commonly used for costs reasons and the prevailing model is the two-stage gearbox (see Fig. 2.30a [26]). For larger turbines, the *planetary system* is prominent. In many late models, gearboxes with one *planetary* stage and two additional parallel-shaft stages are used (see Fig. 2.30b [26]). This combination of *planetary* and parallel-shaft systems lead to a misalignment of the primary and secondary shafts. This is particularly useful for implementing the hollow shaft concept mentioned earlier, where the power supply lines can easily be routed through the gearbox directly to the hollow shaft.



(a) Two-stage parallel shaft gearbox for wind turbines of the 200 to 500 kW power class [26]



(b) Standard gearbox for large wind turbines with one planetary stage and two parallel shafts [26]

Figure 2.30: Examples of gearbox concepts

Finally, through experience, some special demands in this market rose special concerns in terms of:

- Special attention to the smooth running of the tothing. “Cheap” transmissions with simple tothing are unsuitable for wind turbines
- Oil leakages are a problem. Labyrinth-type seals are more reliable than slip-ring type seals. A box design with a top flange is more advantageous than gearboxes with flanges on the input and output sides
- Quality of lubrication is a decisive factor in terms of service life. Oil coolers and filters are indispensable for large gearboxes as well as good control of the maintenance (oil changes)

- The stiffness of the housing is an important criteria for the service life if the housing is integrated into the nacelle structure.

Generator The generator converts mechanical power into electric power. Generators can be divided into *synchronous* generators (SG), which always run at the synchronous speed, dictated by the frequency of the grid, regardless of the applied torque, and *asynchronous/induced* generators (IG) which work with an induced magnetic current in the rotor. The SGs are mechanically more complicated therefore being more expensive, but allow for particular multi-pole solutions in direct-driven generators (gearless solutions). Despite being more robust, simpler and cheaper, the IGs need a reactive magnetizing current, which is either supplied by the grid or power electronics.

In terms of SGs, there are two classical types commonly used: *wound rotor synchronous generator* (WRSG) and *permanent magnet synchronous generator* (PMSG). In the WRSG, the stator windings are directly connected to the grid hence the rotational speed is fixed by the frequency of the supply grid. The rotor winding generates the exciter field, which rotates at synchronous speed. The PMSG has a wound stator and a permanent magnet as a rotor. Although this generator is very efficient, the main drawbacks are the high cost, since permanent magnets are very expensive, and the need for a full-scale power converter to adjust the voltage and frequency between generation and transmission.

On the IGs side, there are two types distinguished by the rotors: *squirrel-cage induction generator* (SCIG) and *wound rotor induction generator* (WRIG). The SCIG possesses a rotor with conducting bars embedded in slots and short-circuited in both ends. This solution is used for its mechanical simplicity, high efficiency and low maintenance requirements. The downside holds in its steep torque speed characteristic, i.e. fluctuations in wind power are transmitted directly into the grid. In the WRIG, we can observe two separate configurations: *OptiSlip or FlexiSlip induction generators* and the *doubly fed induction generator* (DFIG). The OptiSlip or FlexiSlip solutions use a variable external resistance attached to the rotor windings which is changed by an optically controlled converter. Moreover, this configuration eliminates the need for slip rings, which are prone to failure. In the DFIG the rotor and stator are connected to the grid, but while the stator windings are directly connected, the rotor is connected through a back-to-back power converter. Of course the cost of the converter increases for wider speed ranges and the need for slip rings is a disadvantage. The WRIGs allow for a control of the electrical characteristics and the power can be extracted or impressed to the rotor, but are more expensive and not as simple and robust as SCIGs.

Yaw system The yaw system automatically orients the rotor and the nacelle into the wind, being the transition between the nacelle and the tower head. Figure 2.31 [35] represents the assembly of the yaw system in a wind turbine. The yaw bearing can be either a roller bearing or a friction bearing. Though the traditional design consists in roller bearing, four-point ball bearings are being used in more recent designs. The friction bearing presents two sliding synthetic elements and conveys the desirable damping, thus no elaborate yaw brakes or rings are needed. Some large turbines, such as Vestas V-66, are using this solution successfully. For yaw drive, either electric or hydraulic systems can be a solution. Older turbines used the hydraulic solution due to lower costs, smaller sizes and higher torques. But with the evolution of the electric motors, controllable electric yaw drives have gained supremacy in recent turbines. Moreover, some manufacturers produce electric drives with integrated brakes, therefore not needing a separate yaw breaking system.

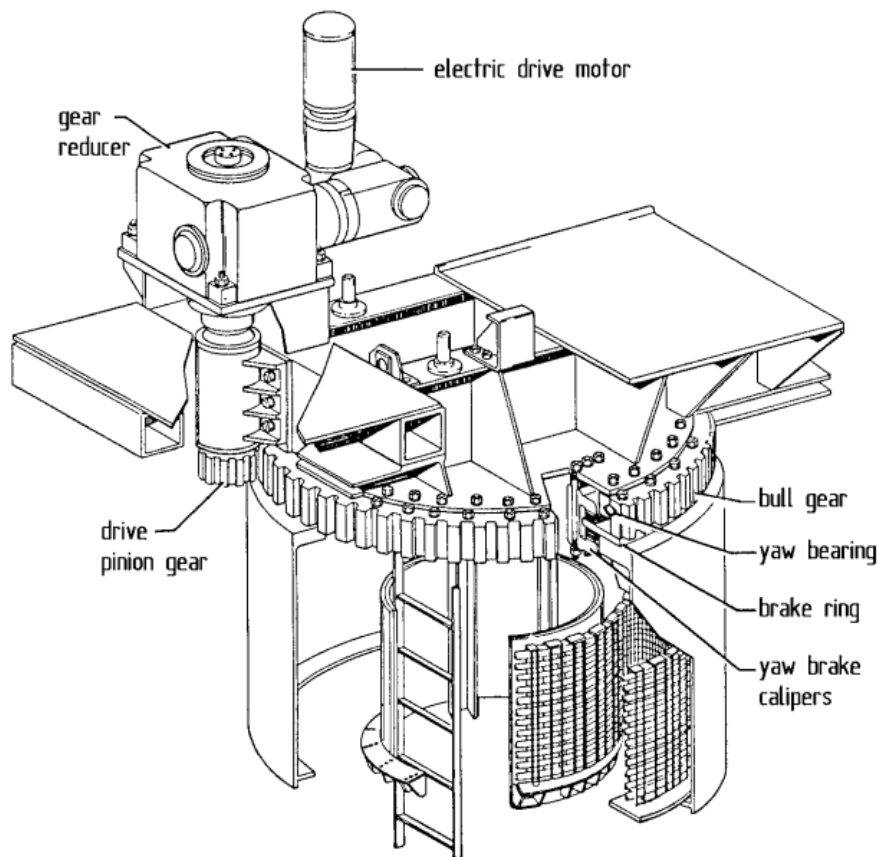


Figure 2.31: Yaw system with assembly of the Westinghouse WTG-0600 [35]

Tower The tower height is a compromise problem, since the rotor power output tends to increase with the tower height, but on the downside the transportations, assembly and erection of the tower as well as servicing of the components tend to be increasingly more difficult and costly. So one could say the optimal value would be the intersection between the two lines representing construction costs and energy yield. But it is not that simple to achieve a general applicability, since there are other factors at stake. For instance in larger turbines construction costs rise more steeply with the tower height than in smaller turbines. Even a more critical factor is the site. Inland sites, i.e. regions with high degree of surface roughness, show a smaller increase of wind speed with height than in shore-based sites. This means that higher towers show better return in inland than, for example, in offshore applications, since we need to go to higher altitudes to obtain good wind speeds.

Establishing the first natural frequency in the best way is an important task in wind turbine design. This determines the material required and hence the construction costs. In terms of materials, the solutions available are steel and concrete. In terms of constructive solutions, depending on the material, there are four main configurations:

1. Lattice tower
2. Concrete tower
3. Free-standing steel tubular tower
4. Guyed steel tubular tower

Lattice tower The simplest method of building high and stiff tower constructions is a three-dimensional truss, so-called *lattice* or *truss towers* (see Fig. 2.32a [26]). In 2006, these structures were gaining reputation in very high towers required for large turbines sited in inland regions.

Concrete tower Steel-reinforced concrete towers were characteristic of the earlier large experimental Danish turbines, being than set aside for steel structures in Denmark projects (see Fig. 2.32b [26]). Recently, concrete towers have gained favour again for tower heights of more than 80 m.

Free-standing steel tubular tower The most common solution currently in use is the free-standing steel tower (see Fig. 2.32c [26]). The dominance on the vibrational behaviour allowed to build steel towers with low design stiffness hence lighter and cheaper configurations.

Guyed steel tubular tower Down-wind rotors call for slender steel tubular towers in order to keep the tower shadow effect as low as possible (see Fig. 2.32d [26]). In order to ensure the required stiffness, these are anchored with steel cables and in some cases with truss structures. Despite the low overall mass, the guys additional anchoring foundations make it not very cost-effective.



(a) MOD-1 with lattice tower [26]



(b) Concrete tower of the Tjaereborg test turbine [26]



(c) Free-standing steel tubular tower of the MOD-2 [26]



(d) Guyed steel tubular tower of a Carter turbine [26]

Figure 2.32: Tower configurations

2.2 A Review on Fatigue

2.2.1 Definition

Fatigue failure is among many types of mechanical failures that were discovered throughout time, presented in Fig. 2.3 [36]. It can be defined as a material failure under repeated loading from which every single cycle induces a damage in the crystal lattice that, though negligible at the beginning, accumulates leading eventually to the complete and unexpected fracture of the material [37].

In conventional approaches, it is recognized that the fatigue embryo is an elementary plastic flow localized in some crystals on the surface of the components, since these are the areas where higher strains are present. At first, the flow of a single grain or few internal grains may be prevented by the surrounding material that does not want to yield leading to plain strain conditions. The damage evolves within the grain into a microscopic crack by the repeated application of loads and eventually it becomes a macroscopic crack, breaking the grain border and joining other micro-cracks in the neighbouring crystals. The integrity of a component is compromised when this crack is formed at the surface, no larger than 300-400 μm [37].

In recent studies, other type of fatigue failure model was discovered, where cracking occurs inside the material, due to either metallic or non-metallic inclusions, referring to a very high number of cycles. This subject will be approached later in this Chapter.

-
1. Excess deformation - elastic, yielding or onset of plasticity
 2. Ductile fracture - substantial plasticity and high-energy absorption
 3. Brittle fracture - little plasticity and low-energy absorption
 4. Impact or dynamic loading - excess deformation or fracture
 5. Creep - excess deformation or fracture
 6. Relaxation - loss or residual stress or external loading
 7. Thermal shock - cracking and/or fracture
 8. Wear - many possible failure mechanisms
 9. Buckling - elastic or plastic
 10. Corrosion, hydrogen embrittlement, neutron irradiation
 11. Stress corrosion cracking (environmental assisted cracking)
 12. Aesthetic aspects
 13. Fatigue - repeated loading
 - a. Fatigue crack nucleation
 - b. Fatigue crack growth
 - c. Constant or variable amplitude loading
 - d. Uniaxial or multiaxial loading
 - e. Corrosion fatigue
 - f. Fretting fatigue
 - g. Creep-fatigue
 - h. Combinations of a. to g.
-

Table 2.3: Mechanical Failure Models [36]

2.2.2 Fatigue stages, influencing factors and regimes

Fatigue stages

Fatigue failure can be characterized in three different stages, from early micro crack formation to complete fracture of the material. The fatigue growth rate that characterizes micro cracks during the very first crystallographic phase of fatigue, defined as Stage I, goes from some fraction to some tens of Angstrom per cycle ($1 \times 10^{-7} - 1 \times 10^{-6} \text{ mm cycle}^{-1}$), depending on the applied stress amplitude and micropores density. The breakthrough of two or three grains only happens after 10^4 to 10^6 cycles, reason why 90 percent to 95 percent of total life may be spent in this phase of fatigue (see Fig. 2.33 [37]), when the applied cyclic stress is close to the *fatigue limit*, opposing to the *low cycle fatigue* where this stage may take just around 20 percent of total life. The generation of cracks develops on

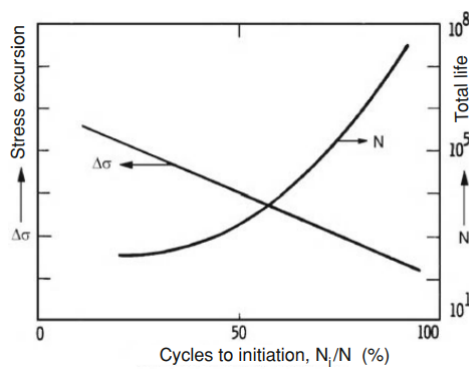


Figure 2.33: Schematic of initiation life fraction N_i/N vs. total life or stress excursion [37]

crystallographic planes along those directions on which the resolved shearing stress reaches a critical value. Due to the casual distribution of the crystallographic planes leads, the planes of maximum shearing stresses have not got the same orientation in surface grains, leading to the growth of microcracks in a zigzag path, as schematized in Fig. 2.34 [37].

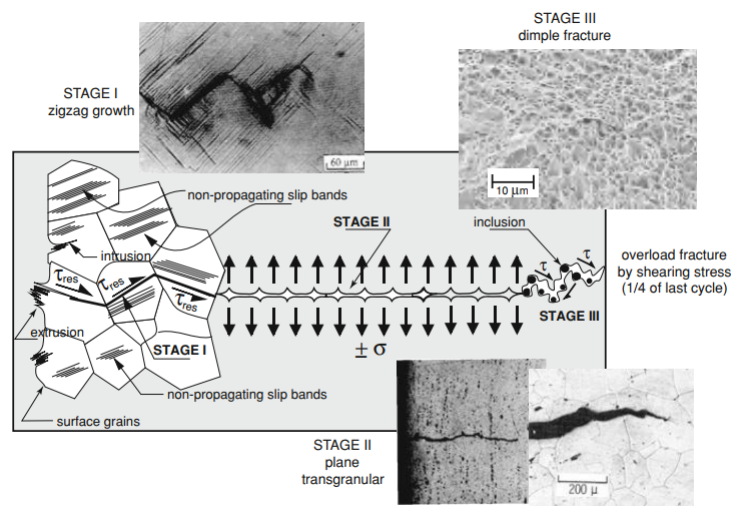


Figure 2.34: Schematic view of STAGE I, STAGE II and STAGE III of fatigue [37]

Once cracks reach a macroscopic size, entering in Stage II, they seem to stop depending on metallurgical factors. After reaching a macroscopic size of 200-400 μm , i.e. two or three

large grains, shear stress τ stops controlling the fatigue growth to give room to a normal stress σ control and cracks start to grow on a plane normal to the principal normal stress which in normal fatigue tests is equal to the direction of the external load (see Fig. 2.34). Here the crack growth rate increases to $1 \times 10^{-2} - 1 \times 10^{-1} \text{ mm cycle}^{-1}$.

By growing in Stage II, the cross section area resistant to crack growth diminishes and becomes more and more overloaded, thus entering in the last stage or Stage III (see Fig. 2.34). Therefore, even though initiated as *high cycle fatigue*, it may turn into *low cycle fatigue* and grow very fast. Now fatigue comes back to be driven by shear stress τ , but this time along the persistent grain boundaries and not the crystallographic planes. In this stage, overload may become so high that triggers a fast dimple rupture, always fed by shearing stresses that open, enlarge and join pores around inclusions [37].

Fatigue regimes

Over one hundred years ago, Wöhler conducted the first fatigue experiments on iron and steel specimens, arriving to the conclusion that the fatigue resistance depended on the applied cyclic stress amplitude σ_a , also conventionally indicated by the symbol S

$$S = \sigma_a = \frac{\sigma_{max} - \sigma_{min}}{2}. \quad (2.7)$$

The maximum stress σ_{max} has an effect on fatigue only in that the higher it is, the lower the amplitude σ_a of alternated stress that leads to failure. This last statement was delineating the effects of mean stress σ_m on fatigue:

$$\sigma_m = \frac{\sigma_{max} + \sigma_{min}}{2}. \quad (2.8)$$

He also concluded there is a lower limit σ_f for stress amplitude, below which cyclic stress could be applied an unlimited number of times without causing the fatigue failure of the material, called *fatigue limit*. Figure 2.35 [37] is a schematic representation of the cyclic stress amplitude versus the number of cycles to failure N_f , in a log-log plot. This plot, called *S-N curve* or *Wöhler's diagram*, is referring to a symmetrical stress cycle in which the maximum stress is equal to the minimum stress, except for the sign ($\sigma_m = 0$).

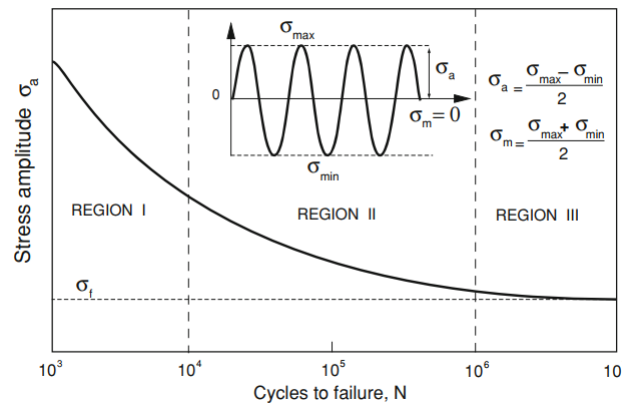


Figure 2.35: *S-N curve*, cyclic stress σ_a versus number of cycles to failure N , also known as *Wöhler's diagram*, showing the three regions that characterize fatigue behaviour [37]

On the curve, it can be distinguished three main characteristic regions. REGION I, from the $1/4$ of cycle to about 10^4 - 10^5 cycles, the material is always stressed in the vicinity

or over the yield strength σ_y and it is the plastic strain that dominates and controls the fatigue life. This region is denominated by *low-cycle fatigue* (LCF). REGION II is the most common in engineering applications. Here the material behaves elastically, at least on a macroscopic scale, and failure occurs under an alternate stress whose amplitude σ_a is always lower than the yield strength σ_y . This region is called by *high-cycle fatigue* (HCF) and it extends up to 10^6 - 10^7 cycles, and for ferrous alloys and titanium alloys, so called conventional alloys, terminating with a sharp knee, while for non-ferrous alloys may continue beyond 10^8 cycles. Beyond this knee starts REGION III, which determines the unlimited life of the material, since the *S-N curve* flattens and fatigue life becomes independent of the number of stress cycles. As earlier said, this stress is called the *fatigue limit* of the material, formerly called *endurance limit*. Below this limit, a load can be applied an infinite number of times without producing failure [37].

Opposing to HCF, LCF is mainly controlled by plastic deformation, therefore the linear relationship between stress and strain given by Hook's law stops being valid for this application and fatigue tests should be run under strain controlled condition, obtaining a ε_a - N curve where

$$\varepsilon_a = \frac{\varepsilon_{max} - \varepsilon_{min}}{2}. \quad (2.9)$$

Here the strain is the controlling parameter while stress is depending on the prior history of deformation. In HCF, the correspondence between stress and strain is linear (dominated by elastic deformation), therefore, the condition under which tests are run is not important. Since the region from LCF is not precisely known, test should be run under strain controlled conditions, even for the entire fatigue curve [37].

The conversion of a ε_a - N curve into a *S-N curve* one does not present many challenges. Experimental observations show an approximately linear relationship between the logarithm of true stress and the logarithm of true strain, denoting a possible relationship between S and ε as

$$\sigma_t = k\varepsilon_t^n \quad (2.10)$$

where k represents the plastic modulus, called *strength coefficient*, replacing the Young's modulus of linear elasticity and n is an exponent of *strain hardening*. Regarding this problem between the difference between strain and stress, ASME Code solves it by converting the strain experimental data into equivalent elastic stresses $\sigma_{a,el}$ as if the material were ideally elastic

$$\sigma_{a,el} = \varepsilon_a \cdot E = \frac{1}{2} \Delta\varepsilon_t \cdot E \quad (2.11)$$

where $\Delta\varepsilon_t$ is the total strain amplitude given to the specimen under fatigue test. Comparing Figure 2.36 [37] it is understood that the difference between stress or strain controlled tests is mainly in LCF, decreasing as tests approach HCF and null in the infinite life region [37].

As stated earlier, not all materials have an horizontal asymptote defining the so called *fatigue limit* such as non-ferrous alloys (see Fig. 2.37 [37]). Indeed, recent studies [38–41] have called the attention for the fact that also some steels may present this type of behaviour.

Generally, life beyond the 10^7 cycles is treated in terms of probabilities. Bathias [38] showed that differences in fatigue strength in this region past beyond what the probabilistic methods concluded, therefore being optimistic regarding the material's fatigue life. High-strength steels are materials that behave like this in *very high cycle fatigue* (VHCF) region described by service lives beyond 10^7 cycles, thus replacing the earlier called *infinite life* region. These materials show a two-fold *S-N curve* as shown schematically in Figure

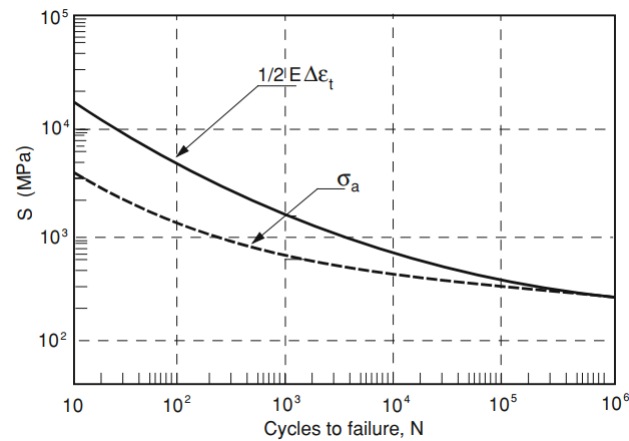


Figure 2.36: Difference between $S-N$ curve derived using equivalent ideally elastic stress procedure and conventional $S-N$ curve obtained directly in stress controlled tests [37]

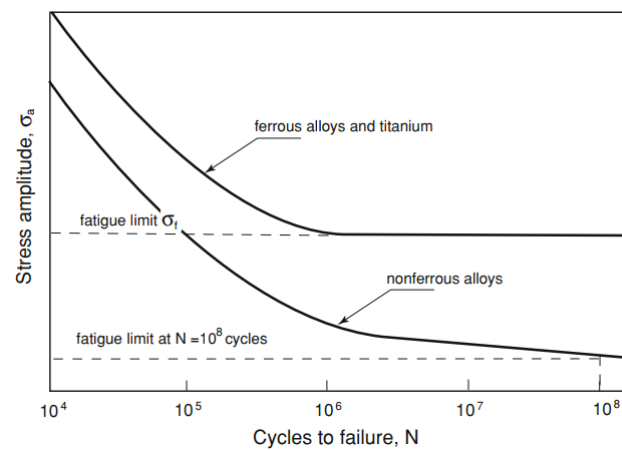


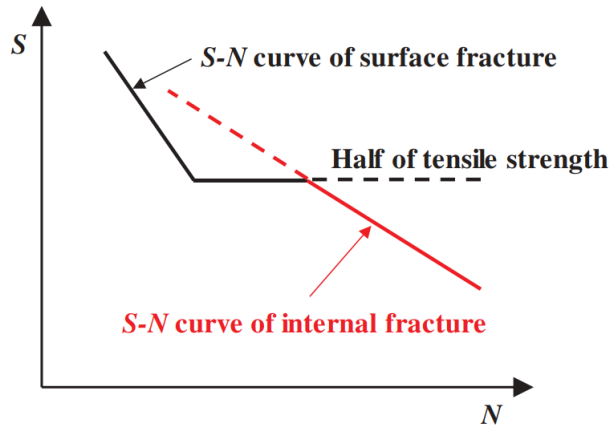
Figure 2.37: Two types of $S-N$ curves [37]

2.38 [39]. This is due to a different failure mode than conventional cracking. Opposing to surface cracking, in VHCF cracking occurs in the interior of the material [38–41]. A possible explanation deals with the fact that plastic deformation is residual, therefore crack initiation is most likely to start at materials defects. The probability of finding a defect in the interior is much greater than finding it on the surface, and is where it normally starts [38].

Influencing factors

In the conventional approaches, experimental data is available for fully reversed bending or axial loading, but is important to note there are many other factors at stake that determine and influence the fatigue life of a specific component, even in the results of experimental observations. The most important aspects would be:

1. Size
2. Type of loading
3. Surface finish

Figure 2.38: Two-fold S - N curve type concept [39]

4. Surface treatments
5. Temperature
6. Frequency
7. Microstructure
8. Environment

Bannantine et al. [42] states that there can be a direct correlation between the experimental data and the actual characteristics based on the expression

$$\sigma_{f,e} = \sigma_f \cdot C_{size} \cdot C_{surf.finish} \cdot C_{load} \dots \quad (2.12)$$

where $\sigma_{f,e}$ and σ_f are the actual and experimental *fatigue limit*, respectively, and the other components are the factors that represent the effect of each aspect stated above.

Size Effect The size aspect negatively influences the fatigue strength. This can be understood if one looks at the conventional failure that initiates at the surface, which is the weakest link. For larger components, the steep gradient is smaller, hence a larger volume of material is subjected to high stress, thus leading to a greater probability of crack initiation. Moreover, in larger specimens, there is a higher probability of microstructural discontinuities in highly stressed regions, adding up to the previous factor. An empirical expression for this factor is expressed by

$$C_{size} = \begin{cases} 1 & \text{if } d \leq 8 \text{ mm} \\ 1.189d^{-0.097} & \text{if } 8 \text{ mm} \leq d \leq 250 \text{ mm} \end{cases} \quad (2.13)$$

where d stands for the diameter of the specimen. Equation (2.13) implies that for diameters smaller than 8 mm the size has no effect on the results. This comes in accordance with the statements made by Stephens et al. [36] which referred to no size effect for specimens with less than 10 mm. Lastly, as one can easily conclude, for axial loading, the absence of gradient is less prominent (can appear only from certain misalignments), therefore, the size effect is not so significant and C_{size} can range from 0.75 to 0.9 [36].

Type of Loading When it comes to loading, there can be 3 main types of loading: bending, axial and torsion. Since the axial loading imposes a constant stress across the cross section of the specimen, there is a greater volume of material subjected to high stress, thus reducing the fatigue strength when compared to bending. The torsion loading imposes even greater damage than tensioning or bending. Conservative estimates for the respective factors are

$$C_{load} = \begin{cases} 0.7 & \text{for axial loading} \\ 0.577 & \text{for torsion loading.} \end{cases} \quad (2.14)$$

Surface Finish As stated already, sometimes conventional fatigue cracks initiate at the surface, therefore, the state of the surface can greatly impact the fatigue life. Scratches, pits, machining marks and poor surface finish can add stress concentration regions to the the ones already imposed by the geometry. Also, this effect is significantly higher for uniform fine-grain materials, such as high steels [36; 42]. Finally, this influence will be more pronounced in *high cycle fatigue*, since it is dominated by crack nucleation as opposing to *low cycle fatigue* which is dominated by crack propagation. Figure 2.39 [43] displays the $C_{surf.finish}$ for different finishes and types of materials.

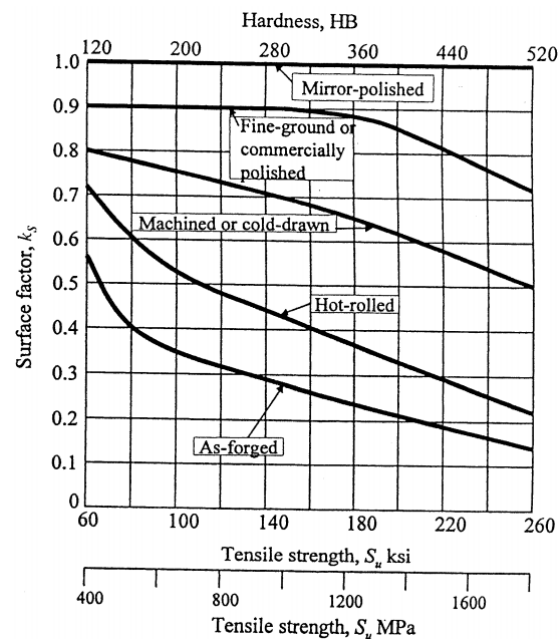


Figure 2.39: Effect of surface finish on the *fatigue limit* of steel [43]

Surface Treatments Besides the surface finish, discussed in the previous paragraph, other surface treatments can decisively affect the fatigue life of a component. The treatments can be divided into: plating, thermal and mechanical. The major reason for this effect are the residual stresses in the surface, which can be beneficial if in compression but very harmful when these convey residual tensile stresses.

Plating treatments, such as chrome and nickel plating can cause up to 60 percent reduction in fatigue strength, due to inducing high residual tensile stresses. In order to alleviate the induced residual stresses, the following operations can be made:

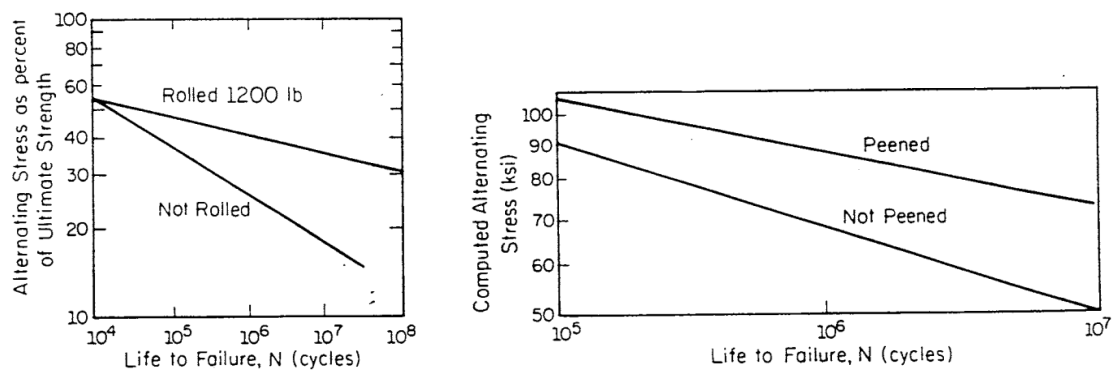
2. Background theory

1. Nitride the part before plating;
2. Shot peen the part before or after plating;
3. Anneal the part after plating.

It is also important to note that when fatigue occurs in a corrosive environment, the extra corrosion resistance offered by plating can more than offset the reduction of fatigue strength seen in a non-corrosive environment.

Thermal Thermal treatments can have either beneficial or detrimental effects on fatigue life. Diffusion processes, such as nitriding or carburizing, are very beneficial to fatigue strength, since not only produce higher strength material at the surface but also cause volumetric changes that lead to residual compressive stresses. On the other side, hot rolling and forging can produce decarbonization and tensile residual stresses, thus leading to a reduction in fatigue strength. Finally, manufacturing processes as welding, grinding and flame cutting can induce residual tensile stresses that also reduce fatigue life.

Mechanical Among the many cold working processes, the two most important are cold rolling and shot peening. Along with producing residual compressive stress, these methods also harden the surface material, thus improving the fatigue life, in great part due to residual stresses. As it can be seen in Figs. 2.40a [44] and 2.40b [45], these treatments have greater influence at higher lives, mainly because shorter lives tend to yield the material due to high strain applied hence removing the compressive stresses induced until then. In the same mindset, high-strength materials are more prone to enhancement since it is more difficult to induce yielding and remove the residual compressive stresses.



(a) Effects of cold rolling on the $S-N$ curve for steel [44] (b) $S-N$ curve of carburized gears in peened and unpeened conditions [45]

Figure 2.40: Effects of mechanical treatments in fatigue life

Temperature Temperature has a detrimental effect on fatigue strength, since materials tend to have higher fatigue strength at lower temperatures and the *fatigue limit* ceases to exist at high temperatures. But, an important aspect to consider is that many materials display a significant reduction in fracture toughness at low temperatures. However, when the temperature is high enough, it may cause annealing and may remove beneficial residual stresses, and for temperatures beyond approximately one half of the melting point, creep becomes significant and the $S-N$ approach is no longer applicable [42].

Frequency Frequency can greatly influence results through heating of the specimens, caused by hysteresis damping, disguising the true behaviour at room temperature. Moreover, heating is dependent on the highly stressed material volume, therefore, axial loading being clearly related with greater heating. In terms of low frequencies, generally up to 200 Hz, frequency effects can be neglected, although fatigue strength tends to be higher at higher frequency values followed with more data scatter [42]. Recently, there has been many developments on the assessment of VHCF behaviour due to ultrasonic fatigue tests, for instance at 20 kHz. These types of test raise the question whether frequency has or not an effect on the results. Regarding this aspect, there are many disagreements between the several studies. On one side, shown in Fig. 2.41, Furuya et al. [39] concludes that frequency has residual effect on results. While on the other hand, both Wood [46] and Chow and Soo [47] state that ultrasonic testing can produce spurious failure or misleading properties, such as local interior failures caused by local overheating (would not occur if there was a longer period of time).

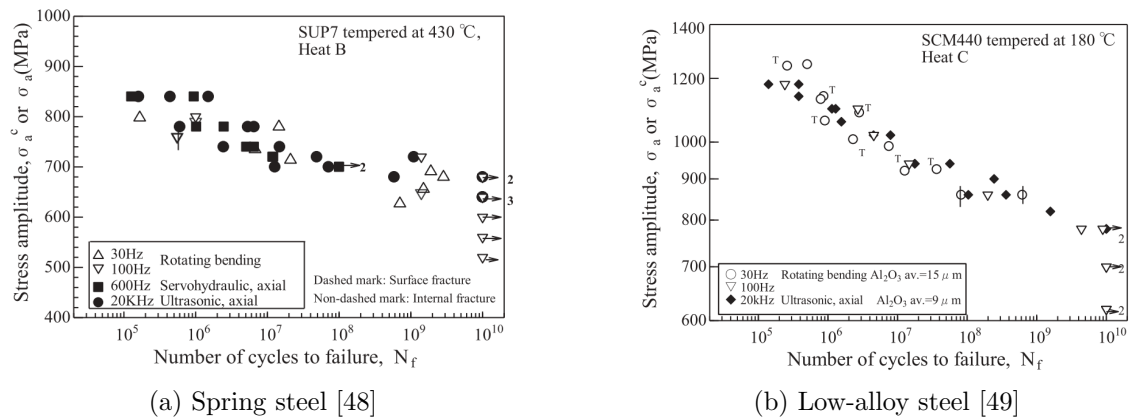


Figure 2.41: Typical ultrasonic fatigue test results for high strength steels

Microstructure Although microstructural aspects are embedded in the $S-N$ curve, and generally do not alter significantly in practical situations, some generalities can be taken from the effects. Fine grains tend to provide better fatigue performances except at elevated temperature, where creep mechanisms dominate (beyond approximately one half of the melting point). Fine grains reduce localized strains along slip bands, decreasing the amount of irreversible slip, and provide more grain boundaries to aid trans-crystalline crack arrest and deflection thus reducing fatigue crack growth rate. Anisotropy caused by cold working aids fatigue resistance when loaded in the direction of the working, due to the elongated grain structure in this direction. Inclusions, voids/porosity and laminations act as stress concentration regions, therefore, being prone to crack nucleation under cyclic loading, reducing fatigue resistance [36].

Environment In a corrosive environment, effects of corrosion and fatigue combined are more harmful than a separate analysis of both with superposition, by effect addition. Figure 2.42 [36] compares the $S-N$ curve for a material subjected to different environments. One can easily conclude that corrosion fatigue can drastically reduce fatigue life of a specific material. The phenomena analysis is rather complex and will not be the purpose of this work. But it can be understood that cyclic loading exposes new fresh metal to corrosion, which tend to create pits that represent stress concentration regions, promoting

crack initiation. The best way to resist to this phenomena comes with using high chrome content steels. Although there are other less efficient ways such as plating or painting [42].

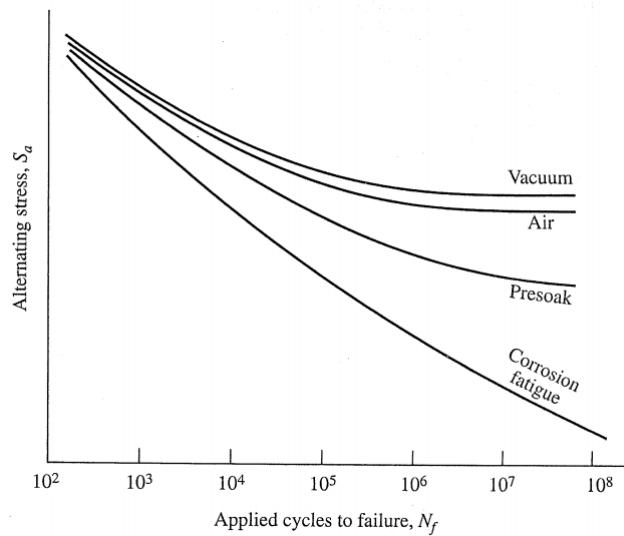


Figure 2.42: Relative $S-N$ behaviour under various environmental conditions [36]

2.2.3 Conventional approaches

S-N Curve

Looking deeper into the *high cycle fatigue* from a design point of view, we need to address the procedures regarding crack initiation prevention, therefore, the $S-N$ approach. As earlier said, conventional steels show the existence of a horizontal asymptote in the $S-N$ curve. Figure 2.43 [50] shows the experimental data on a carbon steel alloy, where the *knee* can be clearly observed at around 10^6 cycles. Many studies showed that the

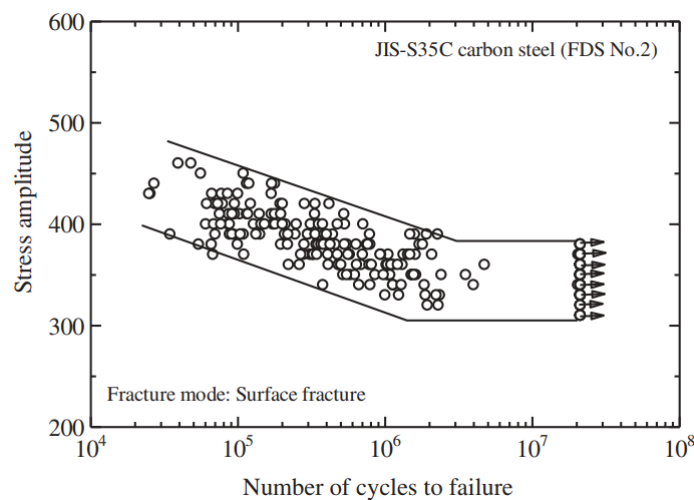


Figure 2.43: Fatigue test results for conventional JIS-S35C carbon steel [50]

ratio between the *fatigue limit* and the *ultimate strength* σ_f/σ_u for many different types of

steels varied from 0.4 to 0.54 [37]. These values are aligned with Duckworth observation who stated that up to 1200 MPa the average value of the *fatigue limit* σ_f related to the ultimate strength σ_u follows the expression

$$\sigma_f = 0.5 \cdot \sigma_u. \quad (2.15)$$

Figure 2.44 [51] also represents various experimental observations for steels and cast irons, called the Dowling diagram. It can be observed that this data also correlates well with Eq. (2.15).

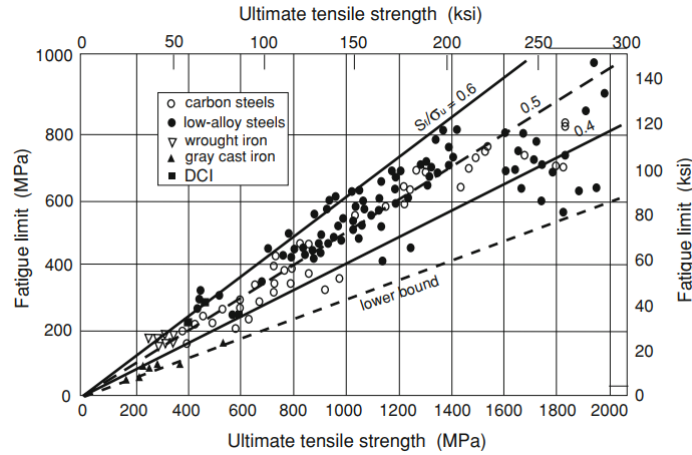


Figure 2.44: *Fatigue limit* versus ultimate strength for various steels and cast iron [51]

Empirical equations for fatigue limit

Many empirical equations that relate the *fatigue limit* to the mechanical properties of materials have been proposed. Svensson et al. [52], based on data collected from carbon steel, Cr-Mo steel and ferritic stainless steel, formulated a relation between the *fatigue limit* and the *ultimate strength* with the expression

$$\sigma_f = 46.3 + 0.49 \cdot \sigma_u + \varepsilon_u \quad (2.16)$$

with ε_u being the residual, with standard deviation to be

$$\Delta(\varepsilon_u) = 16.1 \text{ MPa}. \quad (2.17)$$

Alternatively, knowing steel hardness (in Vickers hardness HV) or yield strength, Svensson et al. [37] also formulated the following equations

$$\begin{aligned} \sigma_f &= 32.0 + 1.58 \cdot \text{HV} + \varepsilon_{\text{HV}} \\ \sigma_f &= 168 + 0.41 \cdot \sigma_s + \varepsilon_s \end{aligned} \quad (2.18)$$

with the following standard deviations on residuals

$$\begin{aligned} \Delta(\varepsilon_{\text{HV}}) &= 17.8 \text{ MPa} \\ \Delta(\varepsilon_s) &= 16.3 \text{ MPa}. \end{aligned} \quad (2.19)$$

The second expression of Eq. (2.18) is unusual, since it introduces the yield strength in relation with the *fatigue limit*, usually related with the ultimate strength. Another

2. Background theory

empirical equation that makes use of Vickers hardness has been proposed by Murakami et al. [53] for hardness less than 400 HV

$$\sigma_f = 1.6 \cdot HV \pm 0.1 \cdot HV \quad (2.20)$$

or in terms of Rockwell C hardness, up to 40/50 HRC

$$\sigma_f = 9.16 \cdot HRC + 308 \quad (2.21)$$

Dowling diagram of Fig. 2.44 [37] widens the field of materials, including also alloyed-steels, wrought steel and cast iron, suggesting a relation of the type

$$\sigma_f = C \cdot \sigma_u \quad (2.22)$$

with the constant of proportionality C varying from 0.3 up to 0.6.

Murakami et al. [53] also correlates the *fatigue limit* to the cross section of the largest defect present in the work piece, projected on the plane normal to the maximum tensile stress direction

$$\sigma_f = K \cdot (HV + 120) \cdot (\sqrt{area_{max}})^{-1/6} \left(\frac{1 - R}{2} \right)^\alpha \quad (2.23)$$

with

$$K = \begin{cases} 1.41 & \text{for surface defects} \\ 1.43 & \text{for sub-surface defects} \\ 1.56 & \text{for internal defects} \end{cases} \quad (2.24)$$

$$\alpha = HV \cdot 10^{-4} + 0.226$$

Figure 2.45 [37] compares predictions from Eq. (2.23) with the experimental data shown on Fig. 2.44 [51]. It testifies that Murakami model is consistent with experimental observations [37].

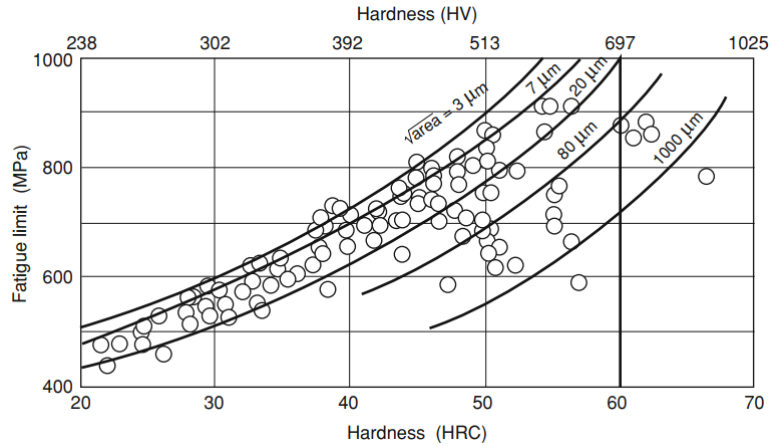


Figure 2.45: Comparison between Murakami predictions for different defect area and experimental data of Fig. 2.44 [37]

Basquin line

In 1910, Basquin [54] concluded that the stress-life $S-N$ data relative to the HCF domain could be plotted linearly in a log-log scale, suggesting a relationship for the elastic curve of the type

$$\varepsilon_a E = \frac{\Delta\varepsilon_t E}{2} = \sigma_a = \sigma'_f (N_f)^b \quad (2.25)$$

where $\varepsilon_a = \Delta\varepsilon_t/2$ is the elastic strain amplitude, E is the Young's modulus, σ_a the elastic stress amplitude, N_f life at σ_a , σ'_f a fatigue strength coefficient and b a fatigue strength exponent or Basquin's exponent. The fatigue strength coefficient σ'_f is equal to the monotonic true failure stress $\sigma_{t,f}$ while b varies from -0.05 to -0.12 . It must be noted that the true failure stress $\sigma_{t,f}$ in a monotonic traction test is higher than the so called engineering tensile strength or *ultimate strength* σ_u , as illustrated in Fig. 2.46 [37]. True stress and strain values can be derived by the engineering curve by the expressions

$$\begin{aligned} \varepsilon_t &= \log(1 + \varepsilon) \\ \sigma_t &= \sigma(1 + \varepsilon). \end{aligned} \quad (2.26)$$

The first expression of Eq. (2.26) is valid until necking occurs, since afterwards deformations no longer are uniform. After this, the specimen assumes an hourglass shape and the notch introduces a local stress concentration, that leads to variable stress distribution, as well as a multiaxial state which increases as the neck gets sharper.

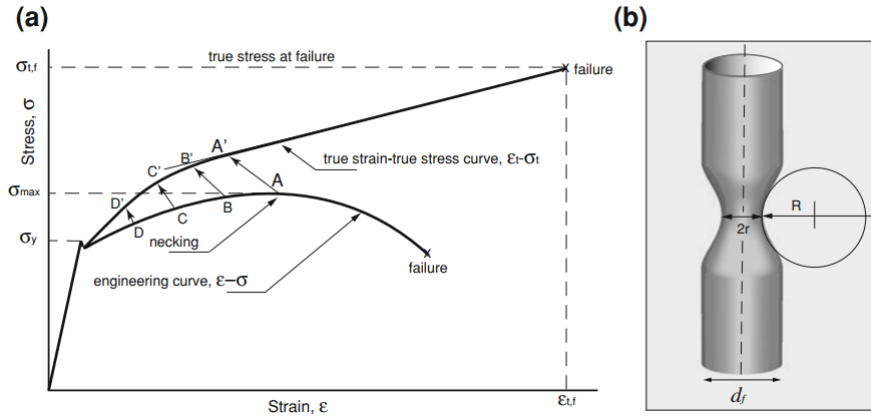


Figure 2.46: **a)** Schematic showing engineering curve $\varepsilon - \sigma$ and true strain-true stress curve $\varepsilon_t - \sigma_t$, **b)** Schematic of traction specimen at necking [37]

Morrow [55] states that the fatigue strength exponent b , which appears in the Eq. (2.25), could be expressed as

$$b = \frac{-n'}{1 + 5n'} \quad (2.27)$$

which means that in *high cycle fatigue*, low values of the cyclic strain hardening exponent n' favour the strength of materials. Moreover, from Eq. (2.25) it derives that the Basquin line can be expressed as

$$N = N_f \left(\frac{\sigma_f}{\sigma_a} \right)^{-1/b} \quad (2.28)$$

with $k = -1/b$ and N_f being the life corresponding to the *fatigue limit* σ_f . As stated earlier, some materials such as cast iron or light metals, do not consider any knee and the Basquin line extends beyond 10^6 cycles with the same slope. However, it has been

observed that under variable amplitude loading, even stress amplitudes lower than the *fatigue limit* may produce failure, specially when preceded with higher amplitude loading. In these cases, fatigue life does not end with a sharp knee but continues beyond the *fatigue limit* with a lower slope. To take this into account, Haibach [56] suggested a correction to the Basquin line slope to apply beyond 10^6 cycles. The new slope reduces from $-1/b = k$ to $2k - 1$

$$N = N_f \left(\frac{\sigma_f}{\sigma_a} \right)^{(2k-1)} \quad (2.29)$$

Figure 2.47 [37] shows bi-linear $S-N$ diagram with the Haibach correction. The Basquin line provides the simplest way to build the $S-N$ diagram, provided that the slope b is known. However, it must be remembered that only the elastic component of the stress amplitude enters in Eq. (2.25). Therefore, the Basquin line approximate the Wöhler curve only in *high cycle fatigue* as shown in Fig. 2.47. When the plastic component cannot be neglected, in general below 10^4 - 10^5 cycles, the Basquin line must be integrated with the Manson-Coffin component [37].

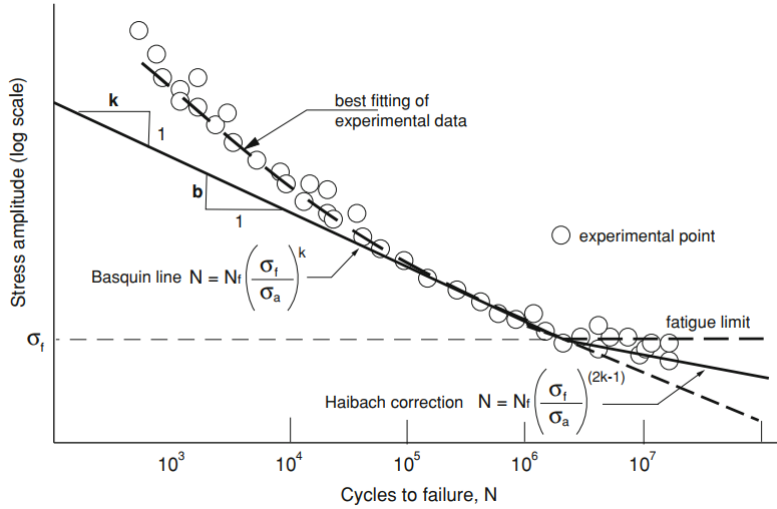


Figure 2.47: Haibach correction to the Basquin line [37]

Mean-stress effect

$S-N$ diagrams or Wöhler's curves are obtained using specimens under symmetrical or complete reversed condition loading where the *stress ratio* given by the expression

$$R = \frac{\sigma_{min}}{\sigma_{max}} \quad (2.30)$$

is $R = -1$ or, in other words, a mean stress, given by Eq. (2.8), equal to zero.

Figure 2.48 [37] shows different types of loading conditions. This emphasizes the fact that within the same stress amplitude σ_a , there can be different sets of mean stresses, which have a different impact on fatigue life, to be assessed ahead. In the first case **a**), a fully reversed stress cycle, the mean stress is equal to zero and a *stress ratio* equal to -1 . In the second case **b**), a non-symmetric stress cycle, the mean stress is positive and $R > 0$. In the third case **c**), the pulsating stress cycle, the mean stress is $\sigma_m = \sigma_a$ and $R = 0$. This serves as a warning to the fact that, since Wöhler's curve is not sensitive to

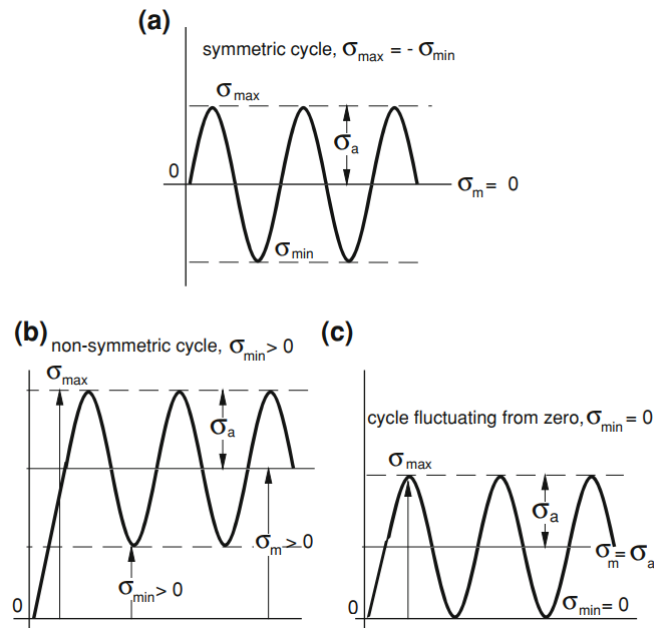


Figure 2.48: **a)** Fully reversed cycle with zero mean stress ($\sigma_m = 0$); **b)** Non-symmetric cycle ($\sigma_m > 0$) and minimum stress $\sigma_{\min} > 0$; **c)** Pulsating cycle fluctuating from zero or from the origin ($\sigma_m = \sigma_a > 0$, $\sigma_{\min} = 0$) [37]

mean stress, one may be induced in error with a specific stress amplitude σ_a and needs to address ways to implement the mean stress effect.

Figure 2.49 [57] shows an example of $S-N$ curves obtained on aluminium alloy type 2024-T351 for three different R ratios. Here, what is important to conclude is that for HCF there is a shift in the fatigue strength, diminishing as the R ratio increases. On the other side, the three curves tend to merge for regions below the 10^4 cycles. On that note, it can be concluded that the mean stress has a negative impact on fatigue life in *high cycle fatigue* that tends to fade for conditions closer to the *low cycle fatigue*. This statement is confirmed by the strain-based fatigue analysis models [37].

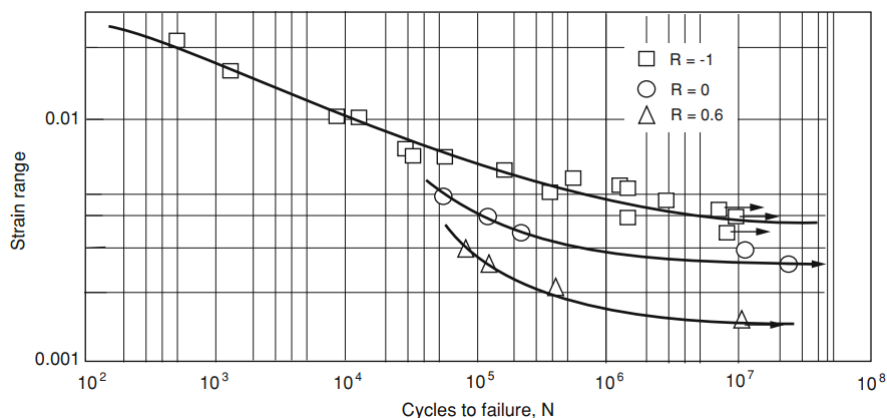


Figure 2.49: Wöhler's curves or $S-N$ diagram obtained on a 2024-T351 aluminum alloy for various R ratios [57]

In the turn of the nineteenth century, several models where developed to tackle the

mean stress effect. Gerber [58] proposed a parabolic dependence of the *fatigue limit* on the mean stress that would go from zero to the *ultimate strength*, known as Gerber parabola. Goodman [59] instead, assumed a linear relationship between σ_f and σ_m joining the two extremes of the Gerber parabola, called the Goodman line. In both cases, the analytical relation that defines the allowable *fatigue limit* when a mean stress is acting is

$$\sigma_{f,m} = \sigma_f \left[1 - \left(\frac{\sigma_m}{\sigma_u} \right)^n \right] \quad (2.31)$$

with $n = 2$ for the Gerber parabola and $n = 1$ for the Goodman line. For a finite life N_f , point σ_f is replaced with the value of the stress amplitude σ_a corresponding to the life cycle N_f on the *S-N curve* obtained under fully reversed loading ($R = -1$). Soderberg [60], on the other hand, proposed that the mean stress would be limited by the yield stress, following the expression

$$\sigma_{f,m} = \sigma_f \left(1 - \frac{\sigma_m}{\sigma_y} \right). \quad (2.32)$$

All these models are displayed in Fig. 2.50 [37]. This concludes that the Soderberg criterion is the most conservative criterion, while the Gerber parabola tends to be the most optimistic between the three models.

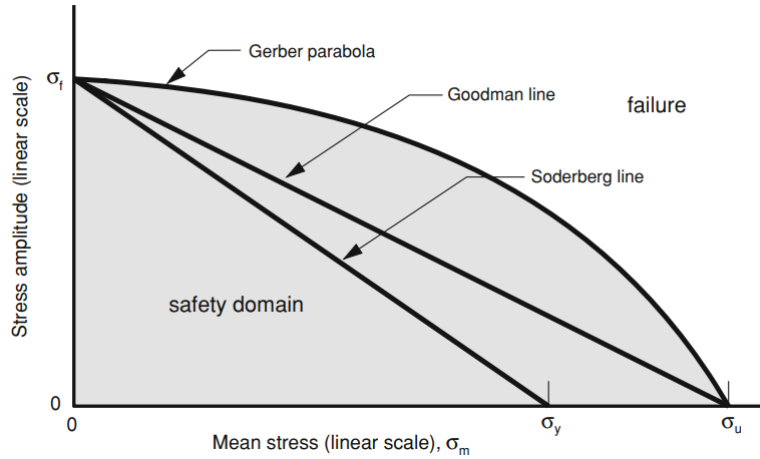


Figure 2.50: Lines of constant fatigue life, uniaxial stress amplitude with tensile mean stress proposed by Gerber, Goodman and Soderberg, respectively [37]

When a component is under compressive mean stress, experimental data shows that *fatigue limit* does not decrease at all, but may even increase. This experimental observations showed that 90 percent of data on steel, aluminium, brass and other alloys, when subjected to a compressive mean stress amplitude, is falling between the Gerber parabola and the Goodman line. This is why the ASME Code adopted the Goodman line as a design criterion. For any stress amplitude it can be written

$$\begin{aligned} \sigma_{f,m} &= \sigma_f \left(1 - \frac{\sigma_m}{\sigma_u} \right) \\ \sigma_{a,m} &= \sigma_a \left(1 - \frac{\sigma_m}{\sigma_u} \right). \end{aligned} \quad (2.33)$$

On the other side, Morrow [61] stated that the mean stress could go beyond the *ultimate strength* of the material until the fatigue strength coefficient σ'_f introduced by Basquin in

Eq. (2.25). Thus Eq. (2.31) becomes

$$\sigma_{f,m} = \sigma_f \left(1 - \frac{\sigma_m}{\sigma'_f} \right)^{-1} \quad (2.34)$$

and Eq. (2.25) becomes

$$\sigma_{f,m} = (\sigma'_f - \sigma_m) \cdot (N_f)^b. \quad (2.35)$$

At the same time, the conventional *fatigue limit* can be written as

$$\sigma_{f,m} = \sigma_f - M \cdot \sigma_m, \quad M = \tan \phi = \frac{\sigma_{a,R=-1} - \sigma_{a,R=0}}{\sigma_{a,R=0}} \quad (2.36)$$

where M is called the Morrow factor and represents the fatigue strength sensitivity to the mean stress. The representation of the Haigh diagram in Fig. 2.51 [37] assesses the differences in the fatigue strength sensitivity affected by the type of loading.

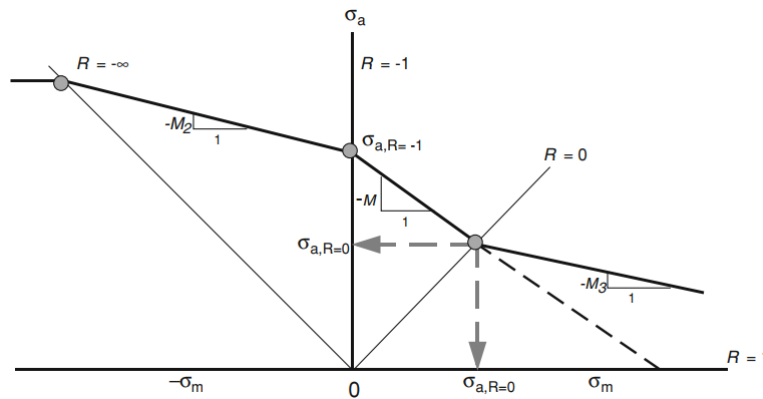


Figure 2.51: Haigh diagram showing the mean stress sensitivity factor M and its dependence on mean stress [37]

In terms of shear stress loading, this stress condition does not produce any physical difference between traction or compression, therefore the Goodman diagram only possesses the positive quadrant. Moreover, shear stress amplitude τ_a or the *fatigue limit* τ_f do not seem to be affected by the mean shear stress τ_m . Figure 2.52 [62] shows that the allowable alternating stress is independent of the mean shear stress τ_m up until higher values, where the presence of notches changes the stress state of pure shear. Experimental data shows that in this region the mean shear stress τ_m decreases the allowable stress amplitude τ_a [37].

Fatigue strength diagrams

In order to compile all the information stated earlier, there are specific diagrams synthesizing the fatigue strength with the effect of cycles to failure and loading conditions, i.e. mean stress conditions. This is the case of Fig. 2.53 [37] that provides the safety domains for compressive and tensile mean stress, also known as the *Haigh diagram*. It comprehends the combination of the *Soderberg line*, both for compressive and tensile mean stress, and the *Goodman line*. In a conservative perspective, the stress amplitude is limited to a maximum determined by the *fatigue limit*. Another way of plotting the *Haigh diagram* is known as the *Smith diagram* or *modified Goodman diagram*, shown in Fig. 2.54 [37]. It

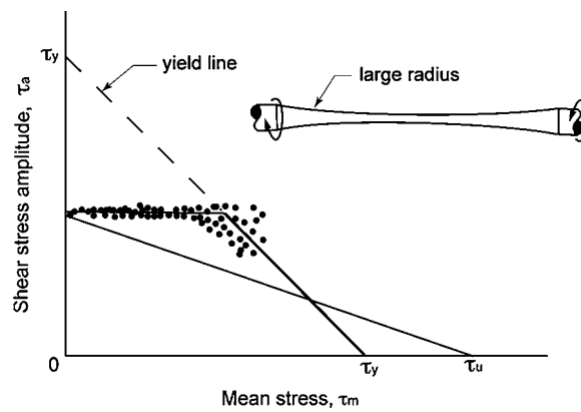


Figure 2.52: τ_m - τ_a diagram for unnotched torsion members of ductile metal [62]

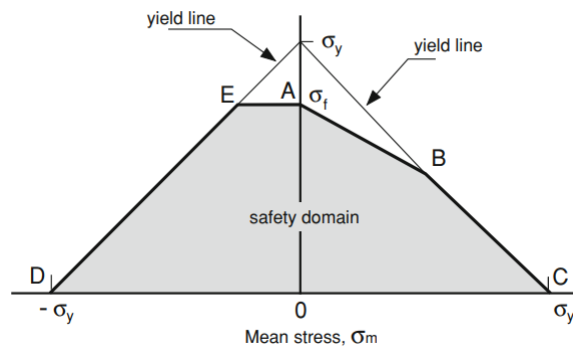


Figure 2.53: *Haigh diagram* representing the safety domain for any combination σ_m - σ_a [37]

provides the total stress excursion $\Delta\sigma_a = \sigma_{max} - \sigma_{min}$. One can also find an even more condensed diagram, the *master curve*, where data is displayed either in terms of σ_a - σ_m or σ_{min} - σ_{max} . Figure 2.55 [63] shows the *master curve* of the AISI 4340 steel, displaying not only the two types of input-output variables but also several curves regarding different values of life at failure N .

Variable Amplitude Loading: Cycle Counting and Life Prediction

Usually, in practical problems, cyclic loading displays a certain variability in terms of amplitude that is referred to as load spectrum or time history. Looking, for example, to the wing of an airplane, subjected to continuous flexural vibrations of variable amplitude during take-off, flying cruise and landing, as schematized in Fig. 2.56 [37]. Atmospheric turbulences at lower altitude, during take-off and landing, induce low frequency with high amplitude, while during cruise at high altitudes, there is a more stable loading, characterized by high frequency low amplitude vibrations.

A question that arises from dealing with variable amplitude cyclic loading is whether cycles can be treated individually or analysed as a single load sequence that is repeated many times and how to combine their effects, i.e. cycle counting and damage progression and accumulation. In this section, one will have a glimpse at some cycle counting techniques as well as some damage accumulation models.

Nowadays, the most commonly used method for cycle counting was proposed by Mat-

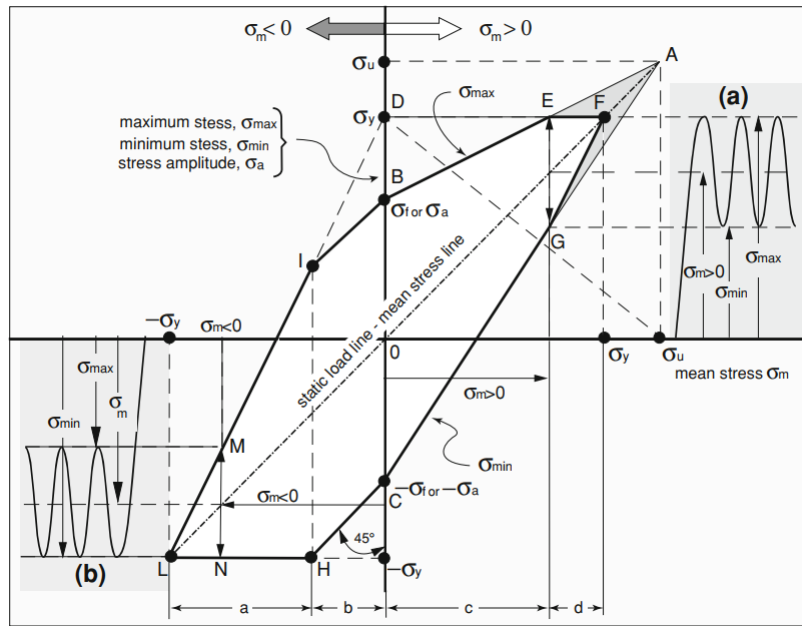


Figure 2.54: *Smith or Modified Goodman diagram* for axial and bending fully reversed loads, ductile metals [37]

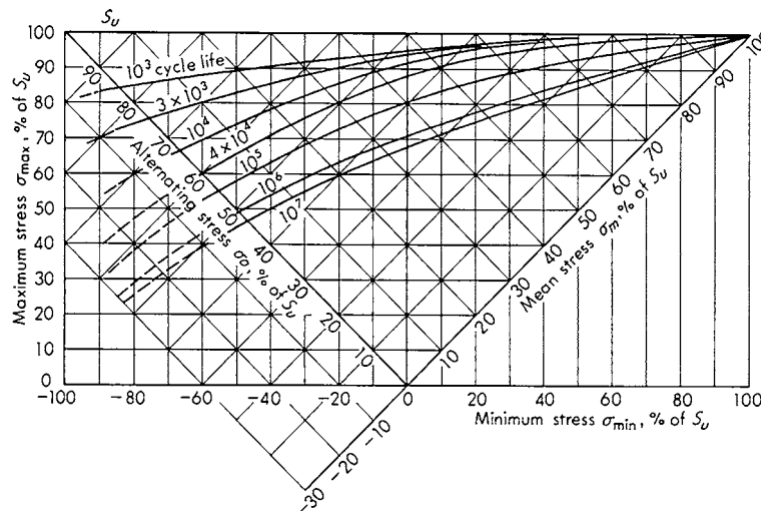


Figure 2.55: *Master curve* for AISI 4340 steel [63]

suishi and Endo [64] known as the *rainflow counting* or *pagoda roof method*. It attempts to identify and separate cycles in a complex time history. The method is analogous to a raindrop falling from a pagoda roof, hence the name *rainflow counting* or *pagoda roof method*.

Firstly, the spectrum is rearranged so that starts and ends at the highest peak stress or strain to prevent counting of half cycles. Then the time axis is rotated by 90° so the time history resembles a pagoda roof. Then one has to imagine a drop falling from the roof. If the fall starts from a peak, it continues to flow till it arrests for one of the following reasons:

- a) meets an opposing peak larger than that from which it came;

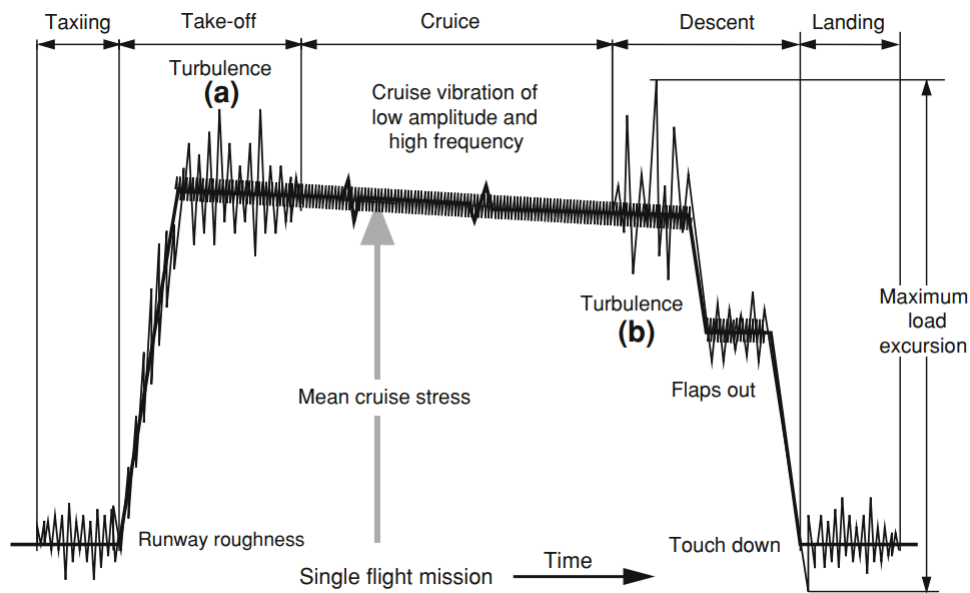


Figure 2.56: Schematic of flexural loads induced in an airplane wing during a flight [37]

b) encounters a previous rain flow.

If the fall begins in a valley, it continues till it arrests for one of the following reasons:

- c) meets a valley deeper than that of departure;
- d) crosses the path of a drop coming from a preceding valley.

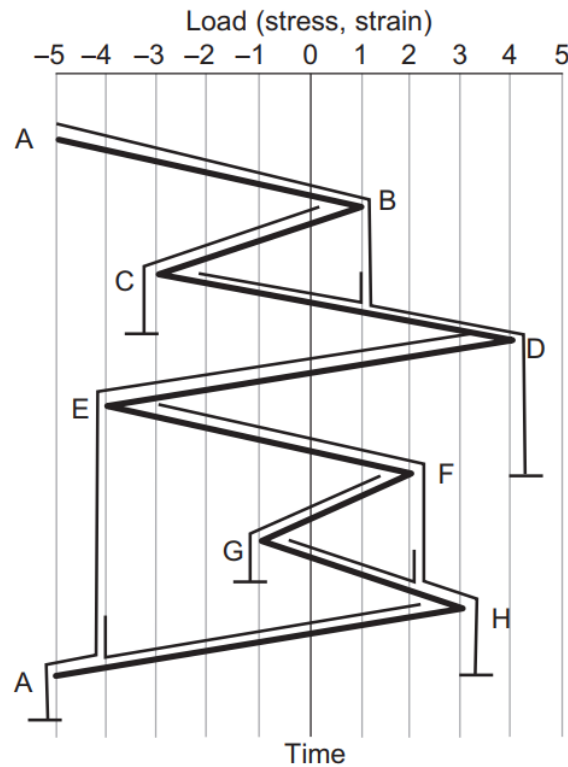
A good way to understand the concept is through a practical example, supported by Fig. 2.57 [65]. Note in Fig. 2.57a [65] that the load spectrum is not rearranged in order to prevent half cycle counting. If one deals with a cyclic behaviour, a rearrangement must be done in order to make sure the largest hysteresis loop is collected. After one has rotated the time axis as schemed in Fig. 2.57b [65], it can be counted the reversals and cycles as follows:

1. Identify the first largest reversal A–D as the flow of the rain starts at A and falls off the second extreme point D, the smallest valley in this load time history;
2. Identify the second largest reversal D–A as the flow initiates at D and ends at the other extreme point, which happens to be the first one, A;
3. In the first largest reversal A–D:
 - a. Identify a reversal B–C as the rain starts flowing at B and terminates at C, because D is a larger maximum than B;
 - b. Identify a reversal C–B as the rain starts flowing at C and meets a previous flow at B;
4. In the second largest reversal D–A:
 - a. Identify a reversal E–H as the rain starts flowing at E and falls off the roof at H;
 - b. Identify a reversal H–E as the rain starts flowing at H and meets a previous flow at E;

- c. Identify a reversal F–G as the rain starts flowing at F and terminates at G, because H is a larger maximum than F;
 - d. Identify a reversal G–F as the rain starts flowing from the successive extreme point G and meets a previous flow at F.
5. All data assessed, it can be obtained cycle AD, BC, EH and FG, with data displayed in Table 2.4



(a) Service load-time history



(b) Rainflow cycle counting

Figure 2.57: Illustration of the rainflow counting technique. Identification of reversals and loading cycles [65]

ASTM E1049-85 also recommends a cycle counting method commonly known as the *three point method*, which is defined by repeatedly evaluating three consecutive peaks/valleys within the time history at a time. As you can see in Fig. 2.58 [36], the “trick” comes from

Cycle counting results						
Number of Cycles	From	To	From	To	Range	Mean
1	A	D	-5	4	9	-0.5
1	B	C	1	-3	4	-1
1	E	H	-4	3	7	-0.5
1	F	G	2	-1	3	0.5

Table 2.4: Cycle counts based on rainflow counting technique

defining two consecutive ranges $X = |P3 - P2|$ and $Y = |P2 - P1|$, counting a hysteresis loop from $P1$ to $P2$ and back to $P1'$, if $X \geq Y$ and no cycle if $Y > X$. In terms of hysteresis loops, the cycles can be determined as hanging (see Fig. 2.58a [36]) or standing (see Fig. 2.58b [36]) cycles, depending on whether $P2$ is a valley or a peak, respectively [36; 42].

Now that the first part of the assessment it is dealt with, i.e. defining the cycles within a spectrum, one has got to understand how damage progresses and accumulates over time. The general mindset regarding this matter is to assume that each individual cycle introduces an unrecoverable damage D unless some treatment, e.g. annealing or surface polishing, is performed. Each hysteresis loop adds up to the damage accumulation from previous fatigue cycles until failure. In general, damage progression deals with cycles of constant amplitude and accumulation refers to a loading spectrum of variable amplitude. When it comes to assessing damage progression, an important parameter to consider is the *cycle ratio* which relates the damage D_i with the ratio between the number of applied cycles n_i and the allowable cycles N_i at the equivalent stress or strain amplitude (considering the mean stress effect)

$$D_i = \left(\frac{n_i}{N_i} \right)^{m_i} \quad (2.37)$$

where the exponent m_i can assume any value depending on the stress amplitude and the considered model.

In 1945 Miner [66] proposed a linear behaviour for damage progression and accumulation that displayed excellent agreement with experimental observations. The *Miner's rule* infers that the fraction of fatigue life used by n_i cycles of a respective stress amplitude S_i is proportional to the correspondent *cycle ratio*, i.e. $m_i = 1$ in Eq. (2.37). Then, by defining a *critical damage* D_{cr} that represents total failure, the failure occurs when

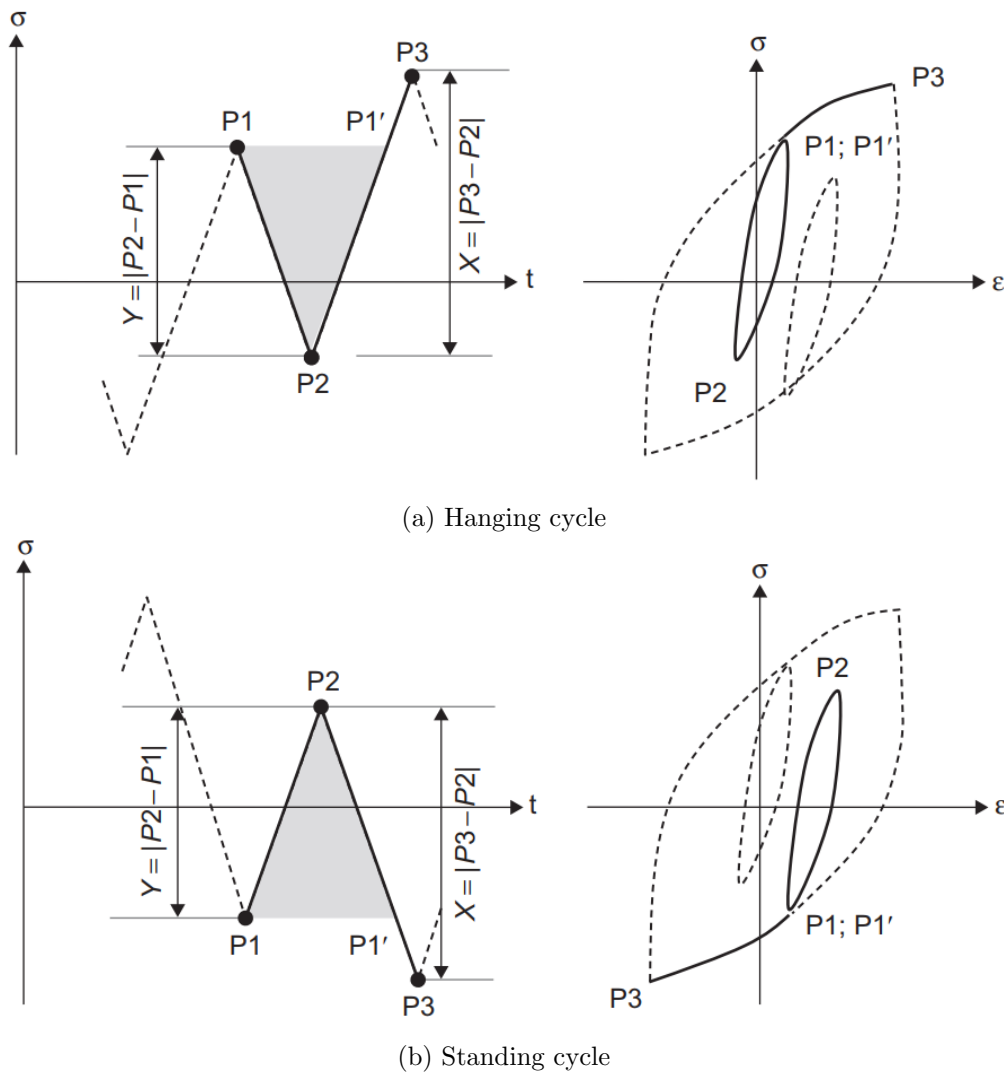
$$D_{cr} = D_{cr} \left(\frac{n_1}{N_1} \right) + D_{cr} \left(\frac{n_2}{N_2} \right) + D_{cr} \left(\frac{n_3}{N_3} \right) + \dots = D_{cr} \sum \left(\frac{n_i}{N_i} \right) \quad (2.38)$$

or

$$1 = \frac{n_1}{N_1} + \frac{n_2}{N_2} + \frac{n_3}{N_3} + \dots = \sum \frac{n_i}{N_i} \quad (2.39)$$

for various blocks of n_i cycles under constant stress amplitudes S_i . It is important to notice that the *Miner's rule* does not consider the time history of a cyclic load in the sense that equal *cycle ratios* produce equal damage, regardless of the order of application, which is a major drawback.

By looking at damage initiation, i.e. creation of micro-cracks, it can take just 0.5 percent of total life to micro-crack formation or about 30 percent depending on whether dealing with high stress amplitudes or near *fatigue limit* ones, respectively. This means that it cannot be used just a single linear relationship for all cases, completely neglecting the relation between loading cycles. If one just approaches the possibility of two cases:

Figure 2.58: ASTM *three point cycle counting rule* [36]

1. Low-stresses to high-stresses
2. High-stresses to low-stresses

it becomes pretty clear. In the first case, low-stress amplitudes may not even create microcrack formation, being totally ineffective when it comes to damage. On the other side, if high amplitudes are applied first, damage would be introduced and the low stresses that till now were ineffective, would induce a damage which needs to be accounted for. Although this may be a concern, the *Miner's rule* can still be applied with relative accuracy if the time history shows a random sequence (see Fig. 2.59c [37]).

Although *Miner's rule* can be used in many situations, with no distinct sequence and blocks of stress amplitudes, there are many situations where there can be noticed clear distinction and sequence in separate blocks of loading in time history. When this happens, the linear approach is no longer applicable since a high to low sequence (see Fig. 2.59a [37]) may lead to a *Miner's rule* conservative approach, i.e. $\sum \frac{n_i}{N_i} < 1$, and a low to high sequence (see Fig. 2.59b [37]) may lead to a *Miner's rule* optimistic approach, i.e. $\sum \frac{n_i}{N_i} > 1$. This situation immediately implies a non-linear model, since the order of loading directly

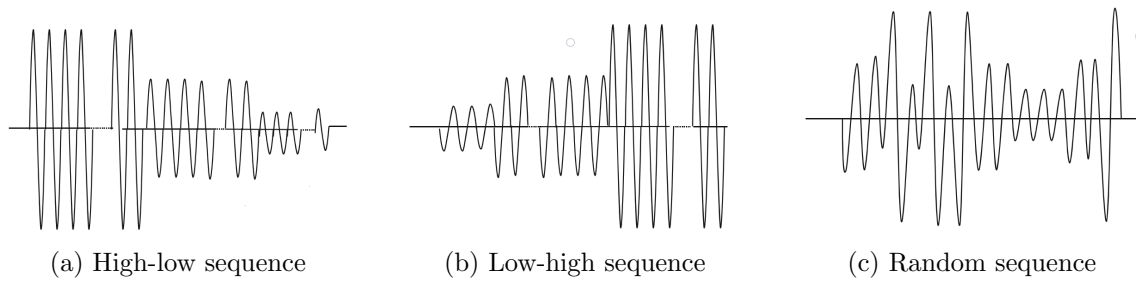
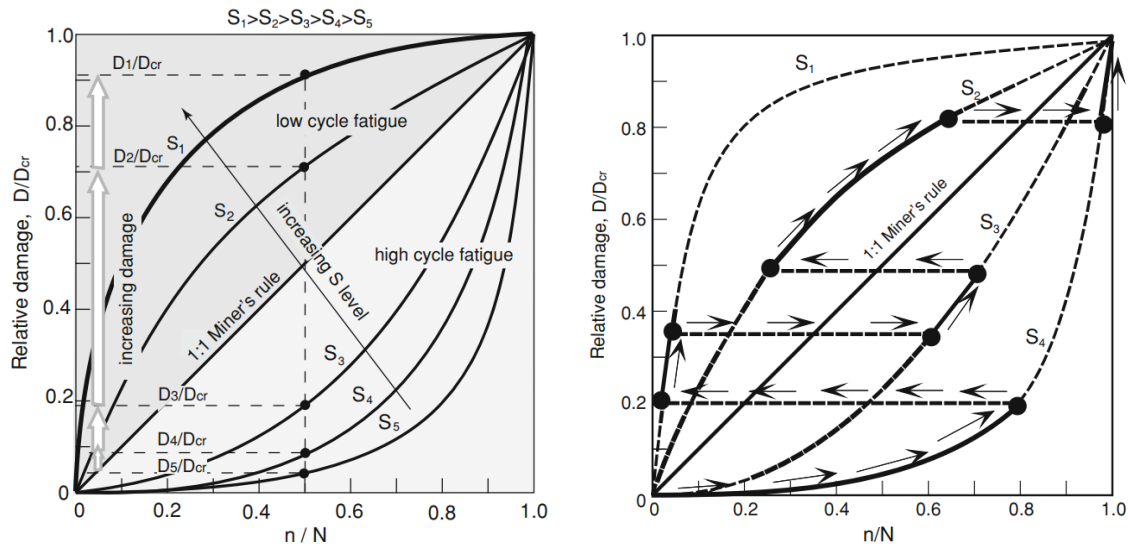


Figure 2.59: Time histories with different orders of application [37]

affects the damage. Many researchers [67–71] have addressed the problem of damage progression and accumulation with a low power dependence of the type expressed by Eq. (2.37). The *high cycle fatigue* domain is characterized by $m > 1$ in which the values of the exponent decreases as the stress amplitudes get larger up until it passes the *Miner's rule*, i.e. $m = 1$, entering the *low cycle fatigue* where $m < 1$, as described in Fig. 2.60a [37]. The process follows a continuous passage from one damage curve relative to a particular



(a) Power low dependence of damage progression and accumulation for different load amplitudes (b) Damage progression and accumulation in a four-block load sequence

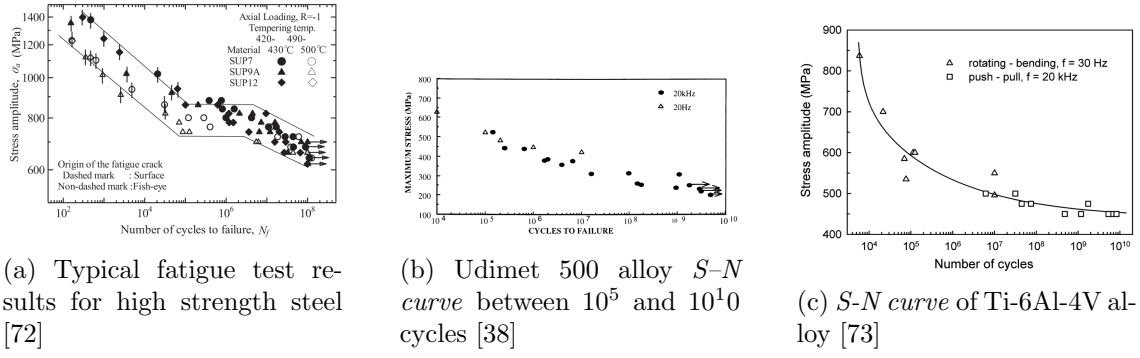
Figure 2.60: Non-linear damage progression and accumulation [37]

stress amplitude block to another and vice versa, as schematized in Fig. 2.60b [37]. The key issue of this approach is the knowledge of the exponents m_i of Eq. (2.37) relative to each individual curve of Figs. 2.60a and 2.60b by a matter of experimental procedures.

Very high cycle fatigue

As mentioned before, some materials are described for not having the so called *fatigue limit*, i.e. the horizontal asymptote of the *S-N curve*. Figure 2.61 shows a compilation of experimental data on *S-N curves* for different types of materials beyond 10^7 cycles in the *very high cycle fatigue* regime. Finite life beyond 10^7 cycles can be detected, with a decrease in the slope of the curve.

Regarding the calculation of the fatigue strength in *very high cycle fatigue*, there are

Figure 2.61: $S-N$ curve of different types of materials

some models that allow to make predictions with some level of confidence. Halford [74] proposed a model to predict behaviour beyond 10^6 based on the LCF curves. It changes the slope of the $S-N$ curve to better represent the shallower feature in VHCF displayed in Fig. 2.61. Two cases are considered, displayed in Fig. 2.62 [75], depending on whether the elastic line slope is steeper or shallower than $b = -0.12$. For steeper slopes, the transition for the smallest slope happens in such way: $b = -0.10$ for 10^6 to 10^7 cycles; $b = -0.06$ for 10^7 to 10^8 cycles; $b = -0.04$ beyond 10^8 cycles. As for shallower slopes, the transition to the shallowest slope $b = -0.04$ occurs in just two steps. This can be expressed analytically by

$$b = -0.12 + \left(\frac{0.082}{90} \right) \arctan [0.403(\log N_f - 5.5)^{2.544}]. \quad (2.40)$$

Manson and Halford [75] proposed a more generic expression for any slope

$$b = -b_0 + \left(\frac{b_0 - b_1}{90} \right) \arctan [\alpha(\log N_f - 5.5)^\beta] \quad (2.41)$$

with b_0 has the elastic line slope in the life range between 10^5 and 10^6 cycles. Furthermore, the model expressed in Eq. (2.41) allows for a smoother variation of the slope b from b_0 to b_1 , with the flexibility of adjusting the pattern of transition with the parameters α and β . Other possible solution relates with the fact that, as earlier said, VHCF strength is dominated by the material's inclusions and cracking starts at these defects. Having that in mind, some models relate the fatigue strength with the inclusions in the material. The first is the Murakami model stated in Eq. (2.23). Wang et al. [40] proposed a modified Murakami model

$$\sigma_w = \frac{\beta(HV + 120)}{(\sqrt{area})^{1/6}} \left[\frac{1 - R}{2} \right]^\alpha \quad (2.42)$$

where

$$\beta = 3.09 - 0.12 \log N_f, \quad \text{for interior inclusions or defects} \quad (2.43a)$$

$$\beta = 2.79 - 0.108 \log N_f, \quad \text{for surface defects} \quad (2.43b)$$

which correlates very well with the experimental data, having an average error of 4.17%. Furuya et al. [39], realising that inclusion size is difficult to take in consideration, formulated a model based on fracture mechanics modified *Paris law*

$$\frac{d\sqrt{area}}{dN} = C(\Delta K \cdot \sqrt{area}^\alpha)^m \quad (2.44)$$

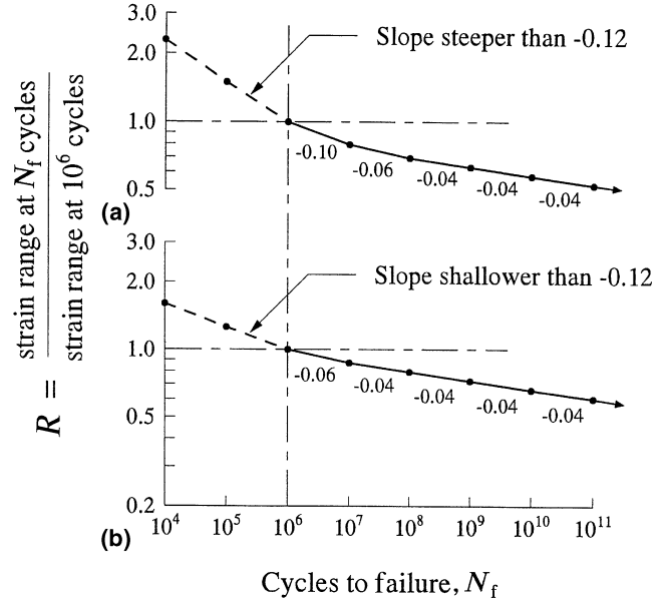


Figure 2.62: Model for extrapolating high-cycle fatigue beyond 10^6 cycles by using elastic line segments of progressively reduced slope [75]. **a)** Slope steeper than 0.12; **b)** Slope shallower than 0.12.

that leads to the relation between stress cycle amplitude σ_a and number of cycles to failure N_f

$$\sigma_a = \frac{1}{\sqrt{\pi}}(D)^{\frac{1}{m}} \times (N_f)^{-\frac{1}{m}} \times (\sqrt{\text{area}_{inc}})^{\left(\frac{1}{m} - \frac{1}{2} - \alpha\right)} \quad (2.45)$$

$$D = \frac{2^{1-m\left(\frac{1}{2}+\alpha\right)} - 1}{C^{1-m\left(\frac{1}{2}+\alpha\right)}}$$

where the parameters C , m and α are determined through conventional fatigue tests, as shown in Fig. 2.64a [39]. The α parameter is computed by achieving the maximum possible correlation coefficient with the experimental data, as shown in Fig. 2.63 [39]. Also a good consistency with the experimental data is shown in Fig. 2.64b.

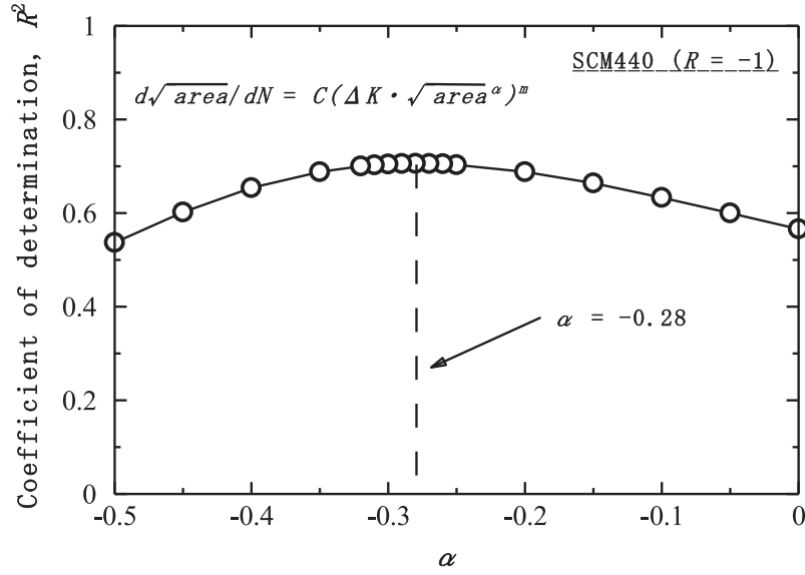
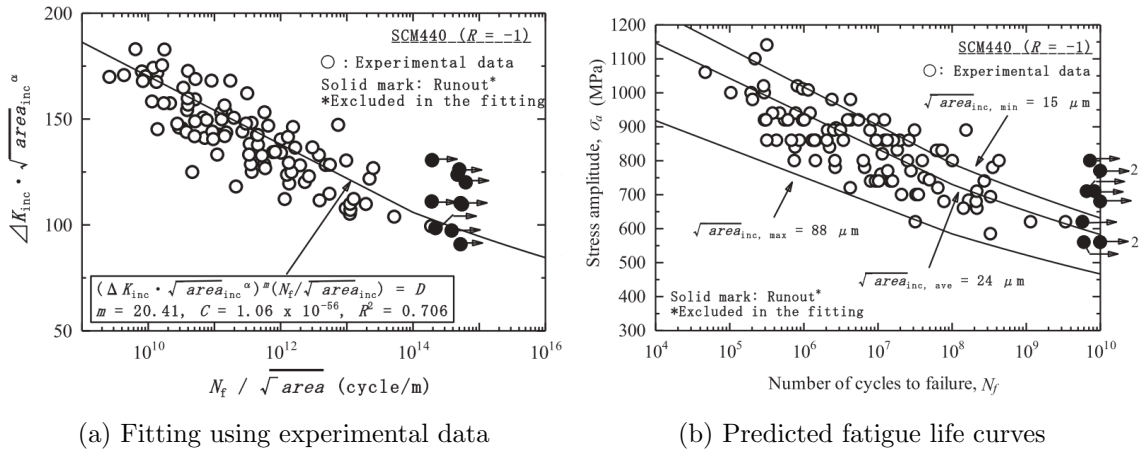
2.2.4 Multiaxial fatigue

The conventional $S-N$ curves are obtained under uniaxial cyclic conditions, generally under push-and-pull tension or fully reversed bending, which are not common in practical cases. In most real cases, stresses acting on a workpiece are multiaxial, either due to the loading condition itself but also because of particular geometrical details, e.g. holes, or discontinuities that cause either triaxial or biaxial stress state [37].

Another important aspect to consider in multiaxial fatigue are the loading conditions, which can be divided in two types:

1. Proportional or *in-phase loads* (IP loads)
2. Non-proportional or *out-of-phase loads* (NP loads)

where IP loads, shown in Fig. 2.65a [37], are characterized by multiple strains or stresses changing simultaneously of the same quantity so that the principal axes maintain a fixed orientation, while NP loads, displayed in Fig. 2.65b [65], are not in phase, thus imposing a rotation of the principal axes throughout time.

Figure 2.63: R^2 values for various values of α in the new model [39]

(a) Fitting using experimental data

(b) Predicted fatigue life curves

Figure 2.64: Predictions of behaviour in VHCF for SCM440 [39]

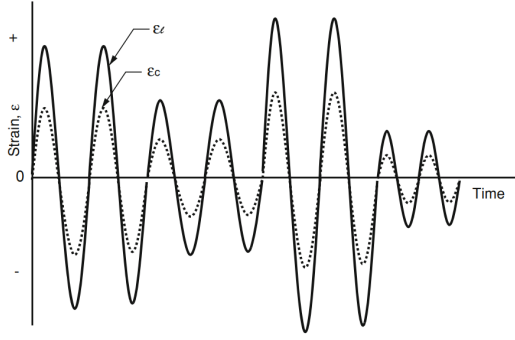
Out-of-phase cyclic loads

The NP loads have been found more damaging than the equivalent IP loads specially in *low cycle fatigue*. It is important to note that if dealing with HCF and beyond, the difference between IP and NP loading is residual. However, the IP or NP loads can be classified according to the biaxial strain ratio $\Delta\gamma/\Delta\varepsilon$ or the non-proportionality factor F_{NP} . Kanazawa et al. [76] proposed a factor of ellipticity of the strain path in the $\gamma/2-\varepsilon$ plot, as shown in Fig. 2.66 [37], or the ratio of the minor to major axis of the circumscribed ellipse. Itoh et al. [77] and Kida et al. [78] proposed another formulation for the NP factor, computed from the strain path, following the expression

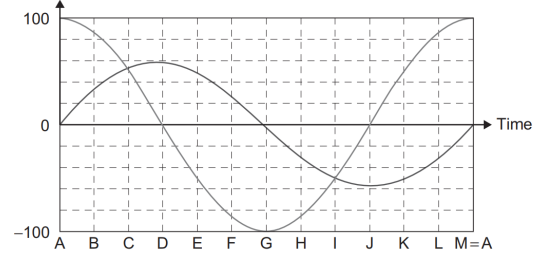
$$F_{NP} = \frac{\pi}{2T\varepsilon_{1,max}} \int_0^T [|\sin \xi(t)|\varepsilon_1(t)] dt \quad (2.46)$$

where $\varepsilon_1(t)$ is the principal strain at time t , $\varepsilon_{1,max}$ is the maximum absolute value of $\varepsilon_1(t)$, $\xi(t)$ is the angle between $\varepsilon_1(t)$ and $\varepsilon_{1,max}$ and T is the time length of the cycle.

2. Background theory



(a) Proportional loads acting in a pressure pipe subjected to pressure excursions [37]



(b) A surface element of a round shaft subjected to 90° out-of-phase normal and shear stress time histories [65]

Figure 2.65: Strain or stress conditions for IP and NP loading

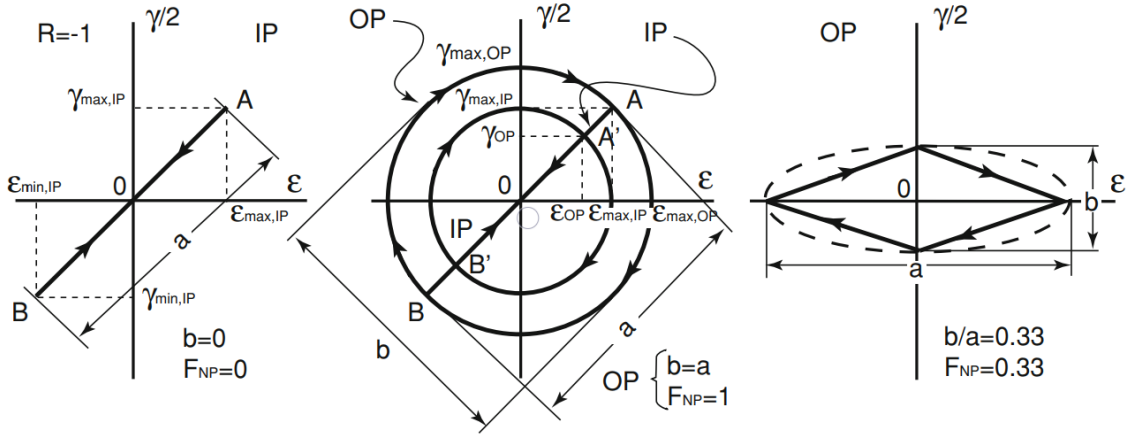


Figure 2.66: Example of IP and OP load paths and illustration of NP factor [37]

Under NP cyclic loading, some materials experience additional material hardening, called non-proportional hardening, which depends on the load path through the factor F_{NP} and a constant α_{NP} that modifies the plastic term $\varepsilon_{p,e}$ by

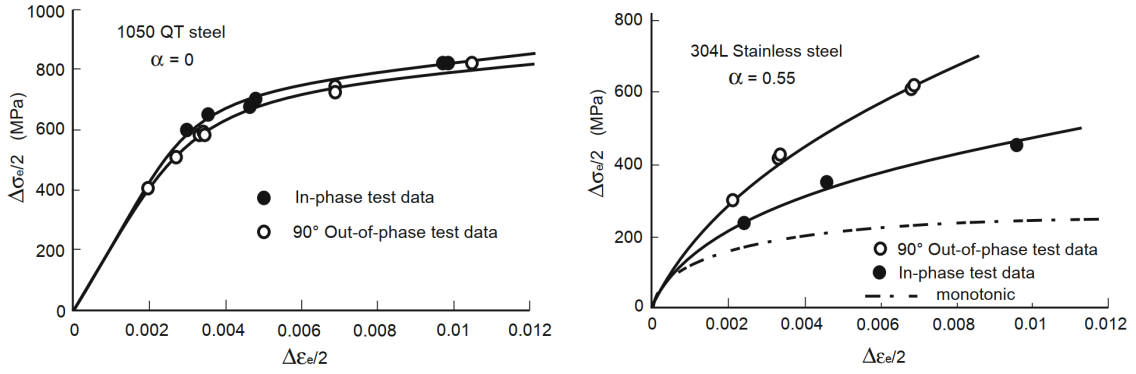
$$\frac{\Delta\varepsilon_{p,e}}{2} = \left[\frac{\Delta\sigma_e}{2 \cdot k(1 + \alpha_{NP}F_{NP})} \right]^{1/n'} \quad (2.47)$$

where k is the plastic modulus, n' is the proportional cyclic hardening exponent and α is the material non-proportional hardening coefficient. Fig. 2.67 [37] shows the impact of the non-proportional hardening coefficient in the strain-stress response. It can definitely be seen additional hardening in materials in the 304L stainless steel alloy with $\alpha_{NP} = 0.55$.

In fact, the non-proportional hardening coefficient α is not easy to compute. However, Borodii [79] developed a method based on the altered fatigue curve $\Delta\varepsilon_r - N_f$, where $\Delta\varepsilon_r$ is the reduced strain range defined as

$$\Delta\varepsilon_r = (1 + \alpha_{NP}F_{NP})(1 + k_{IP} \sin \phi)\Delta\varepsilon \quad (2.48)$$

where k_{IP} is a material parameter related to the proportional deformation and ϕ a rotation angle of an arbitrary cycle path with the principal axis. By running three test, two in an uniaxial state $\Delta\varepsilon_1$ and $\Delta\varepsilon_2$ and one at any non-proportional biaxial deformation with a



(a) 1050 QT tests in non NP hardening and NP hardening conditions

(b) 304 L tests in non NP hardening and NP hardening conditions

Figure 2.67: Equivalent stress–strain response of 1050 QT and 304L SS under non NP hardening and NP hardening conditions [37]

strain range of either $\Delta\varepsilon_1$ or $\Delta\varepsilon_2$ to measure the relative life \bar{N}_2 , α_{NP} can be derived from

$$\alpha_{NP} = \frac{1}{F_{NP}} \left[\left(\frac{\Delta\varepsilon_1}{\Delta\varepsilon_2} \right)^{\frac{\log \frac{N_2}{N_1}}{\log \frac{N_2}{N_1}}} - 1 \right] \quad (2.49)$$

therefore only three tests suffice. Shamsaei and Fatemi [80] proposed a simple model to access the non-proportional hardening coefficient based on the monotonic and cyclic curves of the material, as shown in Fig. 2.68 [37]. From the two curves it is inferred the cyclic hardening coefficient h based on the ratio of the monotonic and cyclic stress values corresponding to a given strain value ε and from this the NP hardening coefficient as

$$h = 1 - \frac{\sigma_M}{\sigma_C} \quad (2.50)$$

$$\alpha_{NP} = 1.6h^2 + 0.6h = 1.6 \left(\frac{\sigma_M}{\sigma_C} \right)^2 - 3.8 \left(\frac{\sigma_M}{\sigma_C} \right) + 2.2.$$

Eq. (2.50) can be rewritten in terms of the uniaxial monotonic and cyclic deformation properties as well as the plastic strain in Eq. (2.47), as

$$\alpha_{NP} = 1.6 \cdot \left(\frac{k}{k'} \right)^2 \left(\frac{\Delta\varepsilon}{2} \right)^{2(n-n')} - 3.8 \cdot \left(\frac{k}{k'} \right) \left(\frac{\Delta\varepsilon}{2} \right)^{n-n'} + 2.2. \quad (2.51)$$

Stress based multiaxial fatigue models

In the assumption there is little plastic deformation in the HCF regime, the pseudo stress components calculated from a linear elastic FEA are employed to estimate fatigue damage parameter and to predict life from synthesized a pseudo stress-life curve, which is considered the most practical fatigue analysis to use in the HCF regime [65]. The various approaches represented here can be divided in three groups based on:

- Empirical equivalent stress
- Stress invariants

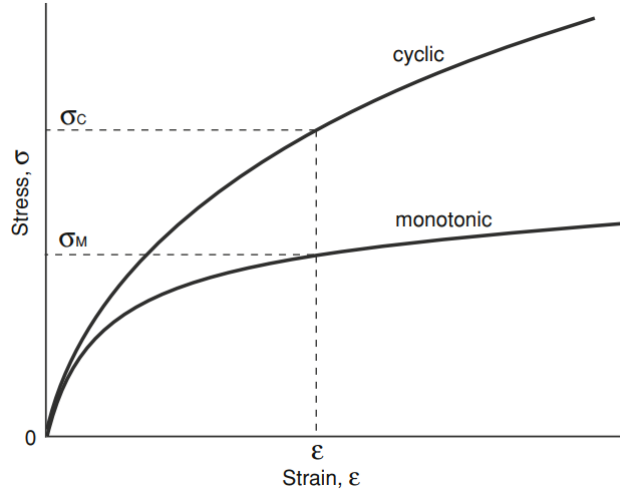


Figure 2.68: Monotonic and cyclic curves and corresponding stresses at a given strain [37]

- Critical plane stress

In terms of the empirical formula approach, this is only possible under biaxial, fully reversed stress state [65]. Nonetheless, most general stress condition in fatigue analysis is represented by a biaxial stress state since fatigue is acting on the free surface of the material, at least in HCF, where the external component of stress is null ($\sigma_z = 0$) [37]. Gough and Pollard [81; 82] found that for materials under in-phase bending-torsional loading the *fatigue limits* of ductile and brittle materials have the following empirical expressions:

$$\left(\frac{\sigma_a}{\sigma_{f,R=-1}}\right)^2 + \left(\frac{\tau_a}{\tau_f}\right)^2 = 1, \quad \text{for ductile materials} \quad (2.52)$$

$$\left(\frac{\sigma_a}{\sigma_{f,R=-1}}\right) + \left(\frac{\tau_a}{\tau_f}\right)^2 = 1, \quad \text{for brittle materials} \quad (2.53)$$

where σ_a and τ_a are the in-phase normal and shear stress amplitudes, respectively, and $\sigma_{f,R=-1}$ and τ_f are the fully reverse *fatigue limits* for normal and shear stresses, respectively. Hashin [83] and Rotvel [84] showed that the Gough-Pollard equations have general application when expressed in terms of principal stresses. Moreover, McDiarmid [85] also concluded that the Gough-Pollard equations have physical interpretation on the fatigue damage mechanism when expressed in terms of normal and shear stresses on the maximum shear stress plane.

Dietmann [86] in Eq. (2.54), and Socie and Marquis [87] in Eq. (2.55), developed more generic formulas for fully reversed loading

$$\left(\frac{\sigma_a}{\sigma_{f,R=-1}}\right)^k + \left(\frac{\tau_a}{\tau_f}\right)^2 = 1 \quad (2.54)$$

$$(R_f - 1) \left(\frac{\sigma_a}{\sigma_{f,R=-1}}\right)^2 + (2 - R_f) \left(\frac{\sigma_a}{\sigma_{f,R=-1}}\right) + \left(\frac{\tau_a}{\tau_f}\right)^2 = 1 \quad (2.55)$$

where

$$R_f = \frac{\sigma_{f,R=-1}}{\tau_f}. \quad (2.56)$$

If one pays close attention, concludes that the Gough-Pollard formulas are particular cases of Eqs. (2.54) and (2.55). For ductile materials where $k = 2$, Eqs. (2.54) and (2.55) are equivalent to Eq. (2.52), while for brittle materials where $k = 1$, Eqs. (2.54) and (2.55) are equivalent to Eq. (2.53).

Taking the Gough-Pollard formulations as a framework, Lee [88] in Eq. (2.57) and Lee and Chiang [89] in Eq. (2.58), formulated a criterion for *fatigue limits* under fully reversed out-of-phase loading

$$\left(\frac{\sigma_a}{\sigma_{f,R=-1}}\right)^{\eta_m(1+\alpha_{NP}\sin\Phi)} + \left(\frac{\tau_a}{\tau_f}\right)^{\eta_m(1+\alpha_{NP}\sin\Phi)} = 1 \quad (2.57)$$

$$\left(\frac{\sigma_a}{\sigma_{f,R=-1}}\right)^{k(1+\alpha_{NP}\sin\Phi)} + \left(\frac{\tau_a}{\tau_f}\right)^{2(1+\alpha_{NP}\sin\Phi)} = 1 \quad (2.58)$$

where $\eta_m = 2$ or $\eta_m = 1.5$ for ductile or brittle materials, respectively, and α_{NP} is the non-proportional hardening coefficient.

Moving on to analytical failure theories, first comes the most basic formulations from solid mechanics, which are: *maximum normal stress theory*, in Eq. (2.59), *maximum shear stress theory (Tresca theory)*, in Eq. (2.60), and the *distortion strain energy theory (Von Mises)* in Eq. (2.61). For each theory, fatigue initiation occurs if the following conditions are verified

$$\sigma_{1,a} \geq \sigma_{f,R=-1} \quad (2.59)$$

$$\sigma_{1,a} - \sigma_{3,a} \geq \tau_f \quad (2.60)$$

$$\sigma_{VM,a} + \alpha_{VM}\sigma_{VM,m} \geq \sigma_{f,R=-1}$$

$$\sigma_{VM,m} = \sigma_{1,m} + \sigma_{2,m} + \sigma_{3,m} = \sigma_{x,m} + \sigma_{y,m} + \sigma_{z,m} \quad (2.61)$$

$$\sigma_{VM,a} = \frac{1}{\sqrt{2}}\sqrt{(\sigma_{1,a} - \sigma_{2,a})^2 + (\sigma_{2,a} - \sigma_{3,a})^2 + (\sigma_{1,a} - \sigma_{3,a})^2}$$

where α_{VM} denotes the mean stress sensitivity factor.

The stress invariant based methods, as the name suggests, are based on the hydrostatic stress σ_H and the second invariant of the stress deviator J_2

$$\sigma_H = \frac{\sigma_1 + \sigma_2 + \sigma_3}{3} \quad (2.62)$$

$$J_2 = \frac{1}{6} [(\sigma_1 - \sigma_2)^2 + (\sigma_1 - \sigma_3)^2 + (\sigma_2 - \sigma_3)^2].$$

It is also important to state that the following formulations will state a safe zone criterion. Sines [90] proposed, probably, the most popular criterion for HCF expressed by

$$\sqrt{J_{2,a}} + \kappa\sigma_{H,m} \leq \lambda \quad (2.63)$$

where the parameters κ and λ can be inferred from a fully reversed torsion test, leading to

$$\kappa = \frac{3\tau_f}{\sigma_{f,R=0}} ; \lambda = \tau_f \quad (2.64)$$

where $\sigma_{f,R=0}$ is the *fatigue limit* from a pulsating bending loading condition. Having in mind the Goodman line to compute $\sigma_{f,R=0}$ and also the result of Eq. (2.63) for a fully reversed bending

$$\frac{\tau_f}{\sigma_f} \leq \frac{1}{\sqrt{3}} \quad (2.65)$$

the Eq. (2.63) becomes

$$\sqrt{J_{2,a}} + \left(\frac{\sqrt{3}\sigma_f}{\sigma_u} \right) \sigma_{H,m} \leq \lambda. \quad (2.66)$$

Also the criterion in Eqs. (2.63) and (2.66) was successfully modified by Sines and Ohgi [91] to include an additional term to take care of non-linear effects due to possible higher mean stresses

$$\sqrt{J_{2,a}} + \nu \cdot (J_{2,m})^\mu + \kappa \sigma_{H,m} \leq \lambda. \quad (2.67)$$

Crossland [92] proposed an alteration to Eq. (2.63) and considered using the maximum hydrostatic stress $\sigma_{H,max}$ rather than the mean

$$\sqrt{J_{2,a}} + \kappa \sigma_{H,max} \leq \lambda \quad (2.68)$$

where the parameters κ and λ can also be inferred from a fully reversed torsion test giving

$$\kappa = \frac{3\tau_f}{\sigma_{f,R=0}} - \sqrt{3}, \quad \lambda = \tau_f. \quad (2.69)$$

Kakuno and Kawada [93] suggested separating the effects of the hydrostatic stress amplitude and of the mean hydrostatic stress

$$\sqrt{J_{2,a}} + \kappa \sigma_{H,a} + \mu \sigma_{H,m} \leq \lambda \quad (2.70)$$

with

$$\kappa = \frac{3\tau_f}{\sigma_f} - \sqrt{3}, \quad \mu = \frac{3\tau_f}{\sigma_{f,R=0}} - \sqrt{3}, \quad \lambda = \tau_f. \quad (2.71)$$

Finally Vu et al. [94] proposed a formulation for out-of-phase loading capable of capturing the phase shift by considering the mean value of J_2

$$\sqrt{\gamma_1 J_2'(t)^2 + \gamma_2 J_{2,mean} + \gamma_3 I_f(I_{1,a}, I_{1,m})} \leq \lambda \quad (2.72)$$

with

$$J_2'(t)e = \sqrt{\frac{(\sigma_{xx}(t) - \sigma_{xx,m})^2}{3} + (\tau_{xy}(t) + \sigma_{xy,m})^2}, \quad (2.73)$$

$$J_{2,mean} = \frac{1}{T} \int_0^T J_2'(t) dt$$

where $\gamma_1 = 0.65$, $\gamma_2 = 0.8636$ and $I_f(I_{1,a}, I_{1,m}) = I_{1,a} + I_{1,m}$ for low strength metals ($\sigma_u < 750$ MPa) and $\gamma_1 = 0.3$, $\gamma_2 = 1.7272$ and $I_f(I_{1,a}, I_{1,m}) = I_{1,a} + \frac{\sigma_f}{\tau_f} I_{1,m}$ for high strength metals ($\sigma_u > 750$ MPa). This approach is consistent with the experimental observations in the sense that has reduced the dependence on mean shear stress but strengthen sensibility to mean normal stress.

Sonsino [95] also formulated a theory called *effective equivalent stress amplitude method* that accounted for the non-proportional hardening as a result of the NP loading conditions. It is assumed that the crack A that is growing along a free surface, showed in Fig. 2.70a, is a typical failure of a ductile material under multiaxial loading. The interaction of shear stress across several interference planes is taken into account by an effective shear stress τ_{arith} given by

$$\tau_{arith} = \frac{1}{\pi} \int_0^\pi \tau_n(\theta) d\theta \quad (2.74)$$

where τ_n are the values of shear stress along the several interference planes. For an out-of-phase sinusoidal loading with a phase shift of Φ in a plane stress condition, the effective

shear stress derived on the Von Mises stress criterion is used to determine the effective equivalent stress amplitude as follows

$$\sigma_{VM,a}(\Phi) = \sigma_{VM,a} \frac{\tau_{arith}(\Phi)}{\tau_{arith}(\Phi=0)} \sqrt{G \cdot \exp \left[1 - \left(\frac{\Phi - 90^\circ}{90^\circ} \right)^2 \right]} \quad (2.75)$$

with

$$\sigma_{VM,a} = \sqrt{\sigma_{x,a}^2 + \sigma_{y,a}^2 - \sigma_{x,a}\sigma_{y,a} + 3C_{size}^2 \tau_{xy,a}^2} \quad (2.76)$$

$$C_{size} = \frac{\sqrt{\sigma_{x,a}^2 + \sigma_{y,a}^2 - \sigma_{x,a}\sigma_{y,a}}}{\sqrt{3}\tau_{xy,a}} \quad (2.77)$$

$$G = \frac{1 + K_{b,t}}{1 + K_{t,t}} \quad (2.78)$$

where $K_{b,t}$ and $K_{t,t}$ are the stress concentration factors due to bending and torsion, respectively, and C_{size} is the size effect factor. C_{size} can be computed by comparing the $S-N$ curves for bending and torsion stresses so that the curves should lie on top of each other. The ratio $\tau_{arith}(\Phi)/\tau_{arith}(\Phi=0)$ represents the non-proportional hardening effect.

Lee et al. [96] proposed the concept of *equivalent non-proportional stress amplitude* defined by

$$\sigma_{VM,a,NP} = \sigma_{VM,a}(1 + \alpha_{NP}F_{NP}) \quad (2.79)$$

where F_{NP} is the non-proportional loading path factor to account the severity of loading paths. In Eq. (2.79) $\sigma_{VM,a}$ employs the condition of maximum value between two arbitrary points among all multiples points in a cycle

$$\sigma_{VM,a} = \max \left\{ \sqrt{\sigma_{x,a}^2 + \sigma_{y,a}^2 - \sigma_{x,a}\sigma_{y,a} + 3\alpha_S^2 \tau_{xy,a}^2} \times \left(\frac{\sigma'_f}{\sigma'_f - \sigma_{eq,m}} \right) \right\} \quad (2.80)$$

with

$$\sigma_{eq,m} = \sigma_{x,m} + \sigma_{y,m}. \quad (2.81)$$

where α_S is the shear-to-normal stress parameter, calculated from Eq. (2.77), σ'_f is the fatigue strength coefficient determined from the best fit of the proportional loading data with a stress ratio of $R = -1$ and $\sigma_{eq,m}$ is the equivalent mean stress, ignoring the effect of torsional mean stress.

Moving on to the critical plane based theories, that are determined from finding out the most severely loaded planes, which are the ones where the crack initiation occurs. Generally, models lie on the concept that fatigue crack initiation occurs on planes which are the most severely loaded in terms of shear stress while the whole fatigue process and life would be dominated by the normal stresses applied to those planes, which tend to “open” the crack and increase its growth rate (see Fig. 2.69) [37].

Findley [97] was the first to introduce the critical plane approach, determining this critical plane by maximizing the linear combination between the shear stress amplitude and maximum normal stress on that plane

$$(\phi_c, \theta_c) = \max_{(\phi, \theta)} [\tau_a(\phi, \theta) + \kappa \sigma_{n,max}(\phi, \theta)]. \quad (2.82)$$

Once determined the critical plane, the criterion is written as

$$\tau_a(\phi_c, \theta_c) + \kappa \sigma_{max}(\phi_c, \theta_c) \leq \lambda \quad (2.83)$$

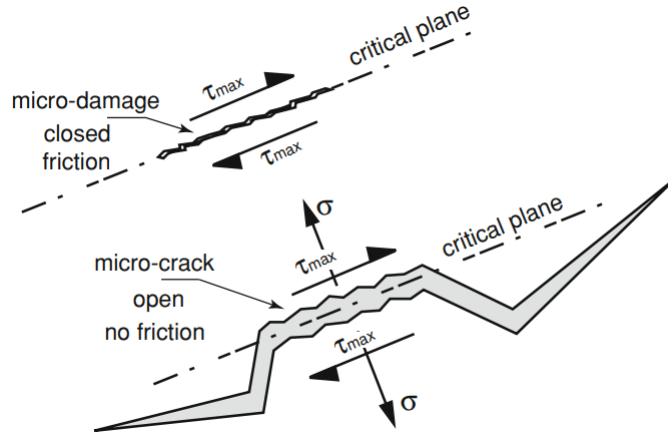


Figure 2.69: A normal stress on the critical plane enables the micro-crack to open overcoming friction interlocking effects [37]

with the parameters κ and λ to be determined, e.g. the proposal earlier explained from a fully reversed torsion test. Under cyclic uniaxial traction with stress ratio $R = \sigma_{min}/\sigma_{max}$ it can be shown that Findley's criterion gives

$$0.5\sigma_a \left[\sqrt{1 + \left(\frac{2\kappa}{1-R} \right)^2} + \frac{2\kappa}{1-R} \right] = \lambda. \quad (2.84)$$

Therefore, it is possible to estimate the *fatigue limit* σ_f relative to any ratio R from the value κ , knowing the *fatigue limit* from a fully reversed loading $\sigma_{f,R=-1}$

$$\frac{\sigma_f}{\sigma_{f,R=-1}} = \frac{\sigma_a}{\sigma_{a,R=0}} = \frac{\sqrt{1 + \kappa^2} + \kappa}{\sqrt{1 + \left(\frac{2\kappa}{1-R} \right)^2} + \frac{2\kappa}{1-R}} \quad (2.85)$$

Matake [98] simplified Findley's model, by just considering the maximum shear stress amplitude to find the critical plane

$$(\phi_c, \theta_c) = \max_{(\phi, \theta)} [\tau_a(\phi, \theta)] \quad (2.86)$$

with the criterion equal to Eq. (2.83). The parameters κ and λ can be inferred by applying a fully reversed torsion loading without static stress and a fully reversed bending load giving

$$\kappa = \frac{2\tau_f}{\sigma_f} - 1, \quad \lambda = \tau_f. \quad (2.87)$$

Equation (2.87) is valid for both Matake and Findley methods. Using the Brown and Miller [99] concept of different crack propagation: case A cracks (see Fig. 2.70a [37]), that grow along the component's surface and case B cracks (see Fig. 2.70b [37]), that grow into the surface; McDiarmid [100; 101] developed a criterion based on a critical plane on which the shear stress amplitude reaches the maximum values, as the Matake and Findley's criterion, but with the differentiation between the crack growth cases

$$\tau_a(\phi_c, \theta_c) + \frac{\tau_f}{2\sigma_u} \sigma_{n,max}(\phi_c, \theta_c) \leq \tau_f \quad (2.88)$$

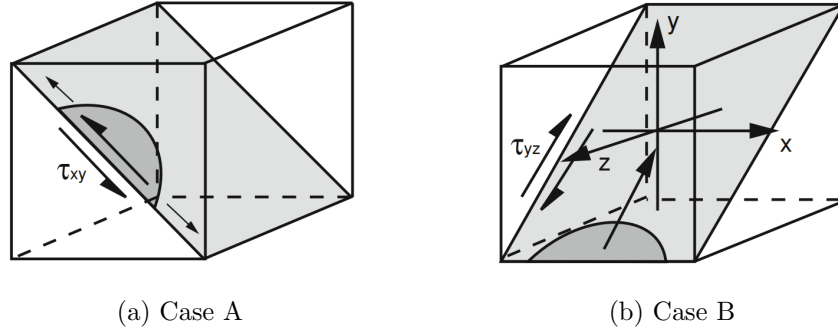


Figure 2.70: Types of cracks in Brown and Miller failure model [37]

where the values $\tau_{f,A}$ and $\tau_{f,B}$ are used depending on whether the critical plane indicates a potential crack propagation path that of case A or case B, respectively. Gaier and Dannbauer [102] proposed that a fatigue crack will likely initiate on the critical plane where the scaled normal stress on the plane $f_{GD} \cdot \sigma_n$ is maximized and exceeds a failure criterion

$$(f_{GD} \cdot \sigma_n)_{max} = \sigma_{E,R=-1} \quad (2.89)$$

with

$$\begin{aligned} \kappa &= \frac{\sigma_{f,R=-1}}{\tau_f} \\ f_{GD} &= 1 + (1 - \kappa)V_S \end{aligned} \quad (2.90)$$

where V_S is the ratio between the maximum and minimum principal stresses, defined as $V = \sigma_1/\sigma_3$ or $V_S = \sigma_3/\sigma_1$ for $|\sigma_3| > |\sigma_1|$ or $|\sigma_1| > |\sigma_3|$, respectively. Moreover, as mentioned earlier, the values for k are 2 and 1 for ductile or brittle materials, respectively. It has been found that this model agrees very well with the experimental data from fully reversed combined in-phase normal and shear stresses [65].

Finally, Dang Van et al. [103] developed a multiscale fatigue approach that uses mesoscopic stresses as inputs for the fatigue analysis. The mesoscopic scale refers to crystalline grains and slip bands. This approach has the special attention of noticing that, even if the macroscopic stress state is elastic, the most unfavourably oriented grains may be experiencing plastic deformation. The theory assumes, for an infinite lifetime, the macroscopic elastic strain tensor $\underline{\varepsilon}^e(t)$ is the sum of the mesoscopic elastic $\underline{\varepsilon}_{meso}^e(t)$ and plastic $\underline{\varepsilon}_{meso}^p(t)$ strain tensors

$$\underline{\varepsilon}^e(t) = \underline{\varepsilon}_{meso}^e(t) + \underline{\varepsilon}_{meso}^p(t). \quad (2.91)$$

Applying Hook's law,

$$\underline{\varepsilon}^e(t) = \frac{\underline{\sigma}(t)}{E} \quad (2.92)$$

$$\underline{\varepsilon}_{meso}^e(t) = \frac{\underline{\sigma}_{meso}(t)}{E_{meso}} \quad (2.93)$$

where E and E_{meso} are the macroscopic and mesoscopic Young's modulus, respectively, and $\underline{\sigma}(t)$ and $\underline{\sigma}_{meso}(t)$ are the macroscopic and mesoscopic stress tensors, respectively. Using Eqs. (2.92) and (2.93), Eq. (2.91) can be rewritten as

$$\underline{\sigma}_{meso}(t) = \frac{E_{meso}}{E} \cdot \underline{\sigma}(t) - E_{meso} \cdot \underline{\varepsilon}_{meso}^p. \quad (2.94)$$

Assuming $E_{meso}/E = 1$, Eq. (2.94) becomes

$$\underline{\sigma}_{meso}(t) = \underline{\sigma}(t) - E_{meso} \cdot \underline{\varepsilon}_{meso}^p = \underline{\sigma}(t) + \underline{\rho}^* \quad (2.95)$$

where $\underline{\rho}^*$ is a deviatoric stress tensor, since it is proportional to the mesoscopic plastic strains. Also, the mesoscopic hydrostatic pressure $\underline{\sigma}_{meso,h}(t)$ is equal to the macroscopic one

$$\underline{\sigma}_{meso,h} = \sigma_h = \frac{1}{3}(\underline{\sigma} : \underline{I})\underline{I}. \quad (2.96)$$

Therefore, the same relation between the macroscopic deviatoric stress tensor $\underline{S}(t)$ and mesoscopic tensor $\underline{s}_{meso}(t)$ can be applied

$$\underline{s}_{meso}(t) = \underline{S}(t) + \underline{\rho}^*. \quad (2.97)$$

Once $\underline{\rho}^*$ is calculated, which is not reviewed in this study, the mesoscopic stress tensor $\underline{s}_{meso}(t)$ can be determined and the instantaneous mesoscopic shear stress is calculated as

$$\tau_{meso}(t) = \frac{1}{2} [s_{meso,1}(t) - s_{meso,3}(t)] \quad (2.98)$$

where $s_{meso,1}(t)$ and $s_{meso,3}(t)$ are the mesoscopic deviatoric principal stresses. The Dang Van criterion is constructed on a mesoscopic approach to fatigue behaviour on a critical shearing plane. It assumes that the mesoscopic shear stress $\tau_{meso}(t)$ is responsible for the crack nucleation in slip bands, while the mesoscopic hydrostatic stress $\sigma_{meso,h}(t)$ will influence the opening of the crack. Hence, the Dang Van fatigue resistance expression is

$$\tau_{meso}(t) + \alpha_{DV} \cdot \sigma_{meso,h}(t) \leq \tau_f \quad (2.99)$$

where α_{DV} is the hydrostatic stress sensitivity, also known as κ in Findley and Mataka methods.

Estimation of fatigue life based on multiaxial criterion

While under variable amplitude multiaxial loading conditions, fatigue damage can be, generally, assessed by two different approaches:

1. Critical plane
2. Equivalent stress or strain

The critical plane approach computes the fatigue damage parameter of each potential failure plane and then the total accumulated damage is calculated based on the uniaxial cycle counting techniques mentioned in section 2.2.3 according to the time history on the respective critical plane.

Regarding the equivalent stress approach, the first to propose a method was Wang and Brown [104], which was well correlated with the experimental data on tubular specimens under combined tension-torsion and internal pressure loading. The Wang-Brown reversal counting technique combines the multiaxial stress time histories ($\sigma_x(t)$, $\sigma_y(t)$ and $\tau_{xy}(t)$) into a single equivalent stress time history $\sigma_{eq}(t)$ and then counts reversals by the following process:

1. Rearrange the equivalent stress time history calculated by

$$\sigma_{eq}(t) = \sqrt{\sigma_x^2(t) + \sigma_y^2(t) - \sigma_x(t)\sigma_y(t) + 3\tau_{xy}^2(t)} \quad (2.100)$$

so that it begins with the maximum equivalent stress;

2. Calculate the relative equivalent stress time history $\Delta\sigma_{eq}(t)$

$$\Delta\sigma_{eq}(t) = \sqrt{\Delta\sigma_x^2(t) + \Delta\sigma_y^2(t) - \Delta\sigma_x(t)\Delta\sigma_y(t) + 3\Delta\tau_{xy}^2(t)} \quad (2.101)$$

where

$$\begin{aligned} \Delta\sigma_x(t) &= \sigma_x(t) - \sigma_x(t_0) \\ \Delta\sigma_y(t) &= \sigma_y(t) - \sigma_y(t_0) \\ \Delta\tau_{xy}(t) &= \tau_{xy}(t) - \tau_{xy}(t_0); \end{aligned} \quad (2.102)$$

3. Collect all the points that cause $\Delta\sigma_{eq}(t)$ to increase, computing the major reversal;
4. Store the remaining points consisting of one or more blocks that start and end with the same value of $\Delta\sigma_{eq}(t)$ and a trailing block;
5. For each of these “uncounted” blocks, treat the first point as the reference point with which to calculate the relative equivalent stress $\Delta\sigma_{eq}(t)$. Proceed to collect points that cause the new $\Delta\sigma_{eq}(t)$ to increase. This process will yield additional reversals (and possibly more uncounted blocks);
6. Repeat step 6 until all the data are counted.

The methods proposed by Lee et al. [96], called Lee-Tjhung-Jordan cycle counting method, and Dong et al. [105], the path dependent maximum range (PMDR) cycle counting method, are variants of the Wang-Brown method. The Lee-Tjhung-Jordan calculates the equivalent stress by the Eq. (2.79) and proceeds in an homologous way as stated above.

The PMDR cycle counting [105] bases on seeking a stress range in a stress space time history. For 2D problems, the stress space is defined has $\sigma_s - \sqrt{\beta}\tau_s$ (see Fig. 2.71 [105]), where the parameter β is a material constant. The procedure for obtaining the respective

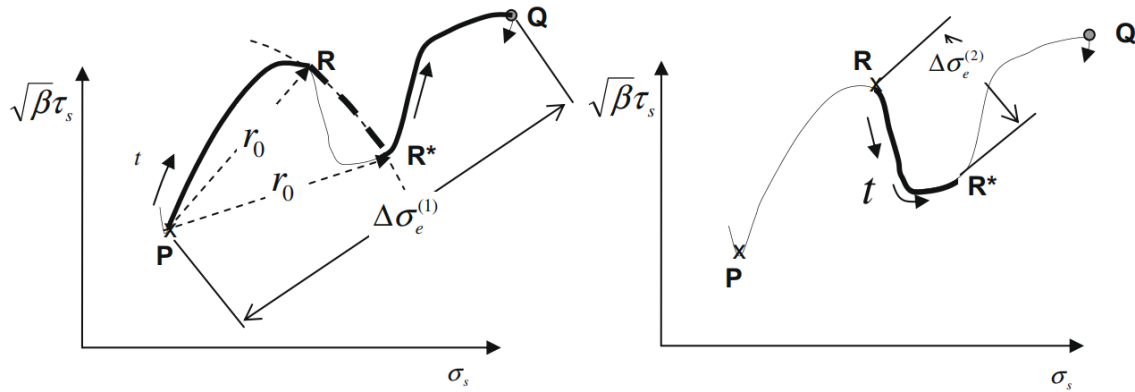


Figure 2.71: Illustration of PMDR cycle counting procedure (2D problem) [105]

cycles are as follows:

1. Map the time histories $\sigma_s(t)$ and $\tau_s(t)$ onto the $\sigma_s - \sqrt{\beta}\tau_s$ stress space, as shown in Fig. 2.71 [105];
2. Search for the maximum possible distance between the initial point and any point along the load path, while maintaining a monotonic increase. For every local maximum, called turning point, define a second cycle from the respective turning point R

2. Background theory

until a point R^* defined by the intersection between the load path and an $P - R$ arc centred in P . Bear in mind that for each middle half cycle found, the computation of the embedding stress range considers the arc $P - R$ for calculation rather than the actual load path. Continue the search until there are no more turning points;

3. For each half cycle, compute the respective stress range $\Delta S_e^{(i)}$, given by the expression

$$\Delta S_e^{(i)} = \int dS_e^{(i)} = \int \sqrt{(d\sigma)^2 + \beta(d\tau)^2}. \quad (2.103)$$

For instance, for the example displayed in Fig. 2.71 [105], the PDMR cycle counting results are displayed in Table 2.5 [105]. Note that the symbol \cap represents the actual load path, while the symbol \cup the virtual circular arc. This is rather important since it affects the stress ranges $\Delta\sigma_e^{(i)}$ from each counted cycle.

When handling 3D problems, an analogous procedure is made by defining a $\sigma_s - \sqrt{\beta_{III}}\tau_s - \sqrt{\beta_{III}}\tau_z$ load path (see Fig. 2.72 [105]). Instead of analysing the middle half cycles through arcs, the projected virtual path is defined from the intersection between the load path and the respective sphere. For computing the stress ranges, logically, it follows the expression

$$\Delta S_e^{(i)} = \int \sqrt{(d\sigma)^2 + \beta_{II}(d\tau_{II})^2 + \beta_{III}(\tau_{III})^2} \quad (2.104)$$

where σ , τ_{II} and τ_{III} are the normal, in-phase and transverse shear, respectively.

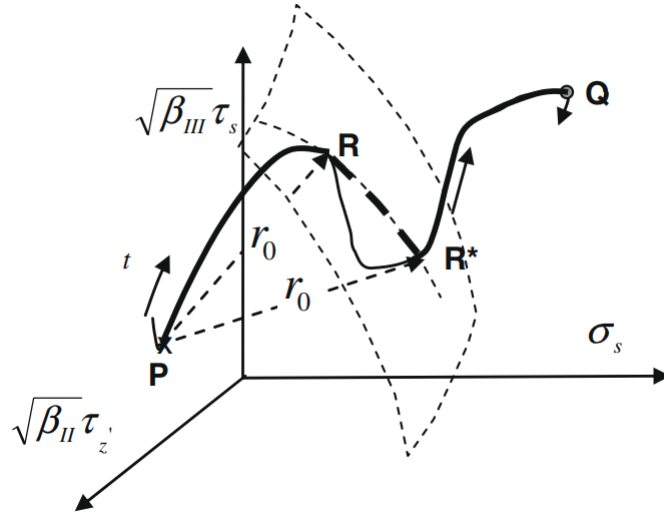


Figure 2.72: PDMR applications 3-D problems [105]

Cycle counted	Reference stress range ($\Delta\sigma_e^{(i)}$)	Effective stress range ($\Delta S_e^{(i)}$)
0.5	P-Q($\Delta\sigma_e^{(1)}$)	$PQ^\cap = PR^\cap RR^{*\cup} + R^*Q^\cap(\Delta S_e^{(1)})$
0.5	R-R*($\Delta\sigma_e^{(2)}$)	$RR^{*\cap}(\Delta S_e^{(2)})$

Table 2.5: PDMR counting results for loading path shown in Fig. 2.71 [105]

2.3 A Review on Structural Optimization

Structural optimization (SO) consists in determining the best material distribution within a specific domain, to safely transmit or support the applied loading conditions. Of course, many factors could come to play, in terms of either manufacturing (minimal member size, etc) or physical (mass, volume, stiffness, stress, etc) constraints, or objectives, such as maximizing stiffness, minimizing volume or mass, reducing a certain displacement, etc. With the development of the finite element method (FEM), this approach is widely used in SO [106]. In SO, there are three main areas regarding the design variables:

1. Size optimization
2. Shape optimization
3. Topology optimization

In size optimization, the designer know what the structure looks like, but is trying to decide the best size of the components that make up that structure, and the domain of the FEM is fixed. A simple example is a cantilever beam, where its length and position are known, but the cross-sectional dimensions (do not confound with shape) are the design variables. The shape optimization, on the other hand, presents the task of designing the form or contour of the boundary of a structural domain, thus altering the domain of the FEM during optimization. This shape or boundary could be either represented by an equation or a set of points. Finally, the topology optimization is the broadest form of SO, where the shape and size come together as design variables with complete freedom to even possess a value of zero (creating voids or holes) or a minimum gage size (e.g. manufacturing constraint). There are several topology optimization methods, which can be divided in two categories [106]:

1. Optimality criteria methods
 - (a) Homogenization method
 - (b) Solid isotropic material with penalization (SIMP)
 - (c) Level set method (LSM)
 - (d) Growth method (truss structures)
2. Heuristic or intuitive methods
 - (a) Fully stressed design
 - (b) Computer-aided optimization (CAO)
 - (c) Soft kill option
 - (d) Evolutionary structural optimization (ESO)
 - (e) Bidirectional ESO
 - (f) Sequential element rejection and admission (SERA)
 - (g) Isolines/Isosurfaces topology design (ITD)

The optimality criteria methods are indirect methods, suitable for problems with a large number of design variables and few constraints. They are often based on the Kuhn-Tucker optimality condition (see Appendix A), therefore, being more rigorous on the optimal design. On the other hand, the heuristic methods are derived from intuition, observations

of engineering processes or biological systems, and cannot guarantee optimality, although they can provide viable efficient solutions. For the purpose of this study, only optimality criteria methods will be revised.

The structural optimization using FEM, usually a linear static problem, is computed in a system of equations with a objective function and constraints. The system is solved and the solution is used for the evaluation of the objective function and the constraints, in an iterative process. The problem is formulated as follows:

$$\begin{aligned} \text{Find } & b \in R^n & (2.105a) \\ \text{to minimize } & J(u) = f(b, u) & (2.105b) \\ \text{subject to } & K(b)u = f & (2.105c) \\ & g_j(b, u) \leq 0, \quad j = 1, \dots, m & (2.105d) \\ & b_L \leq b \leq b_U & (2.105e) \end{aligned}$$

where b is the design variable vector with n elements, constrained by the lower b_L and upper b_U bounds, f is the objective function Eq. (2.105b) is the governing equation of the linear static problem and Eq. (2.105d) are the inequalities constraints, which can limit, displacements, stresses, natural frequencies, volume or mass. The objective function, generally, minimizes the compliance, but can also minimize the mass or volume.

2.3.1 Optimality criteria methods

Homogenization method

The homogenization method consists of solving a shape optimization problem, where the topology is made from an infinite number of micro-scale voids which produces a porous structure. The optimization problem aims to find out the best geometry parameters of each microvoid, thus becoming the design variables, and if a portion of the domain only has voids, then no material is placed in that area. In a 2D problem analysed by FEM using a regular squared finite element (FE), the voids resemble the mesh grid (see Fig. 2.73 [106]), and the design variables are the width (a), height (b) and orientation (θ) of the voids. In order to maximize the stiffness, the following problem is formulated [106]:

$$\begin{aligned} \text{Find } & a_e, b_e, \quad e = 1, \dots, N & (2.106a) \\ \text{to maximize } & J(\{u\}) = \Pi(u) & (2.106b) \\ \text{subject to } & \sum_{e=1}^N (1 - a_e b_e) v_e - \bar{V}_s \leq 0 & (2.106c) \\ & a_e - 1 \leq 0 & (2.106d) \\ & -a_e \leq 0 & (2.106e) \\ & b_e - 1 \leq 0 & (2.106f) \\ & -b_e \leq 0 & (2.106g) \\ & a_e, b_e, \theta_e : e = 1, 2, \dots, N & (2.106h) \end{aligned}$$

where N is the number of FE elements, $\Pi(u)$ is the potential energy in the structure, a_e is the width and b_e is the height of the void, θ_e is the orientation and \bar{V}_s and v_e are the initial and FE volumes, respectively.

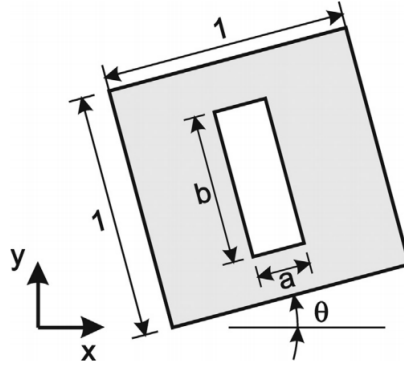


Figure 2.73: Unit cell with material and void domain [106]

Solid isotropic material with penalization (SIMP)

The SIMP method [106–108] is a direct consequence of the homogenization method and is the most widely used method in commercial software for topology optimization. It only uses one design variable per FE, which is an artificial element density ρ_e which dictates the presence of material within an element, with $0 \leq \rho_{min} \leq \rho_e \leq 1$. By altering the density parameter, the iterative process of finding the optimal solution displays a distribution of ρ_e , which in regions close to zero correspond to a no-material zone, while as ρ_e tends to one, corresponds to solid material regions, thus leading to change in the domain volume followed by the expression

$$V = \sum_{e=1}^N \rho_e v_e \quad (2.107)$$

where N is the number of elements and v_e is the original element volume. In a 2D problem it creates a continuous distribution (0-1) with “grey” areas of intermediate density values. In a linear mechanical problem, the Young’s modulus for each element can be expressed by

$$E_e = \rho_e^p E_e^0 \quad (2.108)$$

where E_e^0 and E_e are the original and new elastic modulus, p is the penalty factor that aims to prevent the intermediate values of density, promoting a black-and-white (material or no material) optimal design. Usually, to obtain true designs (0-1) without “grey” areas, a penalty factor $p > 3$ is advised [106; 107]. By altering the Young’s modulus in Eq. (2.108), the design variable indirectly influences the global stiffness of the structure, thus varying its mechanical behaviour. The formulation of the problem for maximizing stiffness is as follows:

$$\text{Find } \rho_e, \quad e = 1, \dots, N \quad (2.109a)$$

$$\text{to minimize } J(\{u\}) = \{F\}^T \{u\} \quad (2.109b)$$

$$\text{subject to } \left[\sum_{e=1}^N \rho_e^p K_e \right] \{u\} = \{F\} \quad (2.109c)$$

$$\sum_{e=1}^N \rho_e v_e \leq \bar{V} \quad (2.109d)$$

$$0 \leq \rho_{min} \leq \rho_e \leq 1 \quad (2.109e)$$

where F and u are the force and displacement vectors, K_e is the original element stiffness matrix and \bar{V} is the volume constraint value.

The process of finding an optimal solution is iterative, updating the density values in each iteration, through an evolutive transformation, following a fix-point type updating scheme [108]:

$$\rho_{k+1} = \begin{cases} \max\{(1 - \zeta)\rho_k, \rho_{min}\} & \text{if } \rho_k \mathcal{B}_k^\eta \leq \max\{(1 - \zeta)\rho_k, \rho_{min}\} \\ \min\{(1 + \zeta)\rho_k, 1\} & \text{if } \min\{(1 + \zeta)\rho_k, 1\} \leq \rho_k \mathcal{B}_k^\eta \\ \rho_k \mathcal{B}_k^\eta & \text{otherwise} \end{cases} \quad (2.110)$$

where ρ_{k+1} is the updated density from the original one ρ_k , ζ is the move limit and η is the tuning parameter. Typical values for ζ and η are 0.2 and 0.5, respectively [107]. The value of \mathcal{B}_k is calculated from the Lagrange multiplier Λ_k as follows:

$$\Lambda_k = p\rho_k^{p-1} E^0 \varepsilon(\{u\}_k) \varepsilon(\{u\}_k) \quad (2.111)$$

$$\mathcal{B}_k = \Lambda_k^{-1} p\rho_k^{p-1} E^0 \varepsilon(\{u\}_k) \varepsilon(\{u\}_k). \quad (2.112)$$

Level set method (LSM)

Both the homogenization and SIMP models are mainly restricted to linear elasticity and particular objective functions, such as compliance, natural frequencies, or compliant mechanisms. The level set method (LSM) [109–113] works by directly controlling the boundaries of a certain domain, thus altering its shape. This is done by an iso-surface of a scalar function

$$S = \{x : \phi(x) = k\} \quad (2.113)$$

where k is an arbitrary iso-value and x is a point in space on the iso-surface ϕ . Therefore, the process of SO is preformed by letting the level set function ϕ dynamically change in time

$$S(t) = \{x(t) : \phi(x(t), t) = k\}. \quad (2.114)$$

By differentiating both sides of Eq. (2.114) with respect to time and applying the chain rule, the so called *Hamilton-Jacobi* type equation

$$\frac{\partial \phi(x, t)}{\partial t} + \nabla \phi(x, t) \frac{dx}{dt} = 0 \quad (2.115)$$

which defines an initial value problem for the level set function ϕ .

This formulation allows a flexible approach, since level sets can easily represent complicated surface shapes, and do not need to re-parametrize the model as it undergoes significant changes in shape. Further, the models can incorporate a large number of degrees of freedom and several numerical techniques have been developed to make the initial value problem of Eq. (2.115) computationally robust and efficient [113].

In order to formulate the SO of a linearly elastic structure with a domain D and boundary ∂D , with an objective function $F(u)$ which can be either physical or geometrical. As mentioned earlier, a fixed reference domain \bar{D} is defined, so that it fully contains the current structure D , i.e. $D \subseteq \bar{D}$. The structural boundary ∂D is to be represented by level set model S as an embedding through a higher dimensional function $\phi(x)$ such that

$S = \{x : x \in \bar{D}, \phi(x) = 0\}$. Note that the convention $k = 0$ is used. Furthermore, we define an inside-outside function for ϕ such that

$$\phi(x) > 0 \quad \forall x \in D \setminus \partial D \quad (2.116)$$

and

$$\phi(x) < 0 \quad \forall x \in \bar{D} \setminus D, \quad (2.117)$$

shown in Fig. 2.74 [113].

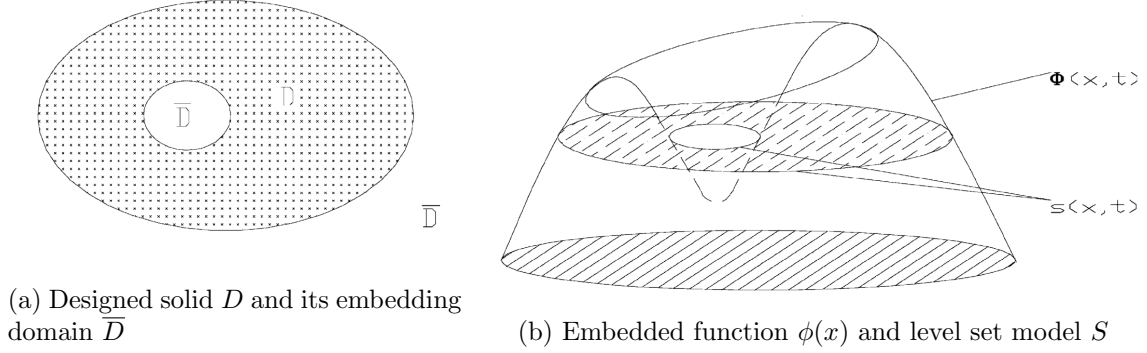


Figure 2.74: Design domains and the level set model [113]

In level set models, the formulation of the optimal design follows:

$$\text{Find } \phi(x, t) \quad (2.118a)$$

$$\text{to minimize } J(u, \phi) = \int_{\bar{D}} F(u)H(\phi)d\Omega \quad (2.118b)$$

$$\text{subject to } a(u, v, \phi) = l(v, \phi), \quad u|_{\partial D} = u_0, \quad \forall v \in U \quad (2.118c)$$

$$\int_{\bar{D}} H(\phi)d\Omega \leq \bar{V} \quad (2.118d)$$

with

$$a(u, v, \phi) = \int_{\bar{D}} E\varepsilon(u)\varepsilon(v)H(\phi)d\Omega \quad (2.119)$$

$$l(v, \phi) = \int_{\bar{D}} pvH(\phi)d\Omega + \int_{\bar{D}} \tau v\delta(\phi)|\nabla\phi|d\Omega \quad (2.120)$$

where $\delta(x)$ and $H(x)$ are the Dirac and Heaviside functions, p are the body forces, τ the boundary forces and v is the virtual displacement field belonging to the space U spanned by the kinematically admissible set of displacements.

However, the conventional LSM may be affected by several unfavourable numerical features, such as velocity extension, reinitialization and the Courant-Friedrichs-Lewy (CFL) condition. To avoid such problems, a comparative supported radial basis function (CSRBF) is used to achieve the interpolation of the implicit level set function, and the design boundary changes by updating a set of expansion coefficients [109]. In the CSRBF formulation, level set function is defined as

$$\phi(x, t) = \varphi(x)\alpha(t) = \sum_{i=1}^N \varphi_i(x)\alpha_i(t) \quad (2.121)$$

where $\varphi(x)$ is the interpolation function of the RBF model and $\alpha(t)$ is the expansion coefficient related with the iterations. Now $\phi(x, t)$ is independent with the spatial variable x and the time variable t .

Now, for instance, optimizing a certain structure by minimizing the compliance, the formulation is as follows:

$$\text{Find } \alpha_i, \quad i = 1, \dots, N \quad (2.122a)$$

$$\text{to minimize } J(u, \phi) = \int_D f(u, v)H(\phi)d\Omega \quad (2.122b)$$

$$\text{subject to } a(u, v, \phi) = l(v, \phi), \quad u|_{\partial D} = u_0, \quad \forall v \in U \quad (2.122c)$$

$$\int_D H(\phi)d\Omega \leq \bar{V} \quad (2.122d)$$

$$\alpha_{min} \leq \alpha_i \leq \alpha_{max}. \quad (2.122e)$$

were $f(u, v)$ is the strain energy density, written as $f(u, v) = \varepsilon^T(u)E\varepsilon(v)/2$, and α_i is limited by determined lower α_{min} and upper α_{max} bounds.

Finally, the updating scheme for each design variable is [109]:

$$\alpha_{k+1} = \begin{cases} \min\{(m+1)\alpha_k, \alpha_{max}\} & \text{if } \min\{(m+1)\alpha_k, \alpha_{max}\} \leq \mathcal{B}_k^\zeta \\ \mathcal{B}_k^\zeta \alpha_k & \text{if } \begin{cases} \max\{(1-m)\alpha_k, \alpha_{min}\} < \mathcal{B}_k^\zeta \alpha_k \\ \mathcal{B}_k^\zeta \alpha_k < \min\{(m+1)\alpha_k, \alpha_{min}\} \end{cases} \\ \max\{(1-m)\alpha_k, \alpha_{min}\} & \text{if } \mathcal{B}_k^\zeta \alpha_k \leq \max\{(1-m)\alpha_k, \alpha_{min}\} \end{cases} \quad (2.123)$$

with

$$\mathcal{B}_k = \frac{\frac{\partial J(u, \phi)}{\partial \alpha_k}}{\max\{\mu, \Lambda_k \frac{\partial G(\phi)}{\partial \alpha_k}\}} \quad (2.124)$$

and the design sensitivities of the objective function and constraint

$$\frac{\partial J(u, \phi)}{\partial \alpha_k} = \int_D f(u, v)\varphi_k \delta(\phi)d\Omega \quad (2.125)$$

$$\frac{\partial G(\phi)}{\partial \alpha_k} = \int_D \varphi_k(x)\delta(\phi)d\Omega. \quad (2.126)$$

where μ is the Lamé parameter, given by $\mu = E/(2 + 2\nu)$, and the damping factor ζ ($0 < \zeta < 1$) and moving limit m ($0 < m < 1$) are the artificial parameters to stabilize the iterative process.

2.3.2 Fatigue constrained optimization

There have been several recent developments [114–118] in order to integrate the fatigue analysis in the optimization algorithm, logically, under the form of constraint. All presented studies used the density based SIMP method. Usually, in a fatigue constrained optimization, the objective function to be minimized is either the volume or mass, due to the direct relation between the cost and performance of a part with its overall mass.

However, some optimizations may aim to minimize compliance [118]. In a FEM analysis, the topology optimization may present the following formulation:

$$\text{Find } \rho_e, \quad e = 1, \dots, N \quad (2.127a)$$

$$\text{to minimize } J(\rho) = \sum_{e=1}^N \rho_e v_e \quad (2.127b)$$

$$\text{subject to } D_e \leq 1, \quad e = 1, \dots, N \quad (2.127c)$$

where D_e represents the fatigue damage in each element.

The fatigue assessment follows the conventional or multiaxial approaches available, that is, based on an equivalent stress model to find the stress spectrum, which is then assessed by the rainflow cycle counting technique. Having the respecting cycles (σ_a , σ_m), the total damage is computed with the Miner's rule (integrating the mean stress effect if needed). In order to compute the time history, several studies [114; 116; 118] propose to use the Von Mises equivalent stress model of Eq. (2.61), while Oest and Lund [117] proposed the Sines model from Eq. (2.63). To cope with the mean stress effect, Nabak et al. [118] used the Goodman line from Eq. (2.31) while Zhang et al. [116] and Jeong et al. [114] both proposed the Morrow correction from Eq. (2.34).

In order to avoid a “checkerboard” solution, some studies [115–117] introduced the density filtered method, where the filtered density $\tilde{\rho}_e$ is a weighted average of the neighbouring design variables, following the expression

$$\tilde{\rho}_e = \frac{\sum_{j \in \mathcal{N}_e} w_j \rho_j}{\sum_{j \in \mathcal{N}_e} w_j}, \quad w_j := \frac{r_0 - r_j}{r_0} \quad (2.128)$$

where \mathcal{N}_e includes all the neighbouring elements, with design variables within the specified radius r_0 from the centroid of the element e , and r_j is the distance between the centroid of the design variable ρ_j and ρ_0 of the neighbouring element.

Other aspect to be aware, is the fact that, due to the local nature of stresses, each element presents a fatigue constraint in the optimization process, which can lead to a cumbersome task and is computationally demanding. To overcome this singularity, all studies introduced the p-norm constraint approach

$$\tilde{D} = \left[\sum_{e=1}^N (D_e)^p \right]^{\frac{1}{p}} \quad (2.129)$$

where p is the p-norm coefficient. The highest the p-norm coefficient, the closer the approximation will be to the maximum fatigue damage in all stresses, but, on the other hand, a low value present a very conservative approach. From the constraint point of view, a conservative value of D_g poses a downsize in the optimization. However, a very high value of the p-norm coefficient will significantly increase the non-linearity of the constraint, therefore making the optimization problem harder to solve. To remedy this issue, an adaptive scaling technique [119] is employed, which modifies the constraint limit on the approximate damage function so that it meets the true maximum damage, following the expression

$$\tilde{D}_{max} \approx c^{(I)} \tilde{D}^{(I)} \quad (2.130)$$

where I denotes the iteration number and c^I is the scaling factor which, for $I > 1$, can be calculated by

$$c^I = \alpha^{(I)} \frac{\tilde{D}_{max}^{(I-1)}}{\tilde{D}^{(I-1)}} + (1 - \alpha^{(I)}) c^{(I-1)} \quad (2.131)$$

where α is the damping parameter varying between $0 < \alpha < 1$, which can also be adapted through each iteration to promote convergence [117], otherwise $\alpha^{(l)} = 1$.

2.3.3 Mathematical programming algorithms

The conventional optimality criteria methods, described in Section 2.3.1, find the optimal solution through a sensitivity analysis. This proves to be a very efficient and fast way to find a solution, reducing its computational cost. The most common algorithms for such methods, i.e. constrained optimization problems, come from mathematical programming, namely sequential convex programming. These methods proceed by maximizing a dual function, which depends only on the Lagrangian multipliers associated with the constraints, required to be non-negative. The reviewed methods are:

1. Convex linearization method (CONLIN)
2. Method of moving asymptotes (MMA)

The application of these mathematical programming techniques is particularly difficult due to the implicit behaviour of the constraints, which are commonly calculated via FEA, calling for many structure reanalysis before achieving the optimal solution.

Finally, for both models it is recommended the use of dual algorithms, since the achieved sub-problems are convex and separable. The utilization of such algorithms is not to be reviewed in this study.

Convex linearization method (CONLIN)

The convex linearization method (CONLIN) [120] performs a linearization of each function defining the optimum design problem with a respect to a proper selected mix of direct and reciprocal variables, so that a convex and separable sub-problem is generated. Considering any differentiable function $c(x)$, the following linearization scheme yields a convex approximation

$$c(x) = c(x^0) + \sum_{+} c_i^0 (x_i - x_i^0) - \sum_{-} (x_i^0)^2 c_i^0 \left(\frac{1}{x_i} - \frac{1}{x_i^0} \right) \quad (2.132)$$

where c_i denotes the first derivatives of $c(x)$ with respect to the design variables x_i . The symbol \sum_{+} (\sum_{-}) means “the summation over the terms for which c_i is positive (negative)”. CONLIN applies this convex linearization scheme to the objective function and all the constraint functions. Therefore, at every iteration, the CONLIN method only requires the evaluation of objective and constraints functions and their first derivatives with respect to the design variables. It is convenient to normalize the design variables so that they equal to unity at the current point x^0

$$x'_i = \frac{x_i}{x_i^0} \rightarrow c'_i = c_i^0 x_i^0. \quad (2.133)$$

The factor $(x_i^0)^2$ disappears from Eq. 2.132, which then becomes

$$c(x') = c(x^0) + \sum_{+} c'_i (x'_i - 1) - \sum_{-} c'_i \left(\frac{1}{x'_i} - 1 \right). \quad (2.134)$$

Applying this linearization technique to each function, and dropping the superscript ', the following explicit sub-problem is formulated:

$$\text{Find } x_i, \quad i = 1, \dots, N \quad (2.135a)$$

$$\text{to minimize } \sum_+ c_{i0}x_i - \sum_- \frac{c_{i0}}{x_i} - \bar{c}_0 \quad (2.135b)$$

$$\text{subject to } \sum_+ c_{ij}x_i - \sum_- \frac{c_{ij}}{x_i} \leq \bar{c}_j, \quad j = 1, \dots, m \quad (2.135c)$$

$$\underline{x}_i \leq x_i \leq \bar{x}_i \quad (2.135d)$$

where c_{ij} denote the first derivatives of the objective function and constraint evaluated at the current point x^0 and the constant \bar{c}_j contains the zero order contributions in the Taylor series expansion

$$\bar{c}_j = \sum_i |c_{ij}|x_i^0 - c_j(x^0), \quad j = 0, \dots, m. \quad (2.136)$$

Method of moving asymptotes (MMA)

The method of moving asymptotes (MMA) [121] is a special type of convex approximation, which promises to very flexible and easy to implement in structural optimization cases.

Being a particular case of convex approximation, it is also based on creating a sub-problem $P^{(k)}$ from the linearization of functions, based on their values and derivatives, to later use the design point in the next iteration $k = k + 1$ from the solution of the current sub-problem $P^{(k)}$. Having said that, the linearization has the following aspect

$$f_i^{(k)} = r_i^{(k)} + \sum_{j=1}^n \left(\frac{p_{ij}^{(k)}}{U_j^{(k)} - x_j} + \frac{q_{ij}^{(k)}}{x_j - L_j^{(k)}} \right) \quad (2.137)$$

where

$$p_{ij}^{(k)} = \begin{cases} (U_j^{(k)} - x_j^{(k)})^2 \frac{\partial f_i}{\partial x_j}, & \text{if } \frac{\partial f_i}{\partial x_j} > 0 \\ 0, & \text{if } \frac{\partial f_i}{\partial x_j} \leq 0 \end{cases} \quad (2.138)$$

$$q_{ij}^{(k)} = \begin{cases} 0, & \text{if } \frac{\partial f_i}{\partial x_j} \geq 0 \\ -(x_j^{(k)} - L_j^{(k)})^2 \frac{\partial f_i}{\partial x_j}, & \text{if } \frac{\partial f_i}{\partial x_j} < 0 \end{cases} \quad (2.139)$$

$$r_i^{(k)} = f_i^{(k)} - \sum_{j=1}^n \left(\frac{p_{ij}^{(k)}}{U_j^{(k)} - x_j} + \frac{q_{ij}^{(k)}}{x_j - L_j^{(k)}} \right) \quad (2.140)$$

where $f_i(x)$ are the objective and constraints functions, n is the number of design variables, and the derivatives $\partial f_i / \partial x_j$ are calculated at the iteration point $x = x^{(k)}$. It is important to note that $L_j^{(k)} \leq x_j \leq U_j^{(k)}$ for every iteration k , and these lower and upper boundaries are called ‘‘moving asymptotes’’, which are updated at every iteration, later to be seen some examples of it.

2. Background theory

Further, the second derivatives of $f_i^{(k)}$, at any point x such that $L_j^{(k)} \leq x_j \leq U_j^{(k)}$ for all $j = 1, \dots, m$, are given by

$$\frac{\partial^2 f_i^{(k)}}{\partial x_j^2} = \frac{2p_{ij}^{(k)}}{(U_j^{(k)} - x_j)^3} + \frac{2q_{ij}^{(k)}}{(x_j - L_j^{(k)})^3} \quad (2.141)$$

and

$$\frac{\partial^2 f_i^{(k)}}{\partial x_j \partial x_l}, \quad \text{if } j \neq l. \quad (2.142)$$

Thus, since $p_{ij}^{(k)} \geq 0$ and $q_{ij}^{(k)} \geq 0$, $f_i^{(k)}$ is a convex function. In particular, at $x = x^{(k)}$

$$\frac{\partial^2 f_i^{(k)}}{\partial x_j^2} = \begin{cases} \frac{2\partial f_i / \partial x_j}{U_j^{(k)} - x_j^{(k)}}, & \text{if } \partial f_i / \partial x_j > 0 \\ -\frac{2\partial f_i / \partial x_j}{x_j^{(k)} - L_j^{(k)}}, & \text{if } \partial f_i / \partial x_j < 0. \end{cases} \quad (2.143)$$

Thus, the closer $L_j^{(k)}$ and $U_j^{(k)}$ are chosen, the larger the second derivatives, and more curvature is given to the approximation function $f_i^{(k)}$, getting a more conservative approximation of the problem.

The ‘‘moving asymptotes’’ can be altered during the optimization by the following:

- If the process tends to oscillate, the asymptotes can be moved closer together, to promote stabilization
- If the process is monotone and slow, the asymptotes can be moved away from the current iteration point, or ‘‘relax’’ the domain

For a reasonable lower \underline{x}_j and upper \bar{x}_j bounds of x_j , and $s < 1$, a simple way to implement this ‘‘rule’’ is presented next:

- For the iteration $k = 0$ and $k = 1$

$$L_j^{(k)} = x_j^{(k)} - (\bar{x}_j - \underline{x}_j) \text{ and } U_j^{(k)} = x_j^{(k)} + (\bar{x}_j - \underline{x}_j) \quad (2.144)$$

- For $k \geq 2$

- If the signs of $x_j^{(k)} - x_j^{(k-1)}$ and $x_j^{(k-1)} - x_j^{(k-2)}$ are opposite, indicating an oscillation in the variable x_j , then let

$$L_j^{(k)} = x_j^{(k)} - s(x_j^{(k-1)} - L_j^{(k-1)}) \quad (2.145)$$

$$U_j^{(k)} = x_j^{(k)} + s(U_j^{(k-1)} - x_j^{(k-1)}) \quad (2.146)$$

- If the signs of $x_j^{(k)} - x_j^{(k-1)}$ and $x_j^{(k-1)} - x_j^{(k-2)}$ are equal, indicating that the asymptotes are slowing down the convergence in the variable x_j , then let

$$L_j^{(k)} = x_j^{(k)} - \frac{x_j^{(k-1)} - L_j^{(k-1)}}{s} \quad (2.147)$$

$$U_j^{(k)} = x_j^{(k)} + \frac{U_j^{(k-1)} - x_j^{(k-1)}}{s} \quad (2.148)$$

Note that this is only an example for updating the asymptotes, which can be updated by many different schemes, according to the application.

Finally, with a linearized approximation of the functions $f_i^{(k)}$ defined by Eq. (2.137), the following sub-problem $P^{(k)}$ is defined

$$\text{Find } x_i, \quad i = 1, \dots, N \quad (2.149a)$$

$$\text{to minimize } \sum_{j=1}^n \left(\frac{p_{0j}^{(k)}}{U_j^{(k)} - x_j} + \frac{q_{0j}^{(k)}}{x_j - L_j^{(k)}} \right) + r_0^{(k)} \quad (2.149b)$$

$$\text{subject to } \sum_{j=1}^n \left(\frac{p_{lj}^{(k)}}{U_j^{(k)} - x_j} + \frac{q_{lj}^{(k)}}{x_j - L_j^{(k)}} \right) + r_l^{(k)} \leq \hat{f}_l, \quad l = 1, \dots, m \quad (2.149c)$$

$$\underline{x}_i \leq x_i \leq \bar{x}_i, \quad i = 1, \dots, N. \quad (2.149d)$$

2.3.4 Special algorithms

The optimality criteria methods tend to proceed optimization through sensitivity analysis, verifying the Kuhn-Tucker conditions. However, this algorithm may only foresee a local minima, missing out on the global optimal point. In order to contour this problem, special optimization algorithms that offer more freedom can be used. For the purpose of this study, the studied algorithms will be:

1. Genetic algorithm (GA)
2. Artificial bee colony algorithm (ABC)

These algorithms both share the similarity with biological processes, namely the Darwinian natural selection for GA and the bee-colony organization for ABC.

Genetic algorithm (GA)

The GAs [122] were first introduced by Holland [123], modelled after the process of natural selection, where a certain population of artificial organisms evolves to better fit the environment. These “organisms”, which each represents a possible optimum solution, compete against one another to best solve the problem. The organisms that are most highly-fit are allowed to serve as parents for the next generation, through single or multiple crossover. After mutation, the child organisms replace the parents, and the evolutionary process iterates. Therefore, through a “survival of the fittest” evolution, the optimization algorithm tends to converge to the global optimal solution.

When it comes to a topology optimization application, the GA performs the optimization through a population of chromosomes, where each chromosome is a coded representation of the design variables, and each multi-gene sub-string (called parameter) represents the value of a certain design variable. This means that while the number of genes in a chromosome may be much larger than the number of design variables, the number of parameters is the same. The required length (in bits) of a parameter controlling a floating-point design variable with an allowable range ($\rho_{min} \leq \rho_i \leq \rho_{max}$) and a desired resolution (given by the increment $\Delta\rho$) is given by

$$l = \frac{1}{\ln 2} \cdot \ln \left[\left(\frac{\rho_{max} - \rho_{min}}{\Delta\rho} \right) \right]. \quad (2.150)$$

It is important to note that the search space increases with the chromosome length by 2^l , which asks for care in terms of minimizing the length l , as well as design variables and its range and resolution. Finally, the decoding part takes form in converting the binary-valued string into a parameter P by decimal conversion and then applying the following decoding scheme:

$$\rho_i = P \cdot \frac{\rho_{max} - \rho_{min}}{2^l - 1} + \rho_{min}. \quad (2.151)$$

First, looking at the fitness evaluation, the constrained optimization deals with a lot of methods in order to ensure that the optimal solution meets the constraints. The standard penalization method is a very simple way to assess this matter. Its difficulty in adjusting the penalization parameters is its major setback. The fitness function is directly related with the objective function, whether for minimizing or maximizing, and, for instance, regarding a 2D stiffness maximization problem, Kane and Schoenauer [124] proposed the following function

$$\mathcal{F} = \frac{1}{A_{con} + \epsilon A_{dis} + \alpha(D_{max} - D_{lim})^+} \quad (2.152)$$

where A_{con} and A_{dis} represent the areas of connected and disconnected material, respectively, D_{max} is the maximum displacement, D_{lim} is the displacement constraint and ϵ and α are the penalty parameters. The parameter ϵ does not influence much on the performance of the algorithm (not related with the limiting constraint) and was set to a fixed value of 0.1.

The drawbacks in defining a fixed value for the parameter α are:

- A small value may result in an optimal solution that violates the constraints;
- A large value ensures that the constraints will be met, but forbids exploration and short-cuts in feasible regions that might be essential to the overall success of the algorithm.

Hence, a logical way to overcome this is to use a dynamic schedule, starting from small value, which allow for the exploration even in infeasible regions, and gradually enforcing the penalization by increasing α such that the constraints are finally met by the whole population. This can be done in two methods. The first method is called the *exogenous* scheme, where the value of α is increased by some multiplicative factor β every M generations. The value of α at the generation i is given by

$$\alpha_i = \alpha_0 \beta^{\frac{i}{M}}. \quad (2.153)$$

Typical values for M and β are 10 and 1.001, respectively, while the initial value α_0 is computed from the average weights and violations of the constraints in the initial population. The second method is the *adaptive* scheme and uses the current population data in order to compute the further values. Some $\bar{\alpha}_i$ is computed from the actual average weights and violations in population i , and α is set to $\bar{\alpha}_i$ if its value is greater than the current value of α , to ensure monotonicity.

However, particularly in early generations, large differences in fitness values will exist between chromosomes in a given generation. This leads to quick dominance of highly-fit chromosomes of the parenting process. In order to not discard completely the low-performance chromosomes, which may still have valuable information to attain, the fitness values of highly-fit chromosome are slightly reduced while the fitness of low-performance chromosomes are increased. Other selection process may be “elitists” in the sense that child

chromosomes are randomly chosen to be replaced with most-highly-fit chromosome from the previous generation to not allow the quality of the child generation to be diminished.

The reproduction process takes place after the fitness-valued selection, and is inspired by the mechanics of chromosome recombination, called “genetic crossover”. The most straightforward operator is the “single-point” crossover, where the genetic information is swapped, creating two child chromosomes from the information of both parents (see Fig. 2.75a [125]). Note that the crossover is not performed in every pair of parent chromosomes, rather than evaluated by a probability specified *a priori* by the programmer.

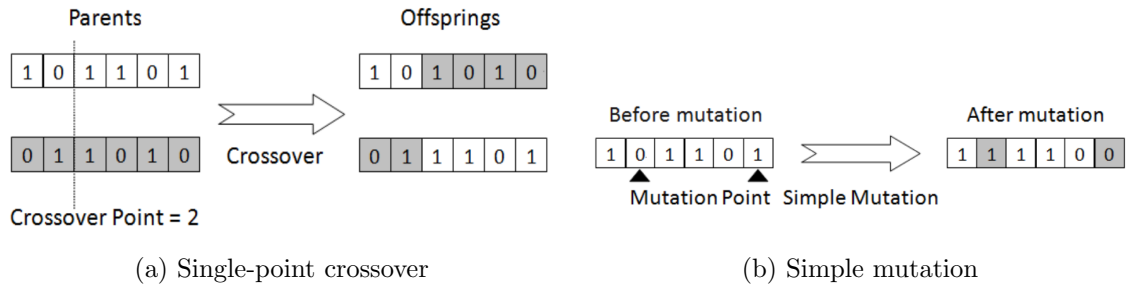


Figure 2.75: Reproduction and mutation processes in GAs [125]

The last process of the iteration regards the mutation of child chromosomes (see Fig. 2.75b [125]), where a routine analyses every gene of the chromosome and through a probability value defined by the programmer decides randomly where to switch the gene from 1 to 0 or vice-versa. This allows for a slight change in the child, thus promoting the search for new possibilities in the search space.

The entire evolution process iterates and evolves until it has either converged into an optimum or reached a pre-determined number of generations. Typically the convergence criteria is related with the percentage of chromosomes which have converged to similar points in the search space.

Artificial bee colony algorithm (ABC)

The ABC algorithm [126] was first introduced by Karaboga [127], for numerical optimization based on the behaviour of honeybee swarm. The model is based on three types of bees: employed bees, onlookers and scouts. The *employed bees* are the ones which are exploiting the food source. The *onlookers* are waiting to receive the information about the food sources from the employed bees. The colony is divided in half by employed bees and onlookers. When a food source is discarded, the respective employed bee abandons it becomes a *scout*, searching for new food sources in the hive.

In this algorithm, the food source represents a candidate solution for the optimization problem and the fitness of the solution is characterized by the nectar amount of the food source. The ABC algorithm is an iterative process and, considering a NS number of food sources (candidate solutions) which is equal to the number of employed bees and onlookers and D as the dimension of each solution vector, which in SO may infer the number of design variables. One can initialize the algorithm with a random population (X_1, \dots, X_{NS}) , where $S_i = \{x_{i1}, \dots, x_{iD}\}$ generated by

$$x_{ij} = x_{min,j} + rand[0, 1] \cdot (x_{max,j} - x_{min,j}) \quad \text{for } j = 1, \dots, D \text{ and } i = 1, \dots, NS \quad (2.154)$$

where $x_{max,j}$ and $x_{min,j}$ respectively represent the upper and lower bounds for the dimension j . The following steps are:

1. Each employed bee searches the neighbourhood of its current food source to determine a new food source using

$$v_{ij} = x_{ij} + \Phi_{ij}(x_{ij} - x_{kj}) \quad (2.155)$$

where $k \in [1, \dots, \text{NS}]$ and $j \in [1, \dots, D]$ are randomly chosen and Φ_{ij} is a random function between $[-1, 1]$. It must be noted that k has to be different from i and parameter values v_{ij} exceeding their boundary values are set to their limits.

2. After generating the new food source, the selection between the previous and new food source will be made through a greedy selection where in case of the fitness of the new option being equal or better than that of X_i , the new food source takes the place of the previous one.
3. The onlooker bee selects a food source by evaluating the information received from all of the employed bees through a probability of choice p_i given by

$$p_i = \frac{f_i}{\sum_{i=1}^{\text{NS}} f_i} \quad (2.156)$$

where f_i is the fitness value of the respective food source X_i . After selecting the food source, the onlooker generates a new candidate using Eq. (2.155), and a greedy selection will be performed just like in employed bees.

4. If a candidate solution cannot be further improved by a predetermined number of trials called *limit*, and the respective employed bee becomes a scout, generating a new candidate using

$$v_{ij} = x_{\min,j} + \text{rand}[0, 1] \cdot (x_{\max,j} - x_{\min,j}) \quad \text{for } j = 1, \dots, D. \quad (2.157)$$

This process iterates until a termination condition is met.

Hadidi et al. [126] also proposed some modifications to the algorithm, the modified artificial bee colony algorithm (MABC), in order to better its performance. First, within the neighbourhood searching, introducing the probability of changing a parameter of a food source, which is defined by a D-dimensional vector of parameters, defined by Pa . Introducing a uniformly distributed random number z , between 0 and 1, for each parameter, if $z < Pa$ the parameter is changed using Eq. (2.155), otherwise remains unchanged.

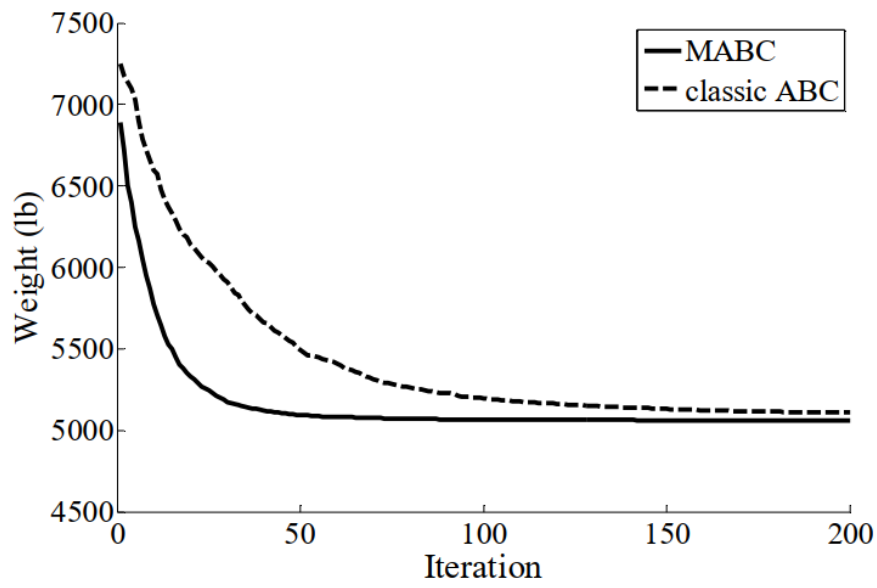
The onlookers approach is modified for a tournament based selection. M food sources are randomly selected to compete with each other and the most-highly-fit candidate is selected as the winner of the tournament, discarding the need for the probability of selection in Eq. (2.156).

Lastly, the scout behaviour is improved, in order to limit the random movement which may not be effective. For this, a Gaussian mutation approach is used, replacing Eq. (2.157) by

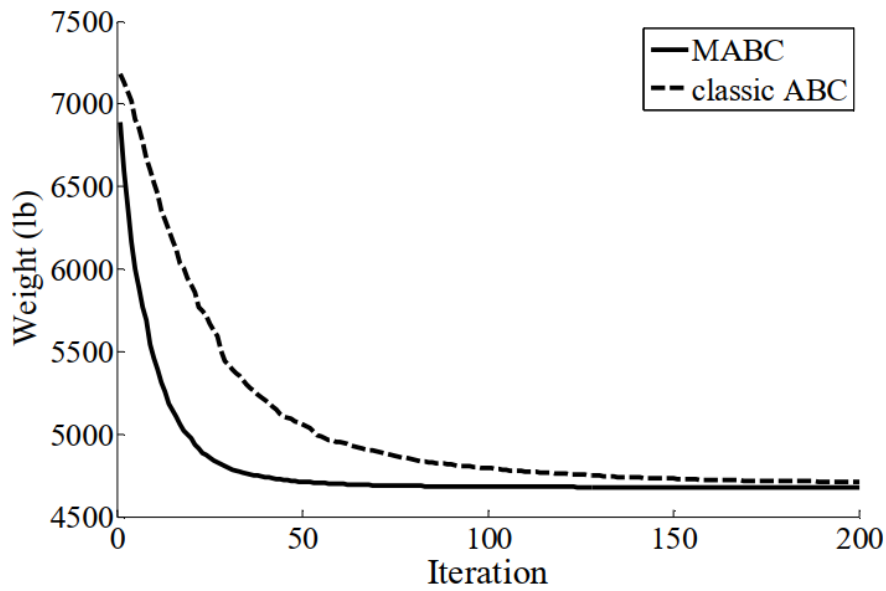
$$v_{ij} = x_{ij} + N(0, \sigma_j) \quad \text{for } j = 1, \dots, D \quad (2.158)$$

where $N(0, \sigma_j)$ is a normally distributed random number with a mean zero and standard deviation σ_j , which decrease gradually throughout the iteration, to promote convergence.

Figs. 2.76a and 2.76b [126] display the convergence histories on a truss optimization with different load cases (case 1 and case 2). It is depicted that the proposed modifications clearly promote a better performance of the algorithm, converging faster on the optimal solution. However, it must be noted that this difference attenuates as the complexity of the problem evolves.



(a) Ten-bar truss case 1



(b) Ten-bar truss case 2

Figure 2.76: Optimization histories [126]

Pitch support optimization

3.1 Introduction

This optimization study is performed on Vestas V164-8.0MW offshore wind turbine (see. Fig 3.1a). This turbine holds a 164m rotor and a rated power of 8.0MW. Any further technical information on the wind turbine model can be found in Appendix B. More specifically, the component to be focused on is the cylinder support, which is a part of the pitch system (see Fig. 3.1b).



(a) Vestas V164-8.0MW installed



(b) Vestas V164-8.0MW pitch system

Figure 3.1: Vestas V164-8.0MW

Being projected for offshore applications, implies a more severe external load spectrum that, in addition to the large size characteristics of the turbine, leads to higher loads during operation. Like in most engineering application, the solution is based on the compromise that if one wants a bigger power output, the respective solicitations will be higher (applied work in the turbine). In this particular case, the blade root diameter is approximately 4.5 m which means a large-scale pitch system. In order to meet the desired performance, Vestas came up with a new solution for this turbine, which was later patented under Patent Cooperation Treaty (PCT) application WO 2017/005264 A1 [128].

3.2 Pitch system

The pitch system in question, displayed in Fig. 3.2, is hydraulically driven by two cylinder actuators, in either a compact or segmented pitch ring system. As mentioned in Section 2.1.4, it is responsible for not only coupling each blade to the hub, but also controlling the blades' position. For this purpose, the components (blades and hub) are connected through the blade bearing, which will be thoroughly explained.

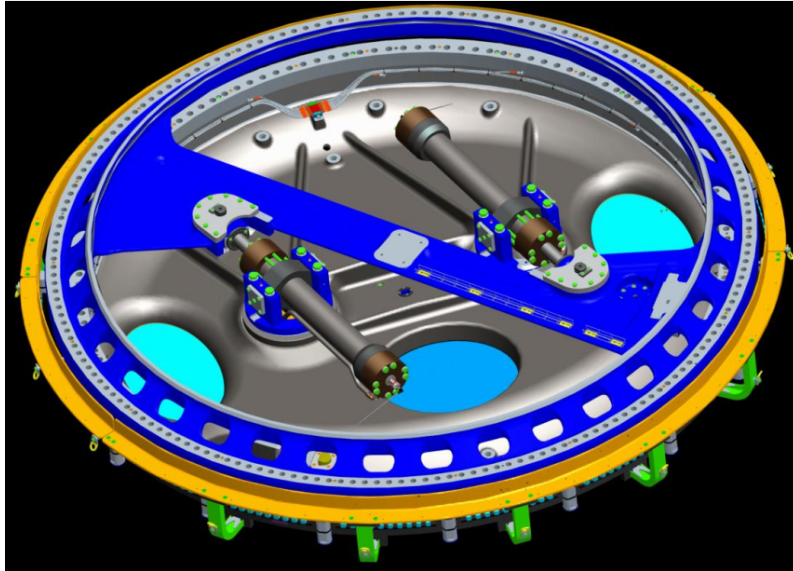


Figure 3.2: Pitch system assembly

Figure B.2 [129] displays the exploded view of the PCT application WO 2012/069062 [129], which is the previous design. The core of the system is the bearing 22, from which the inner ring 30 is mounted to the hub 6 and the outer ring 32 is mounted to the blade. The first coupling member 24 is positioned between the hub 6 and the inner ring 30, while the second coupling member 26 is positioned between the blade and the outer ring 32. These coupling members 24 and 26 provide mounting points for the hydraulic actuators, so that the driving actuators can rotate the inner ring 30 relative to the outer ring 32 thereby pitch the blade relative to the hub 6.

The major breakthrough with the recent invention is the segmented pitch ring (see Fig. 3.3 [128]) of the coupling members, which provides much easier and cost efficient manufacturing, key factors as the dimensions of wind turbines continue to increase. The segmented pitch ring comprises one or more rolled segments and one or more casted segments. Naturally, the majority of the pitch ring, approximately 206 degrees is formed by cold rolling, has better cost and performance, while the other segments are manufactured by casting, to provide better connection features and allowing complex shaped parts.

Having a structure with rolled and casted segments leads to a set of regions with different stiffness within the pitch ring. The interface between the rolled and casted element is spanned by a bridge element 146 (see Fig. 3.3), and the non-uniform stiffness region may promote a weak point susceptible to deformation under high stress. For this reason, the bridge element must be configured in order to provide uniform stiffness across the interface.

Finally, the segmented pitch ring may comprise a beam connecting the diametrically opposed casted elements, to further improve the integrity of the pitch ring. The beam

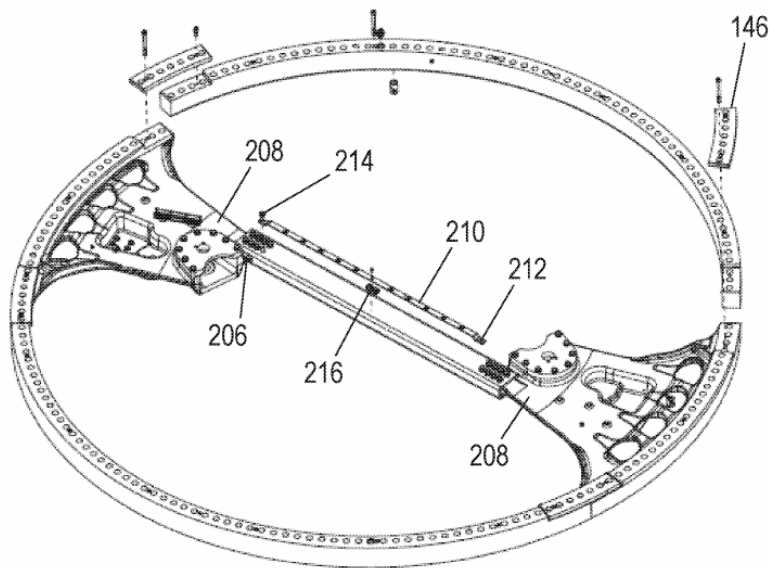


Figure 3.3: Exploded view of the segmented pitch ring [128]

is preferably a hollow, elongate, uniform-section member, manufactured by hot-rolling in order to withstand high stresses while twisting slightly.

3.3 Pitch cylinder support

Living up to the name, the cylinder support is responsible for connecting both hydraulic actuators to the coupling plate. The connection is through a ball bearing (see Fig. 3.4) in order to allow relative movement between the components, which is particularly important for the functionality requirements, as later to be seen. In the current version, the support is composed by two elements:

1. Support plate
2. Hydraulic cylinder support

which are assembled through bolted connections. The support plate is connected directly to the ball bearing and the two cylinder supports are connected to the support plate. The cylinder supports allow pivoting in their holes, also fundamental for the behaviour of the cylinder. This study focuses only on the optimization of the hydraulic cylinder support.

However, engineers at Vestas are already looking at this subject since 2018, proposing new improved solutions. An overview of the designs at stake is displayed in Fig. 3.5. Actually, the design from Figs. 3.5c to 3.5e are child versions of the one proposed in Fig. 3.5b. This because excessive displacements were assessed in the proposal, so other versions were engineered in order to solve the problem. The proposed improvements are namely overlapping components (see Fig. 3.5c), disk support (see Fig. 3.5d) and built-in reinforcements (see Fig. 3.5e). In terms of materials, all the proposed designs are to be made in cast iron, due to the complex shape.

3.3.1 Material requirements

Table 3.1 displays the material information on the current model of the pitch support system. As a simplification, this study does not aim to choose the best material, instead

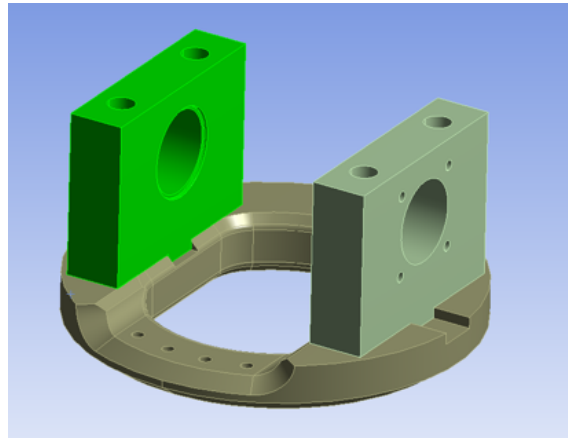


Figure 3.4: Current design of pitch cylinder support

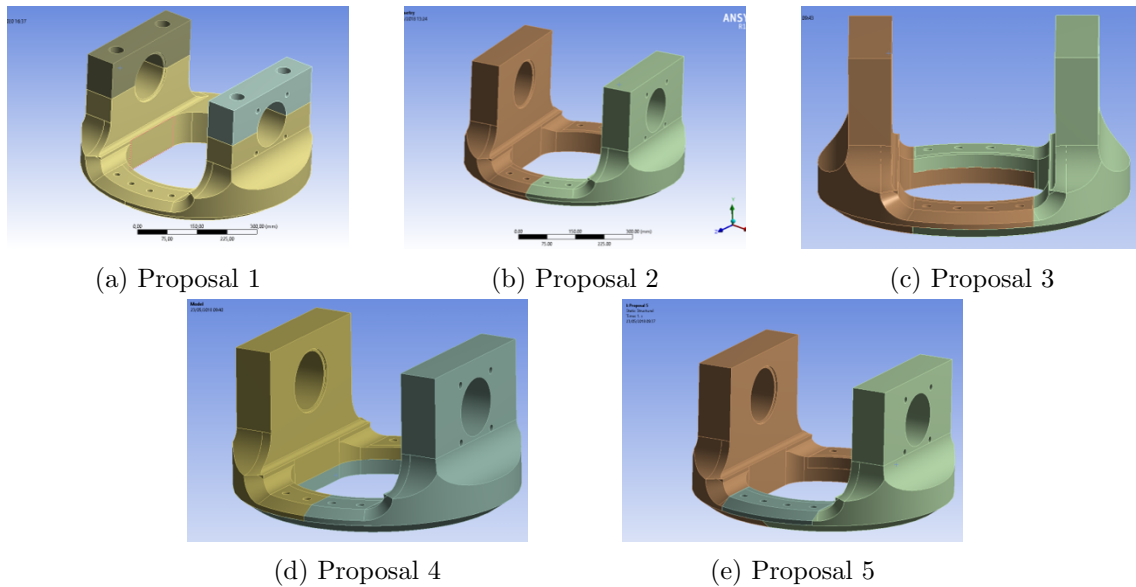


Figure 3.5: Overview of the proposed designs

proposes to optimize the current design maintaining the choice in materials. However, one must be aware that the material choice impacts on the not only on performance but also in manufacturing feasibility, which may constrain the optimal solution. For example, for a solution with a complex shape, casting should be the best manufacturing option, which calls for casting materials such as cast iron.

Another important aspect is the definition of the safety factors for the analysis. Table 3.2 shows the safety factors for the respective materials, defined in the current implemented solution. These are based on the material data uncertainty ($\gamma_{m,fat}$ and $\gamma_{m,ult}$) and the consequences of failure ($\gamma_{n,fat}$ and $\gamma_{n,ult}$). The current safety factor scheme will be maintained in this study, provided that the material selection stays untouched. If any new material is considered, the chosen safety scheme should be properly justified.

Fatigue analysis is also an objective of this study, therefore, the fatigue information of the materials in question is needed. This data will later be used to assess the fatigue damage in the component through its lifetime, allowing to make conclusions about the reliability of the optimal design.

Material properties						
Name	Material	Young's modulus E [GPa]	Poisson's ratio ν	Density ρ [kg mm ⁻³]	Yield strength σ_y [MPa]	Ultimate strength σ_u [MPa]
Support plate	EN-GJS-400-18U-LT	169	0.275	7.1×10^{-6}	220	360
Hydraulic cylinder support	S355J2G3/EN 10025	210	0.3	7.8×10^{-6}	355	426

Table 3.1: Material properties of the current pitch support system

Safety factors				
Material	$\gamma_{m,ult}$	$\gamma_{n,ult}$	$\gamma_{m,fat}$	$\gamma_{n,fat}$
EN-GJS-400-18U-LT	1.10	1.00	1.20	1.15
S355J2G3/EN 10025	1.10	1.00	1.10	1.15

Table 3.2: Safety factors for the materials in the current solution

The computation of the component *SN curve* is proposed through a scaling equation similar to Eq. (2.12), where the corresponding factors are:

1. Mean stresses
2. Surface condition
3. Size/thickness effect
4. Effect of chill casting
5. Quality/NDT level
6. Highly stressed volume
7. Variable amplitude loading
8. Min/max cut-off levels

which estimate the actual fatigue strength from a reference fatigue strength. After combining all the correlation factors for the component in the study, explained in Appendix C, the *SN curve* for this study is displayed in Fig. 3.6. Be aware that the curve has already taken in consideration the safety factor ($\gamma_{m,fat} = 1.38$).

3.3.2 Installation requirements

In terms of functionality requirements, there are some assembly and shape restrictions. First of all, the domain is limited in order to ensure the correct positioning of the cylinder in the system, i.e. the positioning of the cylinder has to remain fixed despite the shape or size of the optimal design (see Fig. 3.8a). Then, the solution needs to ensure the degrees of freedom necessary for good load distribution, i.e. only axial force in the cylinder, therefore,

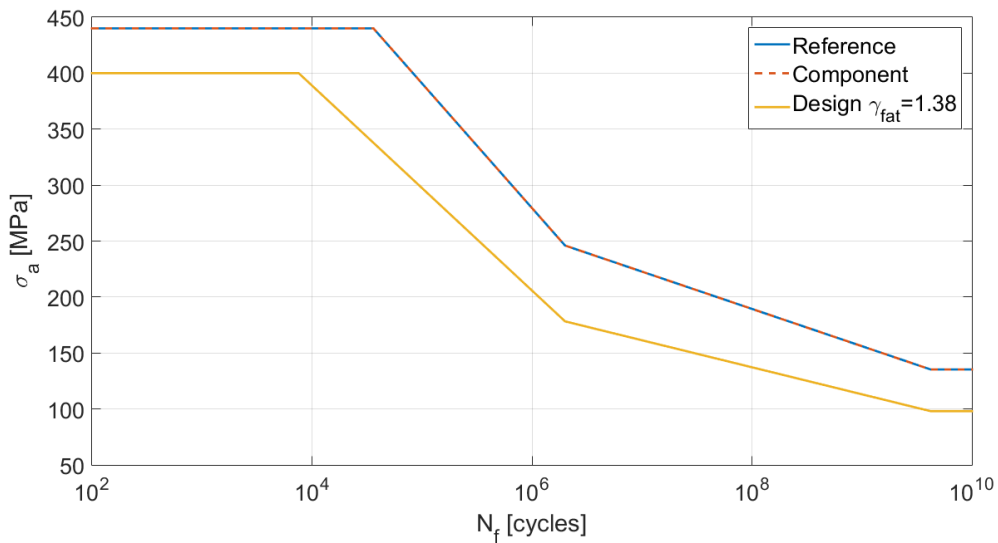


Figure 3.6: Calculated fatigue data (for $R = -1$)

Figure 3.7: EN-GJS-400-18U-LT tension $S-N$ curve

maintaining the same kinematic system (see Fig. 3.8b). Lastly, the connections to other components have to maintain the same, such as bolted connections to the bearing inner ring (see Fig. 3.8c).

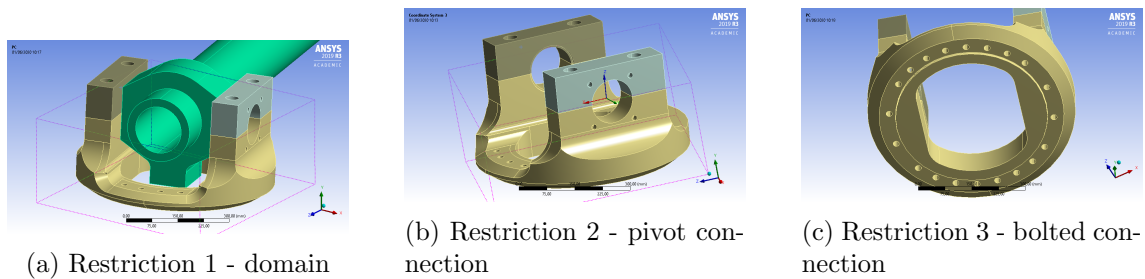


Figure 3.8: Installation requirements for the cylinder support

All the aspects mentioned earlier must be respected in order to allow for good functionality and assembly of the elements. However, there may be some resizing of some characteristics, to be properly justified in such case. Table 3.3 displays a brief summary of the installation restrictions.

Item	Name	Description
1	Hole	Connection to the cylinder
2	Cylinder mounting	Space for the cylinder
3	Surface	Stepped surface in the plate side

Table 3.3: Summary of the installation restrictions

3.3.3 Loads

The loading conditions can be categorized in three main categories:

1. Bolt pre-tension
2. Ultimate failure
3. Fatigue loading

which comprise all the external forces applied to the system, needed both in the static and fatigue analysis.

The assembly of the system has two degrees of freedom: pivot rotation in the connection with the support and at the extremity of the actuator. This helps to maintain a load distribution mainly in the axial direction. Hence, the applied loads are in the O_z direction of the coordinate system displayed in Fig. 3.9.

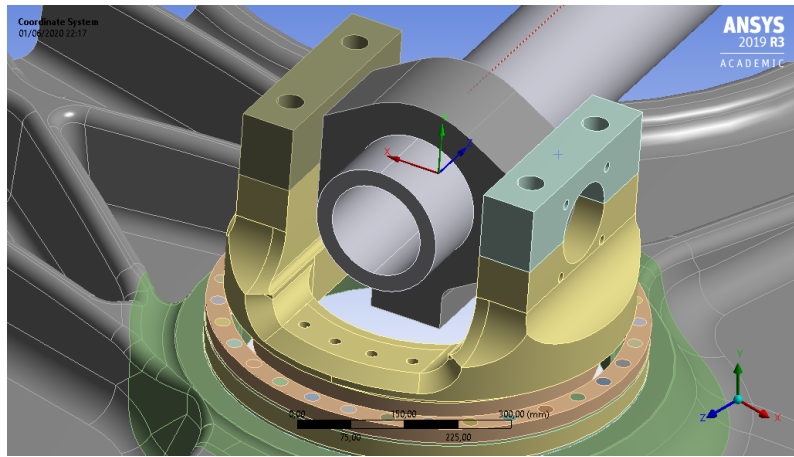


Figure 3.9: Loading coordinate system

In order to compute the axial force actuating in each cylinder, one must look at the scheme displayed in Fig. 3.10a. The pitch system must sustain an induced moment from the blade. The moment is balanced by the the two cylinders (see Fig. 3.10a) that vary with the moment arm c . This moment arm is defined by the pitch angle, and the relationship is displayed in Fig. 3.10b. Since the moment is distributed by two cylinders (reactionary forces), the force actuating in each cylinder follows the expression:

$$F(t) = 0.5 \cdot \frac{M(t)}{c(t)} \quad (3.1)$$

where $M(t)$ is the applied moment and $c(t)$ is the pitch cylinder moment arm.

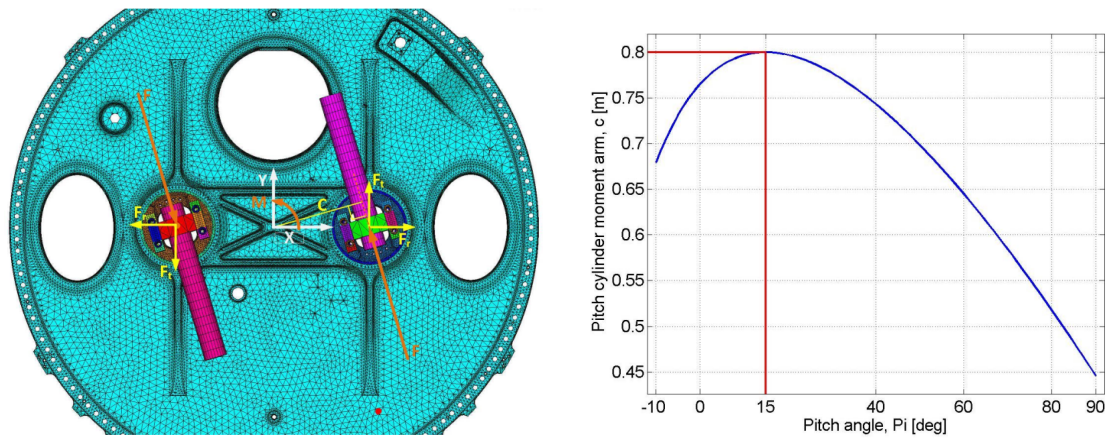
Bolt pre-tension

The bolted connections are divided in three groups:

1. Outer ring - hub late (see Fig. 3.11a)
2. Inner ring - support (see Fig. 3.11a)
3. Brackets - support (see Fig. 3.11b)

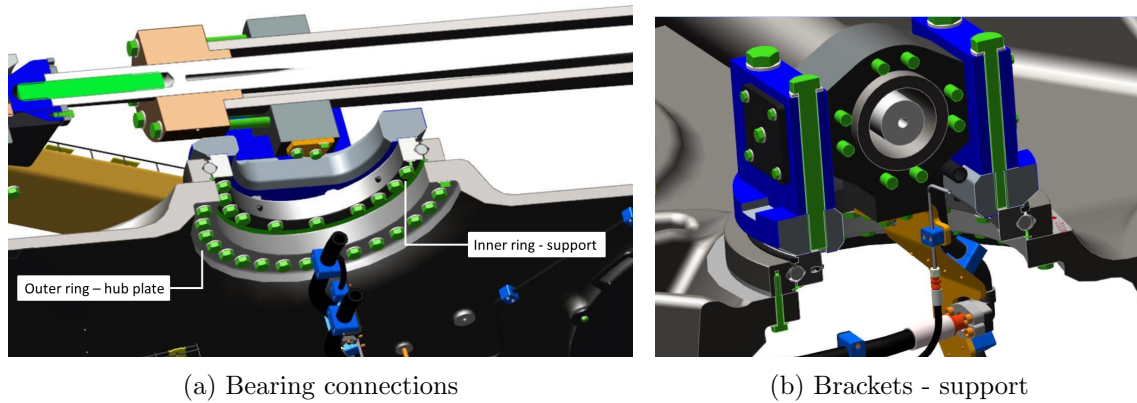
An overview of the bolted connections is displayed in Table 3.4.

3. Pitch support optimization



(a) Pitch system configuration (model and load components) (b) Pitch cylinder moment arm c as a function of the pitch angle

Figure 3.10: Pitch system loading configuration



(a) Bearing connections

(b) Brackets - support

Figure 3.11: Bolted connections in the pitch support system

Ultimate failure

The ultimate failure conditions were taken from the maximum possible pressure inside the cylinder. This pressure is limited by the safety valve, which is set to 310 bar, leading to an extreme load of

$$F_{pitch,max} = 310 \text{ bar} \cdot \frac{\pi(160 \text{ mm})^2}{4} = 623 \text{ kN}. \quad (3.2)$$

Thus, the ultimate failure loading conditions were set to +623 kN and -623 kN.

Fatigue loads

In order to provide a continuous improvement in designing its products, Vestas has specific departments focusing on computing the loads that are present in all the structure, computing the time history of each specific turbine. Although this is not the subject of the study, it is important to understand how to address the information that is available. The process is briefly explained below:

1. Use of operational measurements (sensors) to compute several time histories (example in Fig. 3.12), representing the active loads on critical points in the turbine and

Bolteed connections						
Parts	Number of bolts	Size	Grade	Pre-tension per bolt	Realized average pre-tension	
Outer ring/ hub plate	32	M20	10.9	82.5 kN	82.2 kN	(-0.4%)
Inner ring/ support	20	M20	8.8	100.5 kN	100.6 kN	(+0.1%)
Brackets/ support	4	M36	10.9	485.5 kN	486.3 kN	(+0.2%)

Table 3.4: Summary of the bolted connections

also different wind cases (mean velocity and turbulence)

2. Calculation of the number of cycles for each time history based on frequency of actuation

It is also important to note that each time history is only 10 minutes long, since according to DNV GL-ST-0437 [130], is enough to characterize the wind loading with a valid representation during all lifetime. Moreover, the full number of cycles should represent a total life of 20 to 25 years.

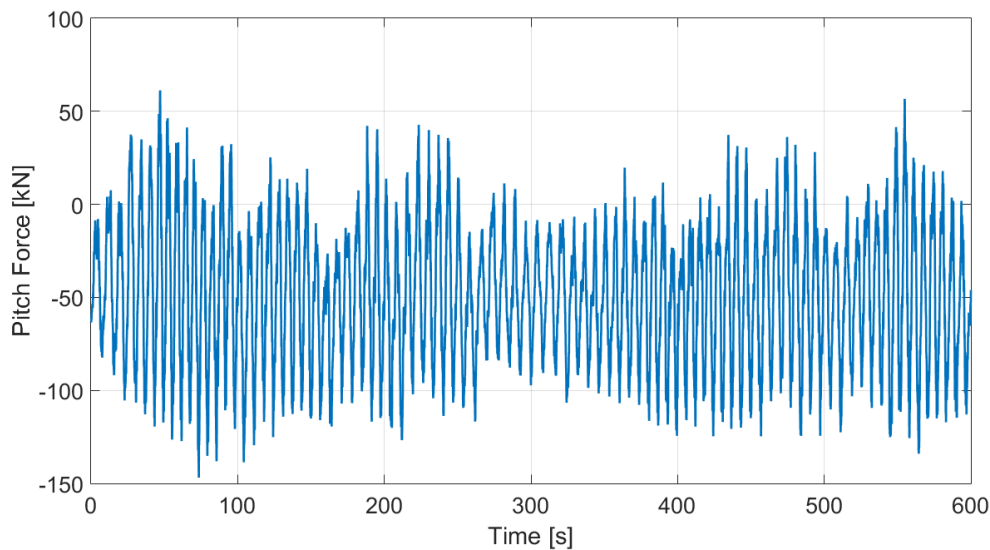


Figure 3.12: Example of a time history from the pitch force of a Vestas V164-8MW turbine

3.4 Overview on the optimization method

The proposed method of this study, displayed in Fig. 3.13, may be divided by two main sequential phases:

1. Topology optimization
2. Parametric optimization

3. Pitch support optimization

In the first stage, a static analysis combined with ansys topology optimization feature was performed, aiming to get an initial optimized shape, later to serve as a model for the size optimization. This initial analysis is performed in a simple FEM model, ignoring complex non-linear contacts and connections such as bolts and bearings. Despite being not as representative of reality as one would expect, this gives a good initial configurations of the optimal design, in an fast and efficient way.

Having worked on the optimal design shape, a CAD design parametrization is to be performed, in order to do a parametric optimization. In this step, a multi-software algorithm was developed, using GA's features. Both static and fatigue analysis were made, recurring to the simplified FEM model, resulting in a fully capable optimal design. Note that the verification analysis is not made, trusting that the comprehensive static and fatigue analysis of the size optimization ensure the performance of the optimal solution.

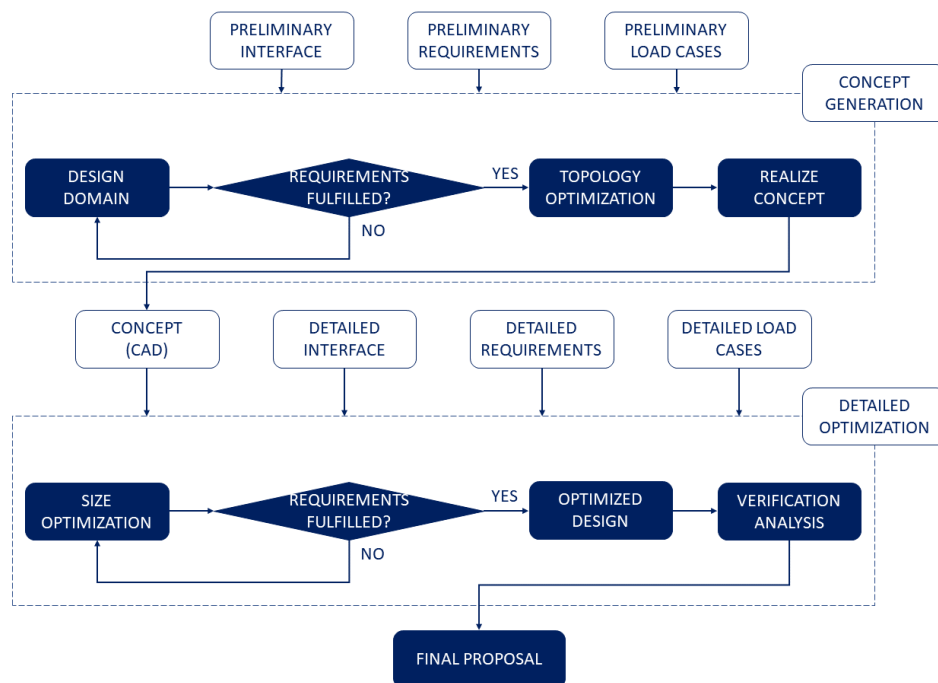


Figure 3.13: Phases of the optimization methods

Topology optimization

As explained in Section 3.4, as for a first approach of the problem, a topology optimization was made. It was expected to gain a sense of what the optimal shape would look like, later to post-process it into a parametrized CAD design for the next step of the optimization: the parametric optimization. The topology optimization was performed recurring to a simplified model. This implies a continuous, contact-free, simple FEM model. At this stage, no fatigue analysis was made, and only a static analysis at the ultimate failure conditions was performed, to serve as ground-base for the Ansys 2019 R3 topology optimization tool.

4.1 Mesh and contacts

Although the system is comprised by an assembly of several parts, the model was meshed ignoring the bolted connections and the bearing, which is simulated by adding an interface body with a certain constitutive matrix (see Fig. 4.1b). Regarding the constitutive matrices for the several components, the model is made by two sets of materials: EN-GJS-400-18LT and S355J2G3/EN 10025. An overview on the material set up is given in Table 4.1.

Material designation

Component	Material	Elastic modulus E [GPa]	Poisson ratio ν	Density ρ [kg mm ⁻³]
Support plate	EN-GJS-400-18LT	169	0.275	7.1×10^{-6}
Hub plate	EN-GJS-400-18LT	169	0.275	7.1×10^{-6}
Slew bearing	S355J2G3/EN 10025	210	0.300	7.8×10^{-6}
Bracket	EN-GJS-400-18LT	169	0.275	7.1×10^{-6}

Table 4.1: Material designation and model properties

The mesh is displayed in Fig. 4.1a and it is comprised by 137809 solid elements and 49522 contact elements, making up a total of 187332 elements and 216635 nodes. Table 4.2 gives an overview on the mesh quality and element types, both for contact and solid elements. Additional information about the elements is available in Appendix D.

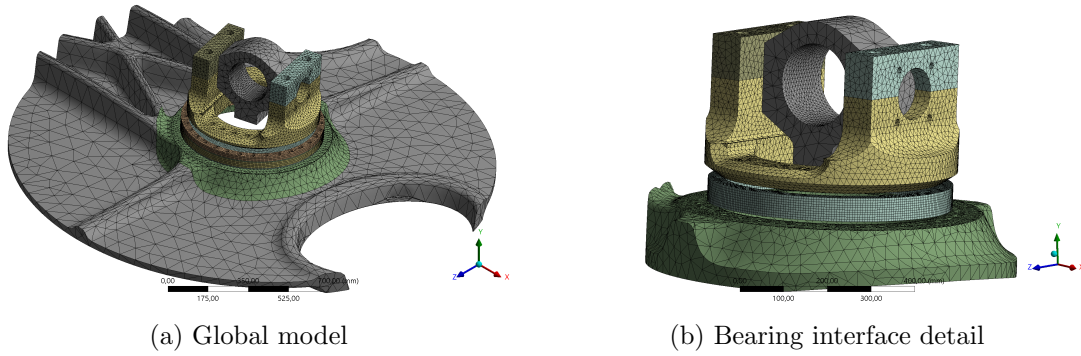


Figure 4.1: Topology optimization model mesh

Mesh quality and attribution

Type	Designation	Number of elements
Solid	SOLID187	100773
Solid	SOLID185	37036
Contact	CONTA174	25729
Contact	TARGE170	23794

Table 4.2: Mesh quality and overview

Since a continuous model is to be achieved, the contacts are always bonded, connecting the interface between the several parts. For a quick understanding, instead of modelling the bolted connections with frictional contacts, the bonded contacts are used for sort of “glueing” the parts together, i.e. linking the interface nodes of the respective parts or bodies. Table 4.3 gives an overview of the set of contacts used.

Contact attribution

Contact	Type	Interface
1	Bonded	Inner ring/ pitch support
2	Bonded	Cylinder connection/ pitch support
3	Bonded	Inner ring/ slew bearing
4	Bonded	Outer ring/ slew bearing
5	Bonded	Hub plate/ outer ring

Table 4.3: Contact overview for the topology optimization model

4.2 Boundary conditions

The boundary conditions (see Fig. 4.2a) are rather simple and straightforward, representing the extreme loading as an input for the optimization process. The model fixes all nodal displacements in the hub plate extreme nodes. It is considered that the spatial location of the nodes is placed sufficiently far away from the force application point, in such a way that the resultant displacements are valid. The cylinder force is applied as a remote force transferred to the cylinder connection through rigid FE connections (see Fig. 4.2b). Although the number of necessary rigid links to ensure valid results was not

assessed, the purpose of the study implies only the load transfer to the cylinder support, hence this aspect is not that critical. The load values are in accordance with Section 3.3.3, comprising two separate load cases:

1. $F=+623$ kN (p623KN)
2. $F=-623$ kN (n623KN)

depending on the direction of the applied load, in the O_z axis of the reference coordinate system (see Fig. 3.9).

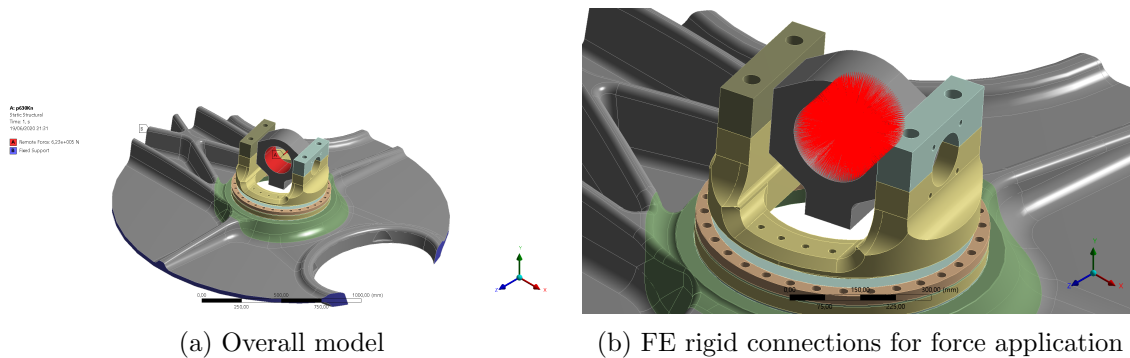


Figure 4.2: Topology optimization model boundary conditions

4.3 Optimization setup

Since the purpose is a fast and efficient approach on the optimal shape for the pitch support, the objective is to minimize compliance. Although this is not the real objective of the study, which is to minimize the mass, it is much more computational efficient to perform a compliance minimization, hence being a fast way to get results on what a performance efficient shape looks like. Moreover, several studies show that the results of topology optimization have better precision in the displacements field rather than the stress values, thus being safer to perform a compliance (stiffness) optimization. Another aspect is the duality of load cases, which can be easily concluded that is characterized by a almost symmetrical problem. For this reason, the optimization will take both load cases in the same weight. Finally, in terms of constraints, several mass restrictions were set, to have a conceptual analysis of what the optimal shape tends to. Also, manufacturing constraints were added, namely the symmetry constraint, supported by the symmetrical characteristic of the problem, based on the coordinate system of Fig. 3.9. Table 4.4 gives an overview of the optimization setup.

4.4 Model simplification

Model simplifications can sometimes result in much faster simulations without significantly damaging the results. Aiming to assess this subject, a simplification was made in the model, in order to widen the results domain, and lay out the computational cost for each simulation.

The simplification was carried out by eliminating the connecting part that transferred the load from the cylinder to the support, thus reducing the number of solid and contact elements in the model. With that said, it is expected to reduce the simulation time.

Optimization setup

Type	Designation	Weight	Constraint
Objective	Compliance (p623KN) - minimization	1	-
Objective	Compliance (n623KN) - minimization	1	-
Constraint	Symmetry	-	O_z
Constraint	Symmetry	-	O_x
Constraint	Mass	-	0.80/ 0.70/ 0.60/ 0.50/ 0.40/ 0.35/ 0.30

Table 4.4: Optimization setup overview

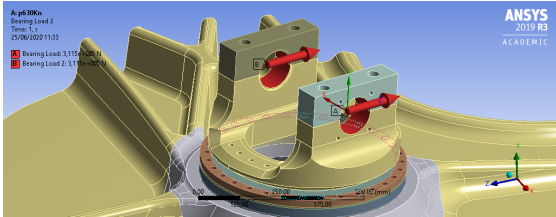
To overcome the load transferring modulation, it can be reasonably concluded that the applied load in each pitch support lug is approximately half of the total load:

$$F_R = \frac{623}{2} = 311.5 \text{ kN}. \quad (4.1)$$

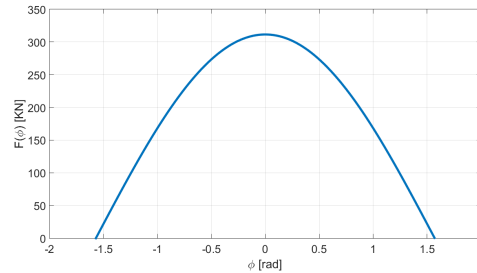
The rotational degree of freedom in the pitch support lug promotes a load distribution similar to a bearing, provided that the transferred moment is negligible. For this reason, a bearing like load distribution in each lug hole (see Fig. 4.3a) was modelled. Considering the lowest degree of inequality, i.e. bearing without clearance, the mathematical expression for the load distribution is

$$F(\phi) = F_R \cdot \cos(\phi) \quad (4.2)$$

where ϕ is the angle between the face normal and the load direction. The load distribution is displayed in Fig. 4.3b. If one takes a closer look at the equilibrium equation understands that this simplification leads to a more severe external load condition. This may result in larger displacements, stresses and compliance.



(a) Load applied in each lug hole



(b) Load distribution in each lug

Figure 4.3: Load application in the simplified model for the topology optimization

Table 4.5 represents the simplified mesh quality and overview, computing a total of 171432 elements and 200403 nodes, representing a nodal reduction of 7.49 percent. Additional information about the elements is available in Appendix D.

4.5 Results

As it would be expected, the topology results will be displayed through a density based shape, where the remaining shape is composed by elements with a density value bigger than a predefined limit, called move limit. For this study, the move limit was set equal to

Mesh quality and attribution

Type	Designation	Number of elements
Solid	SOLID187	91522
Solid	SOLID185	37036
Surface	SURF154	560
Contact	CONTA174	21157
Contact	TARGE170	21157

Table 4.5: Mesh quality and overview

one. Results from both models are displayed later to be compared in terms of performance and accuracy.

4.5.1 Optimal shape

Figures 4.4 and 4.5 represent the topology results for both models. Since the purpose of this optimization is to maximize stiffness for a remaining mass, the voids will appear in the zones that are less solicited, progressing to other regions as the volume restriction gets lower. Bearing this in mind, the results clearly show a large room for optimization in both lugs that connect to the pitch cylinder. Moreover, it is evident the top rounded shape for the optimal design, in both models. Another curious region to optimize is the lower centre region of the lug, which is the second most reduced area in the optimal design. For the remaining regions of the pitch support, the shape optimization is very restricted, due to the bolted connections.

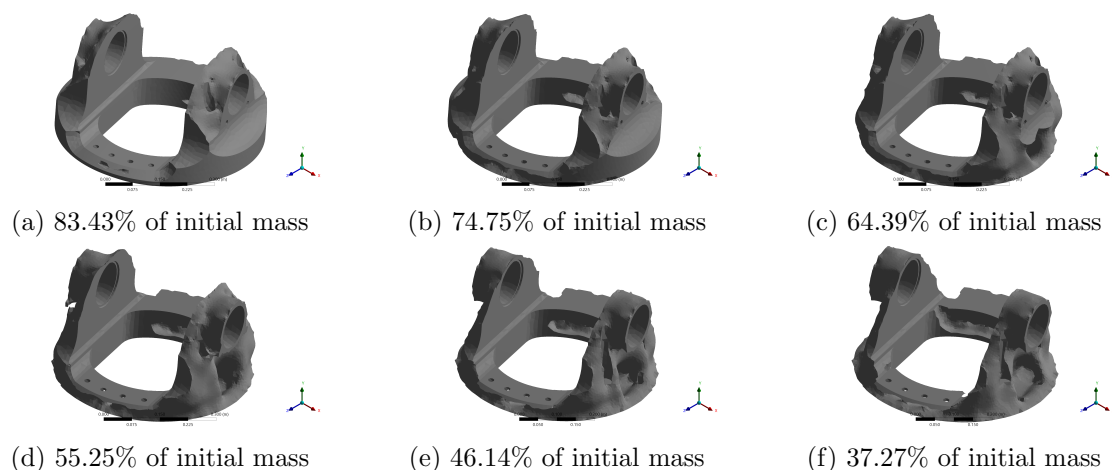


Figure 4.4: Topology results for the initial model

If one looks at the compliance progression with the retained mass, characterized in Fig. 4.6a, easily concludes that the reduction in mass has a toll on the stiffness. But, since the main goal is mass reduction, this characteristic has a negligible relevance for the purpose of the study. Furthermore, the difference between the two curves is explained by the small difference in the displacement and stress fields between the models, supported by the loading method used in the simplified case.

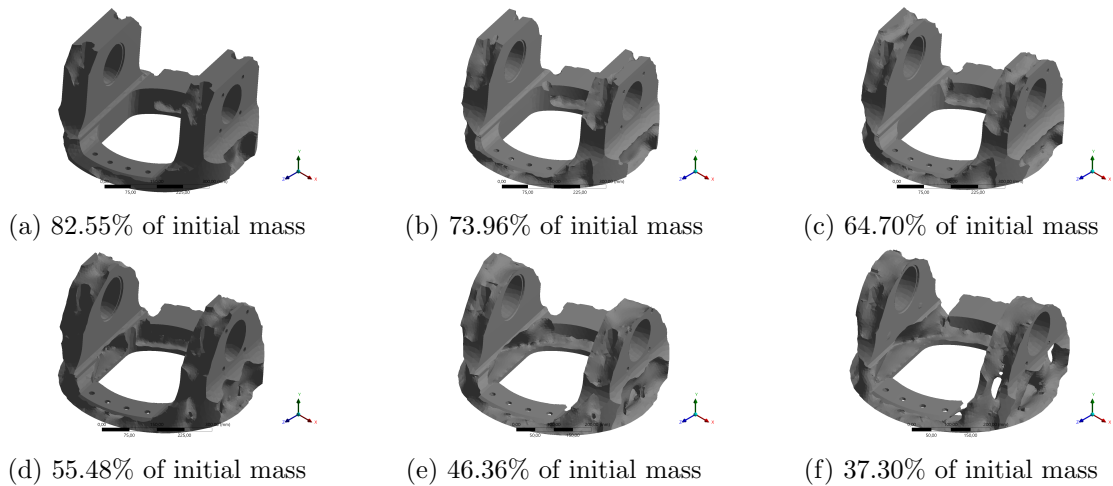
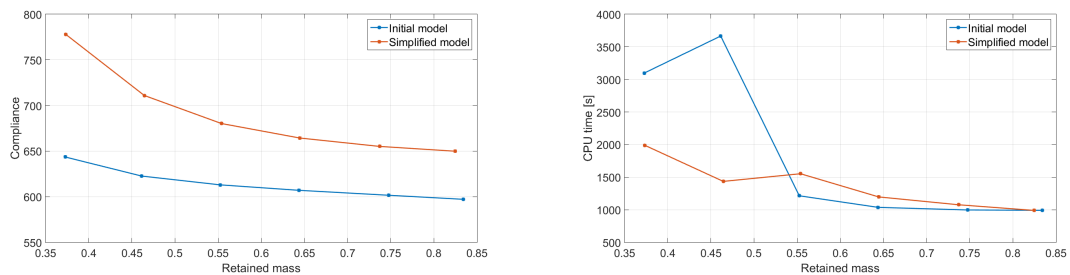


Figure 4.5: Topology results for the simplified model

4.5.2 Performance comparison

The simplification of the model led to a reduction from 138.422 CPU seconds to 107.719 CPU seconds, for a single run of both load cases. Besides, Fig. 4.6b shows the computational cost at each run. For larger values of retained mass, the model simplification is rather ineffective, but as the mass constraint gets lower, the need for more iterations imposes a much higher computational cost in the initial model. To sum up, in total the model simplification comprises a total reduction of 3.06 CPU hours to 2.29 CPU hours, which means a reduction of 25.16 percent.



(a) Retained mass vs. compliance for each optimization run (b) Retained mass vs. CPU time for each optimization run

Figure 4.6: Model comparison for the topology optimization

Parametric optimization

The second phase of the study is the parametric optimization, where the model is focused specifically on the lug region of the pitch support, i.e. a simple and efficient model of the lug's geometry, coupled with static and fatigue analysis to compute the constraint values. As stated earlier, the aim is for making optimization with the help of the genetic algorithm in MATLAB. For this, communication between MATLAB, Ansys and Fatigue Wizard (FatWiz) is to be made. The program itself, and the static and fatigue constraint analysis, will be approached later.

5.1 CAD parametrization

As the name induces, first one needs to define the parameters. For this, and taking into account the results from Section 4.5 (topology optimization), a parametric CAD design (see Fig. 5.1) was developed for the optimization. Bear in mind that the design alterations are directly made in a APDL program, creating a new FEM model each iteration. The outline of the shape is greatly influenced by the topology results, where this “lug like” shape is dominant.

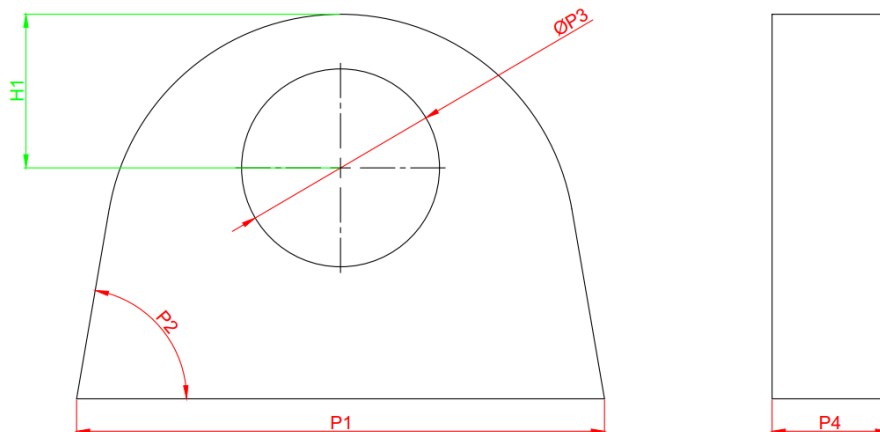


Figure 5.1: Parametric CAD model of the lug

As you can see in Fig. 5.1, there were defined 4 design parameters (highlighted in red), and an extra parameter that is calculated implicitly via the following expression

$$H1 = \frac{P2}{2} + 2.4498 \cdot 10 + 2.6468. \quad (5.1)$$

This parameter considers the necessary space to insert a bolted connection, in this case a M10 bolt. More information on this subject can be found in Appendix F.

For the defined parameters, displayed in Fig. 5.1, lower and upper bounds for the first population were defined in order to control the design domain, hoping for a faster convergence. Note that the algorithm may search values beyond this domain. An overview of the parameter setup is displayed in Table 5.1.

Parameter setup			
Parameter	Name	Lower bound	Upper bound
P1	Width	200 mm	340 mm
P2	Draft	0°	15°
P3	Hole	60 mm	120 mm
P4	Thickness	20 mm	80 mm

Table 5.1: Parameter set-up: lower and upper boundaries of the first population

5.2 Mesh

The FEM analysis is to be made in a 2D model, aiming to improve the computational efficiency. Hence, it was used a mapped mesh (see Fig. 5.2) with 2D quadrilateral elements (PLANE 182). These are first order elements with four nodes, each with two degrees of freedom (translations in the O_x and O_y directions). The mapped mesh is performed so that there are 10 elements in the radial direction from the centre of the hole. Hence, the mesh is always composed by 1200 elements and 1320 nodes.

The preference of first order elements over elements with superior order, such as PLANE 183 elements is justified by the minimization of the computational cost, which is imperative when such analysis is to be performed several hundred times, on average, in each run. Moreover, a brief study on the implications of such choice was made, stating that the result error of the chosen mesh, compared with the superior order elements, is approximately 4 percent, well within a valid range. The first order mesh gains even more strength when one looks at the time cost, which is half of the one from the 8-node elements. Finally, the number of nodes is also a factor since more fatigue calculations are needed in superior order elements. All of the previous aspects combined can significantly increase the simulation time, persuading a mesh simplification with the 4 percent error. The full analysis can be viewed in Appendix G.

5.3 Boundary conditions

Concerning the boundary conditions, all the bottom nodes are fixed (null displacement in all directions), representing the connection with the rest of the system. Regarding the load application, an approximation was modelled with the projection of the total load in each selected node, similar to the case explained in Section 4.4. Basically half of the hole interface region is selected, depending on the direction of the load, and the applied force in each node is proportional to its location, following the expression

$$F_{ef} = F_R \cdot \cos(\phi) = F_R \cdot \frac{x_p}{P3/2} \quad (5.2)$$

where α is the angular location between the node and O_x and x_p is the nodal coordinate in O_x . It is important to notice that the load is directly applied in each node. Therefore, one needs to be model the load respecting the physics of the problem. For this reason, the equilibrium equation is analysed as follows

$$\sum_{i=1}^n F_R \cdot \frac{x_i}{P3/2} = \frac{F_{pitch}}{2} \quad (5.3)$$

where F_{pitch} is the total pitch force, x_i the O_x coordinate of each node, and n the number of nodes in the application region. Restructuring Eq. (5.3), the reference value for the load distribution is

$$F_R = \frac{F_{pitch}}{4} \cdot \frac{P3}{\sum_{i=1}^n x_i}. \quad (5.4)$$

Hence, the load in each nodal point is

$$F_{ef} = \frac{F_{pitch}}{4} \cdot \frac{P3}{\sum_{i=1}^n x_i} \cdot \frac{x_p}{P3/2} \quad (5.5)$$

which gives

$$F_{ef} = \frac{F_{pitch}}{2} \cdot \frac{x_p}{\sum_{i=1}^n x_i}. \quad (5.6)$$

A representation of the boundary conditions in the mesh can be viewed in Fig. 5.2.

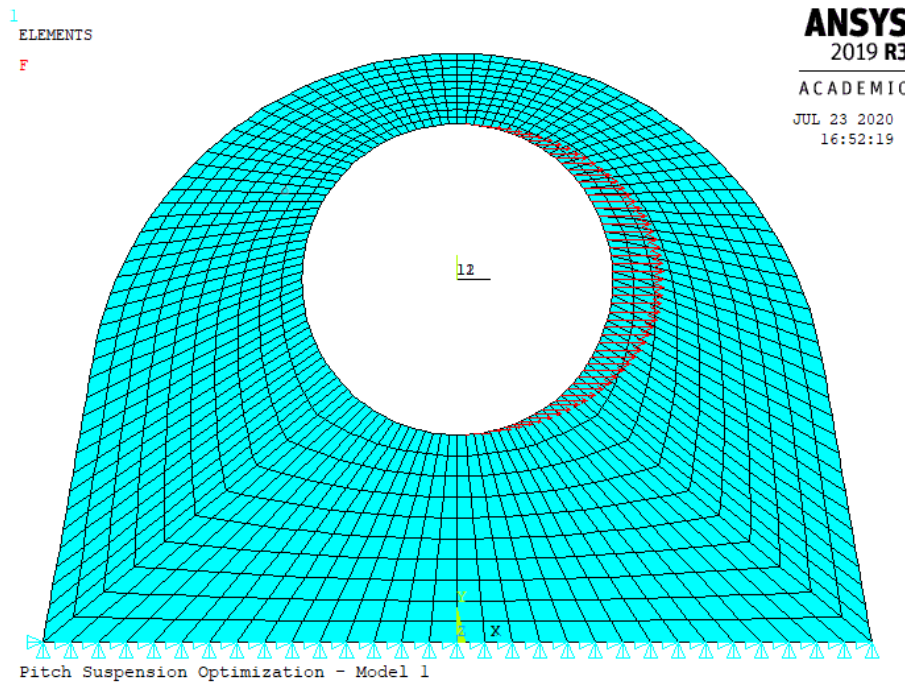


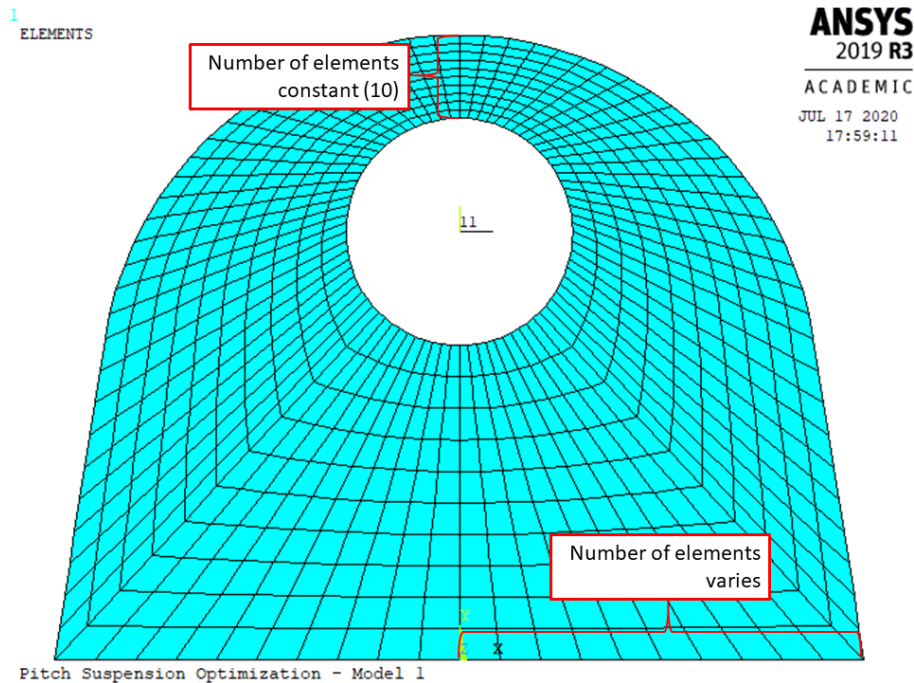
Figure 5.2: Mesh and boundary conditions for the parametric analysis

5.4 Convergence analysis

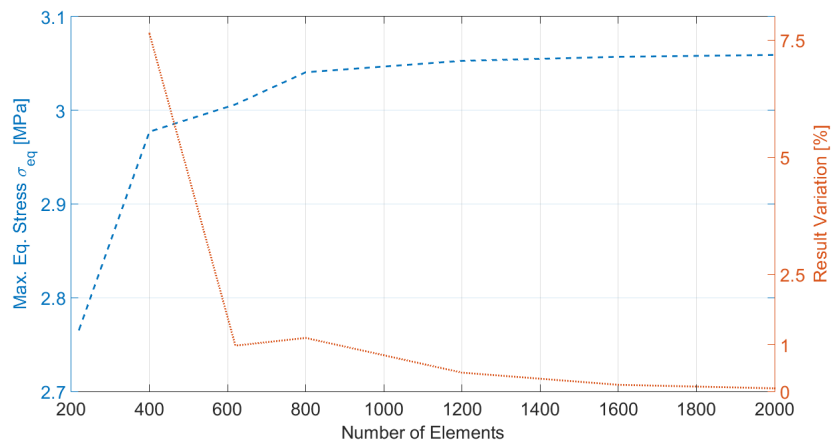
In order to validate the FE model, it was performed a convergence analysis, checking if the solution converges to a specific value as the mesh is refined. The mesh refinement occurs through the hole model and not in a specific region, increasing the number of elements

5. Parametric optimization

along the hole perimeter, but not across the section, where the number of elements remains constant. Check Fig. 5.3a to better understand the layout. Figure 5.3b shows the results for the convergence analysis. It clearly shows a convergence to a solution, with a rapid evolution to an error below 1 percent. This gives confidence to use the model with 1200 elements as its results hold a residual error.



(a) Mesh layout with element division



(b) Maximum stress versus number of elements

Figure 5.3: Convergence analysis overview

5.5 Optimization setup

At this stage, the optimization procedure tackles the main objective head on, aiming to minimize the total mass of the component. This time, the modelled restrictions can be divided into geometrical, to prevent extremely thin solutions, and physical, to represent fatigue life and the ultimate failure load case. The representative layout of the setup is

expressed as

$$\text{Find } P_i \quad i = 1, \dots, 4 \quad (5.7a)$$

$$\text{to minimize } J(\{P\}) = \sum_{e=1}^N \rho \cdot V_e \quad (5.7b)$$

$$\text{subject to } \sigma_{max,extreme} \leq \sigma_y \quad (5.7c)$$

$$SRF_{min} \geq 1 \quad (5.7d)$$

$$P_4/P_3 \geq 0.3 \quad (5.7e)$$

$$L_{member} \geq 10 \text{ mm} \quad (5.7f)$$

where N and V_e are the total number of elements and element volume, respectively, $\sigma_{max,extreme}$ is the maximum value of equivalent von Mises stress in the extreme load case, L_{member} is the member size and SRF_{min} the minimum value of the *safety reserve factor*. The SRF value states of how much safety is related with the loading, i.e. how much could it be increased while ensuring the safe work throughout all life ($D = 1$). Taking into account Fig. 5.4, it can be concluded that

$$D = \frac{A}{A+B} \quad (5.8a)$$

$$SRF = \frac{a}{a+b} \quad (5.8b)$$

and the relation between the SRF and the total damage is

$$SRF = D^{-1/k} \quad (5.9)$$

where k is the respective slope from the *S-N curve*. The reference slope value could be approximated by the mean value given by

$$k = \frac{k_1 + k_2}{2} \quad (5.10)$$

or by a weighted estimate regarding the number of times each slope was used to estimate the damage.

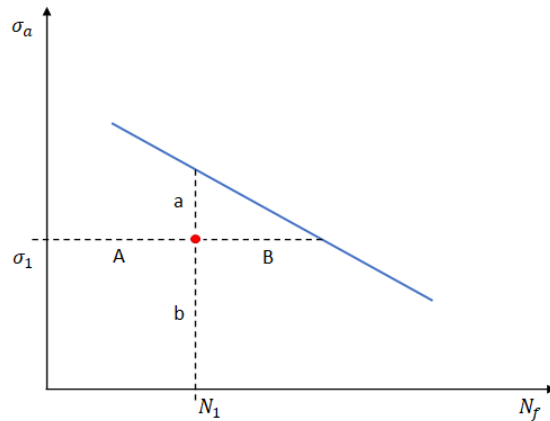


Figure 5.4: Relation between the damage and SRF

Also, since the lug hole is a contact surface, the present model does not properly represent this phenomenon. Hence, the region of analysis excludes the surface of the hole, i.e. the nodes from hole region.

For this purpose, it was developed an algorithm in MATLAB, using its optimization toolbox, to serve as the mainframe for the whole optimization procedure. The optimization algorithm used is the GA briefly explained in Section 2.3.4, which generates the sets of parameters (individuals) and tests them. The algorithm integrates Ansys Mechanical APDL 2019 in batch mode for the FEM analysis and FatWiz for the fatigue calculations. Both the layout of the algorithm and the Fatigue Wizard will be explained later on.

5.5.1 Algorithm

The proposed algorithm (see Fig. 5.5) has a workflow that allows the user to choose weather optimize the geometry regarding an ultimate failure load case condition or fatigue life, and both conditions. In Fig. 5.5, the option for both restrictions is not displayed, but the workflow joins both ultimate failure and fatigue operations, based on one set of parameters (provided by *parameters.inp*) and outputs the maximum stress (provided by *Stress.txt*), the minimum SRF value (provided by *rstSRF.txt*) and the weight of the geometry (provided by *Weigth.txt*). For this option, the optimal parameters represent a geometry that sustains both the ultimate failure and fatigue conditions.

The communication between software is performed trough the *.bat* files, calling each program which than outputs the important values through *.txt* files. This workflow makes possible for MATLAB to control the two programs (Ansys and FatWiz) and recover the important values for the optimization.

Further information on the program is presented in the Appendix H.

GA Algorithm

In order to perform the parameter optimization, a pre-defined genetic algorithm from MATLAB is used. This optimizer aims to minimize a fitness function that is dependent on the parameter set. Therefore, fitness value is the weight of the geometry. But to use the algorithm, the user needs to define its options regarding population size, crossover function, elite individuals, etc, which influences the behaviour of the simulation. The options that are reviewed are:

- Initial population range (*PopInitRange*) - defines the range of all parameters in the initial population via a 2-m matrix, where the first and second lines give the lower and upper bounds, respectively, and m is the number of individual parameters
- Maximum number of generations (*Generations*) - maximum number of generations in the simulation
- Population size (*PopulationSize*) - the number of individuals (sets of parameters) in each generation
- Crossover fraction (*CrossoverFraction*) - fraction of childe that are produced due to crossover of two parent individuals from the previous generation
- Mutation function (*MutationFcn*) - defines not only the way that childe are produced via mutation, but also the fraction of the population
- Convergence tolerance (*TolFun*) - defines the critical value of which if the difference between each generation's best fitness value over a defined number of generations is below, the optimal solution is reached

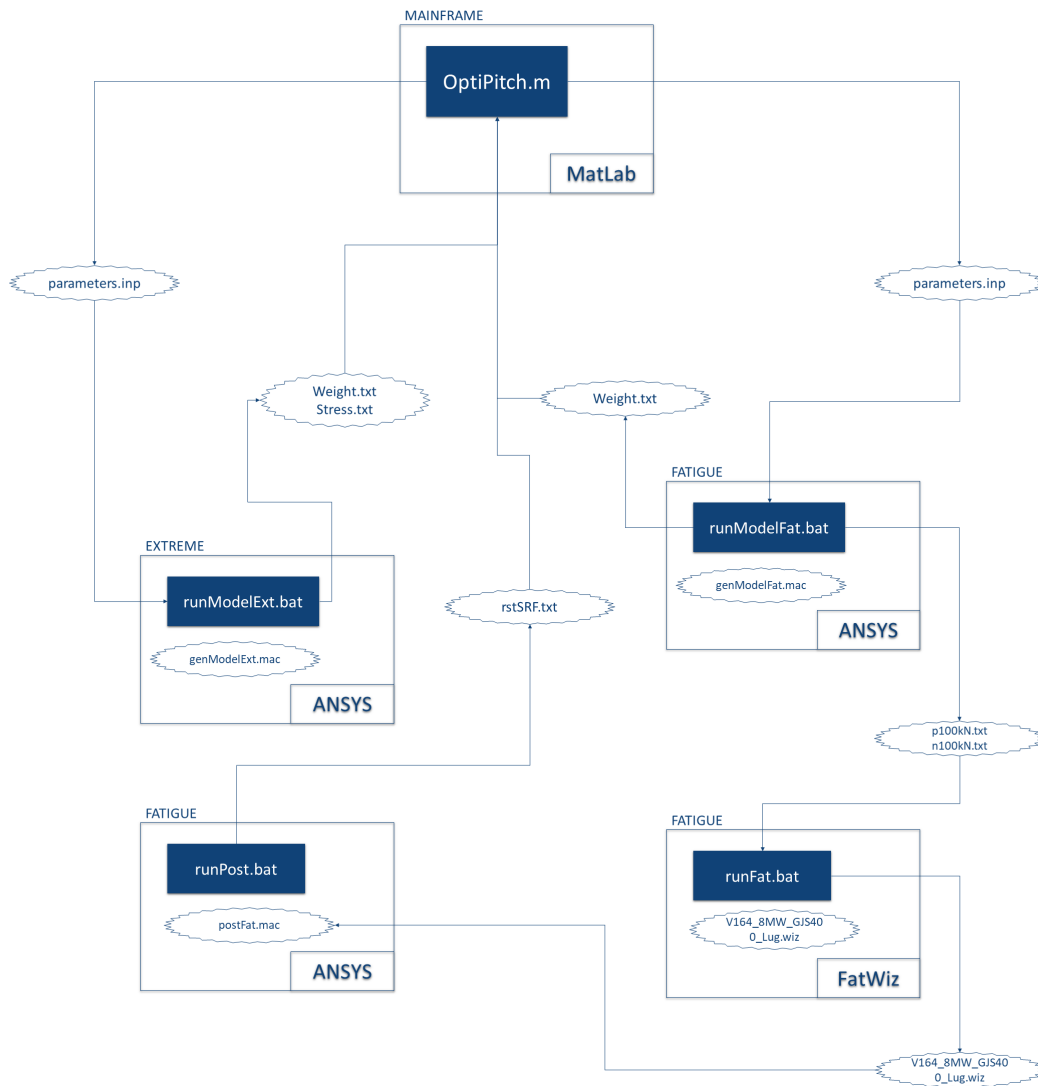


Figure 5.5: Parametric optimization program overview

- Convergence interval (*StallGenLimit*) - defines the number of generation for the convergence analysis
- Population type (*PopulationType*) - sets the type of values that the parameters define, either, vectors, double values, etc
- Selection function (*SelectionFcn*) - defines the way that the best parent individuals are defined
- Number of elite individuals (*EliteCount*) - defines how many number of best individuals remain for the next generation

Several sets of options were tested in order to find a solution that was valid for convergence. Table 5.2 displays the selected options for this case.

Option	Value
<i>PopInitRange</i>	$\begin{bmatrix} 220 & 0 & 40 & 30 \\ 340 & 15 & 120 & 80 \end{bmatrix}$
<i>Generations</i>	100
<i>PopulationSize</i>	40
<i>CrossoverFraction</i>	0.7
<i>MutationFcn</i>	Uniform mutation with 0.1 fraction
<i>TolFcn</i>	0.1
<i>StallGenLimit</i>	20
<i>PopulationType</i>	Vector of double values
<i>SelectionFcn</i>	Roulette
<i>EliteCount</i>	2

Table 5.2: Genetic algorithm options set

5.5.2 Fatigue Wizard

When performing any fatigue calculations, an internal Vestas software called Fatigue Wizard (FatWiz) is used, that outputs the SRF values for the specified domain of analysis. The software takes as input a specific stress state for the respective load condition and the time history of its solicitation. With these inputs, it converts the stress-load distribution into stress-time distribution. After this, for each time history, performs the cycle counting and outputs its damage. Combining all load cases, recurring to an additive process, it computes the total damage/SRF for each node. A graphical overview of the workflow is displayed in Fig. 5.6.

Stress-time interpolation

An important step is the stress-time conversion and it is done in a rather simple process. The stress computation over time is made by a linear interpolation (see Fig. 5.7a) with the expression

$$\sigma_t = F_t \cdot \tan \alpha \quad (5.11)$$

with

$$\tan \alpha = \frac{\sigma_{ref}}{F_{ref}} \quad (5.12)$$

where σ_t is the stress for a specific load F_t and σ_{ref} and F_{ref} are the stress and load from the reference load case. One can improve the interpolation by defining two curves, regarding two opposite directions of loading (see Fig. 5.7b). This means the input should be from two separate load cases and now the computation has two values of *alpha* regarding the load condition. For more complex problems one can add more load cases to approximate a non-linear stress-force interpolation curve.

Cycle counting

After computing the stress spectrum for each time history, the algorithm proceeds on counting the different cycles, with respective stress amplitude σ_a and mean stress σ_m . Fatigue wizard uses the rainflow cycle counting method in order to count each cycle, but provides certain filters to optimize the simulation. Basically the main goal is to reduce the stress time history, and the options are:

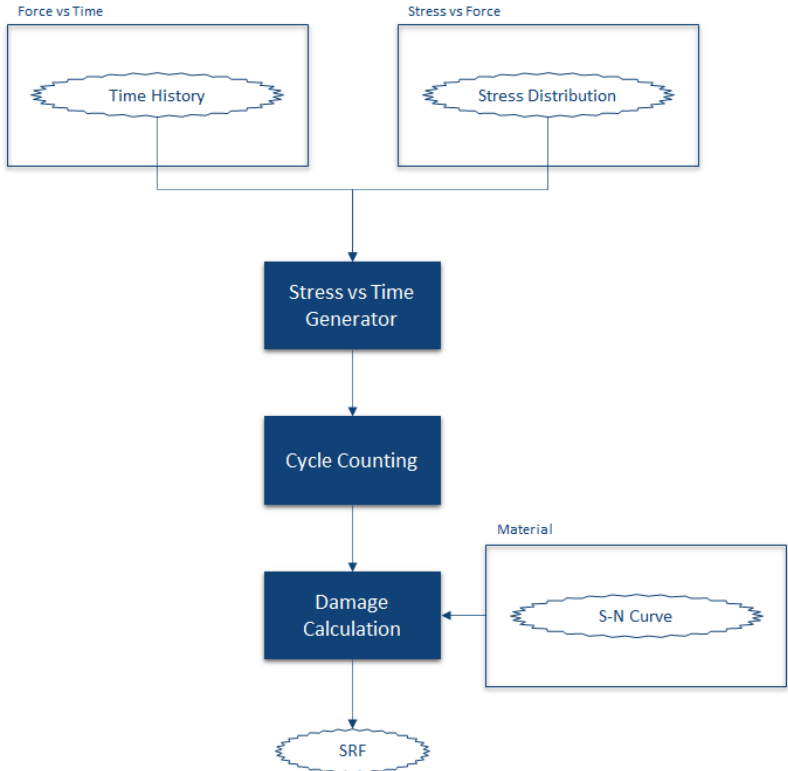


Figure 5.6: Fatigue wizard workflow

- None - there is no reduction and all stress time history is considered
- Simple - only a percentage of the stress time history is considered depending on the specified value
- Peak valley - the time history is reduced in the sense that the “zigs-zags” are filtered out, depending on the specified filter size. For larger sizes, more data is removed
- Adaptive - the program completes 3 simulation runs and performs a peak valley filtration with more precise filter sizes for more critical SRF hotspots, based on Table 5.3

Accuracy level	All hotspots	SRF < 1.5	SRF < 1.1
1	1.80	0.60	0.20
2	1.20	0.42	0.14
3	0.72	0.24	0.08

Table 5.3: Filter size for the adaptive approach

Stress criteria

After having the time history for all stress components, the program has to calculate the equivalent fatigue stress for cycle counting, and this is where the stress criteria comes

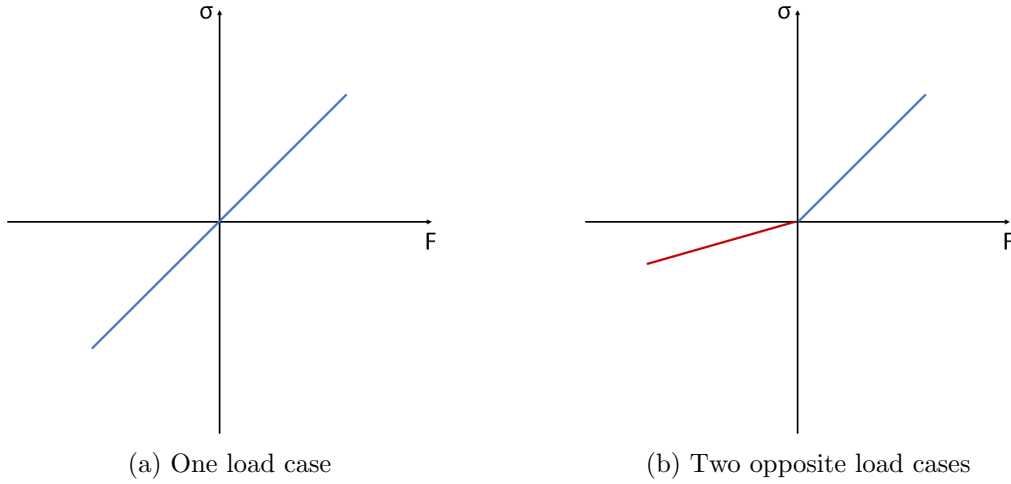


Figure 5.7: Stress interpolation scheme

into play. It defines how the reference value for damage extrapolation is calculated, thus being decisive in the hole process.

FatWiz provides five different options:

- Normal stress σ_{xx} - only σ_{xx} is used
- Normal stress σ_{xx} (critical plane) - only σ_{xx} is used, but the maximum evaluated value in several planes rotated in the O_{zz} plane. The number of planes is defined by the user
- Signed von Mises - the von Mises stress σ_{VM} is used as the reference stress and signed according to the σ_{xx} component
- Signed von Mises (maximum principal) - von Mises stress σ_{VM} is used but signed by the analysis of the principal stresses. If $\sigma_3 > \sigma_1$ (compression) a negative sign is imposed in the von Mises stress reference value
- Maximum principal - the numerical largest value of all principal stresses is used

Mean stress

In order to compute with states with $\sigma_m \neq 0$, a mean stress correction can be used. The available methods are:

- None - no mean stress correction
- Linear - a linear extrapolation is used of

$$\sigma_{a,eq} = \sigma_a - 2\gamma\sigma_m \quad (5.13)$$

where γ is a factor defined by the user

- Bi-linear - based on the linear approach, but for states with $R < -1 \wedge R > 0$ a factor of $\gamma/2$ is used
- Goodman - an approach based on Eq. 2.31, which is also linear but relates with the material's ultimate stress σ_u

$$\sigma_{a,eq} = \sigma_a \left[1 - \frac{\sigma_m}{\sigma_u} \right] \quad (5.14)$$

Damage calculation

The final stage is to compute the total damage for each hotspot, i.e. the nodes of the analysis domain. This step is done based on the Miner's rule of Eq. 2.39 which assumes a linear evolution of the fatigue damage across the component's life, widely used in fatigue analysis.

Simulation setup

After weighting all possibilities for the fatigue analysis, the options set is displayed in Table 5.4.

Option	Preference	Value
Control	Adaptive	3
Stress criteria	Normal stress (critical plane)	24
Mean stress correction	Linear	0.25

Table 5.4: Fatigue Wizard options set

5.6 Results

Several runs were made, for either the ultimate failure condition, fatigue life and both, although, for this specific case, both conditions must be taken into account. This way, is possible to compare the conditions and understand of what is the critical one in this case, among other relevant aspects such as the calculation time. An additional study on the possibility of an equivalent fatigue stress, called meta stress σ_{meta} , was made, in order to understand the viability of performing a fast and efficient fatigue analysis.

5.6.1 Ultimate failure

The simulation under the ultimate failure condition only prospects a valid design for the extreme loading condition (mentioned in Section 3.3.3). This means the results completely ignore the fatigue damage.

Table 5.5 shows the results for the ultimate failure condition case run. The optimal parameter set (see Table 5.5a) gives a total lug mass of 13.5740 kg, representing a total component mass of 119.67 kg. When compared to the current design, it holds a weight reduction of 22.96 percent. In terms of calculation time, the total elapsed time is approximately 53 min and, in terms of CPU time, took about 2 CPUmin. The optimal design can be viewed in Fig. 5.10a.

Finally, the stress distribution of the optimal design can be viewed in Fig. 5.8a. The maximum stress is equal to the critical value, which means that the design is fully optimized for the ultimate failure loading condition.

5.6.2 Fatigue condition

Contrary to the previous Section, the results for a fatigue condition run ignore the extreme loading case and focus only on fatigue life.

Table 5.6 shows an overview of the results for the fatigue condition case run. The optimal parameter set (see Table 5.6a) is characterized by a lug mass of 23.5361 kg, resulting

Optimal parameters			
Width (P1)	Draft (P2)	Hole (P3)	Thickness (P4)
228.3407 mm	5.6952 deg	41.1472 mm	55.8352 mm

(a) Optimal parameter set

Run details	
Total elapsed time [s]	Total CPU time [CPUs]
3166.6010	117.2031

(b) Run details

Table 5.5: Result overview for the ultimate failure condition parametric optimization

in a total component mass of 143.28 kg. This represents a mass reduction of 7.76 percent. By using the fatigue software to compute the life damage, the calculation time significantly rises to a total elapsed time of approximately 2409 min (40 hours) and, in terms of CPU time, took about 11 CPUmin. The optimal design can be viewed in Fig. 5.10b.

Optimal parameters			
Width (P1)	Draft (P2)	Hole (P3)	Thickness (P4)
294.1326 mm	11.4006 deg	43.0395 mm	78.6579 mm

(a) Optimal parameter set

Run details	
Total elapsed time [s]	Total CPU time [CPUs]
144545.4869	660.0469

(b) Run details

Table 5.6: Result overview for the fatigue condition parametric optimization

Figure 5.8b displays the fatigue damage distribution for the optimal design. It can be seen that there are some regions that fall short in terms of fatigue life. However, this regions are not to be accounted as valid results due to the aspects earlier mentioned, related with the contact areas. With that said, one can conclude that the optimal design withstands the fatigue condition.

5.6.3 Ultimate failure and fatigue conditions

In terms of final design, these are the results to be analysed, since the model needs to fulfil both conditions at the same time. Before jumping into any conclusions, one needs to be aware if the results are in line with the previous ones, in terms of the critical constraint, i.e. understanding what is the most strict constraint, which will be the one to control the optimization.

Table 5.7 displays an summary of the results for the ultimate failure and fatigue parametric optimization. The optimal parameter set (see in Table 5.7a) conveys a lug mass of 23.6021 kg which leads to a total component mass of 142.54 kg. This represents a mass reduction of 8.24 percent. The total running times were around the same as the fatigue parametric optimization, with a total elapsed time of approximately 2590 min (43 hours)

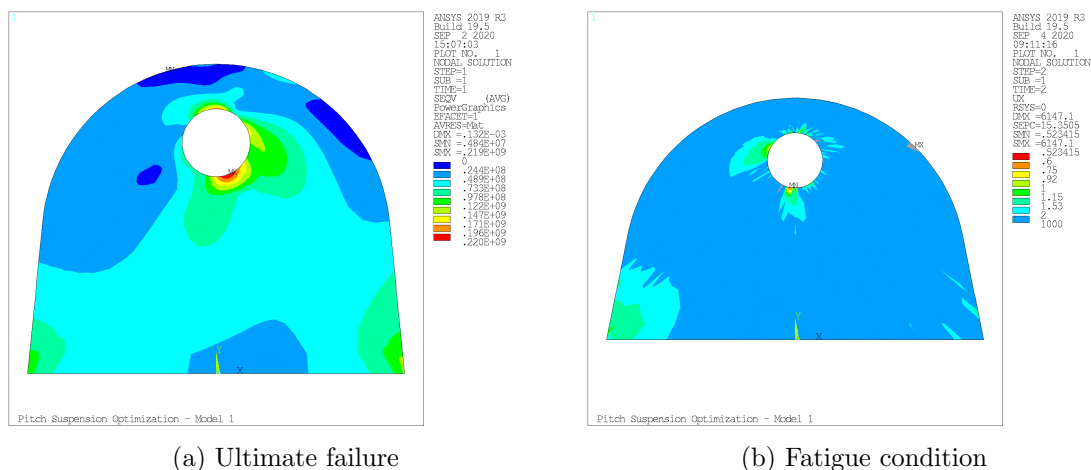


Figure 5.8: Results for the optimal design regarding the ultimate failure and fatigue conditions separate

and 12.6 CPUmin. The optimal design is can be viewed in Fig. 5.10c.

Optimal parameters			
Width (P1)	Draft (P2)	Hole (P3)	Thickness (P4)
292.7120 mm	11.1583 deg	50.3266 mm	78.5258 mm

(a) Optimal parameter set

Run details	
Total elapsed time [s]	Total CPU time [CPUs]
155371.3232	757.9688

(b) Run details

Table 5.7: Result overview for the ultimate failure and fatigue conditions parametric optimization

Figures 5.9a and 5.9b show the results for the optimal design in terms of extreme loading and fatigue life. When it comes to the ultimate failure condition (see Fig. 5.9a), the maximum stress value is 146 MPa, which are significantly lower than the imposed stress limit. In terms of fatigue life (see Fig. 5.9b), again the values might trick the reader in thinking that the design falls short. But, bear in mind that the hole region is out of scope for accuracy reasons (contact region).

5.6.4 Economic outlook

It is also important to understand the economic impact that the proposed design conveys. In this Section, a brief estimate is to be made on the production cost and revenue impact that all three designs represent. Table 5.8 displays the production summary for the intervening materials. Note that the support plate's cost is set aside from EN-GJS-400-18U-LT casting cost, because of the plate's significantly higher complexity in terms of geometry and manufacturing process, since this value reflects the final cost (with machining). Therefore, it would not be accurate to assume the same cost for the new additional connectors in casting. The price for the cylinder support also reflects the final

5. Parametric optimization

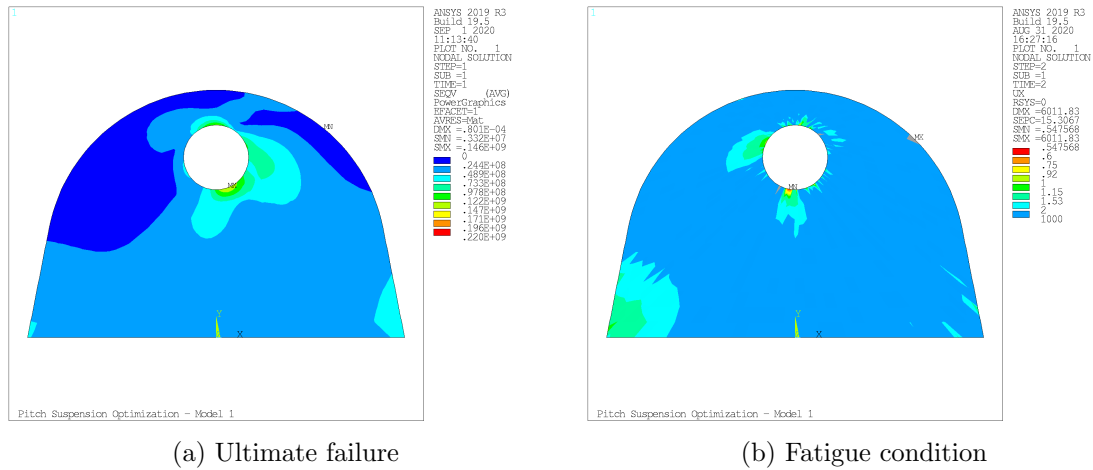


Figure 5.9: Results for the optimal design regarding the ultimate failure and fatigue conditions

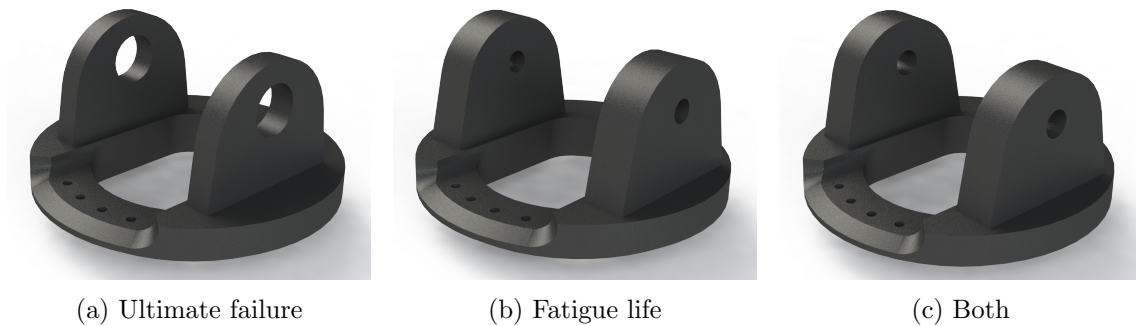


Figure 5.10: Design results for the parametric optimization

value (with machining).

Production summary

Component	Mass [kg]	Production [EUR kg ⁻¹]	Cost	Number of parts [units year ⁻¹]
Support plate	81.03	6.17		864
Cylinder support	37.00	2.73		70
EN-GJS-400-18U-LT Casting	-	2.18		-

Table 5.8: Production summary of the intervening parts

First, a major assumption controls the calculation:

- The production cost of a certain component is linearly dependent on its weight

Logically, this is not exactly true, since there are other factors such as complexity. However, it is a solid assumption for a general estimate. Therefore, since the current design has 3 components assembled together (2 of which are the identical), the total component cost $Cost_{init.design}$ is

$$Cost_{init.design} = P_{sup.plate} \cdot m_{sup.plate} + 2 \cdot P_{cyl.in.support} \cdot m_{cyl.in.support} \quad (5.15)$$

where $P_{sup.plate}$ and $m_{sup.plate}$ are the production cost and component mass, respectively, for the support plate, and $P_{cylin.support}$ and $m_{cylin.support}$ are the production cost and component mass, respectively, for the cylinder support.

For the proposed designs, the production cost will be assumed as equal to the support plate, since it is made by casting of the same material. Since the designs are characterized by a single component, the production cost $Cost_{design}$ of each design is

$$Cost_{design} = P_{sup.plate} \cdot m_{sup.plate} + 2 \cdot P_{casting,gjs400} \cdot m_{design} \quad (5.16)$$

where $P_{casting,gjs400}$ and m_{design} are the casting production cost and the total mass for the optimal design, respectively.

Finally, the total cost of manufacture per year can be calculated by multiplying the production cost of each component with the number of produced parts in a year. This raises the problem related with the discrepancy between the number of manufactured parts of both components (support plate and cylinder supports), which probably relates with the fact the support plate is used in different set-ups with other cylinder supports, depending on the turbine model. That said, the data to be taken into account is the numbers from the cylinder supports. Since there are two per assembly, the reference number is 35.

Taking into account all that as been mentioned in the previous paragraphs, the production cost of each design was calculated and it is summarized in Table 5.9. The proposed design is estimated to cost around EUR 634.09 per unit (9.68% price reduction), which results in a EUR 2,377.49 additional revenue per year.

Economic outlook

Model	Cost [EUR units ⁻¹]	Cost reduction [%]	Cost [EUR year ⁻¹]	Savings [EUR year ⁻¹]
Current	702.02	-	24,570.70	-
Ultimate	584.24	16.78	20,448.23	4,122.47
Fatigue	635.71	9.45	22,249.68	2,321.03
Both	634.09	9.68	22,193.21	2,377.49

Table 5.9: Economic outlook summary

5.6.5 Analysis comparison

In this Section, a analysis comparison is to be made, hoping to validate the results and understand the behaviour of the optimization. Also, the reader can get a more general result summary.

Looking into the running times (see Fig. 5.11), it can be said that the fatigue analysis is the most time consuming and computational costly. Comparing both conditions separately (ultimate and fatigue), the static analysis takes up 1.54 and 38.47 percent of the full analysis, in terms of total elapsed time and CPU time, respectively. Hence, the run with both restrictions active takes approximately the same time as the run with the fatigue restriction only. Having that said, it can be concluded that the fatigue analysis dominates the computational cost of the process. So if one wants to improve this aspect, the main focus should be optimizing the fatigue analysis, e.g. reduce the analysis domain (focus on the critical area).

The most significant conclusion to be taken from the performance results, summarized in Table 5.10, is that the optimal design (ultimate and fatigue restrictions) represents a

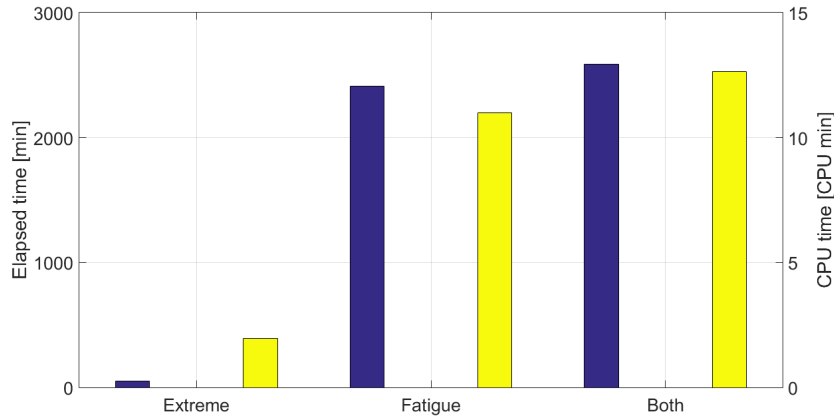


Figure 5.11: Overview on the analysis running times

EUR 2,377.49 extra revenue per year, allied to a 8.24 percent mass reduction. Another important aspect is the dominant restriction. From the result comparison, it can be readily concluded that fatigue life is the critical restriction. If one were to only look at the ultimate failure loading, the optimizer would have more freedom, hence the lighter solution. With that said, the fatigue analysis is the dominant factor either in terms of running times or optimization restrictions, therefore, being the global dominant case.

Performance summary

Model	Mass [kg]	Mass reduction [%]	Cost [EUR units ⁻¹]	Cost [EUR year ⁻¹]	Savings [EUR year ⁻¹]
Current	155.34	-	702.02	24,570.70	-
Ultimate	119.67	22.96	584.24	20,448.23	4,122.47
Fatigue	143.28	7.76	635.71	22,249.68	2,321.03
Both	142.54	8.24	634.09	22,193.21	2,377.49

Table 5.10: Result performance summary

5.6.6 Equivalent fatigue stress condition

As mentioned earlier, a side analysis was made in order to assess the viability of a simplified fatigue analysis. This is rather important because it can save a lot of computational cost, since instead of performing a fatigue analysis for the time history of every geometry, one can extrapolate an equivalent maximum allowed stress that needs to be respected by all the analysis domain, when performing the static analysis.

Note that this starts with the assumption that the worse damage happens at the node with the maximum installed von Mises stress, which can be a target of criticism at first, but for symmetrical examples such as this one and where the critical damage point matches with the maximum stress, point, this is a valid assumption. Hence, the equivalent fatigue stress σ_{meta} is calculated by

$$\sigma_{meta} = SRF \cdot \sigma_{VM,max} \quad (5.17)$$

where SRF is the critical SRF value and $\sigma_{VM,max}$ is the maximum equivalent von Mises stress. Note that, since the geometry is symmetrical, for symmetric load cases, the max-

imum stress is the same for both. Therefore by, computing the σ_{meta} for every iteration, one get an overview on the effects of the geometry on this fictional value, and conclude about this simplified procedure.

The evolution of the σ_{meta} values is displayed in Fig. 5.12a. The values stay within a rather small range of values (42.4847 MPa to 66.9491 MPa) with a mean value of 60.5217 MPa. The frequency of results is displayed in the histogram of Fig. 5.12b. It can be seen that the σ_{meta} distribution is not normal and a large portion of values are from the 60 MPa and 65 MPa (approximately 90%).

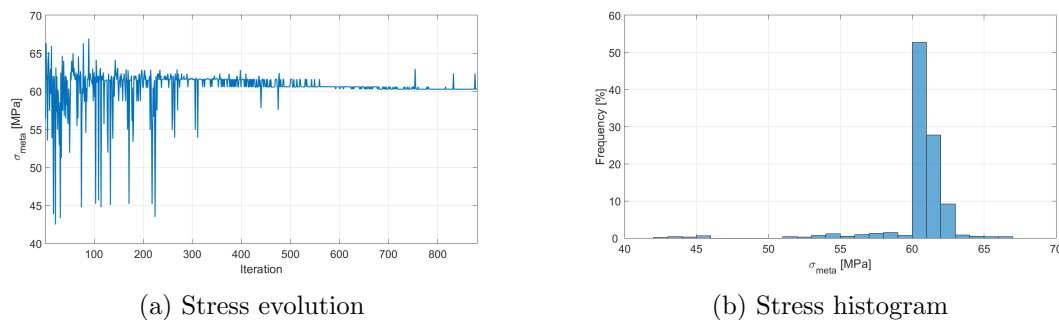


Figure 5.12: Equivalent fatigue stress results

Although this might lead to some misguided conclusion of a certain constant behaviour of the equivalent fatigue stress, one needs to understand the context of the results. In this run, as the solution converges, the σ_{meta} converges to a certain value, hence the constant behaviour at the final iterations. But the purpose of the study was to unveil the independence of the σ_{meta} with the geometry, which does not exist, when the earlier iterations are looked, where a large variation is displayed throughout the simulation, accompanied by a large variation of the parameters set. For this reason, the equivalent fatigue stress approach is not a valid simplification and would convey large deviations from the real results.

Fatigue benchmark

As an addition to this project, it was proposed to take a closer look towards the fatigue models currently used at Vestas, comparing them to other common multiaxial damage models. The goal is to achieve a better understanding of the current method positioning its results with validated fatigue models, and widen the knowledge in terms of multiaxial fatigue methods. For this purpose, specific programs were developed in MATLAB to run the calculations.

The model comparison is to be made using a reference time history, in this case the one displayed in Fig. 3.12 from Chapter 3, and a reference stress spectrum. In order to calculate this stress spectrum, it was used the same method as FatWiz to extrapolate the values from the force time history. With this, an exact match of input is achieved and a better model comparison is in order. Finally, the two reference load cases (positive and negative) were generated via the reference FEM model with the parameters displayed in Table 6.1.

Reference parameters			
Width (P1)	Draft (P2)	Hole (P3)	Thickness (P4)
320 mm	10°	120 mm	80 mm

Table 6.1: Parameter set for the reference model used in the fatigue benchmark

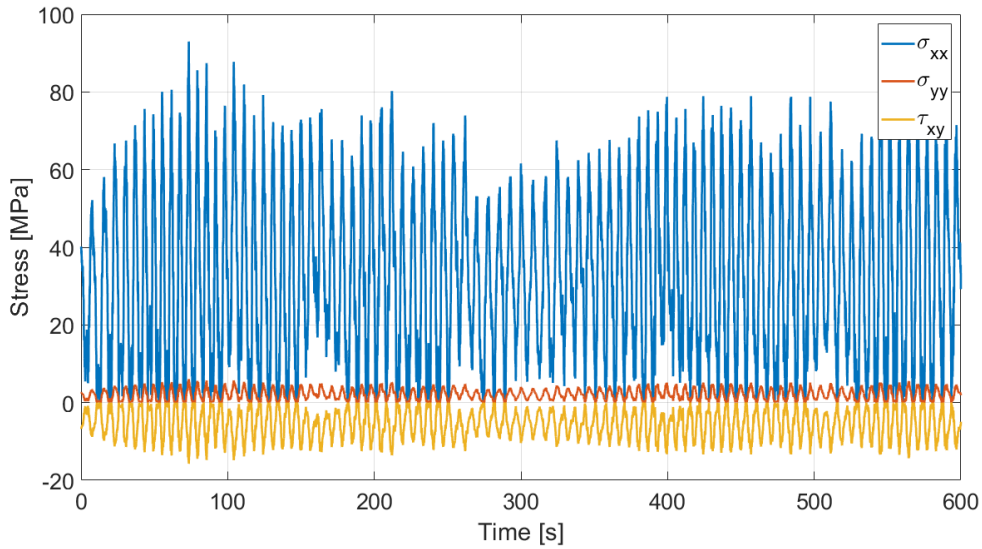
With the help of MATLAB, a bi-linear extrapolation (code in Section J.1) was made to compute the stress time history, which is displayed in Fig. 6.1a. Since one is dealing with a plane stress state, only three out of the six stress components are not null. Due to the bi-linear stress extrapolation, this case deals with proportional load cases. Also, in Fig. 6.1b are displayed the principal stresses. Again, as this is a plane stress state, one of the principal stress components is null, being either σ_2 or σ_3 (dependent on the lowest value being negative or not). The principal stress spectrum is dominated by σ_1 . Looking at Mohr's circle, for a plane stress state, the principal stresses are calculated recurring to the expression

$$\sigma_{1,2,3} = \frac{\sigma_{xx} + \sigma_{yy}}{2} \pm \sqrt{\left(\frac{\sigma_{xx} - \sigma_{yy}}{2}\right)^2 + \tau_{xy}^2}. \quad (6.1)$$

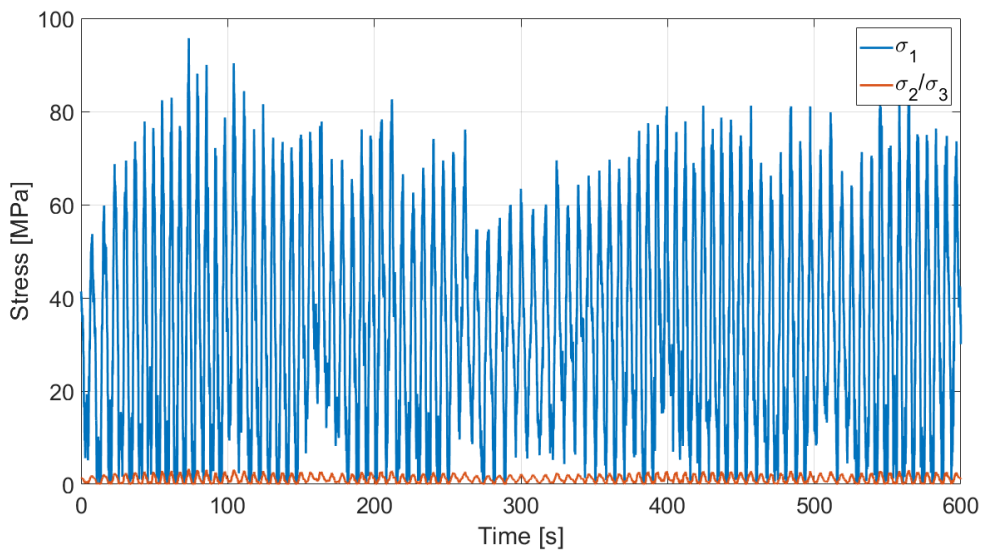
Taking into account Eq. (6.1) and Fig. 6.1b, the following principal stress components relate each other according to

$$\frac{\sigma_{xx} + \sigma_{yy}}{2} \approx \sqrt{\left(\frac{\sigma_{xx} - \sigma_{yy}}{2}\right)^2 + \tau_{xy}^2}. \quad (6.2)$$

Note that this just means that, once again, the load case is proportional and the stress components have a steady fixed relationship, rather than a uniaxial stress state.



(a) Component stresses



(b) Principal stresses

Figure 6.1: Stress spectrum for the fatigue benchmark

6.1 Material properties

The reference material is also the EN-GJS-400-18U-LT cast iron. For this study two different *S-N curves* are needed:

1. Pure tension (tensile stress)
2. Pure torsion (shear stress)

The tension S - N curve was already calculated and is displayed in Fig. 3.6 from Chapter 3.

In terms of torsion fatigue data, the work done by Flass et al. [131] is to be taken into account. Note that the available information is in term of loading rather than stress. So, the conversion was made according to

$$\tau = \frac{M_n \cdot R}{J} \cdot K_{t,torsion} \quad (6.3)$$

with

$$J = \frac{\pi}{2} \cdot (R_{max})^4 \quad (6.4)$$

where M_n is the applied moment, R is the radius of the location of the shear stress whereas R_{max} is the section radius and $K_{t,torsion}$ is the stress concentration factor (SCF) for the torsion load at the critical location.

After the computation with the same correlation factors as in the Appendix C, since is the same component, the pure torsion S - N curve is displayed in Fig. 6.2. Table 6.2 represents an overview of the fatigue data for both cases (pure tension and torsion). Another possible method for estimating the fatigue curves, when no fatigue data is available, is displayed in Appendix I.

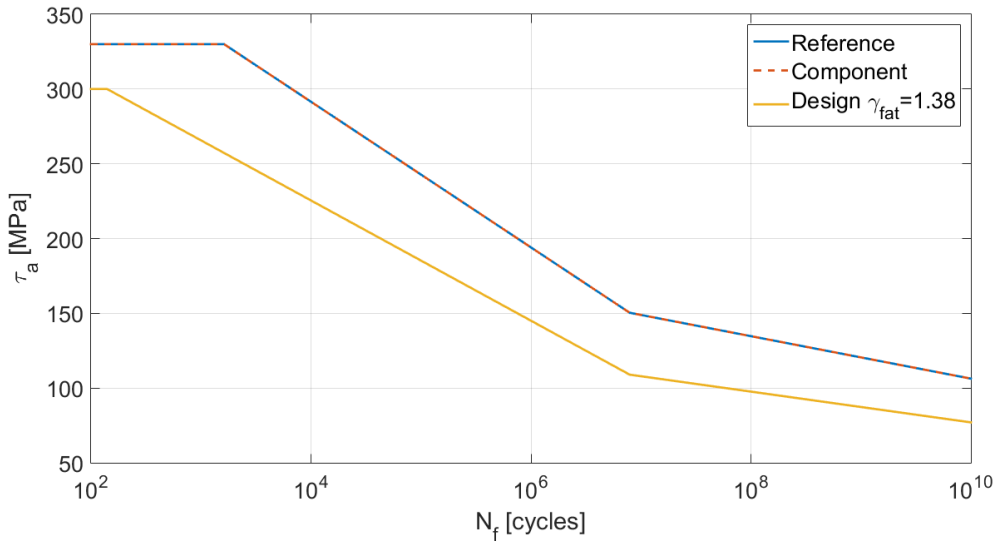


Figure 6.2: Pure torsion S - N curve

Fatigue data					
Type	σ_f [MPa]	τ_f [MPa]	N_f	k_1	k_2
Tension	246	-	2.0E+06	6.9	12.8
Torsion	-	150	7.9E+06	10.8	20.6

Table 6.2: Fatigue data overview

The Findley and Mataka methods require a specific material parameter κ , which relates a pure tensile with a pure torsion state, to be referred again later. In order to define this

parameter, a combination of the two S - N curves is to be made, recurring to the expression

$$\kappa(N_f) = 2 \frac{\tau_a(N_f)}{\sigma_a(N_f)} - 1 \quad (6.5)$$

for each respective fatigue life N_f , where $\tau_a(N_f)$ represents the shear stress amplitude from the pure torsion case and $\sigma_a(N_f)$ the normal stress amplitude from the pure tension case. Figure 6.3 represents the evolution of $\kappa(N_f)$ in *high cycle fatigue* (10^5 - 10^9 cycles). From a conservative point of view, the maximum value is to be taken into account for the fatigue calculations, therefore being

$$\kappa = 0.5711. \quad (6.6)$$

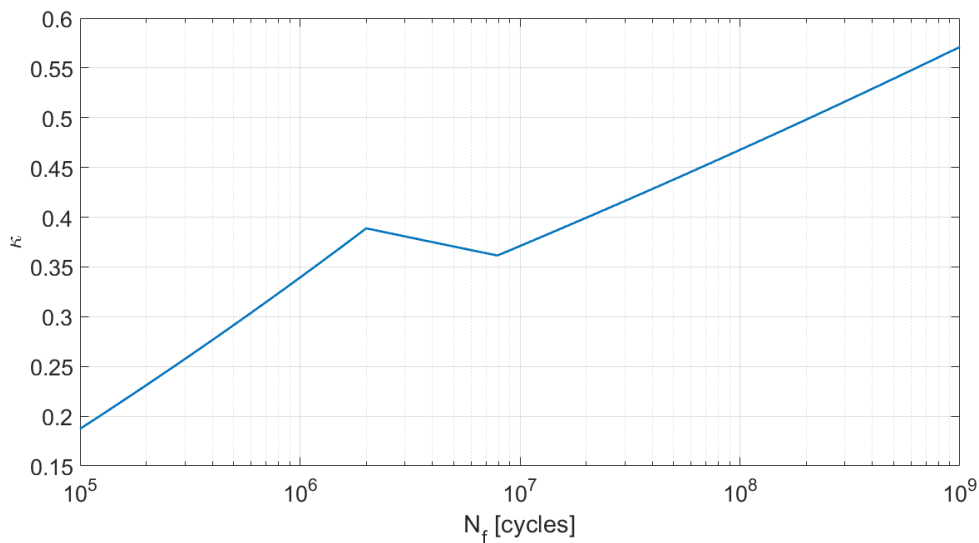


Figure 6.3: Evolution of material parameter κ in *high cycle fatigue*

6.2 Multiaxial fatigue damage models

Moving on to the fatigue damage models, these take part in calculating an equivalent fatigue stress (from the input stress components), later to be subject of cycle counting and damage computation, through Miner's law. The reviewed fatigue damage models are all stress based, being the following:

1. von Mises equivalent stress
2. Critical plane normal stress (DNV GL)
3. Findley criterion
4. Dang Van criterion

As stated in Section 2.2.4, the generality of practical cases assume a multiaxial stress state with complex variable amplitude loading. Although it is a rather recent subject, several multiaxial fatigue models have been developed. According to Flass et al. [131],

the Findley criterion produces the most accurate results, whereas the von Mises method produces significantly conservative results and the critical plane normal stress is non-conservative. It is important to note that this conclusions reflect the analysis only under a load ratio of $R = -1$. But, for the purpose of this study, the Findley criterion was set as the reference method for the model comparison. In the next sections, the methods subject of analysis are briefly explained.

6.2.1 Signed von Mises equivalent stress

The signed von Mises equivalent stress method (see also Section 2.2.4) uses all components and computes a pseudo-parameter according to the expression

$$\sigma_{VMP}(t) = \text{sign}(\max(|\sigma_1|, |\sigma_2|)) \cdot \sqrt{\sigma_{xx}(t)^2 + \sigma_{yy}(t)^2 + \sigma_{xx}(t) \cdot \sigma_{yy}(t) + 3 \cdot \tau_{xy}(t)^2}. \quad (6.7)$$

The pseudo-parameter spectrum is target of cycle counting and the damage calculation is done comparing to the tension fatigue curve. This fatigue model will be computed with the help of MATLAB. The specific code can be examined in Section J.5.

6.2.2 Critical plane normal stress (DNV GL)

The critical plane normal stress (CPNS) method from DNV GL [132], also known as the Mataka [98] criterion, proposes an equivalent fatigue stress calculated as the maximum value of normal stress, evaluated across multiple planes

$$\sigma_{CPNS,a} = \max_{\theta_i} [\sigma_a(\theta_i)] \quad (6.8)$$

where θ_i represents the direction of each evaluated plane. Furthermore, since one is dealing with a plane stress state, the normal stress $\sigma(t)$ for each direction is

$$\sigma(t, \theta_i) = \frac{\sigma_{xx}(t) + \sigma_{yy}(t)}{2} + \frac{\sigma_{xx}(t) - \sigma_{yy}(t)}{2} \cos(2\theta_i) + \tau_{xy} \sin(2\theta_i). \quad (6.9)$$

For the purpose of this study, 24 planes across the full circle were defined. Note that for every critical plane approach, the same 24 planes were defined (holds valid for the following critical plane approaches).

From a practical point of view, it was computed a critical plane normal stress pseudo-parameter σ_{CNP} spectrum, from Eq. (6.9), to be target of rainflow cycle counting and damage calculation, comparing with the torsion fatigue curve. The critical plane is set to be the one that outputs the most damage. The full programme is showed in Section J.2.

6.2.3 Findley criterion

The Findley (see also Section 2.2.4) criterion is also a critical plane method which relates shear and normal stress, in order to find the critical plane prone to failure. This critical plane then sets the direction in which the respective equivalent fatigue stress spectrum is calculated. With that said, the critical plane direction follows the expression

$$\theta_c = \max_{\theta_i} [\tau_a(\theta_i) + \kappa \cdot \sigma_a(\theta_i)] \quad (6.10)$$

where θ_c and θ_i represent the directions of the critical plane and all evaluation planes, respectively. After finding the critical plane the fatigue damage model is related to the shear stress fatigue limit rather than the normal stress fatigue limit, under the expression

$$\tau_a(\theta_c) + \kappa \cdot \sigma_a(\theta_c) \leq \tau_f \quad (6.11)$$

with

$$\kappa = \frac{2\tau_f}{\sigma_f} - 1. \quad (6.12)$$

Finally, the normal stress $\sigma(t, \theta_i)$ is calculated with Eq. (6.9) and the shear stress $\tau(t, \theta_i)$ follows the expression

$$\tau(t, \theta_i) = -\frac{\sigma_{xx}(t) - \sigma_{yy}(t)}{2} \sin(2\theta_i) + \tau_{xy} \cos(2\theta_i). \quad (6.13)$$

Following the same mentality if the previous Section, the Findley pseudo-parameter σ_{FPP} spectrum, for each plane, was computed with the expression

$$\sigma_{FPP}(t, \theta_i) = \tau(t, \theta_i) + \kappa \sigma(t, \theta_i) \quad (6.14)$$

where $\tau(t, \theta_i)$ and $\sigma(t, \theta_i)$ follow the Eqs. (6.13) and (6.9), respectively. The specific code is displayed in Section J.4.

6.2.4 Dang Van criterion

The Dang Van criterion [103] is a multi-scale approach based on the use of mesoscopic stresses instead of macroscopic stresses. A detailed explanation can be found in Section 2.2.4.

For the purpose of this study, since it is a plane stress state, the macroscopic stress tensor $\underline{\sigma}(t)$ is

$$\underline{\sigma}(t) = \begin{bmatrix} \sigma_{xx}(t) & \tau_{xy}(t) \\ \tau_{xy}(t) & \sigma_{yy}(t) \end{bmatrix} \quad (6.15)$$

and the deviatoric stress tensor $\underline{S}(t)$ is

$$\underline{S}(t) = \underline{\sigma}(t) - \underline{\sigma}_h(t) \quad (6.16)$$

where the hydrostatic stress tensor $\underline{\sigma}_h(t)$ is calculated recurring to Eq. (2.96).

Since the loading is proportional, the mesoscopic deviatoric stress tensor $\underline{s}_{meso}(t)$ is equal to the macroscopic value. Therefore, the mesoscopic hydrostatic $\sigma_{meso,h}(t)$ and shear $\tau_{meso}(t)$ stresses follow the expressions

$$\sigma_{meso,h}(t) = \frac{\sigma_{xx}(t) + \sigma_{yy}(t)}{3} \quad (6.17)$$

$$\tau_{meso}(t) = \frac{1}{2} [S_1(t) - S_3(t)] \quad (6.18)$$

where S_1 and S_3 are the principal stresses of the deviatoric stress tensor \underline{S} . With this, the Dang Van pseudo-parameter σ_{DVP} spectrum can be computed

$$\sigma_{DVP}(t) = \tau_{meso}(t) + \kappa \cdot \sigma_{meso,h}(t) \quad (6.19)$$

later to be target of cycle counting and damage calculation. The reference *S-N curve* is from the torsional load case, comparing with the shear fatigue limit τ_f . The specific code for this approach is displayed in Section J.3.

6.3 Fatigue Wizard

Fatigue Wizard is a critical plane approach that evaluates the fatigue damage across several planes. In this case, the number of these planes is 24, in order to keep the consistency between models. This fatigue damage model evaluates only $\sigma_{xx}(t)$, following the expression

$$\sigma_{FWP}(t, \theta_i) = \sigma_{xx}(t) \cdot \cos \theta_i + \tau_{xy}(t) \cdot \sin \theta_i \quad (6.20)$$

where θ_i is the direction of the analysed plane. After the computation of this pseudo-parameter σ_{FWP} spectrum for all planes, the cycle counting and damage calculation is made, returning only the maximum value of damage, referring to the critical plane. The specific code for the application of this method is described in Section J.3.

6.4 Results

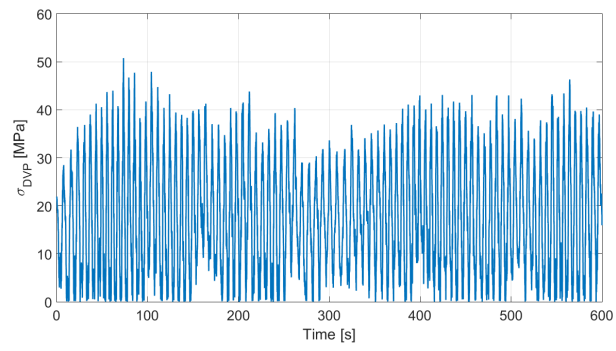
After running the models for the time history displayed in Fig. 6.1a, repeated 106416 times (in line with the FatWiz analysis), the results were stored and are summarized in Table 6.3. Considering the Findley criterion as the reference model, and taking into account the damage values, it can be concluded that the results given by the FatWiz are non-conservative, which is disadvantageous in terms of safety and reliability. When it comes to the other models, the Dang Van approach provides non-conservative, while the Mataka (DNV GL) and von Mises methods are conservative. Note that these results are in accordance with the conclusion of Flass et al. [131], referring to the nature of the results regarding the Findley criterion. Note that, for the relation between the damage and SRF values, the mean slope value was used. This has significant implications on the final results, and in some cases, such as the von Mises method the damage value is conservative while the SRF is non-conservative. This is due to the fact that von Mises deals with a different *S-N curve*, hence having a different mean slope value. The conclusions made by looking at the damage output show confidence because the only value that was inferred by Eq. (5.9) was of the Fatigue Wizard, which displays the same non-conservative behaviour in both cases (SRF and damage).

Result summary				
Method	Damage	Normalized	SRF	Normalized
Findley	0.0268	1.00	1.2594	1.00
Signed von Mises	0.0450	1.68	1.3701	1.09
Critical plane normal stress	0.1866	6.96	1.1128	0.88
Dang Van	0.0186	0.69	1.2890	1.02
Fatigue Wizard	0.0011	0.04	1.9984	1.57

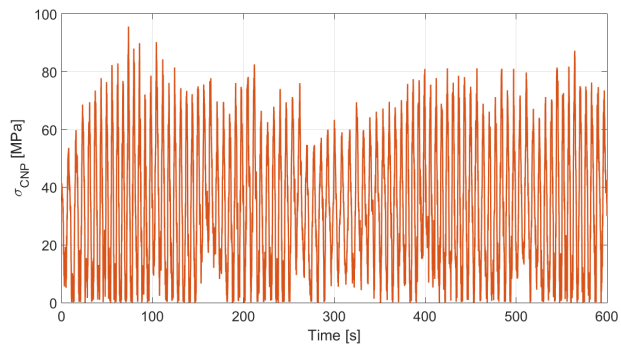
Table 6.3: Result summary for the fatigue benchmark

Figures 6.4a to 6.4d show the equivalent fatigue stress spectrum from all the multiaxial fatigue models from Section 6.2. Be aware that the displayed data is always referring to the critical situation, or plane when it comes to critical plane approaches.

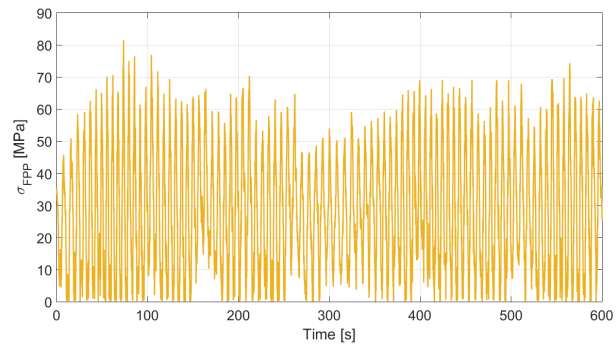
6. Fatigue benchmark



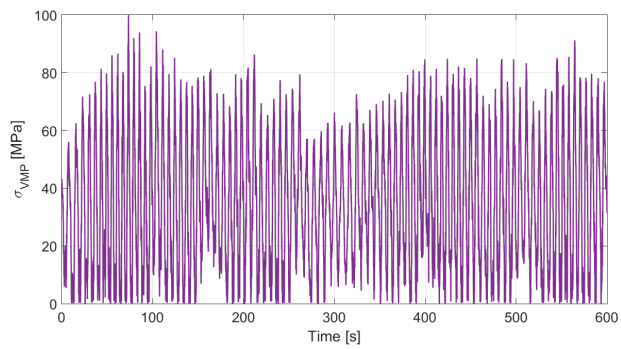
(a) Dang Van



(b) Mataka (DNV GL)



(c) Findley



(d) von Mises

Figure 6.4: Equivalent fatigue stress spectrum for all models

Conclusions

The main objective of this master thesis was to provide a comprehensive review of an efficient approach on the optimization of metallic structures, provided that they are to resist to extreme and fatigue solicitations. Moreover, an extra study was performed, which focused on the benchmark of multiaxial fatigue models, accompanied with a comparison of several approaches. The work developed in this project resulted in an optimal design, that respects both extreme and fatigue loadings, a genetic algorithm optimization program that combines static and fatigue analysis, and a multiaxial fatigue model comparison.

In Chapter 2, a comprehensive review on the several aspects that comprise this project was made, serving as a “kick-off” and aiming to provide the reader a better understanding of the succeeding Chapters. The first Section shows a summary of the wind market, exposing the present status, future prospects, and its technologies, giving a full overview on the concepts and systems that make up a wind turbine. In the next Section, an exposition on fatigue procedures and theories was made, giving an overview on conventional and multiaxial approaches. The last Section focuses on structural optimization, namely topology optimization, synthesizing the most common models and theories. Also, more recent optimization approaches are displayed, such as genetic algorithms.

Chapter 3 introduces the purpose and details of this study, giving the reader a understanding of the goals, restrictions, materials and procedures to be made. In this Chapter, one may find the extensive information on the component subject to analysis, the system and assembly requirements.

In Chapter 4, the topology optimization procedure applied to the reviewed design is detailed, giving a full report on the optimizer, objective function and restrictions, as well as the FEM model. The results of this first study are displayed and commented at the end of the Chapter.

Chapter 5 shows the full information on the parametric optimization made in the design. Firstly, the parametric model is explained, detailing the geometric parameters and FEM modelling, giving a justification for the used model. Following this, the optimization setup is exposed, giving a comprehensive look on the developed program, explaining its functionalities and framework. Lastly, the results of the parametric optimization are summarized and commented on, giving an economic outlook for the proposed design.

Lastly, Chapter 6 exposes the additional study on the benchmark of multiaxial fatigue models, aiming for a comparison of the models, including the internal Vestas’ fatigue analysis software. Details on the reviewed models are shown, as well as the framework of the calculations, and the results are displayed and commented on.

7.1 Main conclusions

When it comes to the structural optimization of the pitch support, the main conclusions to be taken from this study, referred in Chapters 3, 4 and 5, are the following:

- There is a low margin for optimization at the support base region of the pitch support, due to all the bolted connections for the bearing assembly;
- The optimum shape of the cylinder connectors, when it comes to maximizing the stiffness to mass ratio, are “lug-like” connectors;
- The genetic algorithm approach allows a wide range of optimization problems, since it is not based on any gradient calculation, hence being a very versatile way of performing structural optimization;
- An optimization program was developed in MATLAB, which allows a mass minimization, while including static and fatigue analysis restrictions, by combining the FEM analysis in Ansys with the fatigue computation from Vestas’ internal software Fatigue Wizard;
- In this specific case, the fatigue life was the critical restriction, since it was the one that defined the limit of optimization. Also, it was the one that most determined the time of each run, since it was a highly computationally demanding task, making the static analysis residual in terms of time consumption;
- The optimal design provides an 8.24 percent mass reduction, and an additional revenue of EUR 2,377.49 per year;
- A simplified fatigue approach of an equivalent fatigue maximum stress is not possible, since the fatigue results are non-linear.

It is important to note that the development of the parametric optimization program was a critical step of this project. A fast and efficient way of getting the optimal size of a certain geometry, while ensuring that this design sustains extreme conditions or the entire fatigue life, or both, is possible for every engineering procedure at Vestas. The user only needs to modify the inputs, such as the parametric geometry, number of parameters, fatigue analysis options, etc, and the program will do the rest. Also, one needs to make sure that all the genetic algorithm options are well defined for the problem in question.

Regarding the additional benchmark of multiaxial fatigue models, referred in Chapter 6, the main conclusions are:

- Both the Dang Van approach and Fatigue Wizard provided smaller damage results;
- The Mataka (DNV GL) and signed Von Mises methods estimated higher fatigue damage values.

7.2 Future work

The project's main objective was to provide an optimal design proposal. Despite having fulfilled this ambition, if one takes a closer look at the pitch system, rapidly understands that the final design does not allow a proper assembly. For this reason, future work needs to be made in post-processing this design into a valid proposal for assembly matters.

Another aspect concerns the closing of the engineering cycle, in the sense that the design should be worked on in CAD with the aim of tuning some details, such as rounding of corners (to prevent stress concentration regions), later to be fully validated in a full FEM model, which comprises all the assembly to a better representation of reality, with all contacts and extra components properly modelled, namely bolted connections and the bearing.

Regarding the optimization procedure, a two step process was made, where the first approach provided an optimal shape and the second step fine tuned the size of this shape, mainly to be able to add the fatigue restriction to the optimization setup. A significant improvement would be to develop a fully operational topology optimization program, similar to the one developed in this study, with the capability of introducing fatigue life restrictions. This would allow a one step process, outputting the final result having in mind every restriction to the structural design. As stated earlier, bear in mind that the genetic algorithm is versatile in this problems, enabling the application of every possible restriction, such as displacement, stress, stiffness, etc.

Finally, a more intensive fatigue benchmark of several multiaxial fatigue models can be made. At first, it would be very advantageous to be able to introduce the multiaxial fatigue damage models into the optimization process. Secondly, the study could widen the range of applications, testing several types of loadings, such as non-proportional loading, and fatigue models, overviewing more recent fatigue models, such as energy approaches.

References

- [1] A. Remouchamps and M. Bruyneel. Application of a bi-level scheme including topology optimization to the design of an aircraft pylon. *Structural and Multidisciplinary Optimization*, 44:739–750, 2001.
- [2] L. Krog, A. Tucker, M. Kemp, and R. Boyd. Topology optimization of aircraft wing box ribs. *10th AIAA/ISSMO Multidisciplinary Analysis and Optimization Conference*, 2004.
- [3] M. Cavazzuti, L. Splendi, L. D’Agostino, E. Torricelli, D. Costi, and A. Baldini. Structural optimization of automotive chassis: Theory, set up, design. In *Problemes Inverses, Controle et Optimisation de Formes*. Université Paris-Dauphine, Paris, France, 2012.
- [4] J. Lee and F. Zhao. Global wind report 2019. *Global Wind Energy Council (GWEC)*, 2020.
- [5] GWEC (2015). Global wind report: Annual market update. *Global Wind Energy Council (GWEC)*, 2015.
- [6] WEC (2016). World energy resources. *World Energy Council (WEC)*, 2016.
- [7] IRENA (2019). Future of wind: Deployment, investment, technology, grid integration and socio-economic aspects (a global energy transformation paper). *International Renewable Energy Agency (IRENA)*, 2019.
- [8] *Lazard’s levelized cost of energy analysis - version 13.0*. Lazard, 2019.
- [9] Directive 2001/77/ec of the european parliament and of the council. *European Commission*, 2001.
- [10] IRENA (2018). Renewable energy prospects for the european union. *International Renewable Energy Agency (IRENA)*, 2018.
- [11] Directive (eu) 2018/2001 of the european parliament and of the council. *European Commission*, 2018.
- [12] Report from the commission to the european parliament, the council, the european economic and social committee and the committee of the regions: Renewable energy progress report. *European Commission*, 2019.
- [13] Report from the commission to the european parliament, the council, the european economic and social committee and the committee of the regions: Energy prices and costs in europe. *European Commission*, 2019.

REFERENCES

- [14] R. M. Simons and D. J. Hayes. America's clean energy success by the numbers. *Center for American Progress*, 2017.
- [15] R. Wisner and M. Bolinger. Wind technologies market report. *US Department of Energy*, 2018.
- [16] F. Wang, H. Yin, and S. Li. China's renewable energy policy: Commitments and challenges. *Energy Policy*, 2009.
- [17] R. Bridle and L. Kitson. Public finance for renewable energy in china: Building on international experience. *International Institute for Sustainable Development*, 2014.
- [18] T. Yatsui. China's energy policy and related issues towards 2020. *Mitsui Global Strategic Studies Institute*, 2017.
- [19] X. Xu, D. Niu, B. Xiao, X. Guo, L. Zhang, and K. Wang. Policy analysis for grid parity of wind power generation in china. *Energy Policy*, 2019.
- [20] K. Marvel, B. Kravitz, and K. Caldiera. Geophysical limits of global wind power. *Nature Climate Change*, 2012.
- [21] P. Enevoldsen, F.-H. Permien, I. Bakhataoui, A.-K. Krauland, M. Jacobson, G. Xydis, B. Sovacool, S. Valentine, D. Luecht, and G. Oxley. How much wind power potential does europe have? examining european wind power potential with an enhanced socio-technical atlas. *Energy Policy*, 2019.
- [22] D. Elliot, M. Schwartz, S. Haymes, D. Heimiller, G. Scott, L. Flowers, M. Brower, E. Hale, and B. Phelps. 80 and 100 meter wind energy resource potential for the united states. *National Renewable Energy Laboratory*, 2011.
- [23] IEA. World energy outlook 2019. *International Energy Association (IEA)*, 2019.
- [24] A. Kamilkov. Wind power fundamentals. In T. M. Letcher, editor, *Wind Energy Engineering: A Handbook for Onshore and Offshore Wind Turbines*, pages 17–23. Elsevier, 2017.
- [25] A. Betz. The maximum of the theoretically possible exploitation of wind by means of a wind motor. *Wind Engineering*, 37:441–446, 1920.
- [26] E. Hau. *Wind Turbines: Fundamentals, Technologies, Application, Economics*. Springer, 2006.
- [27] R. E. Wilson and P. B. S. Lissaman. *Applied Aerodynamics of Wind Power Machines*. Oregon State University, 1974.
- [28] H. Reents. Windkonzentratoren. *Deutscher Physiker*, 1985.
- [29] IEC. Wind energy generation systems - part 1: Design requirements. *International Electrotechnical Commission*, IEC 61400-1:2019.
- [30] M. H. Zhang. *Wind Resource Assessment nad Micro-siting, Science and Engineering*. China Machine Press, 2015.
- [31] A. D. Hansen. Wind turbine technologies. In T. M. Letcher, editor, *Wind Energy Engineering*, pages 145–160. Elsevier, 2017.

-
- [32] W. Hu, editor. *Advanced Wind Turbine Technology*. Springer, 2018.
- [33] D. Künz and R. Wachsmuth. Rotorblatt in faserverbundbauweise für die windkraftanlage aeolus ii. *BMFT report MBB-UE-0013-92-PUB*, 1992.
- [34] P. Thörnblad. Gears for wind power plants amsterdam. *Second International Symposium on Wind Energy Systems*, pages 3–6, 1978.
- [35] Westinghouse: Technical description wwg-0600 wind turbine, 1985.
- [36] R. I. Stephens, A. Fatemi, R. R. Stephens, and H. O. Fuchs. *Metal Fatigue in Engineering*. John Wiley & Sons, Inc., 2001.
- [37] P. P. Milella. *Fatigue and Corrosion in Metals*. Springer, 2013.
- [38] C. Bathias. There is no infinite fatigue life in metallic materials. *Fatigue & Fracture of Materials & Structures*, 22:559–565, 1999.
- [39] Y. Furuya, H. Hirukawa, and E. Takeuchi. Gigacycle fatigue in high strength steels. *Science and Technology of Advanced Materials*, 2019.
- [40] Q. Y. Wang, J. Y. Berard, A. Dubarre, G. Baudry, S. Rathery, and C. Bathias. Gigacycle fatigue of ferrous alloys. 1999.
- [41] H. Xue, P. Liu, P. Chen, and J. Wang. Fatigue life assessment of a high strength steel 300 m in the gigacycle regime. 2012.
- [42] J. A. Bannantine, J. J. Comer, and J. L. Handrock. *Fundamentals of Metal Fatigue Analysis*. Prentice Hall, Englewood Cliffs, 1990.
- [43] R. C. Juvinall and K. M. Marshek. *Fundamentals of Machine Component Design*. John Wiley & Sons, 1991.
- [44] J. O. Almen and P. H. Black. *Residual Stresses and Fatigue in Metals*. McGraw-Hill, 1963.
- [45] J. C. Straub. "shot-peening". In O. J. Horger, editor, *ASME Handbook: Metals Engineering Design*, page 258. McGraw-Hill, 1965.
- [46] W. A. Wood. Four types of metal fatigue. *George Washington University*, 1972.
- [47] P. Soo and J. G. Y. Chow. Correlation of high- and low-cycle fatigue data for incoloy-800h. *Brookhaven National Laboratory*, 1976.
- [48] Y. Furuya, T. Abe, and S. Matsuoka. 10^{10} -cycle fatigue properties of 1800 mpa-class jis-sup7 spring steel. *Fatigue & Fracture of Materials & Structures*, 26:641–645, 2003.
- [49] Y. Furuya, T. Abe, and E. Takeuchi. Ultrasonic fatigue properties of high-strength materials, nims fatigue data sheet technical document no. 19. *National Institute for Materials Science*, 2013.
- [50] *NRIM fatigue data sheets no. 2*. National Research Institute for Metals, 1978.
- [51] N. E. Dowling. *Mechanical Behavior of Materials: Engineering Methods for Deformation, Fracture and Fatigue*. Prentice Hall, Englewood Cliffs, 1993.

REFERENCES

- [52] T. Svensson, J. Maré, and B. Wadman. Determination of the fatigue limit, methods and problems. *IM Report Swedish Institute of Applied Mathematics*, 2000.
- [53] Y. Murakami and T. Endo. Effect of hardness on crack geometries on δk_{th} of small cracks emanating from small defects. the behaviour of short fatigue cracks. *Mechanical Engineering Publications, London*, pages 275–293, 1986.
- [54] O. H. Basquin. The exponential law of endurance tests. *ASTM*, 10:625–630, 1910.
- [55] J. D. Morrow. Internal friction, damping and cyclic plasticity. *ASTM STP-378*, page 45, 1965.
- [56] E. Haibach. Betriebsfestigkeit (operational integrity). *VDI-Verlag Stahleisen GmbH*, 1986.
- [57] D. L. DuQuesnay, T. H. Topper, M. T. Yu, and M. A. Pompetzki. The effective stress range as a mean stress parameter. *International Journal of Fatigue*, pages 45–50, 1992.
- [58] W. Z. Gerber. Calculation of the allowable stresses in iron structures. *Bavarian Archives of Engineering Associates*, pages 101–110, 1874.
- [59] J. Goodman. Mechanics applied to engineering. *Longman*, 1899.
- [60] C. R. Soderberg. Fatigue of the safety and working stress. *Transactions of the American Society of Mechanical Engineers*, pages 13–28, 1939.
- [61] J. Morrow. *Fatigue Design Handbook. Advances in Engineering*. SAE, 1968.
- [62] R. C. Juvinal. *Engineering Considerations of Stress, Strain and Strength*. Mc GrawHill, 1967.
- [63] Mil-hdbk-5d. In *Military Standardization Handbook*, pages 5–87. Metallic Materials and Elements for Aerospace Vehicle Structures, 1983.
- [64] M. Matsuishi and T. Endo. Fatigue of metals subjected to various stress. *Proceedings of JSME*, 1968.
- [65] Yung-Li Lee, M. E. Barkey, and Hong-Tae Kang. *Metal Fatigue: Analysis Handbook*. Elsevier, 2013.
- [66] M. A. Miner. Cumulative damage in fatigue. *Journal of Applied Mechanics*, 12: 159–164, 1945.
- [67] S. M. Marco and W. L. Starkey. A concept of fatigue damage. *ASME Trans.*, 76: 627–632, 1954.
- [68] F. E. Richard and N. M. Newmark. An hypothesis for the determination of cumulative damage in fatigue. *Proceedings of ASME*, 48:767, 1948.
- [69] R. Spizer and H. T. Corten. *Proceedings ASTM*, 61:719, 1961.
- [70] A. M. Freudenthal. *Symposium on Acoustic Fatigue, ASTM-284*, page 26, 1960.
- [71] H. T. Corten and T. J. Dolan. Cumulative fatigue damage. *Proceedings of International Conference on Fatigue of Metals*, page 235, 1956.

-
- [72] K. Kanazawa, T. Abe, and S. Nishijima. Fundamental fatigue properties of hard steels, nrim fatigue data sheet technical document no. 9. *National Research Institute for Metals*, 1989.
- [73] M. Janeček, F. Nový, P. Hrcuba, J. Stráský, and L. Trško. The very high cycle fatigue behaviour of ti-6al-4v alloy. *International Symposium on Physics of Materials*, 2015.
- [74] G. R. Halford. A recommended procedure for extrapolating strain fatigue curves beyond one million cycles to failure. *ASME*, 1978.
- [75] S. S. Manson and G. R. Halford. *Fatigue and Durability of Structural Materials*. ASM International, 2006.
- [76] K. Kanazawa, K. J. Miller, and M. V. Brown. Low cycle fatigue under out-of-phase loading conditions. *Journal of Engineering Materials and Technology*, 99:222–228, 1977.
- [77] T. Itoh, M. Kameoka, and Y. Obataya. A new model for describing a stable cyclic stress-strain relationship under non-proportional loading based on activation state of slip systems. *Fatigue & Fracture of Engineering Materials & Structures*, 27:957–966, 2004.
- [78] S. Kida, T. Itoh, M. Sakane, M. Ohnami, and D. F. Socie. Dislocation structure and nonproportional hardening of type 304 stainless steel. *Fatigue & Fracture of Engineering Materials & Structures*, 20:1375–1386, 1997.
- [79] M. V. Borodii. Obtaining a low-cycle fatigue strain criterion. *Strength of Materials*, 33:217–223, 2001.
- [80] N. Shamsaei and A. Fatemi. Effect of hardness on multiaxial fatigue behavior and some simple approximations for steels. *Fatigue & Fracture of Engineering Materials & Structures*, 32:631–646, 2009.
- [81] H. J. Gough and H. V. Pollard. The strength of metals under combined alternating stresses. *Proceedings of the Institution of Mechanical Engineers*, pages 3–103, 1935.
- [82] H. J. Gough. Engineering steels under combined cyclic and static stresses. *Journal of Applied Mechanics*, pages 113–125, 1950.
- [83] Z. Hashin. Fatigue failure criteria for combined cyclic stress. *International Journal of Fracture*, pages 101–109, 1981.
- [84] F. Rotvel. Biaxial fatigue tests with zero mean stresses using tubular specimens. *International Journal of Mechanics and Science*, pages 597–613, 1970.
- [85] D. L. McDiarmid. A new analysis of fatigue under combined bending and twisting. *The Aeronautical Journal of the Royal Aeronautical Society*, pages 325–329, 1974.
- [86] H. Dietmann. Werkstoffverhalten unter mehrachsiger schwingender beanspruchung. *Journal of Materials Science and Engineering Technology*, pages 255–263, 1973.
- [87] D. F. Socie and G. B. Marquis. *Multiaxial Fatigue*. SAE International, 2000.
- [88] S. B. Lee. A criterion for fully reversed out-of-phase torsion and bending. In M. Miller and W. Brown, editors, *Multiaxial Fatigue*, pages 553–568. ASTM STP 853, 1985.

REFERENCES

- [89] Y. L. Lee and Y. J. Chiang. Fatigue predictions for components under biaxial reversed loading. *Journal of Testing and Evaluation*, pages 359–367, 1991.
- [90] G. Sines. Behavior of metals under complex static and alternating stresses. In G. Sines and J. L. Waisman, editors, *Metal fatigue*, pages 145–169. McGraw-Hill, New York, 1959.
- [91] G. Sines and G. Ohgi. Fatigue criteria under combined stresses or strains. *ASTM J. Engng. Mater. Technol.*, page 82, 1891.
- [92] B. Crossland. Proceedings of international conference on fatigue of metals. *Institution of Mechanical Engineering*, pages 138–149, 1956.
- [93] H. Kakuno and Y. Kawada. A new criterion of fatigue strength of a round bar subjected to combined static and repeated bending and torsion. *Fatigue Eng. Mater. Struct.*, pages 229–236, 1979.
- [94] Q. H. Vu, D. Halm, and Y. Nadot. Multiaxial fatigue criterion for complex loading based on stress invariants. *International Journal of Fatigue*, 2009.
- [95] M. C. Sonsino. Multiaxial fatigue of welded joints under in-phase and out-of-phase local strains and stresses. *International Journal of Fatigue*, pages 55–70, 1995.
- [96] Y. L. Lee, T. Tjhung, and A. Jordan. A life prediction model for welded joints under multiaxial variable amplitude loading histories. *International Journal of Fatigue*, pages 1162–1173, 2007.
- [97] W. N. Findley. A theory for the effect of mean stress on fatigue of metals under combined torsion and axial load or bending. *Journal of Engineering for Industry*, 1959.
- [98] T. Mataka. An explanation on fatigue limit under combined stress. *Bulletin of JSME*, pages 257–263, 1977.
- [99] M. W. Brown and K. J. Miller. A theory for fatigue under multiaxial stress strain condition. *Institute of Mechanical Engineers*, pages 745–755, 1973.
- [100] D. L. McDiarmid. A general criterion for high cycle multiaxial fatigue failure. *Fatigue & Fracture of Engineering Materials & Structures*, 14:429–454, 1991.
- [101] D. L. McDiarmid. A general criterion for high cycle multiaxial fatigue failure. *Fatigue & Fracture of Engineering Materials & Structures*, 17, 1994.
- [102] C. Gaier and H. Dannbauer. A multiaxial fatigue analysis method for ductile, semiductile, and brittle materials. *Arabian Journal for Science and Engineering*, 33:224–235, 2008.
- [103] K. Dang Vand, B. Griveau, and O. Message. On a new multiaxial fatigue limit criterion: Theory and application. In D. L. McDowell and R. Ellis, editors, *Biaxial and Multiaxial Fatigue*, pages 120–130. Mechanical Engineering Publications, 1982.
- [104] C H. Wang and M. W. Brown. Life prediction techniques for variable amplitude multiaxial fatigue - part 1: Theories. *Journal of Engineering Materials and Technology*, 118:367–370, 1996.

-
- [105] P. Dong, Z. Wei, and J. K. Hong. A path-dependent cycle counting method for variable-amplitude multi-axial loading. *International Journal of Fatigue*, 32:720–734, 2010.
- [106] O. M. Querin, M. Victoria, C. Alonso, R. Ansola, and P. Martí. *Topology Design Methods for Structural Optimization*. Academic Press, 2017.
- [107] M. P. Bendsøe and O. Sigmund. *Topology Optimization: Theory, Methods and Applications*. Springer, 2003.
- [108] G.-J. Park. *Analytic Methods for Design Practice*. Springer, 2007.
- [109] X. Gui, M. Xiao, Y. Zhang, L. Gao, and Y. Liao. Structural topology optimization based on parametric level set method under the environment of ansys secondary development. *Advances in Computer Science Research*, 74:841–850, 2017.
- [110] S. J. Osher and F. Santosa. Level set methods for optimization problems involving geometry and constraints i. frequencies of a two-density inhomogeneous drum. *Journal of Computational Physics*, 171:272–288, 2001.
- [111] J. A. Sethian and A. Wiegmann. Structural boundary design via level set and immersed interface methods. *Journal of Computational Physics*, 163:489–528, 2000.
- [112] G. Allaire, F. Jouve, and A.-M. Toader. Structural optimization using sensitivity analysis and a level-set method. *Journal of Computational Physics*, 194:363–393, 2004.
- [113] M. Y. Wang, X. Wang, and D. Guo. A level set method for structural topology optimization. *Computer methods in applied mechanics and engineering*, 192:227–246, 2003.
- [114] S. H. Jeong, J. W. Lee, G. H. Yoon, and D. H. Choi. Topology optimization considering the fatigue constrain of variable amplitude load based on the equivalent static load approach. *Applied Mathematical Modelling*, 56:626–647, 2017.
- [115] E. Holmberg, B. Torstenfelt, and A. Klarbring. Fatigue constrained topology optimization. *Structural and Multidisciplinary Optimization*, 50:207–219, 2014.
- [116] S. Zhang, C. Le, A. L. Gain, and J. A. Norato. Fatigue-based topology optimization with non-proportional loads. *Structural and Multidisciplinary Optimization*, 61:1011–1025, 2020.
- [117] J. Oest and E. Lund. Topology optimization with finite-life fatigue constraints. *Structural and Multidisciplinary Optimization*, 56:1045–1059, 2017.
- [118] K. Nabaki, J. Shen, and X. Huang. Evolutionary topology optimization of continuum structures considering fatigue failure. *Materias and Design*, 166, 2019.
- [119] C. Le, J. Norato, T. Bruns, C. Ha, and D. Tortonelli. Stress-based topology optimization for continua. *Structural and Multidisciplinary Optimization*, 41:605–620, 2010.
- [120] C. Fleury. Conlin: an efficient dual optimizer based on convex approximation concepts. *Structural Optimization*, 1:81–89, 1989.

REFERENCES

- [121] K. Svanberg. The method of moving asymptotes - a new method for structural optimization. *International Journal for Numerical Methods in Engineering*, 24:359–373, 1987.
- [122] C. D. Chapman. Structural topology optimization via the genetic algorithm. Master’s thesis, Massachusetts University of Technology, 1991.
- [123] J. Holland. *Adaptation in Natural and Artificial Systems*. The University of Michigan Press, 1975.
- [124] C. Kane and M. Schoenauer. Topological optimum design using genetic algorithms. *Control and Cybernetics*, 25, 1996.
- [125] T. Y. Chen and Y. H. Chiou. Structural topology optimization using genetic algorithms. *Proceedings of the World Congress on Engineering*, 3, 2013.
- [126] A. Hadidi, S. K. Azad, and S. K. Azad. Structural optimization using artificial bee colony algorithm. *International Conference on Engineering Optimization*, 2010.
- [127] D. Karaboga. An idea based on honey bee swarm for numerical optimization. *Technical Report TR06, Computer Engineering Department, Erciyes University, Turkey*, 2005.
- [128] M. Christensen, S. Kabus, E. Markussen, and J. L. Neubauer. Segmented pitch ring for a wind turbine blade pitch system, 2017.
- [129] J. Andersen, O. Jeppesen, R. Rowntree, L. Christoffersen, P. Bøttcher, and G. Maden. A pitch system for a wind turbine, 2012.
- [130] DNVGL-ST-0437. Loads and site conditions for wind turbines. *DNV GL*, 2016.
- [131] M. Flass, K. Störzel, and J. Baumgartner. Evaluation of fatigue strength criteria for thick-walled nodular cast iron components from en-gjs-400 under multiaxial load. *MATEC Web of Conferences*, 300, 2019.
- [132] DNVGL-ST-0361. Machinery for wind turbines. *DNV GL*, 2016.
- [133] R. T. Haftka and Z. G’urdal. *Elements of Structural Optimization*. Kluwer Academic Publishers, 1992.
- [134] Vestas (2011). Vestas v164-8.0mw, 2011.
- [135] P. Kohnke, editor. *Ansys Theory Reference*. SAS IP, Inc., 1999.
- [136] Michael C. Y. Niu. *Airframe Stress Analysis and Sizing*. Hong Kong Conmilit Press Ltd., 2011.
- [137] *Steel Construction Manual*. American Institute of Steel Constructions, 13 edition, 2005.
- [138] M.L. Roessle and A. Fatemi. Strain-controlled fatigue properties of steels and some simple approximations. *International Journal of Fatigue*, 22:495–511, 200.
- [139] S. Sharifimehr and A. Fatemi. Evaluation of methods for estimating shear fatigue properties of steels and titanium alloys. *International Journal of Fatigue*, 122:19–34, 2019.

- [140] M.A. Meggiolaro and J.T.P. Castro. Statistical evaluation of strain-life fatigue crack initiation predictions. *International Journal of Fatigue*, 26:463–476, 2004.

Kuhn-Tucker conditions

An optimization problem as

$$\text{Find } x \tag{A.1a}$$

$$\text{to minimize } J(x) \tag{A.1b}$$

$$\text{subject to } H_i(x) = 0, \quad i = 1, \dots, n_e \tag{A.1c}$$

$$G_i(x) \geq 0, \quad i = 1, \dots, n_g \tag{A.1d}$$

may have several local minima. The necessary conditions for a minimum of the constrained problem are obtained using the Lagrange multiplier method. Considering equality constrains only, and using the Lagrange multiplier technique, the Lagrangian function is defined as

$$\mathcal{L}(x, \Lambda) = J(x, \Lambda) - \sum_{j=1}^{n_e} \Lambda_j h_j(x) \tag{A.2}$$

where Λ_j are the unknown Lagrange multipliers. The necessary conditions for a stationary (local minimum) point come by deriving the equation

$$\frac{\partial \mathcal{L}}{\partial x_i} = \frac{\partial J(x)}{\partial x_i} - \sum_{j=1}^{n_e} \Lambda_j \frac{\partial h_j(x)}{\partial x_i} = 0, \quad i = 1, \dots, n, \tag{A.3a}$$

$$\frac{\partial \mathcal{L}}{\partial \Lambda_j} = h_j(x) = 0, \quad j = 1, \dots, n_e. \tag{A.3b}$$

These conditions, however, only apply to a regular point, i.e. a point where the gradients of the constrains are linearly independent, representing a system of $n + n_e$ equations for n_e Lagrange multipliers and n coordinates of the stationary point. For linearly dependent gradients, some constrains can be removed without affecting the solution.

When dealing with inequality constrains, first the constrains are transformed to the equality type by adding slack variables, written as

$$G_j(x) - t_j^2 = 0, \quad j = 1, \dots, n_g \tag{A.4}$$

where t_j is the slack variable which measures how far the j th constrain is from being critical. Now, the Lagrangian function is formed as

$$\mathcal{L}(x, t, \Lambda) = J(x) - \sum_{j=1}^{n_g} \Lambda_j (G_j - t_j^2). \tag{A.5}$$

Differentiating the Lagrangian function it is obtained

$$\frac{\partial \mathcal{L}}{\partial x_i} = \frac{\partial J(x)}{\partial x_i} - \sum_{j=1}^{n_g} \Lambda_j \frac{\partial G_j(x)}{\partial x_i} = 0, \quad i = 1, \dots, n, \quad (\text{A.6a})$$

$$\frac{\partial \mathcal{L}}{\partial \Lambda_j} = -G_j(x) + t_j^2 = 0, \quad j = 1, \dots, n_g, \quad (\text{A.6b})$$

$$\frac{\partial \mathcal{L}}{\partial t_j} = 2\Lambda_j t_j = 0, \quad j = 1, \dots, n_g. \quad (\text{A.6c})$$

At a stationary point, Eqs. (A.6b) and (A.6c) imply that when an inequality constrain is not critical, then the Lagrange multiplier associated with the constrain is zero. Eqs (A.6a) to (A.6c) are the necessary conditions for a stationary regular point and are known as the *Kuhn-Tucker conditions*. Note that for inequality constrains, a regular point is when the *active* (with $t_j = 0$) constrains are linearly independent [133].

Vestas V164-8.0MW

B.1 Technical data

Below is displayed some technical information from Vestas V164-8.0MW wind turbine on:

1. Operation data (see Table B.1)
2. Design parameters (see Table B.1)
3. Electrical aspects (see Table B.2)
4. Constructive information (see Table B.3)

Design and operation

Power regulation	pitch regulated with variable speed
Operating data	
Rated power	8.0 MW
Cut-in-speed	4 m s ⁻¹
Operational rotor speed	4.8 - 12.1 rpm
Nominal rotor speed	10.5 rpm
Operational temperature range	-10 - +25 °C
Extreme temperature range	-15 - +35 °C
Design parameters	
Wind class	IEC S
Annual average wind speed	11 m s ⁻¹
Weibull shape parameter	k 2.2
Weibull scale parameter	12.4 m s ⁻¹
Turbulence intensity	IEC B
1 year mean wind speed V1 (10 minute average)	40 m s ⁻¹
50 year mean wind speed V50 (10 minute average)	50 m s ⁻¹
Max inflow angle (vertical)	0°
Structural design lifetime	25 years

Table B.1: Design and operation aspects of Vestas V164-8.0MW [134]

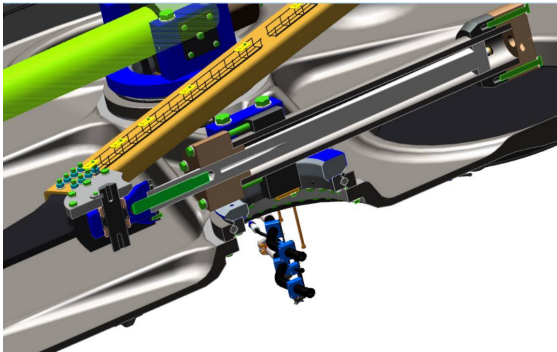
Electrical	
Frequency	50 Hz
Converter type	Full scale converter
Generator type	Permanent magnet
Nominal voltage	33 - 35 and 66 V

Table B.2: Electrical aspects of Vestas V164-8.0MW [134]

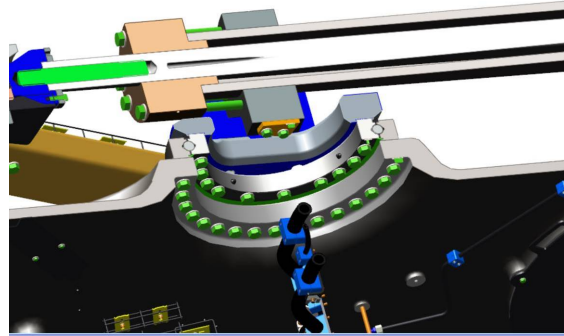
Construction	
Rotor	
Rotor diameter	164 m
Swept are	21.124 m ²
Tower	
Type	Tubular steel tower
Hub heights	Site specific
Blade dimensions	
Length	80 m
Maximum chord	5.4 m
Nacelle dimensions (including hub and coolers)	
Height	8 m
Length	20 m
Width	7.5 m
Weights	
Nacelle (including hub)	390 t±10%
Blade	35 t
Tower	Site dependent

Table B.3: Constructive aspects of Vestas V164-8.0MW [134]

B.2 Pitch system patent



(a) Pivot point installation in the cylinder head



(b) Mounting of the cylinder support on the coupling plate

Figure B.1: Mounting points of hydraulic drives in PCT application WO 2017/005264 A1

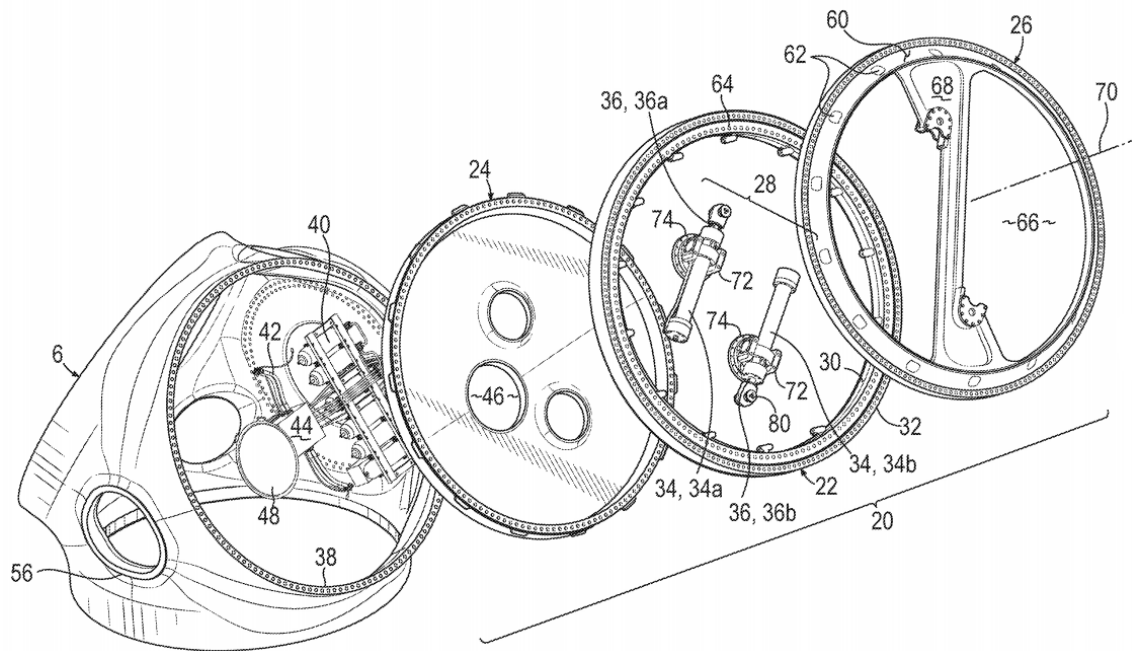


Figure B.2: Exploded view of the pitch system [129]

Fatigue properties for EN-GJS-400-18LT

C.1 Introduction

The present Appendix represents the computation of the fatigue properties of EN-GJS-400-18LT cast iron pitch cylinder support. The study is based on the *SN curve* from experimental observation, later to be used in the estimation of the component's fatigue properties. This estimation is performed by scaling it with several correction factors to compensate the different conditions that affect the component, with relation to the fatigue tests. In this case, the fatigue strength follows the expression

$$\Delta\sigma_{a,comp} = C_{mean} \cdot C_{surf} \cdot C_{Tcast} \cdot C_{Tmach} \cdot C_{chill} \cdot C_{qual} \cdot C_{HBV} \cdot \Delta\sigma_{a,ref} \quad (C.1)$$

where the factors C are the correlation factors and $\Delta\sigma_{a,comp}$ and $\Delta\sigma_{a,ref}$ are the component and reference fatigue amplitude for a certain life N_f , respectively. This approach considers that the effects are independent, which might be inaccurate.

C.2 Reference fatigue strength

Figure C.1 shows several the test results for the SN curve, performed on machined EN-GJS400-18LT test specimens and corrected to $T = 70$ mm which is the reference thickness of this study. The characteristics of the reference *SN curve* is 246 MPa (PS¹=95%, CI²=95%) and $m = 6.9$, shown by the black line.

C.3 Correction factors

The considered conditions affecting the fatigue strength of the component are the following:

- Mean stresses
- Surface condition
- Size/thickness effect
- Effect of chill casting
- Quality/NDT level

¹probability of success

²confidence interval

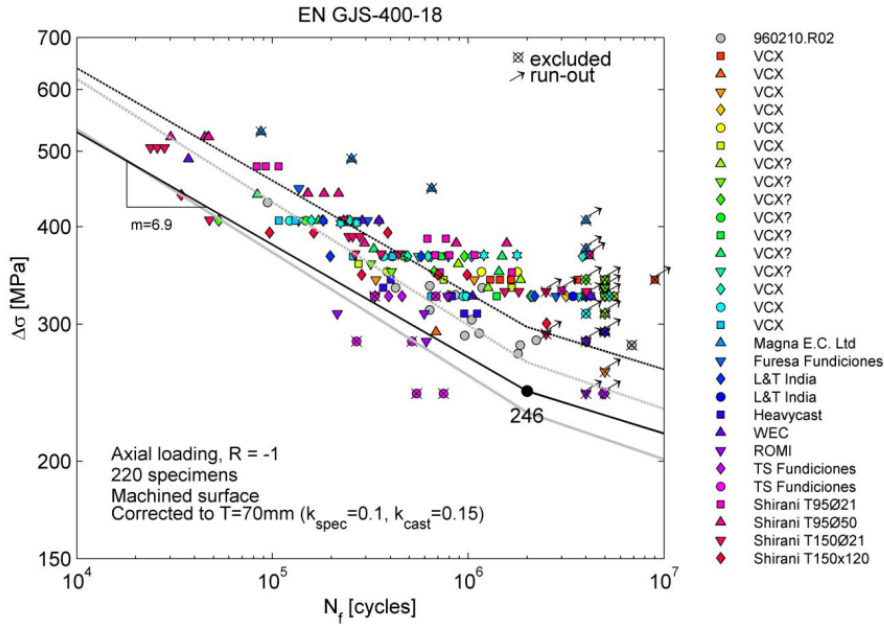


Figure C.1: Fatigue test results corrected for $T = 70$ mm

- Highly stressed volume
- Variable amplitude loading
- Min/max cut-off levels

to be inferred by the respective correction factor in Eq. C.1. It is logical that when performing more corrections to the data, the bigger the error one is incurring. Therefore, if a component experiences significantly different conditions, the specific fatigue strength testing is recommended.

C.3.1 Mean stresses

The available fatigue data displayed in Fig. C.1 is derived from zero mean stress, i.e. fully reversed loading ($R = -1$). The situations where the mean stress is not zero call for a correction factor. For this purpose, the linear mean stress correction was used, with a sensitivity of $M = 0.35$, since it is in good agreement with the Goodman line. Hence, the mean stress correction factor is

$$C_{mean} = \frac{1}{1 - M \left(\frac{R+1}{R-1} \right)}. \quad (C.2)$$

C.3.2 Surface condition

As mentioned already mentioned in Chapter 2, the surface defects play a decisive role in fatigue, being the common region for crack initiation, with the exception of VHCF (very high cycle fatigue). Two surface conditions are considered:

1. Machined surface
2. As-cast surface

Machined surface

The test specimens for the reference *SN curve* were machined and generally light polished to a surface roughness of $R_z = 10 \mu\text{m}$. The correction factor for the machined surface roughness takes the form of

$$C_{Tmach} = \begin{cases} 1.0 & \text{for } R_z \leq 10 \mu\text{m} \\ 1.16 \cdot R_z^{-0.064} & \text{for } R_z > 10 \mu\text{m} \end{cases} \quad (\text{C.3})$$

It is important to note that practical experience states that the degree of polishing has no influence on the fatigue strength of cast iron. This is probably caused by the half-cut-up nodules lying in the surface acting as crack initiation sites. This phenomenon is resembled in Eq. C.3 for the surface qualities of $R_z \leq 10 \mu\text{m}$.

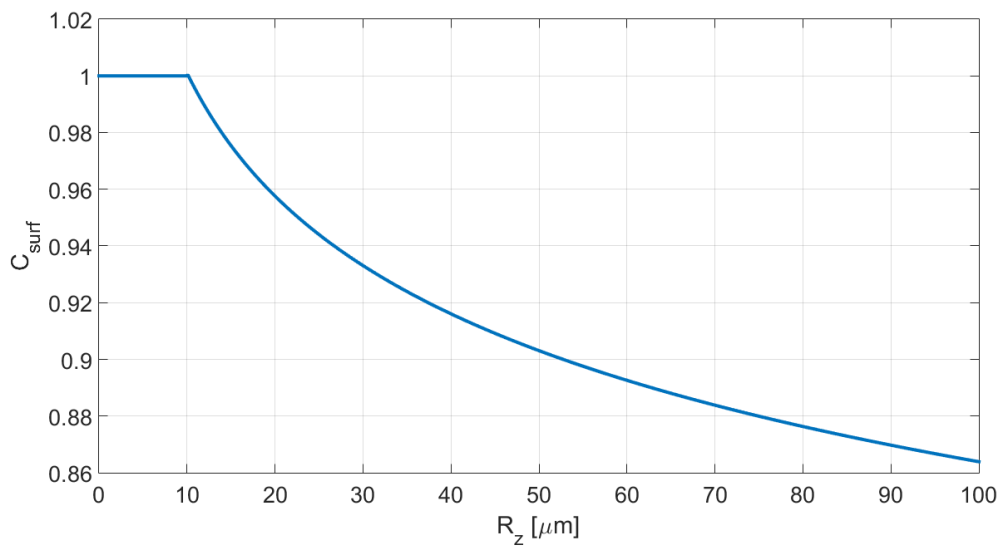


Figure C.2: Surface correction factor for machined surfaces

As-cast (sand blasted) surface

For as-cast surfaces, the following correction factor is recommended:

$$C_{\text{surf}} = 0.9. \quad (\text{C.4})$$

C.3.3 Size/thickness effect

The size/thickness effect comprise the three effects:

1. The statistical size effect: increased possibility of finding a sever defect in a larger test volume
2. The geometrical size effect: stress gradient effect and non-scaling effect, i.e. that stress concentration factors increase with increased thickness
3. The technological effect: decreased material properties found in thick castings, specially internally, where the cooling rate is lower

The size/thickness correction factor may be divided in machined and casting thickness, where the statistical and geometrical aspects rely more on the machined component and the technological effect depends more on the cooling rate of the casting part (casting thickness).

Correction for machined size

The correction factor is derived from the experimental results in Fig. C.3a, from which can be concluded that larger thickness has a detrimental effect. The correction exponent was set to $K_{mach} = 0.10$ and the correction factor follows the expression

$$C_{T_{mach}} = \left(\frac{70 \text{ mm}}{T_{mach}} \right)^{0.10}, \quad T_{mach} \geq 20 \text{ mm.} \quad (\text{C.5})$$

Correction for casting size

The expression for the casting thickness correction factor is derived from Fig. C.3b, which is the same test data as in Fig. C.3a corrected for $T_{mach} = 70 \text{ mm}$, thus comparing the different casting thickness, and follows the expression

$$C_{T_{cast}} = \left(\frac{70 \text{ mm}}{T_{cast}} \right)^{0.15}. \quad (\text{C.6})$$

The thickness T_{cast} is the effective thickness regarding the cooling rate. Therefore, this value may be calculated from a thickness of a block with a equivalent cooling rate to the component.

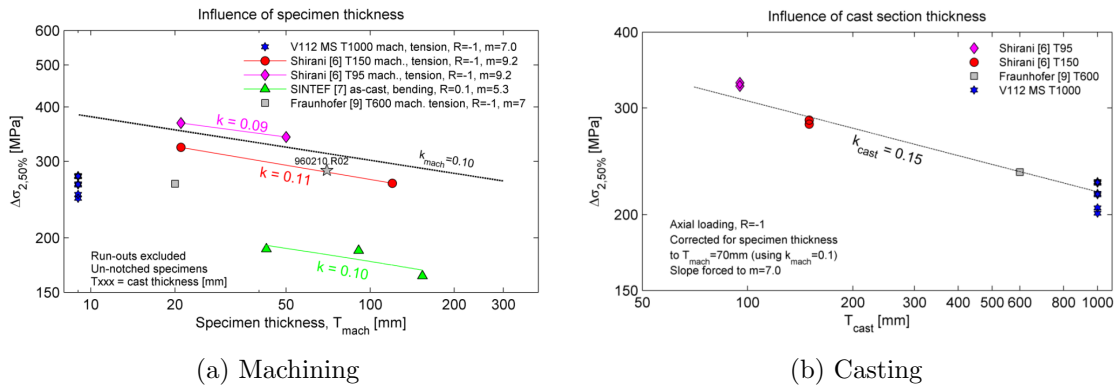


Figure C.3: Effects of machined and casting thickness

C.3.4 Effect of chill casting

The cooling rate of casting can be increased by using metal moulds instead of sand moulds, which is called chill casting. This process tends to have a positive effect in fatigue strength. Therefore, the correction factor for chill casting is

$$C_{chill} \approx 1.50. \quad (\text{C.7})$$

The above correction is only valid for A+ quality zones, since the improvement may be linked with better surface finish obtained due to a finer microstructure.

However, it is important to note that crack propagation rate slightly increases, since the large nodules promoted by slow cooling tend to have a retarding effect on the crack growth. Moreover, rapid cooling may leave residual stresses, due to uneven contractions, which later may lead to intensive crack propagation.

C.3.5 Quality/NDT

The correction factor for the quality of castings is displayed in Table C.1.

Inspection level/zone	Correction factor C_{qual}
A+	1.00
A	0.92
B	0.80
C	0.60

Table C.1: Correction factors for quality of casting

C.3.6 Highly stressed volume effect

For a non-uniform stress distribution, fatigue loading is less severe. Therefore, the highly stressed volume approach (HBV effect from German) is used to calculate the correction factor to estimate this behaviour. The highly stressed volume V_{90} is defined as that having a stress level above 90 percent of the maximum stress. The correction factor behaviour is computed from the experimental data displayed in Fig. C.4, and follows the expression

$$C_{HBV} = \left(\frac{V_{90}}{V_{90,ref}} \right)^{-0.059}, \quad C_{HBV} \leq 1.75 \quad (\text{C.8})$$

where the HBV reference volume $V_{90,ref}$ is

$$V_{90,ref} = 3 \cdot (T_{mach})^3. \quad (\text{C.9})$$

C.3.7 Variable amplitude loading

As reviewed in Section 2.2.3, variable amplitude (VA) loading is considered to be more damaging. While in constant amplitude loading, a small stress amplitude is considered harmless, in VA loading, a large stress amplitude at the beginning may lead to crack initiation for later a small stress amplitude to propagate, which would not happen so far. For this reason, the effect of VA loading is more significant beyond the knee point, i.e. very high cycle fatigue. To assess this problem, the Haibach formulation is to be used, by abandoning the so-called fatigue limit and computing another slope for the high cycle region. This slope is calculated using

$$m_2 = 2m_1 - 1 \quad (\text{C.10})$$

where m_1 is the slope before the knee point and m_2 is the new slope for the VHCF region.

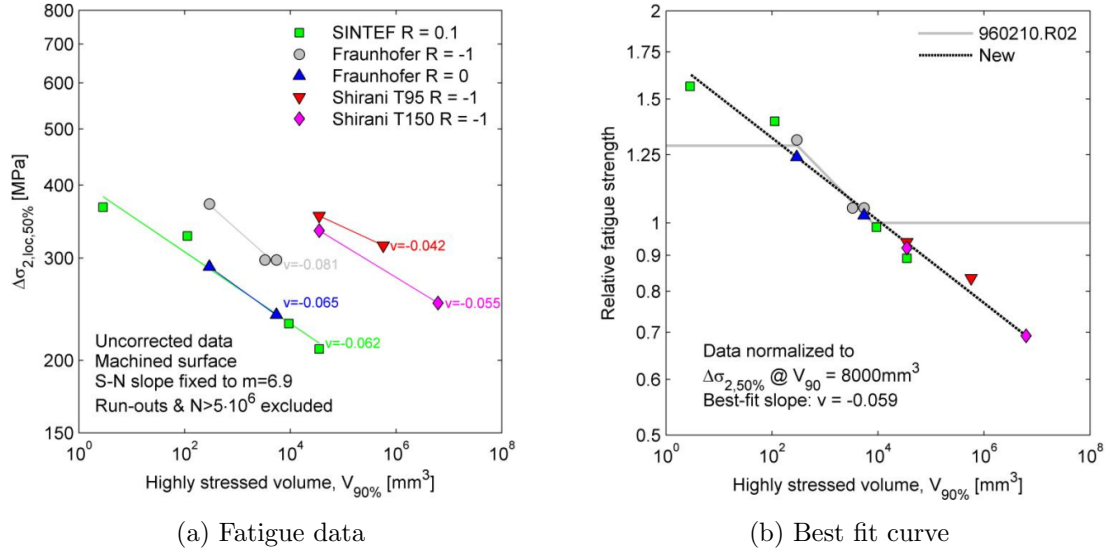


Figure C.4: Formulation of HBV correction factor

C.3.8 Min/max cut-off

The maximum cut-off level aims to prevent the analysis from dealing with non-linear plasticity, therefore leading to a value of

$$\Delta\sigma_{max,CO} = 2 \cdot \sigma_y. \quad (C.11)$$

The minimum cut-off value is set to 55 percent of the fatigue strength for the component

$$\Delta\sigma_{min,CO} = 0.55 \cdot \Delta\sigma_{f,CO}. \quad (C.12)$$

In order to justify the minimum cut-off, the component must be well protected against corrosion. Otherwise, the *SN curve* continues downwards and there is no minimum cut-off level, i.e. $\Delta\sigma_{min,CO} = 0$.

C.4 Component fatigue strength

For the sake of simplification, the correction factors were set to unity, meaning that the component is under conditions similar to testing. Naturally, this implies a certain amount of uncertainty, dampened by the safety factor.

The design safety factor is compiled from two separate components, one for the loading conditions and another for the material itself, both given in Table 3.2. When combined, the overall design safety factor is

$$\gamma_{fat} = \gamma_{m,fat} \cdot \gamma_{n,fat} = 1.20 \cdot 1.15 = 1.38. \quad (C.13)$$

Taking all the previous aspects in consideration, the design reference *SN curve* is displayed in Fig. C.5.

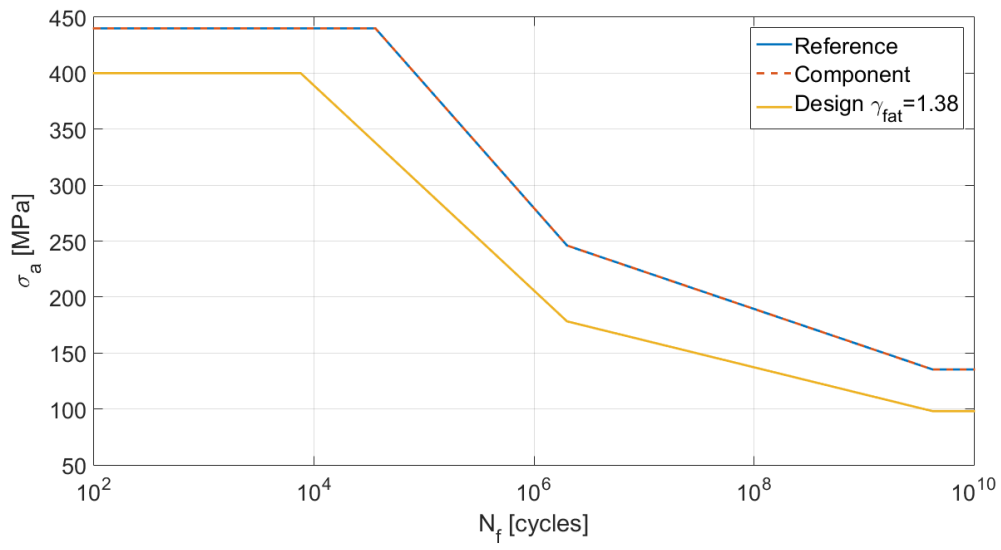


Figure C.5: SN curve for EN GJS400-18LT

Ansys element reference

This Appendix synthesizes the extra information on all the elements used in the FEM modelling. For each element, a brief summary is given, referring general aspects, such as application, number of nodes, geometry, etc. The mentioned elements can be divided into four main categories:

- Structural solid elements
- Structural plane elements
- Other elements

D.1 Structural solid elements

The structural solid elements are applied in three-dimensional structural analysis, i.e. aiming to obtain stresses and displacements as an output. Since one is dealing with a three-dimensional domain, there are three degrees of freedom (DOF) for each node: translations in O_x , O_y and O_z . The reviewed elements for this category are:

1. SOLID185
2. SOLID186
3. SOLID187

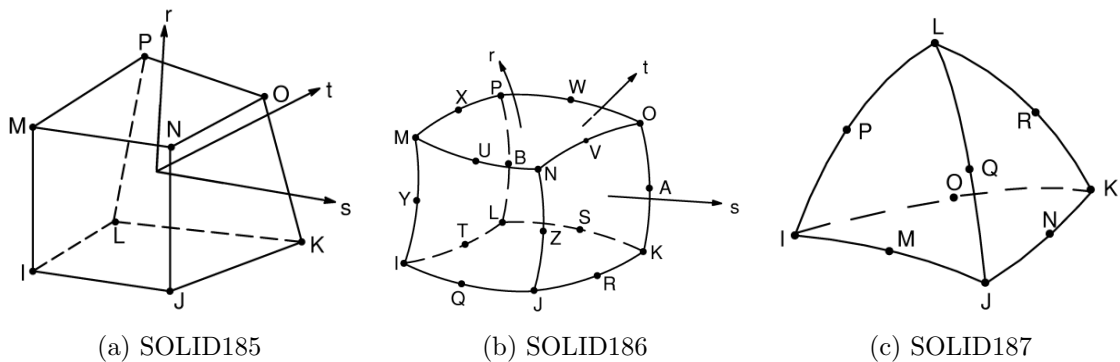


Figure D.1: Structural solid elements geometry [135]

D.1.1 SOLID185

The SOLID185 (see Fig. D.1a [135]) element is a 8-node solid element capable of coping with plasticity, hyperelasticity, stress stiffening, creep and large deflection or strain. It can be modelled into two different types:

1. Homogenous structural solid
2. Layered structural solid

The homogenous option is suitable for modelling solids, while the layered option is best for layered thick shells or solids. Also, this element may use selective or uniform reduced integration. The enhance strain formulations introduce 13 internal DOF to prevent shear and volumetric locking, and 9 DOF to prevent shear locking. If mixed displacement-pressure (u-P) formulation is employed with the enhanced strain formulations, only 9 DOF for overcoming shear locking are activated. The shape functions N_i are as follows:

$$\begin{aligned}
 N_1 &= \frac{1}{8}(1-s)(1-t)(1-r) & N_2 &= \frac{1}{8}(1+s)(1-t)(1-r) \\
 N_3 &= \frac{1}{8}(1+s)(1+t)(1-r) & N_4 &= \frac{1}{8}(1-s)(1+t)(1-r) \\
 N_5 &= \frac{1}{8}(1-s)(1-t)(1+r) & N_6 &= \frac{1}{8}(1+s)(1-t)(1+r) \\
 N_7 &= \frac{1}{8}(1+s)(1+t)(1+r) & N_8 &= \frac{1}{8}(1-s)(1+t)(1+r)
 \end{aligned} \tag{D.1}$$

with

$$u = \sum_{i=1}^8 N_i \cdot u_i \tag{D.2a}$$

$$v = \sum_{i=1}^8 N_i \cdot v_i \tag{D.2b}$$

$$w = \sum_{i=1}^8 N_i \cdot w_i \tag{D.2c}$$

where u_i are the nodal displacements.

D.1.2 SOLID186

The SOLID186 (see Fig. D.1b [135]) is a higher order 20-node solid element that exhibits quadratic displacement. It supports plasticity, hyperelasticity, stress stiffening, creep and large deflection or strain. It also has mixed formulation capability for simulating deformations of nearly incompressible elastoplastic materials, and fully incompressible hyperelastic materials. Similar to SOLID185, it may be modelled as a homogenous or layered solid. Moreover, its geometry may be altered in accordance to the application, transforming into four types: brick, wedge, pyramid or tetrahedral. For each geometry there is a different set of shape functions. For the brick type, they assume the form:

$$\begin{aligned}
N_1 &= \frac{1}{8}(1-s)(1-t)(1-r)(-s-t-r-2) & N_2 &= \frac{1}{8}(1+s)(1-t)(1-r)(s-t-r-2) \\
N_3 &= \frac{1}{8}(1+s)(1+t)(1-r)(s+t-r-2) & N_4 &= \frac{1}{8}(1-s)(1+t)(1-r)(-s+t-r-2) \\
N_5 &= \frac{1}{8}(1-s)(1-t)(1+r)(-s-t+r-2) & N_6 &= \frac{1}{8}(1+s)(1-t)(1+r)(s-t+r-2) \\
N_7 &= \frac{1}{8}(1+s)(1+t)(1+r)(s+t+r-2) & N_8 &= \frac{1}{8}(1-s)(1+t)(1+r)(-s+t+r-2) \\
N_9 &= \frac{1}{4}(1-s^2)(1-t)(1-r) & N_{10} &= \frac{1}{4}(1+s)(1-t^2)(1-r) \\
N_{11} &= \frac{1}{4}(1-s^2)(1+t)(1-r) & N_{12} &= \frac{1}{4}(1-s)(1-t^2)(1-r) \\
N_{13} &= \frac{1}{4}(1-s^2)(1-t)(1+r) & N_{14} &= \frac{1}{4}(1+s)(1-t^2)(1+r) \\
N_{15} &= \frac{1}{4}(1-s^2)(1+t)(1+r) & N_{16} &= \frac{1}{4}(1-s)(1-t^2)(1+r) \\
N_{17} &= \frac{1}{4}(1-s)(1-t)(1-r^2) & N_{18} &= \frac{1}{4}(1+s)(1-t)(1-r^2) \\
N_{19} &= \frac{1}{4}(1+s)(1+t)(1-r^2) & N_{20} &= \frac{1}{4}(1-s)(1+t)(1-r^2)
\end{aligned} \tag{D.3}$$

with

$$u = \sum_{i=1}^{20} N_i \cdot u_i \tag{D.4a}$$

$$v = \sum_{i=1}^{20} N_i \cdot v_i \tag{D.4b}$$

$$w = \sum_{i=1}^{20} N_i \cdot w_i. \tag{D.4c}$$

D.1.3 SOLID187

SOLID187 (see Fig. D.1c [135]) is a higher order, 10-node tetrahedral solid element. The element has a quadratic displacement behaviour, and is well suited for modelling irregular meshes. Similar to the previous elements, is capable of dealing with plasticity, hyperelasticity, stress stiffening, creep and large deflection or strain. Moreover, has mixed formulation capability for simulating deformations of nearly incompressible elastoplastic, and fully incompressible hyperelastic materials. The shape functions for this specific element are:

$$\begin{aligned}
N_1 &= L_1(2L_1 - 1) & N_2 &= L_2(2L_2 - 1) \\
N_3 &= L_3(2L_3 - 1) & N_4 &= L_4(2L_4 - 1) \\
N_5 &= L_1L_2 & N_6 &= L_2L_3 \\
N_7 &= L_1L_3 & N_8 &= L_1L_4 \\
N_9 &= L_2L_4 & N_{10} &= L_3L_4
\end{aligned} \tag{D.5}$$

with

$$u = \sum_{i=1}^{10} N_i \cdot u_i \quad (\text{D.6a})$$

$$v = \sum_{i=1}^{10} N_i \cdot v_i \quad (\text{D.6b})$$

$$w = \sum_{i=1}^{10} N_i \cdot w_i \quad (\text{D.6c})$$

where L_i are the volume coordinates.

D.2 Structural plane elements

The structural plane elements are applied in two-dimensional structural studies. This means they also allow for an axisymmetric model with or without torsion, i.e. a fully symmetrical model around an axis, representing only half domain as a simplification of the problem. In a two-dimensional domain there are two degrees of freedom per node: translations in O_x and O_y . If torsion is considered, an extra DOF to each node: a rotation around O_y . The reviewed elements are:

1. PLANE182
2. PLANE183

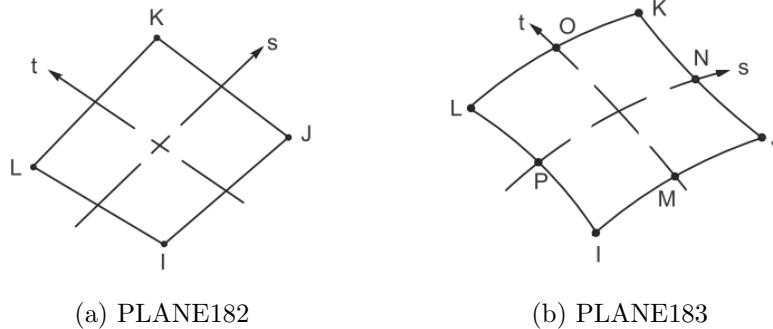


Figure D.2: Structural plane elements geometry [135]

D.2.1 PLANE182

PLANE182 (see Fig. D.2a [135]) is a 4-node plane element, capable of performing with with plasticity, hyperelasticity, stress stiffening, creep and large deflection or strain. Moreover, has mixed formulation capability for simulating deformations of nearly incompressible elastoplastic, and fully incompressible hyperelastic materials. It is also capable of assuming a triangular geometry when suited. In this case, the shape functions assume the form:

$$N_1 = L_1 \quad N_2 = L_2 \quad N_3 = L_3 \quad (\text{D.7})$$

with

$$u = \sum_{i=1}^3 N_i \cdot u_i \quad (\text{D.8a})$$

$$v = \sum_{i=1}^3 N_i \cdot v_i. \quad (\text{D.8b})$$

For the quad element, the interpolation functions are:

$$\begin{aligned} N_1 &= \frac{1}{4}(1-s)(1-t) & N_2 &= \frac{1}{4}(1+s)(1-t) \\ N_3 &= \frac{1}{4}(1+s)(1+t) & N_4 &= \frac{1}{4}(1-s)(1+t) \end{aligned} \quad (\text{D.9})$$

with

$$u = \sum_{i=1}^4 N_i \cdot u_i \quad (\text{D.10a})$$

$$v = \sum_{i=1}^4 N_i \cdot v_i. \quad (\text{D.10b})$$

D.2.2 PLANE183

PLANE183 (see Fig. D.2b [135]) is a higher order 2D, 8-node or 6-node element, depending on the geometry. This means that it can assume a quadrangular (8-node) or triangular (6-node) geometry. It has a quadratic displacement behaviour well suited from modelling irregular meshes. It is capable of performing with with plasticity, hyperelasticity, stress stiffening, creep and large deflection or strain. Moreover, has mixed formulation capability for simulating deformations of nearly incompressible elastoplastic, and fully incompressible hyperelastic materials. For the quadrangular shape, the interpolation functions are:

$$\begin{aligned} N_1 &= \frac{1}{4}(1-s)(1-t)(-s-t-1) & N_2 &= \frac{1}{4}(1+s)(1-t)(s-t-1) \\ N_3 &= \frac{1}{4}(1+s)(1+t)(s+t-1) & N_4 &= \frac{1}{4}(1-s)(1+t)(-s+t-1) \\ N_5 &= \frac{1}{2}(1-s^2)(1-t) & N_6 &= \frac{1}{2}(1+s)(1-t^2) \\ N_7 &= \frac{1}{2}(1-s^2)(1+t) & N_8 &= \frac{1}{2}(1-s)(1-t^2) \end{aligned} \quad (\text{D.11})$$

with

$$u = \sum_{i=1}^8 N_i \cdot u_i \quad (\text{D.12a})$$

$$v = \sum_{i=1}^8 N_i \cdot v_i. \quad (\text{D.12b})$$

For the triangular geometry, the shape functions assume the form:

$$\begin{aligned} N_1 &= L_1(2L_1 - 1) & N_2 &= L_2(2L_2 - 1) & N_3 &= 2L_3 - 1 \\ N_4 &= 4L_1L_2 & N_5 &= 4L_2L_3 & N_6 &= 4L_3L_1 \end{aligned} \quad (\text{D.13})$$

with

$$u = \sum_{i=1}^6 N_i \cdot u_i \quad (\text{D.14a})$$

$$v = \sum_{i=1}^6 N_i \cdot v_i. \quad (\text{D.14b})$$

D.3 Other elements

This Section comprises all the other types of used elements, being contact, target, surface and beam elements.

D.3.1 CONTA174

CONTA174 (see Fig. D.3 [135]) is a 8-node surface-to-surface contact, used to represent contact and sliding between three-dimensional target surfaces and a deformable surfaces, defined by this element. Hence, it is located on the surfaces of 3D solid (SOLID185, SOLID186, SOLID187) and shell (SHELL281) elements with or without mid-side elements.

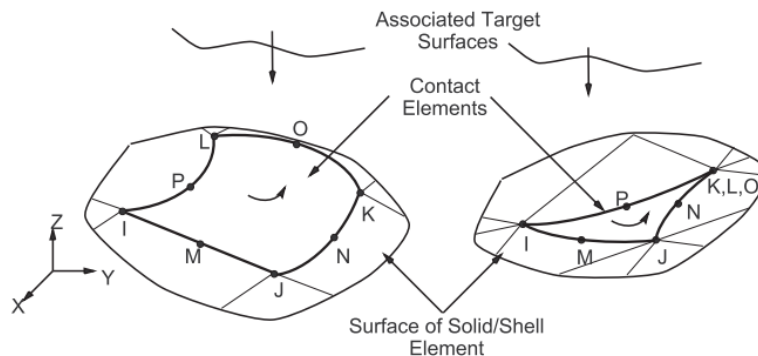


Figure D.3: CONTA174 element geometry [135]

CONTA174 can assume a quadrangular or triangular shape. For the quad shape, the interpolation functions and displacements assume the organization of Eqs. (D.11), (D.12a) and (D.12b). For the triangular geometry, the displacement behaviour follows Eqs. (D.13), (D.14a) and (D.14b).

D.3.2 TARGE170

In the study of contact between two bodies, it is commonly used the “contact-target” pair concept, i.e. the surface of one body is conventionally taken as a contact while the surface of the other body as a target surface. For flexible-rigid contact, the contact surface is associated with the deformable body, while for flexible-flexible contact, the both contact and target surface correspond to deformable bodies. Hence, TARGE170 (see Fig. D.4 [135]) is simply a geometric entity in space that senses and responds when one or more contact elements move into a target segment element [135].

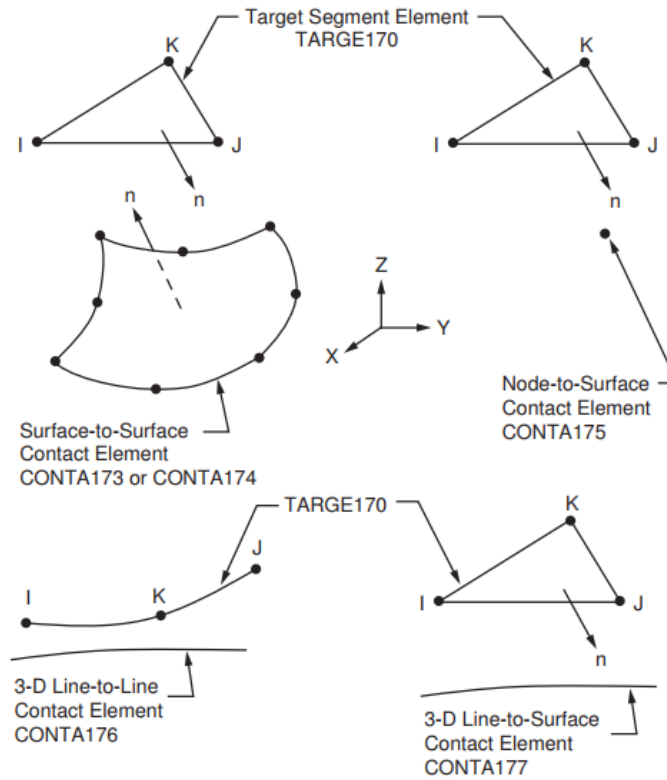


Figure D.4: TARGE170 geometry overview [135]

D.3.3 SURF154

SURF154 (see Fig. D.5 [135]) is used for various load and surface effect, such as uniform or distributed pressure, application in three-dimensional structural analysis. The element can be defined by four to eight nodes, allowing for the choice of a quadrangular or triangular geometry, with or without mid-side nodes. For a 8-node (with mid-side nodes)

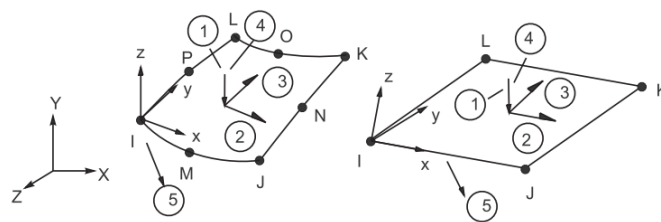


Figure D.5: SURF154 geometry overview [135]

and 4-node (without mid-side nodes) quad shape, the displacement behaviour follows Eq. (D.11) with

$$w = \sum_{i=1}^8 N_i \cdot w_i \tag{D.15}$$

and Eq. (D.9) with

$$w = \sum_{i=1}^4 N_i \cdot w_i \tag{D.16}$$

respectively. For a 6-node (with mid-side nodes) triangular shape, the displacement behaviour follows Eq. (D.13) with

$$w = \sum_{i=1}^6 N_i \cdot w_i. \quad (\text{D.17})$$

For a 3-node (without mid-side nodes) triangular element, the displacement is not explicitly defined. A discrete Kirchhoff theory (DKT) element is used instead.

D.3.4 BEAM188

BEAM188 (see Fig. D.6 [135]) is a three-dimensional, 2-node beam element, suitable for analysing slender to moderately thick beam structures. The element is based on Timoshenko beam theory, which includes shear deformation effects. Moreover, it provides options for restrained or unrestrained warping of cross-sections. BEAM188 has six or seven DOF per node: translations and rotations in/about the O_x , O_y and O_z directions, with a possibility for an extra DOF to account the warping effect. This element is well suited for liner, large rotation, and/or larger strain non-linear applications. Moreover, it also supports elasticity, plasticity and creep.

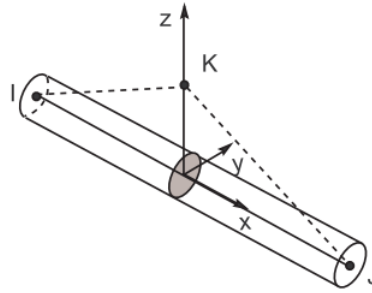


Figure D.6: BEAM188 geometry overview [135]

BEAM188 also gives the option to choose a linear, quadratic or cubic interpolation for the DOF. According to the chosen distribution, the element assumes the following organization:

Linear

$$N_1 = \frac{1}{2}(1 - s) \quad N_2 = \frac{1}{2}(1 + s) \quad (\text{D.18})$$

with

$$\begin{aligned} u &= \sum_{i=1}^2 N_i \cdot u_i, & v &= \sum_{i=1}^2 N_i \cdot v_i, & z &= \sum_{i=1}^2 N_i \cdot z_i, \\ \theta_x &= \sum_{i=1}^2 N_i \cdot \theta_{x,i}, & \theta_y &= \sum_{i=1}^2 N_i \cdot \theta_{y,i}, & \theta_z &= \sum_{i=1}^2 N_i \cdot \theta_{z,i}. \end{aligned} \quad (\text{D.19})$$

Quadratic

$$N_1 = \frac{1}{2}(-s + s^2) \quad N_2 = \frac{1}{2}(s + s^2) \quad N_3 = \frac{1}{2}(1 - s^2) \quad (\text{D.20})$$

with

$$\begin{aligned}
 u &= \sum_{i=1}^3 N_i \cdot u_i, & v &= \sum_{i=1}^3 N_i \cdot v_i, & z &= \sum_{i=1}^3 N_i \cdot z_i, \\
 \theta_x &= \sum_{i=1}^3 N_i \cdot \theta_{x,i}, & \theta_y &= \sum_{i=1}^3 N_i \cdot \theta_{y,i}, & \theta_z &= \sum_{i=1}^3 N_i \cdot \theta_{z,i}.
 \end{aligned} \tag{D.21}$$

Cubic

$$\begin{aligned}
 N_1 &= \frac{1}{16}(-9s^3 + 9s^2 + s - 1) & N_2 &= \frac{1}{16}(9s^3 + 9s^2 - s - 1) \\
 N_3 &= \frac{1}{16}(27s^3 - 9s^2 - 27s + 9) & N_4 &= \frac{1}{16}(-27s^3 - 9s^2 - 27s + 9)
 \end{aligned} \tag{D.22}$$

with

$$\begin{aligned}
 u &= \sum_{i=1}^4 N_i \cdot u_i, & v &= \sum_{i=1}^4 N_i \cdot v_i, & z &= \sum_{i=1}^4 N_i \cdot z_i, \\
 \theta_x &= \sum_{i=1}^4 N_i \cdot \theta_{x,i}, & \theta_y &= \sum_{i=1}^4 N_i \cdot \theta_{y,i}, & \theta_z &= \sum_{i=1}^4 N_i \cdot \theta_{z,i}.
 \end{aligned} \tag{D.23}$$

Lug optimization - analytic approximation

If one cares to look closely to the pitch support, finds that the interface with the hydraulic cylinder resembles a lug, both in terms of shape and in loading. Therefore, a simplification can be made aiming to preform an analytic optimization based on the loading conditions, in order to have a fast and efficient first approach on the optimal size of the component.

The optimization was carried out using MATLAB, using both mathematical programming and genetic algorithms, in order to assess their differences, advantages and setbacks. Although this approach is an over-simplification, the fast computation of the results and the validated methodology based on empirical observations give solid advantages in using it as a first approach. It is also important to note that the proposed method is only validated for steel and aluminium alloys. Safety factors were used to take this problem into account.

E.1 Lug analysis - transverse force

The used method was proposed by Niu [136] and it serves a wide range of applications, since it has a dedicated approach for each load case:

1. Axial load ($\alpha = 0$ deg)
2. Transverse load ($\alpha = 90$ deg)
3. Oblique load (0 deg $< \alpha < 90$ deg)

For the purpose of this study, only case II (transverse load) was used.

Analysing the lug represented in Fig. E.1, five design variables define the problem, directly influencing the results. In this particular case, the D and L variables are constant, for installation constraints, while the rest are the unknown variables from the optimization problem, i.e. the “real” design variables.

The method proposes to determine the maximum allowable shear force for a specific material and design variables. For this reason, the inputs are the mentioned variables and the yield strength σ_y for the respective material. The constants for the problem are displayed in the Table E.1.

Another important aspect are the restrictions of this analysis. This comprises the safety factors to be accounted as well as constraints to design variables. Having said that, the problem restrictions are as follows:

1. Fitting safety factor of $\lambda = 1.15$

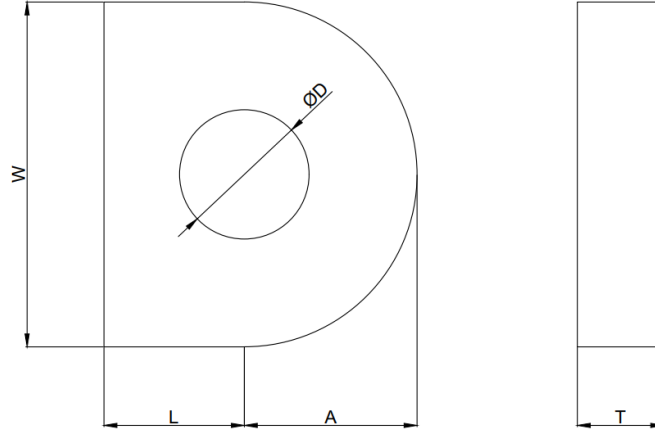


Figure E.1: Lug Schematic

Problem constants		
Yield strength	Hole diameter D	Hole height L
220 MPa	120 mm	130 mm

Table E.1: Lug analysis problem constants

2. Minimum safety factor of $\gamma = 1.2$
3. Thickness to hole diameter ratio $T/D > 0.3$

Restriction 3 implies that the thickness of the lug must be $T > 36$ mm.

The maximum shear force for a specific design, working only in the linear-elastic regime, is given by the expression

$$P_{uly} = K_{uly} \cdot A_{br} \cdot \sigma_y \quad (\text{E.1})$$

with

$$A_{br} = D \cdot T \quad (\text{E.2})$$

where A_{br} is the projected bearing area and K_{uly} is the efficiency factor. This factor, which comes from empirical analysis and displays a non-linear behaviour, is dependent on

$$K_{uly} = \left(\frac{A_{av}}{A_{br}} \right) \quad (\text{E.3})$$

with

$$A_{av} = \frac{6}{3/A_1 + 1/A_2 + 1/A_3 + 1/A_4} \quad (\text{E.4})$$

where the respective areas are displayed in Fig. E.2a. The curve fitting for this parameter

was performed by a polynomial regression and its behaviour is displayed in Fig. E.2b. The factor K_{uly} follows the expression

$$K_{uly} = -0.0168 \left(\frac{A_{av}}{A_{br}} \right)^3 - 0.338 \left(\frac{A_{av}}{A_{br}} \right)^2 + 1.4251 \left(\frac{A_{av}}{A_{br}} \right) - 0.0056. \quad (\text{E.5})$$

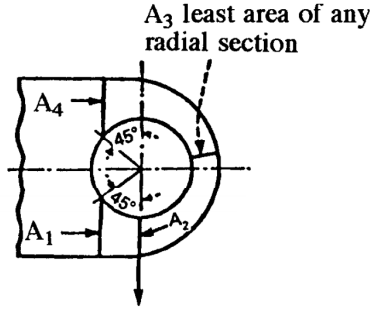
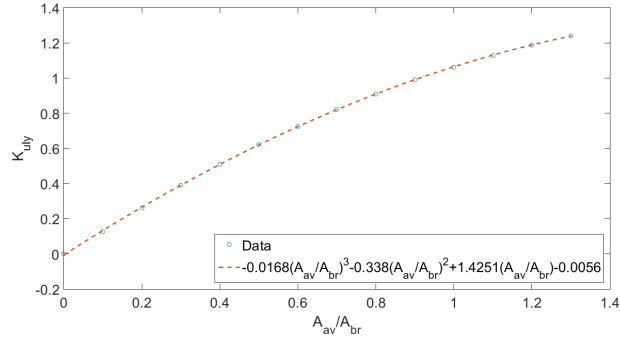
(a) Design areas for the K_{av} computation(b) Efficiency factor K_{uly} curve fitting

Figure E.2: Efficiency factor computation

E.2 Lug optimization

As mentioned earlier, MATLAB optimization tools were used, namely the mathematical programming and genetic algorithms. The design variables are the thickness T , width W and height A . The objective function is to minimize the total volume, defined by

$$J(W, T, A) = T \cdot [W \cdot L + \pi(W/2)^2 - W(W/2 - A) - \pi(D/2)^2] = T \cdot [W^2(\pi/4 - 1/2) + W(L + A) - \pi D^2/4] \quad (\text{E.6})$$

In terms of variable constraints, the thickness and height must be restricted in the lower bound. The height cannot be smaller than the radius of the hole, for functionality purposes, since there must be material around the hole. For the purpose of facilitating convergence in both methods, lower and upper bounds were set. Also, a mechanical constraint must be set, related with the application specifically, since the lug must withstand the extreme conditions, defined by

$$P_{uly} \geq \frac{1}{2} \cdot 623 \text{ kN} \cdot \lambda \cdot \gamma = 429.87 \text{ kN}. \quad (\text{E.7})$$

Having said that, the overall layout of the optimization problem is

$$\text{Find } W, T, A \quad (\text{E.8a})$$

$$\text{to minimize } J(W, T, A, D, L) = T \cdot [W^2(\pi/4 - 1/2) + W(L + A) - \pi D^2/4] \quad (\text{E.8b})$$

$$\text{subject to } P_{uly} \geq 429.87 \text{ kN} \quad (\text{E.8c})$$

$$D = 120 \text{ mm}, \quad L = 130 \text{ mm} \quad (\text{E.8d})$$

$$150 \text{ mm} \leq W \leq 200 \text{ mm} \quad (\text{E.8e})$$

$$36 \text{ mm} \leq T \leq 50 \text{ mm} \quad (\text{E.8f})$$

$$80 \text{ mm} \leq A \leq 120 \text{ mm} \quad (\text{E.8g})$$

Finally, the optimization process leaded by the genetic algorithm was processed in five runs, with different number of maximum generations. A very small value was chosen for the convergence limit, so that the process runs all the way to the final number of generations, saving the best set of values. With this, the goal is to assess the influence of the number of iterations in the result as well as the computation cost. The limit of generations was set by: 100, 500, 1000, 2000 and 10000. In terms of the other parameters, the setting is displayed in Table E.2.

GA settings	
Parameter	Value
Generations	100,500,1000,2000,10000
Population size	100
Crossover fraction	0.7
Migration fraction	0.1
Migration interval	50,250,500,1000,5000
Convergence limit	1×10^{-6}
Elite count	20

Table E.2: Overview on the genetic algorithm setting for the lug analysis

E.3 Results

Tables E.3a and E.3b display the results from the optimization analysis, taken from each algorithm. After close observation, the reader can easily conclude that the mathematical programming approach presents a more precise and efficient process for this application. In addition to returning the best result, it is immeasurably faster than the genetic algorithm, specially for results characterized from smaller constraint deviations.

Another curious aspect is that the genetic algorithm does not seem to converge to any particular solution. Well this is to be expected from this type of algorithms, since the possible solutions are infinite and the design only selects iteratively the best outcome. As one might expect, with more iterations (generations) the solution tends to be closer to the constraint, i.e. more optimal. This is supported by the result in Table E.3a.

GA results

Generations	Width [mm]	Thickness [mm]	Height [mm]	Volume [$\times 10^6 \text{mm}^3$]	Capacity^a	Elapsed time [s]
100	177.5237	38.5143	91.2577	1.4236	1.0010	2.0252
500	178.1494	36.4487	101.4161	1.4206	1.0005	6.8111
1000	181.5073	36.3774	94.8963	1.4156	1.0007	14.0799
2000	173.3164	39.5458	93.6215	1.4245	1.0000	27.7777
10000	178.8790	38.4507	89.4887	1.4259	1.0001	158.1655

(a) Genetic algorithm

Mathematical programming results

Width [mm]	Thickness [mm]	Height [mm]	Volume [$\times 10^6 \text{mm}^3$]	Capacity	Elapsed time [s]
181.7819	36.0000	96.3345	1.4135	1.0000	0.0986

(b) Mathematical programming algorithm

Table E.3: Result overview of the lug analysis

Figures E.3a to E.3e display the previous point very clearly. Each image displays the intersection between the optimal solutions with a linearized capacity equal to unity, i.e. the design space that comprises a null constraint deviation, and the solutions with the same linearized volume as the respective result. Note that the result is one of the points of the intersection between these planes. This means that just for the specified volume,

there are an infinite number of solutions, each of them a very close approximation of the optimal solution, but nonetheless an approximation with a defined deviation.

However, for the mathematical programming solution, represented in Fig. E.3f, the solution is the intersection of the design space for the specific volume and the optimal values for null constraint deviation in one point, ensuring this is the best possible solution, in terms of “squeezing” the design space as best as the optimization process can. Therefore, this is the preferred solution, representing a volume reduction of 71.63 percent.

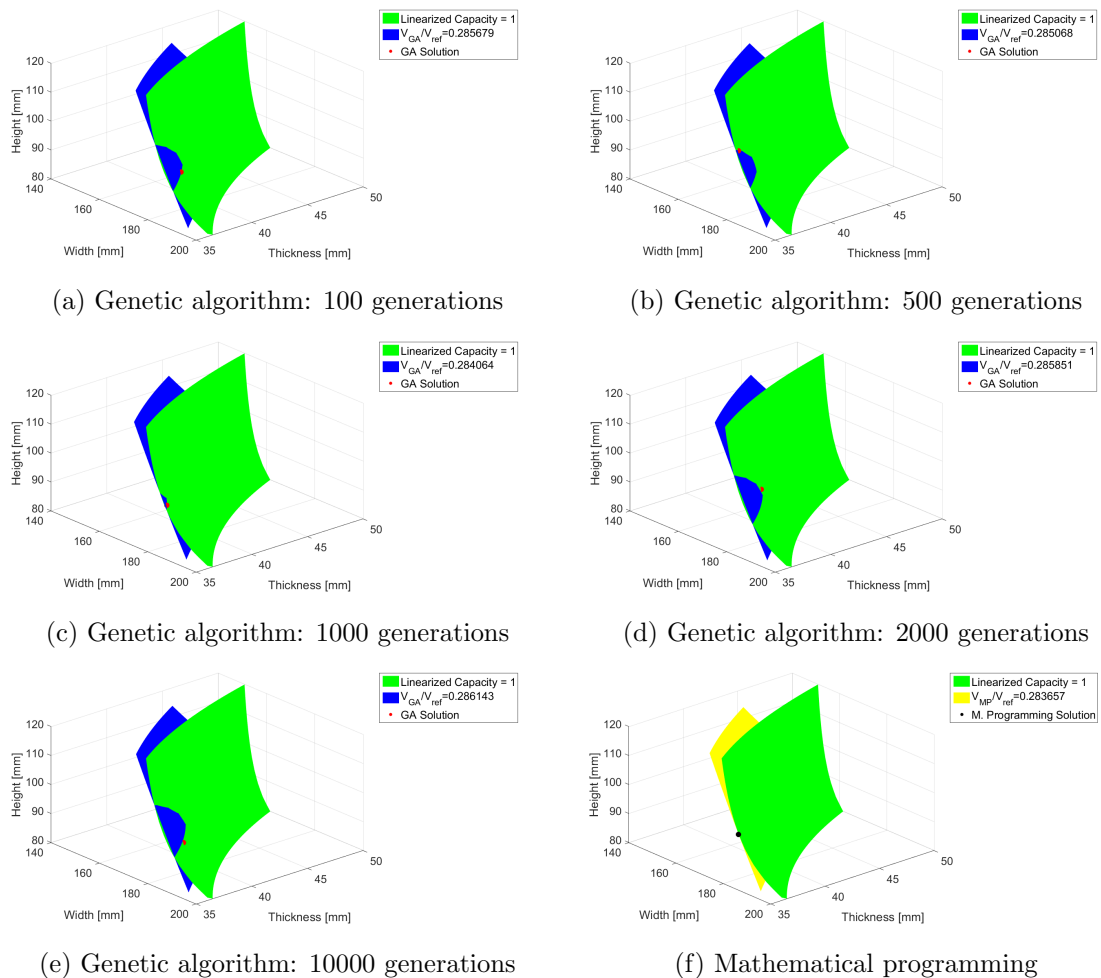


Figure E.3: Solutions design space analysis

E.4 MATLAB code

E.4.1 Optimization mainframe

```

1 %*****ANALYTICAL OPTIMIZATION*****
2 function OptLug(lwidth ,uwidth ,lthick ,uthick ,lheight ,uheight ,...
3     genlimit)
4 %Parameters range*****
5 plimit=[lwidth ,lthick ,lheight ;uwidth ,uthick ,uheight ];
6 %*****

```

```
7 %Constants*****
8 %Hole diameter:
9 D=120;
10 %Extreme load:
11 Pmax=623e3 * 1.15 * 1.2 / 2;
12 %Lug length:
13 l=130;
14 %Reference volume:
15 Vref=(230*320 - pi*120^2/4) * 80;
16 %Material tensile yield strength
17 sy=220;
18 %*****
19
20 %*****GENETIC ALGORITHM OPTIMIZATION*****
21 %Initialize variables
22 P1=zeros(length(genlimit),6);
23 R1=zeros(length(genlimit),1);
24 for i=1:length(genlimit)
25 %GA options
26 options=gaoptimset('PopInitRange',plimit,'Generations',...
27     genlimit(i),'PopulationSize',100,'CrossoverFraction',0.7,...
28     'MigrationFraction',0.1,'MutationFcn',...
29     {@mutationuniform,0.01},'MigrationInterval',...
30     0.5*genlimit(i),'TolFun',1e-6,'StallGenLimit',Inf,...
31     'PopulationType','doubleVector','SelectionFcn',...
32     @selectionroulette,'EliteCount',20,'PlotFcns',...
33     {@gaplotbestf},'TimeLimit',3600);
34
35 %GA optimization
36 tic
37 [P,fval]=ga(@fitnessfunction,3,options);
38 et=toc;
39 R=fval/Vref;
40 P1(i,1:3)=P;P1(i,4)=fval;P1(i,5)=pmax(P(1),P(2),P(3),D,sy,Pmax);
41 P1(i,6)=et;
42 R1(i)=R;
43 end
44 display(P1(:,1:3))
45 display(P1(:,4))
46 display(P1(:,5))
47 display(P1(:,6))
48 display(R1)
49 %*****
50
51 %*****MATLAB CONSTRAINED MINIMIZATION*****
52 %Initialize variables
53 P2=zeros(1,6);
54
55 fun = @(x)x(2) * (x(1)^2 * (pi/4 - 0.5) + x(1) * (1 + x(3)) - pi * D^2/4);
```

```

56
57 x0=[200,60,120];
58
59 lb=[lwidth,lthick,lheight];
60 ub=[uwidth,uthick,uheight];
61
62 A=[];b=[];Aeq=[];beq=[];
63
64 nonlcon=@nonlconst;
65 tic
66 [x,fval]=fmincon(fun,x0,A,b,Aeq,beq,lb,ub,nonlcon);
67 et=toc;
68 display(x)
69 display(fval)
70 P2(1,1:3)=x;P2(1,4)=fval;P2(1,5)=pmax(x(1),x(2),x(3),D,sy,Pmax);
71 P2(1,6)=et;
72 R=fval/Vref;
73 R2=R;
74 display(P2(1,1:3))
75 display(P2(:,4))
76 display(P2(:,5))
77 display(P2(:,6))
78 display(R2)
79 %*****
80
81 %Plot function behaviour*****
82 width=lwidth:(uwidth-lwidth)/100:uwidth;
83 thick=lthick:(uthick-lthick)/100:uthick;
84 height=lheight:(uheight-lheight)/10:uheight;
85
86 plot4d(width,thick,height,D,l,Pmax,Vref,sy,P1,P2,R1,R2);
87 %*****
88 end
89
90
91 %*****AUXILIARY FUNCTIONS*****
92 %Non linear constraint
93 function [c,ceq]=nonlconst(x)
94 Abr=120*x(2);
95 A1=((x(1)/2)-120/2*sin(pi/4))*x(2);A4=A1;
96 A2=(x(1)/2-120/2)*x(2);
97 A3=(x(3)-120/2)*x(2);
98 Aav=6/(3/A1+1/A2+1/A3+1/A4);
99
100 %Max shear force
101 K=-0.0168*(Aav/Abr)^3-0.338*(Aav/Abr)^2+1.4251*(Aav/Abr)-0.0056;
102 Py=(220*K*Abr);
103
104 c=623e3*1.15*1.2/2/Py-1;

```

```
105 ceq = [];  
106 end  
107  
108 %Plot solutions  
109 function plot4d(w,t,a,d,l,Pmax,Vref,sy,P1,P2,R1,R2)  
110 [x,y,z]=meshgrid(w,t,a);  
111 Abr=d*y;  
112 A1=((x./2)-d/2*sin(pi/4)).*y;A4=A1;  
113 A2=(x./2.-d/2).*y;  
114 A3=(z-d/2).*y;  
115 Aav=6./(3./A1+1./A2+1./A3+1./A4);  
116  
117 %Max shear force  
118 K=-0.0168*(Aav./Abr).^3-0.338*(Aav./Abr).^2+1.4251*(Aav./Abr)...  
119     -0.0056;  
120 Py=(sy*K.*Abr)./Pmax;  
121  
122 %Volume  
123 V=(y.*(x.^2*(pi/4-0.5)+x.*(1+z)-pi*d^2/4))./Vref;  
124  
125 %Plot  
126 for i=1:length(R1)  
127 figure  
128 p = patch(isosurface(x,y,z,Py,1));  
129 set(p,'FaceColor','green','EdgeColor','none')  
130 view(49,35)  
131 grid on  
132 xlabel('Width [mm]')  
133 ylabel('Thickness [mm]')  
134 zlabel('Height [mm]')  
135 set(gca,'FontSize',20)  
136 hold all;  
137  
138 p1 = patch(isosurface(x,y,z,V,R1(i)));  
139 set(p1,'FaceColor','blue','EdgeColor','none')  
140 hold all  
141  
142 p3 = scatter3(P1(i,1),P1(i,2),P1(i,3),100,'red','filled');  
143 legend([p,p1,p3],{'Linearized Capacity = 1',...  
144     sprintf('V_{GA}/V_{ref}=%2f',R1(i)),'GA Solution'},...  
145     'FontSize',20)  
146 hold off  
147 end  
148  
149 figure  
150 p = patch(isosurface(x,y,z,Py,1));  
151 set(p,'FaceColor','green','EdgeColor','none')  
152 view(49,35)  
153 grid on
```

```

154 xlabel('Width [mm]')
155 ylabel('Thickness [mm]')
156 zlabel('Height [mm]')
157 set(gca,'FontSize',20)
158 hold all;
159
160 p2 = patch(isosurface(x,y,z,V,R2));
161 set(p2,'FaceColor','yellow','EdgeColor','none')
162 hold all
163
164 p4 = scatter3(P2(1),P2(2),P2(3),100,'black','filled');
165
166 legend([p,p2,p4],{'Linearized Capacity = 1',...
167     sprintf('V_{MP}/V_{ref}=%2f',R2),...
168     'M. Programming Solution'},'FontSize',20)
169 hold off
170 end
171
172 %Maximum capacity
173 function P = pmax(w,t,a,d,sy,Pmax)
174 Abr=d*t;
175 A1=((w/2)-d/2*sin(pi/4))*t;A4=A1;
176 A2=(w/2-d/2)*t;
177 A3=(a-d/2)*t;
178 Aav=6/(3/A1+1/A2+1/A3+1/A4);
179
180 %Max shear force
181 K=-0.0168*(Aav/Abr)^3-0.338*(Aav/Abr)^2+1.4251*(Aav/Abr)...
182     -0.0056;
183 P=sy*K*Abr/Pmax;
184 end
185 %*****

```

E.4.2 Fitness function

```

1 %*****FITNESS FUNCTION*****
2 function fitvalue=fitnessfunction(P)
3 %Constants*****
4 %Hole diameter:
5 D=120;
6 %Extreme load:
7 Pmax=623e3*1.15*1.2/2;
8 %Lug length:
9 l=130;
10 %Material tensile yield strength
11 sy=220;
12 %Read parameters*****
13 %Width:
14 W=P(1);
15 %Thickness:

```

```

16 t=P(2);
17 %Height:
18 a=P(3);
19 %Compute the maximum yield force****
20 Abr=D*t;
21 A1=(W/2-D/2*sin(pi/4))*t;A4=A1;
22 A2=(W/2-D/2)*t;
23 A3=(a-D/2)*t;
24 Aav=6/(3/A1+1/A2+1/A3+1/A4);
25
26 K=-0.0168*(Aav/Abr)^3-0.338*(Aav/Abr)^2+1.4251*(Aav/Abr)...
27     -0.0056;
28 Py=K*Abr*sy;
29
30 %Fitnesss function value*****
31 if ((t/D>0.3)&&(a>D/2)&&(W>D)&&(Py>=Pmax))
32     fitvalue=t*(W^2*(pi/4-0.5)+W*(1+a)-pi*D^2/4);
33 else
34     fitvalue=10^9;
35 end
36 end
37 %*****

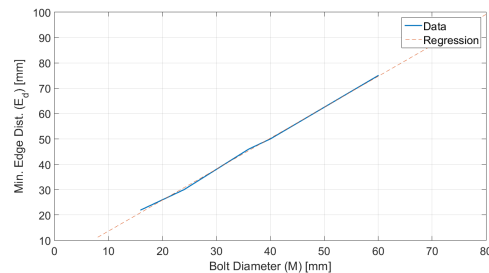
```

Minimum edge distance for bolted connections

A recurrent design aspect is the minimum edge distance in bolted connections, which is the distance from the centre of the hole to an edge of the connected part in any direction. The American Institute of Steel Constructions (AISC) [137] reviewed this problem and came up with an analytic correlation between the minimum distance and the size of the bolt. This correlation is displayed in Fig. F.1a [137].

TABLE J3.4M Minimum Edge Distance, ^[a] mm, from Center of Standard Hole ^[b] to Edge of Connected Part		
Bolt Diameter (mm)	At Sheared Edges	At Rolled Edges of Plates, Shapes or Bars, or Thermally Cut Edges ^[c]
16	28	22
20	34	26
22	38 ^[d]	28
24	42 ^[d]	30
27	48	34
30	52	38
36	64	46
Over 36	1.75d	1.25d

^[a] Lesser edge distances are permitted to be used provided provisions of Section J3.10, as appropriate, are satisfied.
^[b] For oversized or slotted holes, see Table J3.5M.
^[c] All edge distances in this column are permitted to be reduced 3 mm when the hole is at a point where required strength does not exceed 25 percent of the maximum strength in the element.
^[d] These are permitted to be 32 mm at the ends of beam connection angles and shear end plates.



(a) Minimum edge distance correlation in mm [137] (b) Linear regression of the minimum edge distance

Figure F.1: Overview on the minimum edge distance

Aiming to input the computation of this value as a reference for the parametric design in Chapter 5, a linear regression is to be made, assuming the respective error. The incurring error is mainly due to the difference in material, since this relation is to be applied to a cast iron part rather than a steel one. Nonetheless, it is believed to be a good approximation and a solid reference value. A graphic overview of this process is depicted in Fig. F.1b. The linear correlation displayed is expressed by

$$E_d = 1.2209 \cdot M + 1.4553 \tag{F.1}$$

where M is the nominal diameter of the bolt, e.g. M10, and E_d is the minimum value of the edge distance, computed in millimetres.

Comparison between first and superior order elements

Aiming for a better understanding of the consequences regarding the element choice for the mesh of the model used in the parametric optimization (see Chapter 5), a study was made comparing the result output of the same model, using the two types of elements.

The choice of the mesh elements is an important aspect in FEM modelling and may significantly impact the results. The stress/deformation and geometric interpolation are key aspects for this subject, since the type of element directly impacts these two characteristics. A brief explanation in what way it impacts is presented next.

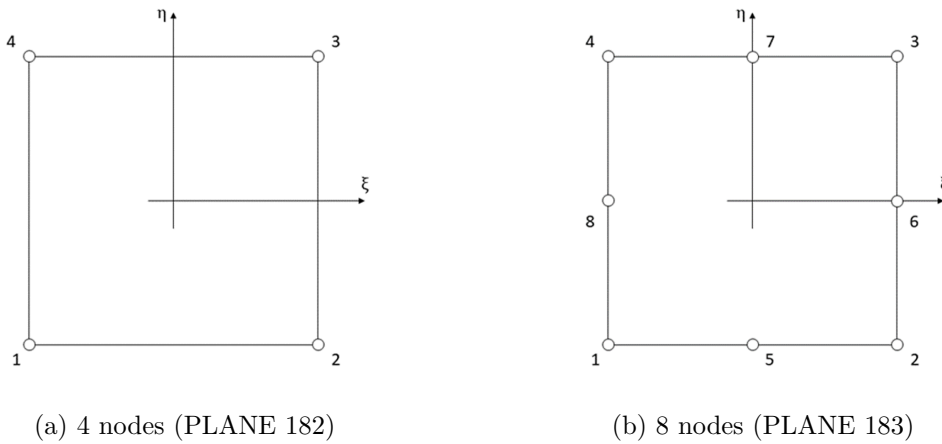


Figure G.1: Coordinate system for 2D quadrilateral elements

G.1 Quadrilateral 4-node element

The quadrilateral 4-node elements (see Fig. G.1a), referenced in Ansys by PLANE 182, are first order elements with the following shape functions

$$N_1 = \frac{1}{4}(1 - \xi)(1 - \eta) \tag{G.1a}$$

$$N_2 = \frac{1}{4}(1 + \xi)(1 - \eta) \tag{G.1b}$$

$$N_3 = \frac{1}{4}(1 + \xi)(1 + \eta) \tag{G.1c}$$

$$N_4 = \frac{1}{4}(1 - \xi)(1 + \eta) \tag{G.1d}$$

and the displacement in a certain point is

$$u = \sum_{i=1}^4 N_i \cdot u_i \quad (\text{G.2a})$$

$$u = \sum_{i=1}^4 N_i \cdot v_i \quad (\text{G.2b})$$

where ξ and η are the point coordinates. Hence, for a displacement vector

$$\{d\} = \begin{Bmatrix} u_1 \\ v_1 \\ \vdots \\ u_4 \\ v_4 \end{Bmatrix} \quad (\text{G.3})$$

the displacement in an arbitrary point can be resumed in the matrix form by

$$\{u\} = [N] \times \{d\} \quad (\text{G.4})$$

with

$$[N] = \begin{bmatrix} N_1 & 0 & N_2 & 0 & N_3 & 0 & N_4 & 0 \\ 0 & N_1 & 0 & N_2 & 0 & N_3 & 0 & N_4 \end{bmatrix}. \quad (\text{G.5})$$

Taking into account that the deformation is

$$\{\varepsilon\} = \mathcal{L}[N] \times \{d\} \quad (\text{G.6})$$

where \mathcal{L} is a differential operator so that

$$\mathcal{L}[N] = \begin{bmatrix} \frac{\partial N_1}{\partial \xi} & 0 & \dots & \frac{\partial N_4}{\partial \xi} & 0 \\ 0 & \frac{\partial N_1}{\partial \eta} & \dots & 0 & \frac{\partial N_4}{\partial \eta} \\ \frac{\partial N_1}{\partial \eta} & \frac{\partial N_1}{\partial \xi} & \dots & \frac{\partial N_4}{\partial \eta} & \frac{\partial N_4}{\partial \xi} \end{bmatrix}. \quad (\text{G.7})$$

Equations (G.1a) to (G.1d) and (G.7) are decisive in understanding the consequences of such elements. The geometrical approximations given in (G.1a) to (G.1d) are linear as well as the stress/deformation distribution, given in (G.7).

G.2 Quadrilateral 8-node element

For the 8-node quadrilateral elements (see Fig. G.1b), referenced in Ansys by PLANE 183, the shape functions are

$$N_1 = \frac{1}{4}(1 - \xi)(1 - \eta)(-\xi - \eta - 1) \quad (\text{G.8a})$$

$$N_2 = \frac{1}{4}(1 + \xi)(1 - \eta)(\xi - \eta - 1) \quad (\text{G.8b})$$

$$N_3 = \frac{1}{4}(1 + \xi)(1 + \eta)(\xi + \eta - 1) \quad (\text{G.8c})$$

$$N_4 = \frac{1}{4}(1 - \xi)(1 + \eta)(-\xi + \eta - 1) \quad (\text{G.8d})$$

$$N_5 = \frac{1}{2}(1 - \xi^2)(1 - \eta) \quad (\text{G.8e})$$

$$N_6 = \frac{1}{2}(1 + \xi)(1 - \eta^2) \quad (\text{G.8f})$$

$$N_7 = \frac{1}{2}(1 - \xi^2)(1 + \eta) \quad (\text{G.8g})$$

$$N_8 = \frac{1}{2}(1 - \xi)(1 + \eta^2) \quad (\text{G.8h})$$

interpolating the displacements with

$$u = \sum_{i=1}^8 N_i \cdot u_i \quad (\text{G.9a})$$

$$v = \sum_{i=1}^8 N_i \cdot v_i. \quad (\text{G.9b})$$

Proceeding in the same way as in the previous section, it can be easily concluded that now both the geometrical and stress/deformations approximations are of higher order.

G.3 Mesh comparison

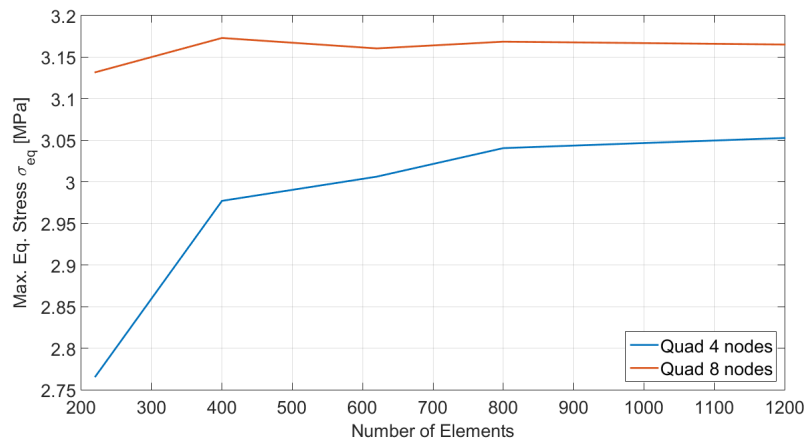
Taking into account what has just been explained, one can understand that the higher order elements (PLANE 183) provide better results, not only due to the more accurate stress/deformation distributions, but also the better approximation of circular geometries such as the centre hole, in the case of Chapter 5. However, the bigger number of nodal points rises the computational cost, which can be a problem when running a big or very refined model, or running lots of simulations in one single run. Here, the first order element (PLANE 182) has less computational cost. For this reason, a result comparison is to be made in order to assess the output of both meshes (first and superior order) in order to understand the consequences of both choices and decide in accordance.

First an foremost, the results given by the 8-node quad mesh are considered the reference for comparison, i.e. correct, and this study was made by varying the refinement of the mesh the same ways as in Section 5.4. The most refined first order mesh (1200 elements 4-node quad mesh) was the one used in the parametric optimization.

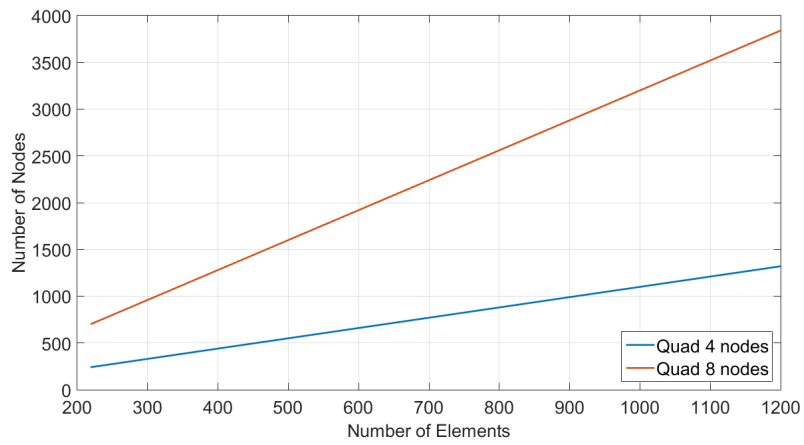
Analysing Fig. G.2a, it can be observed a convergence of both models, where the first order mesh converges to a smaller error, of around 4 percent. Basically, it states that the results provided by the used model convey, at least, an error of 4 percent. Figure G.2b shows the number of nodes with regards of the mesh elements. A logic relationship of node-element is shown where the higher order as twice the nodes than the first order mesh. This leads to an increase in the computational cost, supported in Fig. G.2c, by a factor of approximately two.

To sum up, the first order mesh is more efficient in terms of computation cost, with the downside of conveying worse results. Despite this fact, the 4 percent error provided by the used mesh (1200 elements) is acceptable, hence being the one used since it has a smaller computational cost.

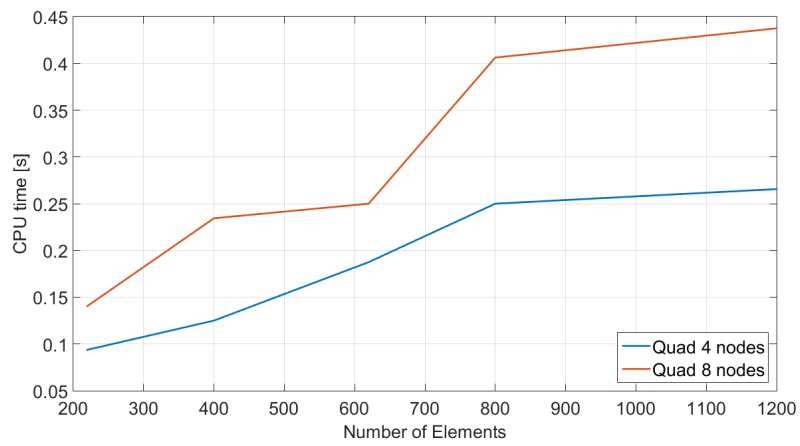
G. Comparison between first and superior order elements



(a) Convergence analysis



(b) Number of nodes



(c) Computational cost

Figure G.2: Mesh comparison for both meshes

Parametric optimization program

H.1 Matlab code

H.1.1 Optimization mainframe

```

1 function OptiPitch(type)
2 %*****GA Parametric Optimization*****
3 %*****Options for the Genetic Algorithm*****
4 %Definition of the matrix for parameter limits:
5 llimit=[220,0,40,30];
6 ulimit=[340,15,120,80];
7 plimit=[llimit;ulimit];
8 npar=length(llimit);
9 %Maximum number of generations:
10 genlimit=100;
11 %GA options:
12 options=gaoptimset('PopInitRange',plimit,'Generations',....
13     genlimit,'PopulationSize',40,'CrossoverFraction',0.7,...
14     'MigrationFraction',0.1,'MutationFcn',...
15     {@mutationuniform,0.01},'MigrationInterval',...
16     0.5*genlimit,'TolFun',0.1,'StallGenLimit',20,...
17     'PopulationType','doubleVector','SelectionFcn',...
18     @selectionroulette,'EliteCount',2,'PlotFcns',...
19     {@gaplotbestf,@gaplotrange},'TimeLimit',3600);
20 %*****
21 %Create a directory for images
22 mkdir RSTs
23 switch type
24     case 'FAT'
25 %*****
26 %*****FATIGUE ANALYSIS*****
27 %*****
28 %Create a fatigue folder
29 mkdir RSTs/FAT
30 %*****Initializing of the Genetic Algorithm*****
31 %P – Parameter values;
32 %fval–fitness function value for P

```

```
33 %@fitnessfunction – calls fitnessfunction.m (objective function)
34 %npar – number of design variables (number of parameters)
35 %options – defined above as gaoptimset
36 tic
37 t=cputime;
38 [P, fval]=ga(@fitnessfunctionfat ,npar , options );
39 cput=cputime-t;
40 et=toc;
41 %*****
42
43 %*****Saving Results for the Optimal Design*****
44 %Video of the evolution of the design
45 makevideo('RSTs/FAT/', 'runFAT.avi');
46
47 %Save the graphic evolution of the GA algorithm
48 saveas(gcf, 'runOverviewFat.png');
49
50 %Write optimal parameters for final run
51 fileID=fopen('parameters.inp', 'w+');
52 fprintf(fileID, 'P1=%f\n', abs(P(1)));
53 fprintf(fileID, 'P2=%f\n', abs(P(2)));
54 fprintf(fileID, 'P3=%f\n', abs(P(3)));
55 fprintf(fileID, 'P4=%f\n', abs(P(4)));
56 fclose(fileID);
57
58 %Run model for optimal parameters
59 runSimulation('BEST');
60 movefile('OptiPitch000.png', 'rstOptFat.png');
61
62 %Save optimal parameters in txt file
63 fileID=fopen('rstBestFat.txt', 'w+');
64 fprintf(fileID, 'P1=%f\n', abs(P(1)));
65 fprintf(fileID, 'P2=%f\n', abs(P(2)));
66 fprintf(fileID, 'P3=%f\n', abs(P(3)));
67 fprintf(fileID, 'P4=%f\n', abs(P(4)));
68 fclose(fileID);
69
70 %Save fitness value of optimal
71 fileID=fopen('fitBestFat.txt', 'w+');
72 fprintf(fileID, 'W=%f\n', fval);
73 fclose(fileID);
74
75 %Save elapsed time of run
76 fileID=fopen('cpuTimeFat.txt', 'w+');
77 fprintf(fileID, 'ET=%f\n', cput);
78 fclose(fileID);
79
80 %Save elapsed time of run
81 fileID=fopen('elapsedTimeFat.txt', 'w+');
```

```

82 fprintf(fileID, 'ET=%f\n', et);
83 fclose(fileID);
84
85     case 'EXT'
86 %*****
87 %*****EXTREME ANALYSIS*****
88 %*****
89 %Create a extreme folder
90 mkdir RSTs/EXT
91 %*****Initializing of the Genetic Algorithm*****
92 %P – Parameter values;
93 %fval–fitness function value for P
94 %@fitnessfunction – calls fitnessfunction.m (objective function)
95 %npar – number of design variables (number of parameters)
96 %options – defined above as gaoptimset
97 tic
98 t=cputime;
99 [P, fval]=ga(@fitnessfunctionext, npar, options);
100 cput=cputime-t;
101 et=toc;
102 %*****
103
104 %*****Saving Results for the Optimal Design*****
105 %Video of the evolution of the design
106 makevideo('RSTs/EXT/', 'runEXT.avi');
107
108 %Save the graphic evolution of the GA algorithm
109 saveas(gcf, 'runOverviewExt.png');
110
111 %Write optimal parameters for final run
112 fileID=fopen('parameters.inp', 'w+');
113 fprintf(fileID, 'P1=%f\n', abs(P(1)));
114 fprintf(fileID, 'P2=%f\n', abs(P(2)));
115 fprintf(fileID, 'P3=%f\n', abs(P(3)));
116 fprintf(fileID, 'P4=%f\n', abs(P(4)));
117 fclose(fileID);
118
119 %Run model for optimal parameters
120 runSimulation('EXT');
121 movefile('OptiPitch000.png', 'rstOptExt.png');
122
123 %Save optimal parameters in txt file
124 fileID=fopen('rstBestExt.txt', 'w+');
125 fprintf(fileID, 'P1=%f\n', abs(P(1)));
126 fprintf(fileID, 'P2=%f\n', abs(P(2)));
127 fprintf(fileID, 'P3=%f\n', abs(P(3)));
128 fprintf(fileID, 'P4=%f\n', abs(P(4)));
129 fclose(fileID);
130

```

```

131 %Save fitness value of optimal
132 fileID=fopen( 'fitBestExt.txt', 'w+' );
133 fprintf( fileID, 'W=%f\n', fval );
134 fclose( fileID );
135
136 %Save elapsed time of run
137 fileID=fopen( 'cpuTimeExt.txt', 'w+' );
138 fprintf( fileID, 'ET=%f\n', cpuet );
139 fclose( fileID );
140
141 %Save elapsed time of run
142 fileID=fopen( 'elapsedTimeExt.txt', 'w+' );
143 fprintf( fileID, 'ET=%f\n', et );
144 fclose( fileID );
145
146     case 'BOTH'
147 %*****
148 %*****BOTH CONDITIONS*****
149 %*****
150 %Create both folders
151 mkdir RSTs/FAT
152 mkdir RSTs/EXT
153
154 %*****Initializing of the Genetic Algorithm*****
155 %P – Parameter values;
156 %fval–fitness function value for P
157 %@fitnessfunction – calls fitnessfunction.m (objective function)
158 %npar – number of design variables (number of parameters)
159 %options – defined above as gaoptimset
160 tic
161 t=cputime;
162 [P, fval]=ga( @fitnessfunctionboth, npar, options );
163 cpuet=cputime-t;
164 et=toc;
165 %*****
166
167 %*****Saving Results for the Optimal Design*****
168 %Create run videos
169 makevideo( 'RSTs/EXT/', 'runEXT.avi' );
170 makevideo( 'RSTs/FAT/', 'runFAT.avi' );
171
172 %Save the graphic evolution of the GA algorithm
173 saveas( gcf, 'runOverviewBoth.png' );
174
175 %Write optimal parameters for final run
176 fileID=fopen( 'parameters.inp', 'w+' );
177 fprintf( fileID, 'P1=%f\n', abs(P(1)) );
178 fprintf( fileID, 'P2=%f\n', abs(P(2)) );
179 fprintf( fileID, 'P3=%f\n', abs(P(3)) );

```



```

180 fprintf(fileID, 'P4=%f\n', abs(P(4)));
181 fclose(fileID);
182
183 %Run model for optimal parameters
184 runSimulation('BEST');
185 waitfor(exist('OptiPitch000.png', 'file'));
186 runSimulation('EXT');
187 waitfor(exist('OptiPitch001.png', 'file'));
188
189
190 %Save optimal parameters in txt file
191 fileID=fopen('rstBestBoth.txt', 'w+');
192 fprintf(fileID, 'P1=%f\n', abs(P(1)));
193 fprintf(fileID, 'P2=%f\n', abs(P(2)));
194 fprintf(fileID, 'P3=%f\n', abs(P(3)));
195 fprintf(fileID, 'P4=%f\n', abs(P(4)));
196 fclose(fileID);
197
198 %Save fitness value of optimal
199 fileID=fopen('fitBestBoth.txt', 'w+');
200 fprintf(fileID, 'W=%f\n', fval);
201 fclose(fileID);
202
203 %Save elapsed time of run
204 fileID=fopen('cpuTimeBoth.txt', 'w+');
205 fprintf(fileID, 'ET=%f\n', cpuet);
206 fclose(fileID);
207
208 %Save elapsed time of run
209 fileID=fopen('elapsedTimeBoth.txt', 'w+');
210 fprintf(fileID, 'ET=%f\n', et);
211 fclose(fileID);
212
213 %Save plot results of optimal parameters
214 movefile('OptiPitch000.png', 'rstOptFat.png');
215 movefile('OptiPitch001.png', 'rstOptExt.png');
216 end
217 end
218 %*****

```

H.1.2 Fitness function for the extreme condition

```

1 function fitvalue=fitnessfunctionext(P)
2 %*****Writing of the design variables from the optimizer*****
3 %Vector P=[p1,p2,p3,p4]
4 %Write new parameters in the parameters file:
5 fileID=fopen('parameters.inp', 'w+');
6 fprintf(fileID, 'P1=%f\n', abs(P(1)));
7 fprintf(fileID, 'P2=%f\n', abs(P(2)));
8 fprintf(fileID, 'P3=%f\n', abs(P(3)));

```

```

9 fprintf( fileID , 'P4=%f\n' , abs(P(4)) );
10 fclose( fileID );
11 %*****
12 %Auxiliar values
13 Ang=P(2) *3.1415/180;
14 h1=P(3) /2+2.4498*10+2.6468;
15 R=(P(1) / (2*tan(Ang)) - (140+h1)) * sin(Ang) / (1-sin(Ang));
16 SMAX=220e6;
17
18 if (R-P(3)/2>=10)&&(R/h1>=1)&&(P(4)/P(3) >=0.3)
19     %*****Run Ansys Program
20     %*****
21     %Run with the new P values in parameters.inp
22     runSimulation( 'EXT' );
23
24     %Read the value of weight:
25     fileID=fopen( 'Weight.txt' , 'r' );
26     WGH=fscanf( fileID , '%f' , [1,1] );
27     fclose( fileID );
28
29     %Read the critical damage value
30     fileID=fopen( 'Stress.txt' , 'r' );
31     STRS=fscanf( fileID , '%f' , [1,1] );
32     fclose( fileID );
33
34     if (STRS/SMAX <= 1) %strength constraints
35         fitvalue=WGH;
36     else
37         fitvalue=10^9;
38     end
39 else
40     fitvalue=10^9;
41 end
42 %*****

```

H.1.3 Fitness function for the fatigue condition

```

1 function fitvalue=fitnessfunctionfat(P)
2 %*****Writing of the design variables from the optimizer*****
3 %Vector P=[p1,p2,p3,p4]
4 %Write new parameters in the parameters file:
5 fileID=fopen( 'parameters.inp' , 'w+' );
6 fprintf( fileID , 'P1=%f\n' , abs(P(1)) );
7 fprintf( fileID , 'P2=%f\n' , abs(P(2)) );
8 fprintf( fileID , 'P3=%f\n' , abs(P(3)) );
9 fprintf( fileID , 'P4=%f\n' , abs(P(4)) );
10 fclose( fileID );
11 %*****
12 %Auxiliar values

```

```

13 Ang=P(2)*3.1415/180;
14 h1=P(3)/2+2.4498*10+2.6468;
15 R=(P(1)/(2*tan(Ang))-(140+h1))*sin(Ang)/(1-sin(Ang));
16
17 if (R-P(3)/2>=10)&&(R/h1>=1)&&(P(4)/P(3)>=0.3)
18     %*****Run Ansys Program
19     %*****
20     %Run with the new P values in parameters.inp
21     runSimulation('FAT');
22
23     %Read the value of weight:
24     fileID=fopen('Weight.txt','r');
25     WGHT=fscanf(fileID,'%f',[1,1]);
26     fclose(fileID);
27
28     %Read the critical stress value
29     fileID=fopen('rstEqStress.txt','r');
30     STRS=fscanf(fileID,'%f',[1,1])*10^(-6);
31     fclose(fileID);
32
33     %Read the critical damage value
34     fileID=fopen('rstSRF.txt','r');
35     SRF=fscanf(fileID,'%f',[1,1]);
36     fclose(fileID);
37
38     %Store meta stress data
39     fileID=fopen('fatWiz\metaSTRS.txt','a+');
40     fprintf(fileID,'%d\n',STRS);
41     fclose(fileID);
42
43     if (SRF >= 1) %fatigue constraint
44         fitvalue=WGHT;
45     else
46         fitvalue=10^9;
47     end
48 else
49     fitvalue=10^9;
50 end
51 %*****

```

H.1.4 Fitness function for extreme/fatigue combined conditions

```

1 function fitvalue=fitnessfunctionboth(P)
2 %*****Writing of the design variables from the optimizer*****
3 %Vector P=[p1,p2,p3,p4]
4 %Write new parameters in the parameters file:
5 fileID=fopen('parameters.inp','w+');
6 fprintf(fileID,'P1=%f\n',abs(P(1)));
7 fprintf(fileID,'P2=%f\n',abs(P(2)));

```

```

8 fprintf( fileID , 'P3=%f\n' , abs(P(3)) );
9 fprintf( fileID , 'P4=%f\n' , abs(P(4)) );
10 fclose( fileID );
11 %*****
12 %Auxiliar values
13 Ang=P(2) * 3.1415/180;
14 h1=P(3) / 2 + 2.4498*10 + 2.6468;
15 R=(P(1) / (2*tan(Ang)) - (140+h1)) * sin(Ang) / (1 - sin(Ang));
16 SMAX=220e6;
17
18 if (R-P(3)/2 >= 10) && (R/h1 >= 1) && (P(4)/P(3) >= 0.3)
19     %*****Run Ansys Program
20     %*****
21     %Run with the new P values in parameters.inp
22     runSimulation( 'FAT' );
23     waitfor( exist( 'rstSRF.txt' , 'file' ) );
24     runSimulation( 'EXT' );
25
26     %Read the value of weight:
27     fileID=fopen( 'Weight.txt' , 'r' );
28     WGH=fscanf( fileID , '%f' , [1,1] );
29     fclose( fileID );
30
31     %Read the critical stress value
32     fileID=fopen( 'Stress.txt' , 'r' );
33     STRS=fscanf( fileID , '%f' , [1,1] ) * 10^(-6);
34     fclose( fileID );
35
36     %Read the critical damage value
37     fileID=fopen( 'rstSRF.txt' , 'r' );
38     SRF=fscanf( fileID , '%f' , [1,1] );
39     fclose( fileID );
40
41     if (SRF >= 1) && (STRS/SMAX <= 1)    %fatigue constraint
42         fitvalue=WGH;
43     else
44         fitvalue=10^9;
45     end
46 else
47     fitvalue=10^9;
48 end
49 %*****

```

H.1.5 External programs interaction

```

1 function runSimulation( type )
2 %*****Run Main Control Process*****
3 %Delete all previous misplaced files and folders
4 delete *.out

```

```

5 delete *.rst
6 delete *.err
7 delete *.full
8 delete *.stat
9 delete *.dsp
10 delete *.mnr
11 delete *.esav
12 delete *.asv
13 switch type
14     case 'FAT'
15         delete fatWiz\fatWizStress\n100kN.txt
16         delete fatWiz\fatWizStress\p100kN.txt
17         delete *.db
18         delete *.ans
19         delete *.wrz
20         delete rstSRF.txt
21         delete rstEqStress.txt
22         %Run ansys model for both load cases
23         fileID=fopen('output.txt','w');
24         fclose(fileID);
25         !runModelFat.bat
26         waitfor(exist('fatwiz/fatWizStress/n100kN.txt','file'));
27         %Run matlab to overwrite stress results
28         overwriteRSTs;
29         waitfor(exist('runMatlabFlag.txt','file'))
30         %Run fatigue analysis
31         !runFatWiz.bat
32         waitfor(exist('V164_8MW_GJS400_Lug.ans','file'));
33         %Run post process plot (SRF)
34         !runPost.bat
35
36         %Move image to result folder
37         n=length(dir('RSTs/FAT/*.png'));
38         movefile('OptiPitch000.png',sprintf('RSTs/FAT/%d.png',n
39             +1));
40     case 'EXT'
41         delete Stress.txt
42         %Run ansys model for only one load case
43         fileID=fopen('output.txt','w');
44         fclose(fileID);
45         !runModelExt.bat
46
47         %Move image to result folder
48         n=length(dir('RSTs/EXT/*.png'));
49         movefile('OptiPitch000.png',sprintf('RSTs/EXT/%d.png',n
50             +1));
51     case 'BEST'
52         delete fatWiz\fatWizStress\n100kN.txt
53         delete fatWiz\fatWizStress\p100kN.txt

```

```

52     delete *.db
53     delete *.ans
54     delete rstSRF.txt
55
56     %Run ansys model for both load cases
57     fileID=fopen('output.txt','w');
58     fclose(fileID);
59     !runModelFat.bat
60     waitfor(exist('fatwiz/fatwizstress/n100kN.txt','file'));
61     %Run matlab to overwrite stress results
62     overwriteRSTs;
63     waitfor(exist('runMatlabFlag.txt','file'))
64     %Run fatigue analysis
65     !runFatWizBest.bat
66     waitfor(exist('V164_8MW_GJS400_Lug_Best.ans','file'));
67     %Run post process plot (SRF)
68     !runPostBest.bat
69 end
70 end
71 %*****

```

H.1.6 Stress distribution overwriting

```

1 function overwriteRSTs
2 %*****Overwrite Model Stress Values*****
3 %Overwrite the p100Kn.txt file
4 fileID=fopen('.\fatWiz\fatWizStress\p100kN.txt','r');
5 f=fread(fileID);
6 fclose(fileID);
7 f=char(f.'');
8 f=strrep(f,'0.000E+000','0.100E+000');
9 fileID=fopen('fatWiz\fatWizStress\p100kN.txt','w+');
10 fprintf(fileID,'%s',f);
11 fclose(fileID);
12
13 %Overwrite the n100Kn.txt file
14 fileID=fopen('.\fatWiz\fatWizStress\n100kN.txt','r');
15 f=fread(fileID);
16 fclose(fileID);
17 f=char(f.'');
18 f=strrep(f,'0.000E+000','0.100E+000');
19 fileID=fopen('fatWiz\fatWizStress\n100kN.txt','w+');
20 fprintf(fileID,'%s',f);
21 fclose(fileID);
22
23 %Create a flag file for the end of process
24 fileID=fopen('runMatlabFlag.txt','w');
25 fclose(fileID);
26 end
27 %*****

```

H.1.7 Video from run

```

1 function video=makevideo(directory,name)
2 pngNo=size(dir(sprintf('%s*.png',directory)),1);
3 video=VideoWriter(name);
4 open(video);
5 for i=1:pngNo
6     fileID=sprintf('%s%d.png',directory,i);
7     image=imread(fileID);
8     writeVideo(video,image);
9 end
10 close(video);
11 end

```

H.2 APDL code

H.2.1 Model generation for extreme condition

```

1 !-----!
2 !-----!
3 !----- Date: 07/07/2020 -----!
4 !----- Rui Magalhaes, RMDAS -----!
5 !----- Pitch lug optimization -----!
6 !-----!
7 !-----!
8
9 finish
10
11 /clear
12
13 /filename, OptiPitch, 0
14 /title, Pitch Suspension Optimization - Model 1
15 pscontrol, all, on
16 !Enable shared-memory parallel operations
17 /graphics, power, on
18 !Enable power graphics
19
20 /inp, parameters, inp
21 !Upload parameter set to the model generator
22
23 /units, mks
24
25 !Compute keypoint extra parameters
26 Ang=P2*3.1415/180
27 h1=P3/2+2.448*10+2.6468
28 R=(P1/(2*tan(Ang))-(140+h1))*sin(Ang)/(1-sin(Ang))
29 D=R-h1
30 Y1=D-R*sin(Ang)
31 X1=R*cos(Ang)
32
33 !Force
34 Fpitch=623e3*1.1
35
36 /prep7

```

H. Parametric optimization program

```
37
38 !-----!
39 !----- Material properties -----!
40 !-----!
41
42 mp, ex, 1, 169e9           !Elastic modulus
43 mp, nuxy, 1, 0.275        !Poisson coefficient
44 mp, dens, 1, 7.1e3        !Density
45
46 !-----!
47 !----- Mesh properties -----!
48 !-----!
49
50 et, 1, 182, , , 3         !plane182
51 r, 1, P4/1000             !element thickness
52
53 !-----!
54 !----- Geometry design - Lug -----!
55 !-----!
56
57 clocal, 11, 0, 0, 0.140, 0, 0, 0, 0
58 csys, 11
59
60 !Generate design keypoints
61 k, 1, -P1/2000, -0.140, 0
62 k, 2, -X1/1000, -Y1/1000, 0
63 k, 3, X1/1000, -Y1/1000, 0
64 k, 4, P1/2000, -0.140, 0
65 k, 5, 0, 0, 0
66 k, 6, 0, -D/1000, 0
67 k, 7, 0, P3/2000, 0
68 k, 8, -P3/2000, 0, 0
69 k, 9, 0, -P3/2000, 0
70 k, 10, P3/2000, 0, 0
71 k, 11, 0, h1/1000, 0
72
73 !Lines
74 lstr, 1, 2                 !L1
75 lstr, 3, 4                 !L2
76 lstr, 4, 1                 !L3
77 !Arcs
78 larc, 2, 11, 6, R/1000    !L4
79 larc, 3, 11, 6, R/1000    !L5
80 larc, 7, 8, 5, P3/2000    !L6
81 larc, 8, 9, 5, P3/2000    !L7
82 larc, 9, 10, 5, P3/2000   !L8
83 larc, 10, 7, 5, P3/2000   !L9
84
85 !-----!
86 !----- Mesh -----!
87 !-----!
88
89 !Auxiliar lines
90 ldiv, 8, 0.5              !L10
91 ldiv, 7, 0.5              !L11
92 ldiv, 3, 0.5              !L12
```



```
93 lstr, 7, 11 !L13
94 lstr, 2, 8 !L14
95 lstr, 3, 10 !L15
96 lstr, 1, 13 !L16
97 lstr, 4, 12 !L17
98 lstr, 9, 14 !L18
99
100 !Element division
101 NE1=30
102 NE2=10
103 lesize, 1, , , NE1/2
104 lesize, 2, , , NE1/2
105 lesize, 3, , , NE1/2
106 lesize, 4, , , NE1
107 lesize, 5, , , NE1
108 lesize, 6, , , NE1
109 lesize, 7, , , NE1/2
110 lesize, 8, , , NE1/2
111 lesize, 9, , , NE1
112 lesize, 10, , , NE1/2
113 lesize, 11, , , NE1/2
114 lesize, 12, , , NE1/2
115 lesize, 13, , , NE2
116 lesize, 14, , , NE2
117 lesize, 15, , , NE2
118 lesize, 16, , , NE2
119 lesize, 17, , , NE2
120 lesize, 18, , , NE2
121
122
123 !Areas
124 al, 3, 8, 17, 18 !A1
125 al, 1, 7, 14, 16 !A2
126 al, 2, 10, 15, 17 !A3
127 al, 4, 6, 13, 14 !A4
128 al, 5, 9, 13, 15 !A5
129 al, 11, 12, 16, 18 !A6
130
131 !Mesh
132
133 type, 1
134 mat, 1
135 real, 1
136 amesh,all
137
138 allsel
139
140 !-----!
141 !----- Boundary conditions - p100kN -----!
142 !-----!
143
144 csys,0
145
146 !Fixed support
147 nsel, s, loc, y, 0 !Select bottom nodes
148 d, all, ux, 0 !Fix x displacement
```

H. Parametric optimization program

```
149 d, all, uy, 0                                !Fix y displacement
150
151 csys, 11
152 clocal, 12, cylin
153 csys, 12
154
155 !Extreme load
156 nsel, s, loc, x, P3/2000-0.001, P3/2000+0.001
157 nsel, r, loc, y, -90, 90
158 csys, 0
159 SelNode=0
160 Sum=0
161 *get, nodeCount, node, , count
162 *do, nodeID, 1, nodeCount
163     nodeNo=ndnext(SelNode)
164     Sum=Sum+nx(nodeNo)
165     SelNode=nodeNo
166 *enddo
167 SelNode=0
168 *do, nodeID, 1, nodeCount
169     nodeNo=ndnext(SelNode)
170     Fef=Fpitch*nx(nodeNo)/(2*Sum)
171     f, nodeNo, fx, Fef
172     SelNode=nodeNo
173 *enddo
174
175 finish
176
177 !-----!
178 !----- Solve -----!
179 !-----!
180
181 /solu
182 time, 1
183 antype, 0
184 nlgeom, 0
185 outres, all, all
186 irlf, -1
187 solve
188
189 !-----!
190 !----- Post processing -----!
191 !-----!
192
193 /post1
194
195 set, last
196
197 irlist
198 *get, W, elem, , mtot, x
199
200 /output, Weight, txt
201 *vwrite, W
202 (F15.4, '      ')
203 /output
204
```

```

205 nsel, all
206 nsel, s, loc, x, P3/2000-0.001, P3/2000+0.001
207 nsel, inve
208 nsort, s, eqv
209 *get, STRS, sort, , max
210
211 /output, Stress, txt
212 *vwrite, STRS
213 (F15.4,'      ')
214 /output
215
216 /show, png, 0
217 png, qual, 50,
218 png, orient, horiz
219 png, color, 2
220 png, tmod, 1
221 /rgb, index, 100, 100, 100, 0
222 /rgb, index, 0, 0, 0, 15
223 /gfile, 1200,
224
225 allsel
226 /dscale, all, off
227 /contour, all, 9, 0, , 220e6
228 plnsol, s, eqv
229
230 /cmap, _tempcmap_, cmp, , save
231 /cmap, _tempcmap_, cmp
232 /delete, _tempcmap_, cmp
233 /show, close
234 /device, vector, 0

```

H.2.2 Model generation for fatigue condition

```

1  !-----!
2  !-----!
3  !----- Date: 07/07/2020 -----!
4  !----- Rui Magalhaes, RMDAS -----!
5  !----- Pitch lug optimization -----!
6  !-----!
7  !-----!
8
9  finish
10
11 /clear
12
13 /filename, OptiPitch, 0
14 /title, Pitch Suspension Optimization - Model 1
15 pscontrol, all, on
16 !Enable shared-memory parallel operations
17 /graphics, power, on
18 !Enable power graphics
19
20 /header, off, off, off, off, , off
21 /page, 50000, , 50000
22 /format, 7, e, 12, 3
23

```

H. Parametric optimization program

```
24 /inp, parameters, inp
25 !Upload parameter set to the model generator
26
27 /units, mks
28
29 !Compute keypoint extra parameters
30 Ang=P2*3.1415/180
31 h1=P3/2+2.448*10+2.6468
32 R=(P1/(2*tan(Ang))-(140+h1))*sin(Ang)/(1-sin(Ang))
33 D=R-h1
34 Y1=D-R*sin(Ang)
35 X1=R*cos(Ang)
36
37 !Force
38 Fpitch=100e3
39
40 /prep7
41
42 !-----!
43 !----- Material properties -----!
44 !-----!
45
46 mp, ex, 1, 169e9           !Elastic modulus
47 mp, nuxy, 1, 0.275       !Poisson coefficient
48 mp, dens, 1, 7.1e3       !Density
49 r, 1
50
51 !-----!
52 !----- Mesh properties -----!
53 !-----!
54
55 et, 1, 182, , , 3        !plane182
56 r, 1, P4/1000           !element thickness
57
58 !-----!
59 !----- Geometry design - Lug -----!
60 !-----!
61
62 clocal, 11, 0, 0, 0.140, 0, 0, 0, 0
63 csys, 11
64
65 !Generate design keypoints
66 k, 1, -P1/2000, -0.140, 0
67 k, 2, -X1/1000, -Y1/1000, 0
68 k, 3, X1/1000, -Y1/1000, 0
69 k, 4, P1/2000, -0.140, 0
70 k, 5, 0, 0, 0
71 k, 6, 0, -D/1000, 0
72 k, 7, 0, P3/2000, 0
73 k, 8, -P3/2000, 0, 0
74 k, 9, 0, -P3/2000, 0
75 k, 10, P3/2000, 0, 0
76 k, 11, 0, h1/1000, 0
77
78 !Lines
79 lstr, 1, 2                !L1
```

```

80 lstr, 3, 4                                !L2
81 lstr, 4, 1                                !L3
82 !Arcs
83 larc, 2, 11, 6, R/1000 !L4
84 larc, 3, 11, 6, R/1000 !L5
85 larc, 7, 8, 5, P3/2000 !L6
86 larc, 8, 9, 5, P3/2000 !L7
87 larc, 9, 10, 5, P3/2000 !L8
88 larc, 10, 7, 5, P3/2000 !L9
89
90 !-----!
91 !----- Mesh -----!
92 !-----!
93
94 !Auxiliar lines
95 ldiv, 8, 0.5                                !L10
96 ldiv, 7, 0.5                                !L11
97 ldiv, 3, 0.5                                !L12
98 lstr, 7, 11                                !L13
99 lstr, 2, 8                                  !L14
100 lstr, 3, 10                                !L15
101 lstr, 1, 13                                !L16
102 lstr, 4, 12                                !L17
103 lstr, 9, 14                                !L18
104
105 !Element division
106 NE1=30
107 NE2=10
108 lesize, 1, , , NE1/2
109 lesize, 2, , , NE1/2
110 lesize, 3, , , NE1/2
111 lesize, 4, , , NE1
112 lesize, 5, , , NE1
113 lesize, 6, , , NE1
114 lesize, 7, , , NE1/2
115 lesize, 8, , , NE1/2
116 lesize, 9, , , NE1
117 lesize, 10, , , NE1/2
118 lesize, 11, , , NE1/2
119 lesize, 12, , , NE1/2
120 lesize, 13, , , NE2
121 lesize, 14, , , NE2
122 lesize, 15, , , NE2
123 lesize, 16, , , NE2
124 lesize, 17, , , NE2
125 lesize, 18, , , NE2
126
127
128 !Areas
129 al, 3, 8, 17, 18                            !A1
130 al, 1, 7, 14, 16                            !A2
131 al, 2, 10, 15, 17                          !A3
132 al, 4, 6, 13, 14                          !A4
133 al, 5, 9, 13, 15                          !A5
134 al, 11, 12, 16, 18                        !A6
135

```

H. Parametric optimization program

```
136 !Mesh
137
138 type, 1
139 mat, 1
140 real, 1
141 amesh,all
142
143 allsel
144 save, beforeRun, db
145
146 !-----!
147 !----- Boundary conditions - p100kN -----!
148 !-----!
149
150 csys,0
151
152 !Fixed support
153 nsel, s, loc, y, 0           !Select bottom nodes
154 d, all, ux, 0               !Fix x displacement
155 d, all, uy, 0               !Fix y displacement
156
157 csys, 11
158 clocal, 12, cylin
159 csys, 12
160
161 !Extreme load
162 nsel, s, loc, x, P3/2000-0.001, P3/2000+0.001
163 nsel, r, loc, y, -90, 90
164 csys, 11
165 SelNode=0
166 Sum=0
167 *get, nodeCount, node, , count
168 *do, nodeID, 1, nodeCount
169     nodeNo=ndnext(SelNode)
170     Sum=Sum+nx(nodeNo)
171     SelNode=nodeNo
172 *enddo
173 SelNode=0
174 *do, nodeID, 1, nodeCount
175     nodeNo=ndnext(SelNode)
176     Fef=5.0296*Fpitch*nx(nodeNo)/(2*Sum)
177     f, nodeNo, fx, Fef
178     SelNode=nodeNo
179 *enddo
180
181 finish
182
183 !-----!
184 !----- Solve -----!
185 !-----!
186
187 /solu
188 time, 1
189 antype, 0
190 nlgeom, 0
191 outres, all, all
```

```

192 irlf, -1
193 solve
194
195 !-----!
196 !----- Post processing -----!
197 !-----!
198
199 /post1
200
201 save, beforeRun, db
202
203 set, last
204
205 irlist
206 *get, W, elem, , mtot, x
207
208 /output, Weight, txt
209 *vwrite, W
210 (F15.4, '      ')
211 /output
212
213 allsel
214 /output, fatwiz/fatwizstress/p100kN, txt
215 prnsol, s, comp
216 /output
217
218 finish
219
220 !-----!
221 !----- Boundary conditions - n100kN -----!
222 !-----!
223
224 /prep7
225
226 !Delete previous forces
227 allsel
228 fdele, all, fx
229
230 !Extreme load
231 csys, 12
232 nsel, s, loc, x, P3/2000-0.001, P3/2000+0.001
233 nsel, r, loc, y, 90, 270
234 csys, 11
235 SelNode=0
236 Sum=0
237 *get, nodeCount, node, , count
238 *do, nodeID, 1, nodeCount
239     nodeNo=ndnext(SelNode)
240     Sum=Sum+nx(nodeNo)
241     SelNode=nodeNo
242 *enddo
243 SelNode=0
244 *do, nodeID, 1, nodeCount
245     nodeNo=ndnext(SelNode)
246     Fef=-5.0296*Fpitch*nx(nodeNo)/(2*Sum)
247     f, nodeNo, fx, Fef

```

```

248         SelNode=nodeNo
249 *enddo
250
251 finish
252
253 !-----!
254 !----- Solve -----!
255 !-----!
256
257 /solu
258 time, 1
259 antype, 0
260 nlgeom, 0
261 outres, all, all
262 irlf, -1
263 solve
264
265 !-----!
266 !----- Post processing -----!
267 !-----!
268
269 /post1
270
271 set, last
272
273 allsel
274 /output, fatwiz/fatwizstress/n100kN, txt
275 prnsol, s, comp
276 /output
277
278 csys, 12
279 nsel, s, loc, x, P3/2000-0.001, P3/2000+0.001
280 nsel, inve
281 nsort, s, eqv
282 *get, STRS, sort, , max
283
284 /output, Stress, txt
285 *vwrite, STRS
286 (F15.4,'      ')
287 /output,

```

H.2.3 Fatigue results post-processing

```

1 !-----!
2 !-----!
3 !----- Date: 21/07/2020 -----!
4 !----- Rui Magalhaes, RMDAS -----!
5 !----- Plot Fatigue Results -----!
6 !-----!
7 !-----!
8
9 resume, beforeRun, db
10
11 /filename, OptiPitch, 0
12 /title, Pitch Suspension Optimization - Fatigue Results
13

```



```

14 /input, V164_8MW_GJS400_LUG, ans
15
16 *vput, fatigue(1), node, , u, x, ! replace by new values for ux
17
18 lcdef, 1, , , !define loadcase of first
   set
19 rappnd, mystep, mystep, !append to the .rst file in a
   separate loadstep,
20
   !for example,
   loadstep = 12,
   time = 12
21 /color, cntr, 12, 1 !color scale
22 /color, cntr, 11, 2
23 /color, cntr, 10, 3
24 /color, cntr, 9, 4
25 /color, cntr, 8, 5
26 /color, cntr, 7, 6
27 /color, cntr, 6, 7
28 /color, cntr, 5, 8
29 /color, cntr, 4, 9
30
31 /cval, , 0.60, 0.75, 0.92, 1.0, 1.15, 1.53, 2, 1000
32
33 set, mystep !read in the
   results
34
35 csys, 12
36 nsel, s, loc, x, P3/2000-0.001, P3/2000+0.001
37 nsel, inve
38 nsel, r, loc, x, 0, P3/2000+0.03
39 nsort, u, x
40
41 *get, SRF, sort, , min
42
43 /output, rstSRF, txt
44 *vwrite, SRF
45 (F15.4,' ')
46 /output,

```

H.3 Batch files

H.3.1 Run Ansys for the extreme condition

```

1 SET ANS_CONSEC=YES
2 SET ANSYS_LOCK=OFF
3 SET KMP_STACKSIZE=2048k
4 "C:\Program Files\ANSYS Inc\ANSYS Student\v195\ansys\bin\winx64\
   ANSYS195.exe" -b -i genModelExt.mac -o output.txt

```

H.3.2 Run Ansys for the fatigue condition

```

1 SET ANS_CONSEC=YES
2 SET ANSYS_LOCK=OFF
3 SET KMP_STACKSIZE=2048k
4 "C:\Program Files\ANSYS Inc\ANSYS Student\v195\ansys\bin\winx64\
   ANSYS195.exe" -b -i genModelFat.mac -o output.txt

```

H.3.3 Run Fatigue Wizard

```
1 FatigueWizard_2_699.exe -b V164_8MW_GJS400_Lug.wiz
```

H.3.4 Run Fatigue post processing

```
1 "C:\Program Files\ANSYS Inc\ANSYS Student\v195\ansys\bin\winx64\  
  ANSYS195.exe" -b -i postFat.mac -o output.txt
```

Estimation of fatigue curves under unknown fatigue data

I.1 Introduction

Most of the available materials' data are the monotonic, since they can be easily obtained from a monotonic test. However, most components, in service, experience cyclic loadings, and therefore, fatigue damage. For this reason, fatigue properties are crucial for component design, although are not so easily obtained and available, due to the complexity and cost of fatigue testing. Hence, it is important to find an accurate way to estimate fatigue properties from the general monotonic properties.

There are two approaches to predict crack initiation:

1. *S-N approach* (or Basquin's equation)
2. Strain-life method (or Coffin-Manson relationship)

As stated in Section 2.2.3, the *S-N approach* can be represented as

$$\sigma_a = \sigma'_f (2N_f)^b \quad (\text{I.1})$$

where σ_a represents the stress amplitude, $2N_f$ is the number of reversals to failure, and σ'_f and b are material properties, called fatigue strength coefficient and exponent, respectively. The strain-life approach relates the strain amplitude ε_a with the number of reversals to failure $2N_f$ as

$$\varepsilon_a = \frac{\sigma'_f}{E} (2N_f)^b + \varepsilon'_f (2N_f)^c \quad (\text{I.2})$$

assuming that the total elastic amplitude is equal to the sum of the elastic and plastic extensions, represented in the first and second terms of the second member of Eq. (I.2), respectively. The parameters ε'_f and c represent the fatigue ductility coefficient and exponent, respectively.

So as can be seen, if one needs to access the fatigue strength of a certain component, must define at least two fatigue properties to perform the calculations. This Chapter will focus on providing different relationships that allow to calculate fatigue properties and curves based on purely monotonic properties, allowing the user to proceed with relatively accurate fatigue analysis even in cases of unknown fatigue data.

I.2 Estimation of fatigue properties with tensile data

Roessle and Fatemi [138] performed an extensive study on a total of 69 steels, with values of Brinell hardness ranging from 80 to 660, and the ultimate strength σ_u , ranging from 345 MPa to 2585 MPa, providing a broad range of steels for the correlations.

In terms of the fatigue limit σ_f , two linear correlations with both hardness HB and tensile strength σ_u can be applied

$$\sigma_f = 1.43 \cdot \text{HB}, \quad R^2 = 0.91 \quad (\text{I.3a})$$

$$\sigma_f = 0.38 \cdot \sigma_u, \quad R^2 = 0.86. \quad (\text{I.3b})$$

The transition life N_t indicates when a material will experience equal amounts of elastic and plastic strains. A linear correlation with hardness was defined following the relationship

$$\log(2N_t) = 5.755 - 0.0071 \cdot \text{HB}, \quad R^2 = 0.89. \quad (\text{I.4})$$

The fatigue strength coefficient σ'_f (MPa) was defined in terms of hardness and ultimate strength under the relationships

$$\sigma'_f = 4.25 \cdot \text{HB} + 225, \quad R^2 = 0.86 \quad (\text{I.5a})$$

$$\sigma'_f = 1.04 \cdot \sigma_u + 225, \quad R^2 = 0.88. \quad (\text{I.5b})$$

The fatigue ductility coefficient cannot be defined according to tensile data, since the results did not show good accordance with any of the revised properties. Hence, Roessle and Fatemi proposed a new method for estimating this value from the fatigue strength coefficient σ'_f and the transition fatigue life N_t as

$$\varepsilon'_f = \frac{\sigma'_f(2N_t)^b}{E(2N_t)^c} \quad (\text{I.6})$$

where the nominator represents the transition fatigue strength $\sigma_t = \sigma'_f(2N_t)^b$. A strong correlation with hardness was also found for this parameter, represented by the expression

$$\sigma_t = 0.004 \cdot (\text{HB})^2 + 1.15 \cdot \text{HB}, \quad R^2 = 0.97. \quad (\text{I.7})$$

In terms of computing the fatigue exponents, Morrow [55] related their values with the cyclic strain hardening exponent n' , following the expressions

$$b = -\frac{-n'}{1 + 5n'} \quad (\text{I.8a})$$

$$c = -\frac{1}{1 + 5n'}. \quad (\text{I.8b})$$

However, in for the study by Roessle and Fatemi [138] these relationships proved to be poor approximations. The fatigue strength exponent b values ranged from -0.057 to -0.140, with an average value of -0.09, and the fatigue ductility exponent c ranged between -0.39 and -1.04, with an mean value of -0.60. Hence, if there is now information about these exponents, the approximated value to be considered are the referred average values, i.e. $b = -0.09$ and $c = -0.60$.

I.3 Estimation of strain-life curves based on hardness and the elasticity modulus

In terms of the strain the strain-controlled fatigue, the strain-life curve can be approximated to Eq. (I.2), and for the shear strain as

$$\gamma_a = \frac{\tau'_f}{G}(2N_f)^{b_0} + \gamma'_f(2N_f)^{c_0} \quad (\text{I.9})$$

where the τ'_f , γ'_f , b_0 and c_0 are the shear fatigue properties, and G is the shear modulus, which relates to the Young's modulus E with

$$G = \frac{E}{2(1 + \nu)} \quad (\text{I.10})$$

where ν is the Poisson's ration. If the uniaxial fatigue properties are available or computed with the relationships of the previous Section, different criteria may be applied to estimate the shear fatigue properties from these value. Sharifimehr and Fatemi [139] concluded that the Von Mises equivalent strain criteria was the better correlation criterion for ductile behaving materials and the maximum principal criteria was a better approach for brittle materials. The mentioned relationships are

$$\text{Von Mises equivalent strain: } \tau'_f = \frac{\sigma'_f}{\sqrt{3}}, \quad \gamma'_f = \sqrt{3}\varepsilon'_f, \quad b_0 = b, \quad c_0 = c \quad (\text{I.11a})$$

$$\text{Maximum principal strain: } \tau'_f = \frac{\sigma'_f}{1 + \nu}, \quad \gamma'_f = 2\varepsilon'_f, \quad b_0 = b, \quad c_0 = c. \quad (\text{I.11b})$$

However, in the case of the absence of the uniaxial fatigue properties, Roessle and Fatemi [138] proposed an equation that allows the estimation of the uniaxial strain-life curve with monotonic properties, following the expression

$$\varepsilon_a = \frac{4.25 \cdot \text{HB} + 225}{E} (2N_f)^{-0.09} + \frac{0.32 \cdot (\text{HB})^2 - 478 \cdot \text{HB} + 191000}{E} (2N_f)^{-0.56}. \quad (\text{I.12})$$

In the case Brinell hardness is also unknown, it may be estimated with the following relationship [138]

$$\sigma_u = 0.0012 \cdot (\text{HB})^2 + 3.3 \cdot \text{HB}. \quad (\text{I.13})$$

The *S-N curves*, or so called stress-life fatigue curves, may be also computed directly from the Basquin's equation displayed in Eq. (I.1). In case the uniaxial fatigue data is not available, it can be computed recurring to the relationships displayed in the previous Section.

However, this approach does not compute the stress-life curves directly from the monotonic properties. For this purpose, *S-N curves* may be calculated recurring to a stress-strain relation for the cyclic behaviour. For this purpose, the Ramberg-Osgood relationships are used

$$\varepsilon_a = \frac{\sigma_a}{E} + \left(\frac{\sigma_a}{K'} \right)^{1/n'} \quad (\text{I.14})$$

$$\gamma_a = \frac{\tau_a}{G} + \left(\frac{\tau_a}{K'_0} \right)^{1/n'_0} \quad (\text{I.15})$$

for tension and shear fatigue behaviour, respectively. The parameters K' and K'_0 are the tensile and shear cyclic strength coefficients respectively, and n'_0 is the shear cyclic hardening exponent. Taking into account Eqs. (I.8a) and (I.8b), it can be easily derived that the cyclic hardening coefficients can be calculated by

$$n' = \frac{b}{c} \quad (\text{I.16a})$$

$$n'_0 = \frac{b_0}{c_0}. \quad (\text{I.16b})$$

The cyclic strength coefficients are calculated with the following expressions:

$$K' = \frac{\sigma'_f}{(\varepsilon'_f)^{n'}} \quad (\text{I.17a})$$

$$K'_0 = \frac{\tau'_f}{(\gamma'_f)^{n'_0}}. \quad (\text{I.17b})$$

Meggiolaro and Castro [140] also summarized an extensive work done in this matter, providing several other expressions to calculate the Coffin-Mason's parameters. These relationships are displayed in Table I.1 [140].

I.4 Methodology

In order to assess the validity of the method within this study, a brief estimation for the EN-GJS-400-18U-LT cast iron was made, later to be compared with the calculated *S-N curves* (see Figs. 3.6 and 6.2) as reference data. For this purpose, only the monotonic tensile properties such as the Young's modulus, yield and ultimate strength, and Poisson's coefficient are known. These values can be found in Table 3.1 from Chapter 3. It is also important to note that no safety factors will be applied in this study, only accounting for the reference fatigue data.

The calculation process assumed the following steps:

- For the tension fatigue curve $\sigma_a - N_f$:
 1. Estimate the material's Brinell hardness recurring to Eq. (I.13);
 2. Compute the tension fatigue curve $\varepsilon_a - N_f$ with Eq. (I.12);
 3. Compute the tension *S-N curve* recurring to the stress-strain relationship from Eq. (I.14), taking in consideration Eq. (I.16a) and (I.17a).
- For the torsion fatigue curve $\tau_a - N_f$:
 1. Calculate the shear fatigue properties from the uniaxial data recurring to Eq. (I.11b) assuming ductile behaviour, and Eq. (I.11a) assuming brittle behaviour, giving the following expressions:

$$\tau'_f = \frac{4.25 \cdot \text{HB} + 225}{\sqrt{3}}, \quad \gamma'_f = \sqrt{3} \cdot \frac{0.32 \cdot (\text{HB})^2 - 478 \cdot \text{HB} + 191000}{E}, \quad (\text{I.18})$$

$$b_0 = -0.09, \quad c_0 = -0.56$$

$$\tau'_f = \frac{4.25 \cdot \text{HB} + 225}{1 + \nu}, \quad \gamma'_f = 2 \cdot \frac{0.32 \cdot (\text{HB})^2 - 478 \cdot \text{HB} + 191000}{E}, \quad (\text{I.19})$$

$$b_0 = -0.09, \quad c_0 = -0.56$$

respectively;

2. Compute the torsion fatigue curve $\gamma_a - N_f$ with Eq. (I.9);
3. Compute the torsion *S-N curve* recurring to the stress-strain relationship from Eq. (I.15), taking into consideration Eqs. (I.16b) and (I.17b).

Since EN-GJS-400-18U-LT is a semi-ductile cast iron, both ductile and brittle relationships were used to compute shear fatigue properties.

I.5 Results

The calculations were done for the complete range of cycles until failure, from 10^2 cycles up until 10^{10} cycles, comprising all the fatigue regimes. The purpose is to compare the estimated curves with the fatigue $S-N$ data available, computing the error. Note that for the shear fatigue behaviour, two estimated curves are compared, aiming to decide which curve is best suited.

Figures I.1a and I.1b display the results for this study, both for tensile and shear cases. For EN-GJS-400-18U-LT cast iron, the curves were poorly estimated, with over-conservative results.

For the tension load case (see Fig. I.1a), at higher number of cycles the estimation approximates from the reference curve, tending to a better approximation. However, in the LCF regime, where the plastic behaviour takes a significant portion of the damage, the curves deviate from each-other. This is expected because the $S-N$ curve is not valid for the lower life cycles, being a stress controlled test.

In torsion fatigue behaviour (see Fig. I.1b), the maximum principal strain relationship better estimates the fatigue properties, proving to deliver a more approximate curve. This would be expected because, despite being a ductile cast iron, these materials tend to show brittle behaviour, in general. In this case, the curves show similar behaviour throughout all the entire life range, but, display an approximation for higher life cycles.

Finally, estimation of tensile and torsion¹ estimations provide valid $S-N$ curves considering a scatter factor of 2, depicted in Figs. I.1c and I.1d.

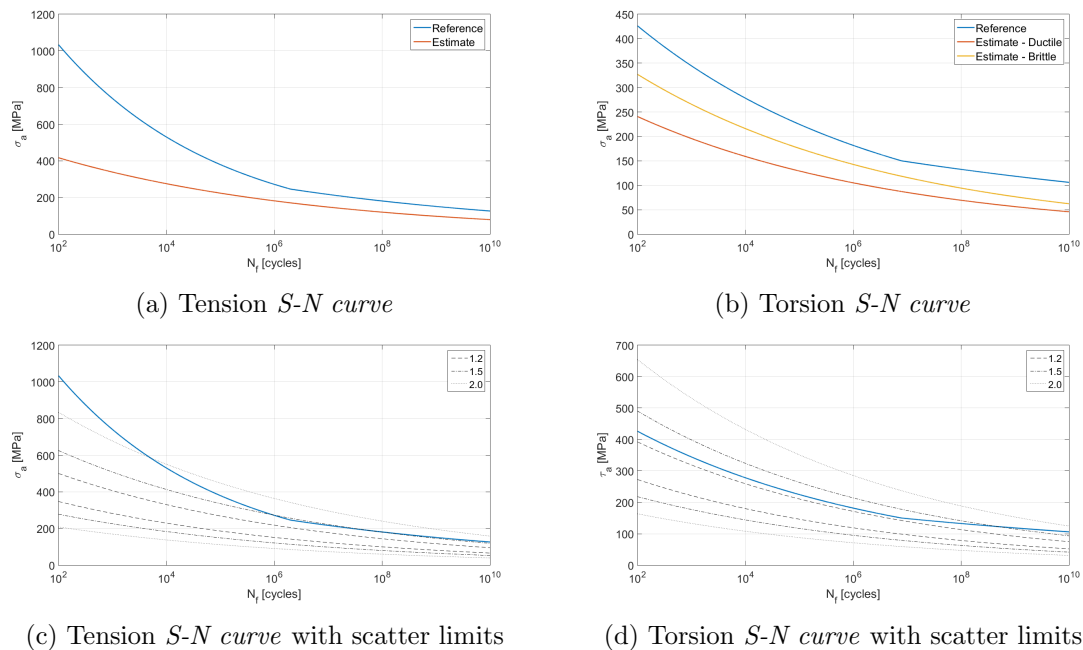


Figure I.1: Results for EN-GJS-400-18U-LT

¹for the maximum principal strain correlation criterion

Estimation methods for Coffin-Manson's parameters				
Estimate	σ'_f	ϵ'_f	b	c
Manson's universal slopes	$1.9 \cdot \sigma_u$	$0.76 \cdot \left[\ln \left(\frac{1}{1-RA} \right) \right]^{0.6}$	-0.12	-0.6
Manson's four-point	$1.25\sigma_f \cdot 2b$	$\frac{0.125}{20^c} \cdot \left[\ln \left(\frac{1}{1-RA} \right) \right]^{3/4}$	$\frac{\log(0.36 \cdot \sigma_u / \sigma_f)}{5.6}$	$\frac{1}{3} \log \frac{0.0066 - \sigma'_f (2 \times 10^4)^b / E}{0.239 \cdot \{\ln[1/(1-RA)]\}}$
Raske-Morrow	-	$0.002 \cdot (\sigma'_f / \sigma_y^2)^{1/n'}$	-	-
Mitchell (steels)	$\sigma_u + 345$	ϵ_f	$\frac{1}{6} \log \frac{0.5 \cdot \sigma_u}{\sigma_u + 345}$	-0.6 ³ . or -0.5 ⁴ .
Muralidharan-Manson	$0.623E \left(\frac{\sigma_u}{E} \right)^{0.832}$	$0.0196 \left(\frac{\sigma_u}{E} \right)^{-0.53} \cdot \left[\ln \left(\frac{1}{1-RA} \right) \right]^{0.155}$	-0.09	-0.56
Bäumel-Seeger (steels)	$1.5 \cdot \sigma_u$	$0.812 - 74 \cdot \frac{\sigma_u}{E}$ or 0.59^5 .	0.087	0.58
Bäumel-Seeger (Al and Ti)	$1.67 \cdot \sigma_u$	0.35	-0.095	-0.69
Ong	$\sigma_u \cdot (1 + \epsilon_f)$	ϵ_f	$\frac{1}{6} \log \frac{(\sigma_u/E)^{0.81}}{6.25 \cdot \sigma_f/E}$	$\frac{1}{4} \log \frac{0.0074 - \sigma'_f (10^4)^b / E}{2.074 \cdot \epsilon_f}$
Medians (steels)	$1.5 \cdot \sigma_u$	0.45	-0.09	-0.59
Medians (Al alloys)	$1.9 \cdot \sigma_u$	0.28	-0.11	-0.66

1. reduction in area
2. cyclic yield strength
3. for ductile steels
4. for strong steels
5. if $\sigma_u/E \leq 0.003$

Table I.1: Summary of Coffin-Manson's parameters estimations [140]

Matlab programs for the fatigue benchmarking

J.1 Bi-linear extrapolation of stress spectrum

```

1 function StressSpectrum(node)
2 %*****Computation of stress spectrum for specific node*****
3 %Read load case files
4 %p100kN
5 fileID=fopen( '.\fatWiz\fatWizStress\p100kN.txt' );
6 pdata=textscan( fileID , '%*f%f%f%f%f%f%f' , 'Delimiter' , '\n' , ...
7     'TreatAsEmpty' , ' ' , 'headerlines' , 3);
8 fclose( fileID );
9 pdata=cell2mat( pdata );
10 %n100kN
11 fileID=fopen( '.\fatWiz\fatWizStress\n100kN.txt' );
12 ndata=textscan( fileID , '%*f%f%f%f%f%f%f' , ...
13     'Delimiter' , '\n' , 'headerlines' , 3);
14 fclose( fileID );
15 ndata=cell2mat( ndata );
16 %*****
17 %Stress normalization options [100Kn load case]
18 Sp=pdata( node , : ) ./ 100;
19 Sn=ndata( node , : ) ./ 100;
20 fileID=fopen( 'FPitch.txt' );
21 Fpitch=textscan( fileID , '%f' , 'Delimiter' , '\n' );
22 fclose( fileID );
23 Fpitch=cell2mat( Fpitch );
24 %*****
25 %Stress spectrum calculation
26 S=zeros( length( Fpitch ) , length( Sp ) );
27 for i=1:length( Fpitch )
28     if Fpitch( i ) >= 0
29         S( i , : ) = Fpitch( i ) * Sp;
30     else
31         S( i , : ) = abs( Fpitch( i ) ) * Sn;
32     end
33 end
34 %*****

```

```

35 %Output to txt file
36 dlmwrite( 'StressSpec.txt',S);
37 end

```

J.2 Critical plane normal stress (DNV GL)

```

1 function Out=normalcritplane(rep)
2 %*****Critical plane normal stress*****
3 %Stress spectrum
4 fileID=fopen( 'StressSpec.txt' );
5 S=textscan( fileID , '%f,%f,%f,%f,%f,%f', 'Delimiter', '\n' );
6 fclose( fileID );
7 S=cell2mat( S );
8 %*****Compute equivalent stress*****
9 %Number of planes
10 np=24;
11 ang=linspace( 0,2*pi, np );
12 %Critical plane stress
13 Seq=zeros( length( S ),1 );
14 vmax=0;
15 imax=0;
16 t=linspace( 0,600, length( S ) );
17 for j=1:length( ang )
18     for i=1:length( S )
19         Seq( i)=(S( i,1)+S( i,2 ))/2+(S( i,1)-S( i,2 )) / ...
20             2*cos( 2*ang( j ) )+S( i,4 ) * sin( 2*ang( j ) );
21     end
22     %Rainflow cycle count
23     M=rainflow( Seq, t );
24     %Damage
25     D=0;
26     for i=1:length( M )
27         %Mean stress correction
28         s=meanstress( M( i,2 ),M( i,3 ), 'Linear' );
29         D=D+M( i,1 ) / nfat( s );
30     end
31     if D>vmax
32         vmax=D;
33         imax=j ;
34     end
35 end
36 Sf=zeros( length( S ),1 );
37 for i=1:length( S )
38     Sf( i)=(S( i,1)+S( i,2 ))/2+(S( i,1)-S( i,2 )) / ...
39         2*cos( 2*ang( imax ) )+S( i,4 ) * sin( 2*ang( imax ) );
40 end
41 %Display von mises parameter spectrum
42 t=linspace( 0,600, length( S ) );
43 figure( 'Name', 'Normal critical plane pseudo-parameter spectrum' )

```

```

44 plot(t,Sf*10^(-6),'LineWidth',2);
45 xlabel('Time [s]');
46 ylabel('\sigma_{NPP} [MPa]');
47 set(gca,'FontSize',20);
48 %*****Compute fatigue damage*****
49 %Damage
50 D=0;
51 M=rainflow(Sf,t);
52 for i=1:length(M)
53     %Mean stress correction
54     s=meanstress(M(i,2),M(i,3),'Linear');
55     D=D+M(i,1)/nfat(s);
56 end
57 Out=[D*rep,(D*rep)^(-2/(10.8+20.6))];
58 end
59 %*****Auxiliary functions*****
60 %S-N curve definition (Torsion)
61 function n=nfat(s)
62 if s>=300e6
63     n=7.9e6*(109e6/(300e6))^10.8;
64 elseif (s>=109e6)&&(s<300e6)
65     n=7.9e6*(109e6/s)^10.8;
66 elseif (s>77.02e6)&&(s<109e6)
67     n=7.9e6*(109e6/s)^20.6;
68 else
69     n=1e10;
70 end
71 end
72 %Mean stress correction
73 function s=meanstress(sa,sm,type)
74 switch type
75     case 'Goodman'
76         s=sa*(1+sm/(400e6));
77         if s>=2*220e6
78             s=2*220e6;
79         elseif s<0
80             s=0;
81         end
82     case 'Gerber'
83         s=sa*(1+(sm/(400e6))^2);
84         if s>=2*220e6
85             s=2*220e6;
86         elseif s<0
87             s=0;
88         end
89     case 'Soderberg'
90         s=sa*(1+sm/(220e6));
91         if s>=2*220e6
92             s=2*220e6;

```

```

93         elseif s<0
94             s=0;
95         end
96     case 'Linear'
97         s=sa+2*0.25*sm;
98         if s>=2*220e6
99             s=2*220e6;
100        elseif s<0
101            s=0;
102        end
103    end
104    end

```

J.3 Dang Van criterion

```

1  function Out=dangvan(rep)
2  %*****Findley critical plane model*****
3  %Stress spectrum
4  fileID=fopen('StressSpec.txt');
5  S=textscan(fileID,'%f,%f,%f,%f,%f,%f','Delimiter','\n');
6  fclose(fileID);
7  S=cell2mat(S);
8  %*****Compute equivalent stress*****
9  %Material factor
10 k=0.5711;
11 t=linspace(0,600,length(S));
12 Seq=zeros(length(S),1);
13 for i=1:length(S)
14     Sm=zeros(2,2);
15     Sm(1,1)=S(i,1);Sm(1,2)=S(i,4);Sm(2,1)=Sm(1,2);Sm(2,2)=S(i,2)
16     ;
17     Sh=1/3*(Sm/eye(2))*eye(2);
18     Sf=Sm-Sh;
19     sh=(S(i,1)+S(i,2))/3;
20     s=eig(Sf);
21     if(min(s)<0)
22         ss=1/2*(max(s)-min(s));
23     else
24         ss=1/2*(max(s)-0);
25     end
26     Seq(i)=ss+k*sh;
27 %Display von mises parameter spectrum
28 figure('Name','Dang Van pseudo-parameter spectrum');
29 plot(t,Seq*10^(-6),'LineWidth',2);
30 xlabel('Time [s]');
31 ylabel('\sigma_{DVP} [MPa]');
32 set(gca,'FontSize',20);
33 %*****Compute fatigue damage*****

```

```

34 %Damage
35 D=0;
36 M=rainflow (Seq , t ) ;
37 for i =1:length (M)
38     %Mean stress correction
39     s=meanstress (M(i , 2 ) ,M(i , 3 ) , 'Linear ' ) ;
40     D=D+M(i , 1 ) /nfat ( s ) ;
41 end
42 Out=[D*rep , (D*rep) ^ ( -2/(10.8+20.6) ) ] ;
43 end
44 %***** Auxiliary functions *****
45 %S-N curve definition (Torsion)
46 function n=nfat (s)
47 if s >=300e6
48     n=7.9e6 * (109e6 / (300e6) ) ^ 10.8 ;
49 elseif (s >=109e6) && (s < 300e6)
50     n=7.9e6 * (109e6 / s) ^ 10.8 ;
51 elseif (s > 77.02e6) && (s < 109e6)
52     n=7.9e6 * (109e6 / s) ^ 20.6 ;
53 else
54     n=1e10 ;
55 end
56 end
57 %Mean stress correction
58 function s=meanstress (sa , sm , type)
59 switch type
60     case 'Goodman '
61         s=sa * (1 + sm / (400e6) ) ;
62         if s >= 2 * 220e6
63             s = 2 * 220e6 ;
64         elseif s < 0
65             s = 0 ;
66         end
67     case 'Gerber '
68         s=sa * (1 + (sm / (400e6) ) ^ 2) ;
69         if s >= 2 * 220e6
70             s = 2 * 220e6 ;
71         elseif s < 0
72             s = 0 ;
73         end
74     case 'Soderberg '
75         s=sa * (1 + sm / (220e6) ) ;
76         if s >= 2 * 220e6
77             s = 2 * 220e6 ;
78         elseif s < 0
79             s = 0 ;
80         end
81     case 'Linear '
82         s=sa + 2 * 0.25 * sm ;

```

```

83         if s >= 2*220e6
84             s = 2*220e6;
85         elseif s < 0
86             s = 0;
87         end
88     end
89 end

```

J.4 Findley criterion

```

1  function Out=findley(rep)
2  %*****Findley critical plane model*****
3  %Stress spectrum
4  fileID=fopen('StressSpec.txt');
5  S=textscan(fileID, '%f,%f,%f,%f,%f,%f', 'Delimiter', '\n');
6  fclose(fileID);
7  S=cell2mat(S);
8  %*****Compute equivalent stress*****
9  %Number of planes
10 np=24;
11 ang=linspace(0, 2*pi, np);
12 %Material factor
13 k=0.5711;
14 %Critical plane stress
15 vmax=0;
16 imax=0;
17 t=linspace(0, 600, length(S));
18 for j=1:length(ang)
19     Seq=zeros(length(S), 1);
20     for i=1:length(S)
21         Sn=(S(i,1)+S(i,2))/2+(S(i,1)-S(i,2))/2*cos(2*ang(j)) ...
22             +S(i,4)*sin(2*ang(j));
23         Ss=-(S(i,1)-S(i,2))/2*sin(2*ang(j)) ...
24             +S(i,4)*cos(2*ang(j));
25         Seq(i)=Ss+k*Sn;
26     end
27 %Rainflow cycle count
28 M=rainflow(Seq, t);
29 %Damage
30 D=0;
31 for i=1:length(M)
32     %Mean stress correction
33     s=meanstress(M(i,2), M(i,3), 'Linear');
34     D=D+M(i,1)/nfat(s);
35 end
36 if D > vmax
37     vmax=D;
38     imax=j;
39 end

```

```

40 end
41 Sf=zeros(length(S),1);
42 for i=1:length(S)
43     Sn=(S(i,1)+S(i,2))/2+(S(i,1)-S(i,2))/2*cos(2*ang(imax))...
44         +S(i,4)*sin(2*ang(imax));
45     Ss=-(S(i,1)-S(i,2))/2*sin(2*ang(imax))...
46         +S(i,4)*cos(2*ang(imax));
47     Sf(i)=Ss+k*Sn;
48 end
49 %Display von mises parameter spectrum
50 t=linspace(0,600,length(S));
51 figure('Name','Findley pseudo-parameter spectrum');
52 plot(t,Sf*10^(-6),'LineWidth',2);
53 xlabel('Time [s]');
54 ylabel('\sigma_{FPP} [MPa]');
55 set(gca,'FontSize',20);
56 %*****Compute fatigue damage*****
57 %Damage
58 D=0;
59 M=rainflow(Sf,t);
60 for i=1:length(M)
61     %Mean stress correction
62     s=meanstress(M(i,2),M(i,3),'Linear');
63     D=D+M(i,1)/nfat(s);
64 end
65 Out=[D*rep,(D*rep)^(-2/(10.8+20.6))];
66 end
67 %*****Auxiliary functions*****
68 %S-N curve definition (Torsion)
69 function n=nfat(s)
70 if s>=300e6
71     n=7.9e6*(109e6/(300e6))^10.8;
72 elseif (s>=109e6)&&(s<300e6)
73     n=7.9e6*(109e6/s)^10.8;
74 elseif (s>77.02e6)&&(s<109e6)
75     n=7.9e6*(109e6/s)^20.6;
76 else
77     n=1e10;
78 end
79 end
80 %Mean stress correction
81 function s=meanstress(sa,sm,type)
82 switch type
83     case 'Goodman'
84         s=sa*(1+sm/(400e6));
85         if s>=2*220e6
86             s=2*220e6;
87         elseif s<0
88             s=0;

```

```

89         end
90     case 'Gerber'
91         s=sa*(1+(sm/(400e6))^2);
92         if s>=2*220e6
93             s=2*220e6;
94         elseif s<0
95             s=0;
96         end
97     case 'Soderberg'
98         s=sa*(1+sm/(220e6));
99         if s>=2*220e6
100             s=2*220e6;
101         elseif s<0
102             s=0;
103         end
104     case 'Linear'
105         s=sa+2*0.25*sm;
106         if s>=2*220e6
107             s=2*220e6;
108         elseif s<0
109             s=0;
110         end
111 end
112 end

```

J.5 Signed Von Mises equivalent stress

```

1 function Out=vonmisesfat(rep)
2 %*****Von mises fatigue equivalent stress model*****
3 %Stress spectrum
4 fileID=fopen('StressSpec.txt');
5 S=textscan(fileID,'%f,%f,%f,%f,%f,%f','Delimiter','\n');
6 fclose(fileID);
7 S=cell2mat(S);
8 %Compute equivalent stress
9 Seq=zeros(length(S),1);
10 for i=1:length(S)
11     s1=(S(i,1)+S(i,2))/2+sqrt((S(i,1)-S(i,2))^2/4+S(i,4)^2);
12     s2=(S(i,1)+S(i,2))/2-sqrt((S(i,1)-S(i,2))^2/4+S(i,4)^2);
13     if abs(s1)>=abs(s2)
14         if s1 >= 0
15             Seq(i)=sqrt(S(i,1)^2+S(i,2)^2+S(i,1)*S(i,2)+...
16                 3*S(i,4)^2);
17         elseif s1 < 0
18             Seq(i)=-sqrt(S(i,1)^2+S(i,2)^2+S(i,1)*S(i,2)+...
19                 3*S(i,4)^2);
20         end

```



```

21     else
22         if s2 >= 0
23             Seq(i)=sqrt(S(i,1)^2+S(i,2)^2+S(i,1)*S(i
24                 ,2) ...
25                 +3*S(i,4)^2);
26             elseif s2 < 0
27                 Seq(i)=-sqrt(S(i,1)^2+S(i,2)^2+S(i,1)*S(
28                     i,2) ...
29                     +3*S(i,4)^2);
30         end
31     end
32 %Display von mises parameter spectrum
33 t=linspace(0,600,length(S));
34 figure('Name','Von mises stress parameter spectrum');
35 plot(t,Seq*10^(-6),'LineWidth',2);
36 xlabel('Time [s]');
37 ylabel('\sigma_{VMP} [MPa]');
38 set(gca,'FontSize',20);
39 %Rainflow cycle count
40 M=rainflow(Seq,t);
41 %*****Compute fatigue damage*****
42 %Damage
43 D=0;
44 for i=1:length(M)
45     %Mean stress correction
46     s=meanstress(M(i,2),M(i,3),'Linear');
47     D=D+M(i,1)/nfat(s);
48 end
49 Out=[D*rep,(D*rep)^(-2/(6.9+12.8))];
50 %*****Auxiliary functions*****
51 %S-N curve definition (Tensile)
52 function n=nfat(s)
53 if s>=400e6
54     n=2e6*(178.26e6/(400e6))^6.9;
55 elseif (s>=178.26e6)&&(s<400e6)
56     n=2e6*(178.26e6/s)^6.9;
57 elseif (s>98.0435e6)&&(s<178.26e6)
58     n=2e6*(178.26e6/s)^12.8;
59 else
60     n=((246e6)^12.8*2e6)/((135e6)^12.8);
61 end
62 end
63 %Mean stress correction
64 function s=meanstress(sa,sm,type)
65 switch type
66     case 'Goodman'
67         s=sa*(1+sm/(400e6));

```

```

68     if s >= 2*220e6
69         s = 2*220e6;
70     elseif s < 0
71         s = 0;
72     end
73     case 'Gerber'
74         s = sa * (1 + (sm / (400e6))^2);
75         if s >= 2*220e6
76             s = 2*220e6;
77         elseif s < 0
78             s = 0;
79         end
80     case 'Soderberg'
81         s = sa * (1 + sm / (220e6));
82         if s >= 2*220e6
83             s = 2*220e6;
84         elseif s < 0
85             s = 0;
86         end
87     case 'Linear'
88         s = sa + 2*0.25*sm;
89         if s >= 2*220e6
90             s = 2*220e6;
91         elseif s < 0
92             s = 0;
93         end
94 end
95 end

```

Anslys examples

In order to work efficiently with Ansys WB 2019 R3, several exercises were made to introduce the basic functionalities and tools that the software provides. The work mainly focused on the static analysis and topology optimization tool, but some other areas such as modal and transient analysis were briefly looked at. Aiming for a progressive evolution, first the most classic and simple example was assessed, namely the cantilever beam, with a concentrated force and the free end. Then, a more complex situation was computed, looking to optimize a hook supported with pre-tensioned bolted connections and a concentrated load. Here is a scheme of the examples:

- Cantilever beam
 - Concentrated load at the midpoint of the free end
 - Concentrated load at the extreme of the free end

- Hook

For every example, the model formulation (meshing, boundary conditions) and the results are exposed, for the static (stress, displacements) and topology optimization (density output) analysis. Lastly, note that for all the examples, a default linear elastic material was employed called “structural steel”. Its parameters can be observed in Table K.1.

E [GPa]	Poisson ratio ν	Density ρ [kg m ⁻³]	σ_y [MPa]	σ_u [MPa]
200	0.3	7850	250	460

Table K.1: Material properties of Ansys structural steel

K.1 Cantilever beam

The cantilever model is a classical example both in static and topology analysis, therefore being a good starting point not only for its simplicity, but also for allowing validation with the literature results. The beam has a rectangular cross section. As earlier stated, the beam is subjected to a concentrated load, in the vertical direction. Table K.2 gives an overview of the initial geometry (see Fig. K.1) and loading conditions.

Span [mm]	Thickness [mm]	Heigh [mm]	Load [kN]
2000	400	1000	300

Table K.2: Geometry and loading aspects for the cantilever beam example

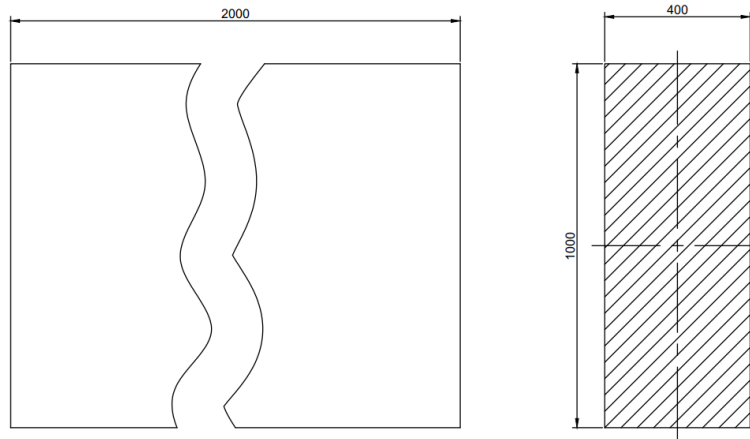
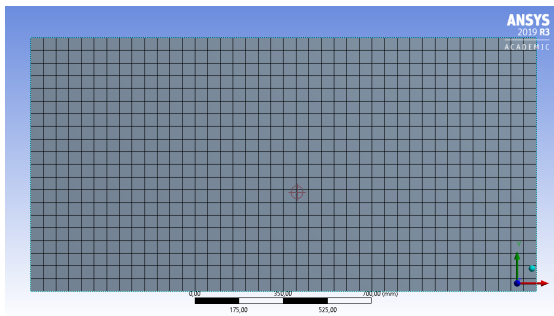


Figure K.1: Cantilever initial geometry

K.1.1 Mesh

Regarding the mesh, 800 plane elements (PLANE 183), displayed in Fig. K.2a, adding up to a total of 2521 nodes, with plane stress conditions, neglecting the displacements across the beam thickness. Note that there are two extra elements (CLOAD201), for aiding the application of the concentrated load.



(a) Mesh (PLANE183) for the cantilever beam

```

*** ELEMENT MATRIX FORMULATION TIMES
TYPE   NUMBER  ENAME   TOTAL CP  AVE CP
-----
1       800  PLANE183  0.094    0.000117
2         2  CLOAD201  0.000    0.000000
Time at end of element matrix formulation CP = 0.578125.
    
```

(b) Mesh properties for the cantilever beam

Figure K.2: Meshing aspects for the cantilever beam example

K.1.2 Boundary conditions

For the boundary conditions (see Fig. K.3), all the degrees of freedom in the nodes on the fixed support region are constrained (no displacements), and a concentrated load is applied at the free end. Here, two load cases are in order:

1. Load at midpoint (see Fig. K.3a)
2. Load at the low-end extreme (see Fig. K.3b)

differing only at the location of the applied load.

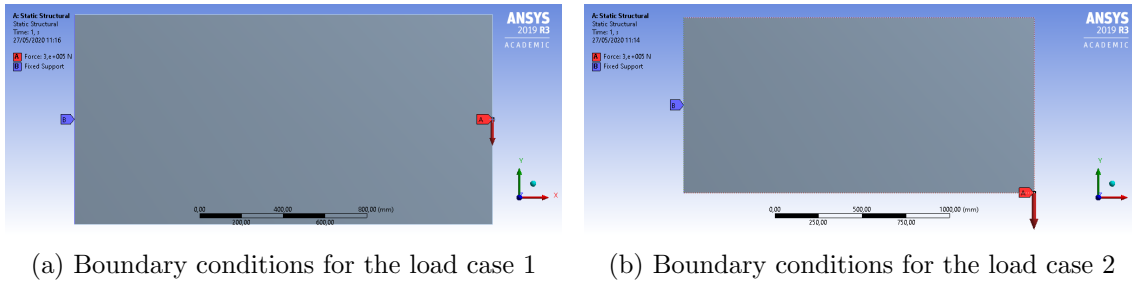


Figure K.3: Boundary conditions for the cantilever beam example

K.1.3 Optimization setup

Making use of Ansys topology optimization tool, a density based algorithm was proposed, to minimize compliance with a minimum mass restriction. In terms optimization region, only the regions of applied boundary conditions were excluded.

K.1.4 Results

Figures K.4 and K.6 display the optimal solutions for each mass restriction. One can conclude that, as the restrictions loosens, in both load cases, the geometry evolves to a thin section truss structure. This results are in agreement with the literature [109]. The optimal structures better distribute the load, as displayed in Figs. K.5 and K.7, resulting in a stiffer geometry.

Tables K.3 and K.4 present an overview of the overall results in terms of weight reduction, stresses and displacements. Analysing the tables, it can be concluded that the load case 2 is more severe, since an optimization is more harmful in terms of maximum stress and displacement. Finally, it can be concluded that the displacement is the most sensitive parameter, when relating with the changes in the design variables.

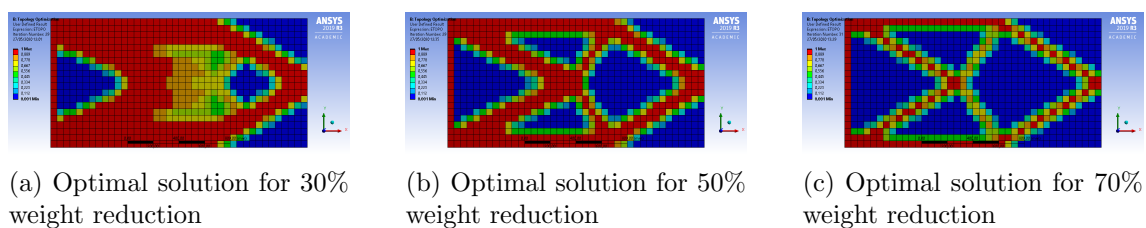


Figure K.4: Optimal solutions for load case 1

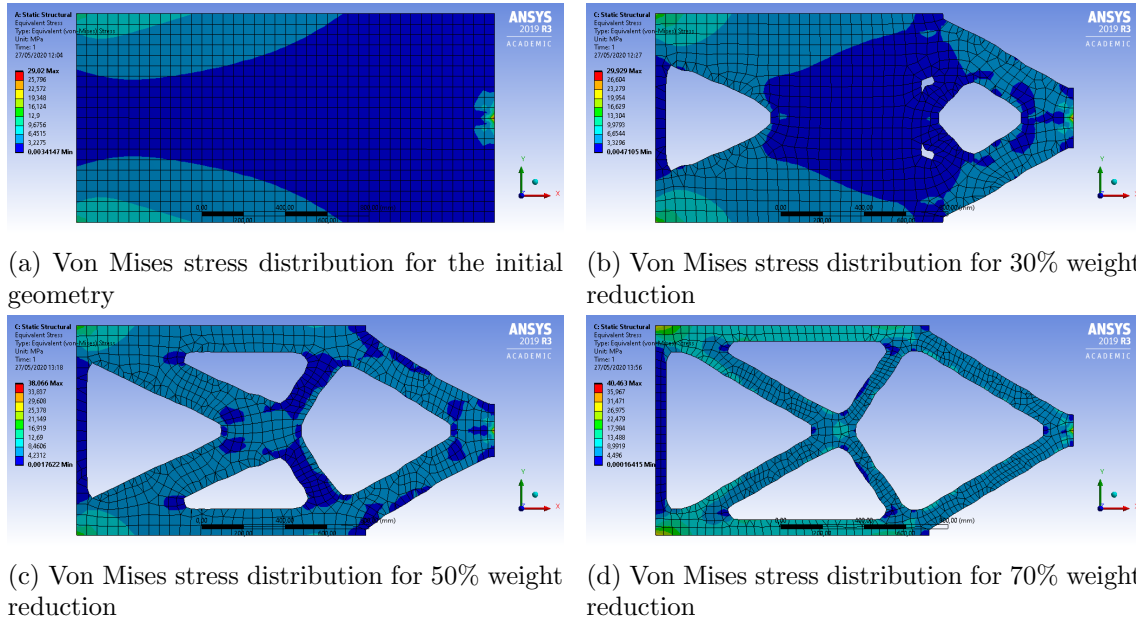


Figure K.5: Stress results for load case 1

Model	Weight reduction	Max. Stress [MPa]	Max. Displacement [mm]
Initial	-	29.020	0.1497
70% mass	30%	29.020	0.1730
50% mass	50%	38.066	0.2325
30% mass	70%	40.463	0.3657

(a) Absolute values for stress and displacement

Model	Weight reduction	Stress variation	Displacement variation
70% mass	30%	3.13%	15.56%
50% mass	50%	37.17%	55.31%
30% mass	70%	39.43%	144.29%

(b) Model comparison

Table K.3: Results overview for load case 1

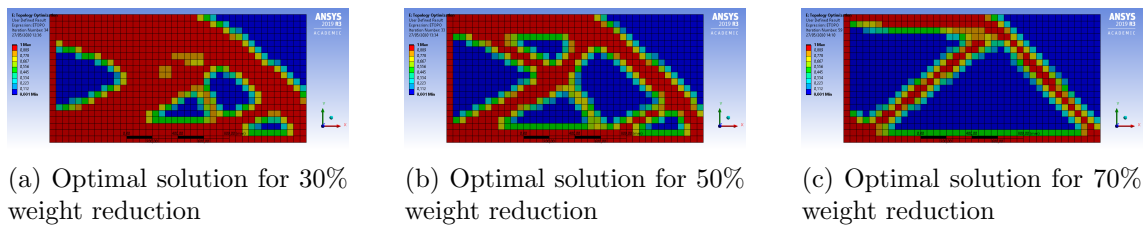
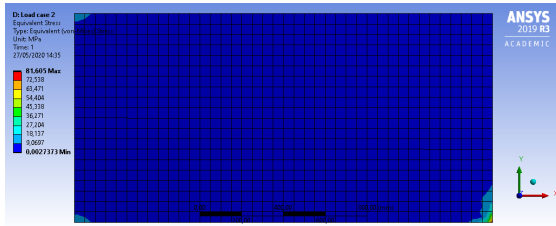
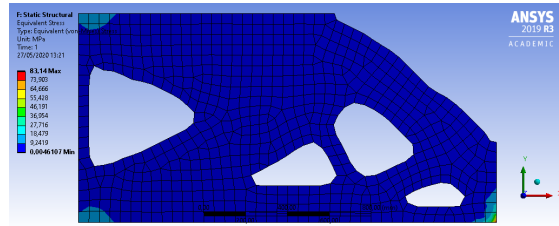


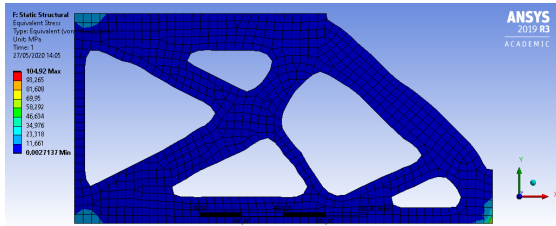
Figure K.6: Optimal solutions for load case 2



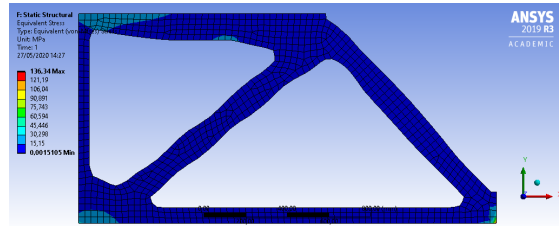
(a) Von Mises stress distribution for the initial geometry



(b) Von Mises stress distribution for 30% weight reduction



(c) Von Mises stress distribution for 50% weight reduction



(d) Von Mises stress distribution for 70% weight reduction

Figure K.7: Stress results for load case 2

Model	Weight reduction	Max. Stress [MPa]	Max. Displacement [mm]
Initial	-	81.605	0.1765
70% mass	30%	83.140	0.2050
50% mass	50%	104.920	0.2642
30% mass	70%	136.340	0.4345

(a) Absolute values for stress and displacement

Model	Weight reduction	Stress variation	Displacement variation
70% mass	30%	1.88%	16.15%
50% mass	50%	28.57%	49.69%
30% mass	70%	67.07%	146.18%

(b) Model comparison

Table K.4: Results overview for load case 2

K.2 Hook support

Looking for a more challenging optimization problem, is proposed to minimize the compliance of a hook geometry in order to obtain a better performance. The geometry of the hook can be observed in Fig. K.8. The complexity of the example comes with modelling the hook in accordance with reality. This comes by simulating the bolted connections and its pre-tension, as well as contacts. Therefore, the model geometry is composed by the hook, the bolts and a support body for fixing the hook.

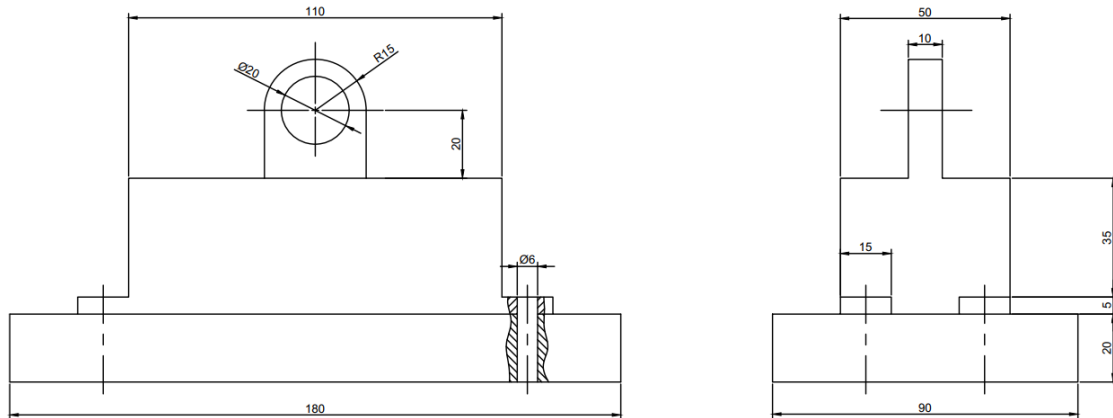


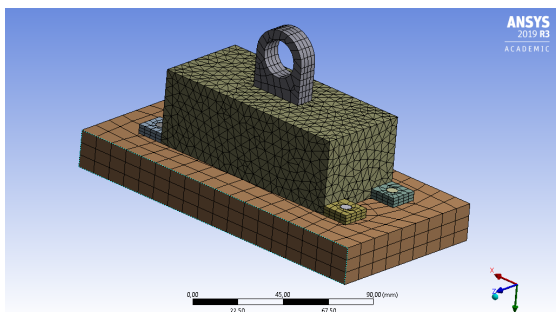
Figure K.8: Hook initial geometry

K.2.1 Mesh

The formulated mesh is composed by two different elements:

- Beam elements (BEAM188)
- Solid elements (SOLID186/SOLID187)

In total, they add up to 20 beam elements and 16410 solid elements. An overview on the mesh data is displayed in Fig. K.9. Additional elements are added in the pre-processing to compute the contacts (CONTA174) and pre-tensioning (PRETS179).



(a) Mesh for the hook example

*** ELEMENT MATRIX FORMULATION TIMES					
TYPE	NUMBER	ENAME	TOTAL CP	AVE CP	
1	5	BEAM188	0.000	0.000000	
2	5	BEAM188	0.000	0.000000	
3	5	BEAM188	0.000	0.000000	
4	5	BEAM188	0.000	0.000000	
5	699	SOLID186	0.172	0.000246	
6	69	SOLID186	0.000	0.000000	
7	60	SOLID186	0.000	0.000000	
8	152	SOLID186	0.031	0.000206	
9	15253	SOLID187	1.531	0.000100	
10	60	SOLID186	0.016	0.000260	
11	63	SOLID186	0.016	0.000248	
12	54	SOLID186	0.016	0.000289	

(b) Mesh properties for the hook example

Figure K.9: Meshing aspects for the hook example

K.2.2 Contacts and joints

Since one is dealing with multiple bodies, must model the contacts or joints between the elements of the interface regions. To simulate the connection of the bolts, a fixed joint is defined on the support side and in the head of the bolt, the last with a pinball region to characterize the crushing of the material by the bolt's head. A contact is defined between the hook and the support, which is a no-separation contact. Table K.5 provides an overview of the contact and joints. However, there is room for improvement in this part. For instance simulating a friction contact in the hook-support interface. But, in order to not compromise the computational cost, only simple linear contacts are employed.

Item	Type	Members	Quantity	Formulation	Observations
1	Contact	Hook/Support	1	No separation	-
2	Joint	Bolt/Support	4	Fixed	-
3	Joint	Bolt/Hook	4	Fixed	Pinball radius of 5 mm; rigid behaviour

Table K.5: Overview of contact/joint modelling for the hook example

K.2.3 Boundary conditions

The boundary conditions (see Fig. K.10) are divided in a two step analysis. In the first analysis a pre-tension load is applied to the beam elements characterizing the bolts, and fixing the load towards the next step, where a vertical load is applied to the hook. In all steps, all degrees of freedom corresponding the nodes in the bottom face of the support are constrained (fixed support). Table K.6 displays an overview of the boundary conditions.

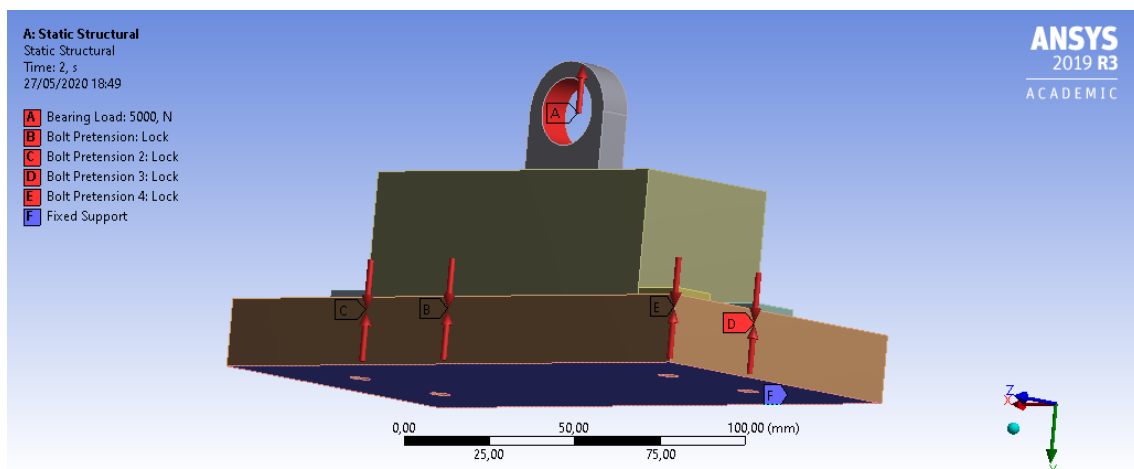


Figure K.10: Boundary conditions for the hook example

Item	Type	Members	Quantity	Value [kN]
1	Fixed support	Support (bottom face)	1	-
2	Bearing load	Hook	1	5 (Y component)
3	Bolt pre-tension	Bolt	4	5

Table K.6: Overview on boundary conditions for the hook example

K.2.4 Optimization setup

Despite dealing with multiple bodies, only the centre chunk of the hook is the optimization domain. Both the body where the load is applied and the bodies for the bolted connections are not advisable to suffer modification due to installation requirements. Moreover, the centre part of the hook is where there is more room for improvement, in terms of weigh and stress distribution.

The main goal is to minimize the compliance, but several constraints were applied to obtain a desirable solution. In terms of constraints, there are four types:

1. Mass
2. Global Von Mises stress
3. Minimum member size
4. Symmetry

Table K.7 displays an overview for the optimization constrain.

Item	Type	Name	Goal	Value
1	Objective	Compliance	Minimize	-
2	Constraint	Mass	Minimum	65% (of initial)
3	Constraint	Member size	Minimum	10 mm
4	Constraint	Symmetry	Y Plane	-
5	Constraint	Symmetry	X Plane	-

Table K.7: Overview of the optimization setup for the hook example

K.2.5 Results

Figure K.11 displays the optimal solution for several weight reductions. It can be concluded that the optimized solution evolves towards a “spider-like” truss structure, in agreement with the example from Section K.1.

Table K.8 is an overview of the results of the optimization study. The massive increase in maximum stress¹ and displacement² suggests a high sensitivity towards the model changes in the respective domain. However, this may also state the fact that the initial domain was over conservative, proven by the maximum stress in the 70% weight reduction optimal solution.

¹the maximum stress concerns only the optimized domain

²the displacement concerns the overall model value

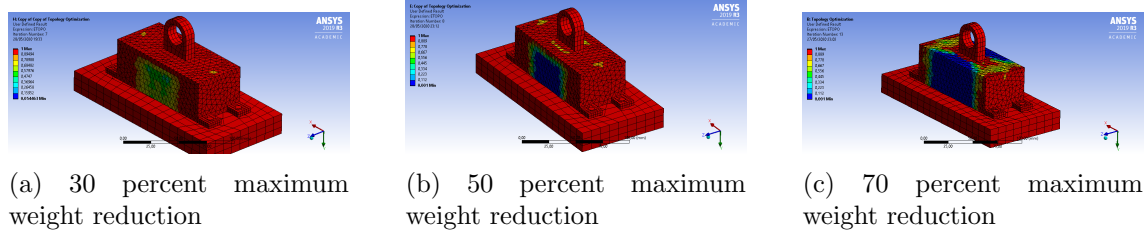


Figure K.11: Optimal solutions for the hook example

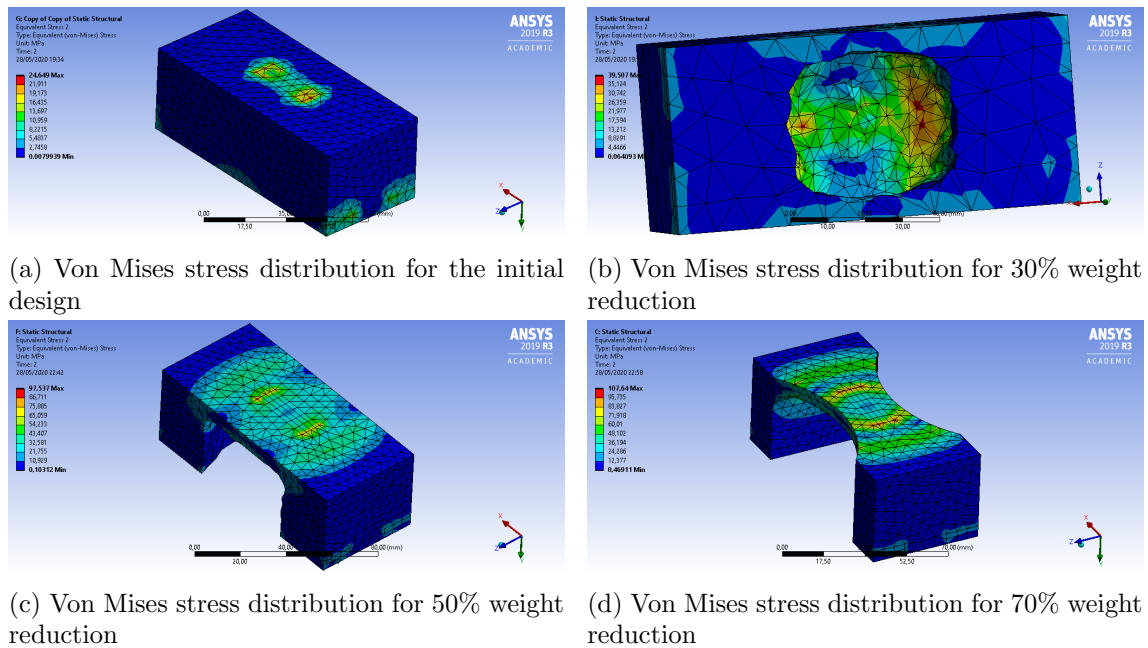


Figure K.12: Stress results for the hook example

Model	Weight reduction	Max. Stress [MPa]	Max. Displacement [mm]
Initial	-	29.020	0.0227
70% mass	30%	24.649	0.0272
50% mass	50%	39.517	0.0426
30% mass	70%	107.64	0.0549

(a) Absolute values for stress and displacement

Model	Weight reduction	Stress variation	Displacement variation
70% mass	30%	60.32%	19.82%
50% mass	50%	275.70%	87.67%
30% mass	70%	336.69%	141.85%

(b) Model comparison

Table K.8: Results overview for the hook example

K.2.6 Additional notes

In order to overcome some modelling difficulties, not stated in the previous sections, some program procedures were needed, to achieve the desired optimal solution. This because the optimal solution needs to have practical viability in the sense that the optimal domain needs to connect the region where the load is applied to the domains of the connecting bolts. Therefore, the optimized body was separated and an exclusion region (for the optimization) was set at the interface with the other bodies. Aiming to hold together the five bodies, bonded contacts were created to connected the respective nodes.

Finally, difficulties were found in modelling the optimal shape for the 70% weight reduction, given by the complex shape, therefore not allowing for the Ansys educational version to cope with it. To overcome this problem, a simplification of the optimal design was made, respecting the overall shape and dimensions. So, bear in mind that some deviations in terms of mass reduction may be present.